THE UNIVERSITY OF ALBERTA

PENETRATION OF PARTICLES THROUGH RECTANGULAR AND L-SHAPED CRACKS

By

CHWEN-JYH JENG

A THESIS

SUMITTED TO THE FACULTY OF GRADUATE STUDIES AND

RESEARCH IN PARTIAL FULFILMENT OF THE REQUIREMENTS FOR

THE DEGREE OF DOCTOR OF PHILOSOPHY

IN

ENVIRONMENTAL SCIENCE

DEPARTMENT OF CIVIL & ENVIRONMENTAL ENGINEERING

EDMONTON, ALBERTA

SPRING 2003

National Library
of Canada

Acquisitions and
Bibliographic Services

395 Wellington Street
Ottawa ON K1A 0N4
Canada

Bibliothèque nationale
du Canada

Acquisisitons et
services bibliographiques

395, rue Wellington
Ottawa ON K1A 0N4
Canada

Your file Votre référence
ISBN: 0-612-82120-X
Our file Notre référence
ISBN: 0-612-82120-X

The author has granted a non-exclusive licence allowing the National Library of Canada to reproduce, loan, distribute or sell copies of this thesis in microform, paper or electronic formats.

The author retains ownership of the copyright in this thesis. Neither the thesis nor substantial extracts from it may be printed or otherwise reproduced without the author's permission.

L'auteur a accordé une licence non exclusive permettant à la Bibliothèque nationale du Canada de reproduire, prêter, distribuer ou vendre des copies de cette thèse sous la forme de microfiche/film, de reproduction sur papier ou sur format électronique.

L'auteur conserve la propriété du droit d'auteur qui protège cette thèse. Ni la thèse ni des extraits substantiels de celle-ci ne doivent être imprimés ou aturement reproduits sans son autorisation.

Canada

UNIVERSITY OF ALBERTA

LIBRARY RELEASE FORM

NAME OF AUTHOR: CHWEN-JYH JENG

TITLE OF THESIS: PENETRATION OF PARTICLES THROUGH RECTANGULAR AND L-SHAPED CRACKS

DEGREE: DOCTOR OF PHILOSOPHY

YEAR THIS DEGREE WAS GRANTED: 2003

Permission is hereby granted to the University of Alberta Library to reproduce single copies of this thesis and to lend or sell such copies for private, scholarly, or scientific research purposes only.

The author reserves all other publication and other rights in association with the copyright in the thesis, and except as herein before provided, neither the thesis nor any substantial portion thereof may be printed or otherwise reproduced in any material form whatever without the author's prior written permission.

(Signed) Chwen-jyh Jeng

PERMANENT ADDRESS:

10-10516-79 Avenue
Edmonton, Alberta, T6E 1R8

Dated April 15, 2003

THE UNIVERSITY OF ALBERTA

FACULTY OF GRADUATE STUDIES AND RESEARCH

The undersigned certify that they have read, and recommend to the Faculty of Graduate Studies and Research, for acceptance, a thesis entitled PENETRATION OF PARTICLES THROUGH RECTANGULAR AND L-SHAPED CRACKS submitted by CHWEN-JYH JENG in partial fulfillment of the requirements for the degree of DOCTOR OF PHILOSOPHY in ENVIRONMENTAL ENGINEERING.

.....Dr. Warren B. Kindzierski
Supervisor

.....Dr. Dan W. Smith
Co-Supervisor

.....Dr. Ian D. Buchanan
Committee Chair

.....Dr. Mark Loewen
Committee Member

.....Dr. Brian Fleck
Committee Member

.....Dr. Grant Allen
External Examiner

Date April 14, 2003

ABSTRACT

This study simulates particle penetration through typical cracks in residential buildings. The modeling approach combined an infiltration model and several particle deposition models to simulate penetration through rectangular cracks and L-shaped cracks. The modeling considered particle deposition induced from Brownian diffusion and/or gravitational sedimentation. An L-Shaped crack was treated as the combination of a horizontal and a vertical rectangular sections to estimate overall particle penetration coefficients.

For air infiltration modeling, this study used a semi-empirical model to estimate infiltration flow through rectangular and L-shaped cracks. A chamber was designed to validate the model. Experimental results indicated that this model agreed well with experimental results for both types of cracks. Using this model, infiltration flow field was assumed laminar. The laminar flow assumption was validated with an entrance length parameter. It was found that entrance length was mostly less than 5% of the crack length for typical residential conditions ($\Delta P \leq 10$ Pa). The laminar flow assumption was generally valid for crack heights (H) < 0.5 mm and crack lengths (L) > 30 mm cracks.

This study used a particle transport model to estimate particle penetration coefficient (P_p) for cracks of arbitrary incline angles. The model was used to simulate particle penetration through rectangular cracks and L-shaped cracks. For the same crack geometries, the model indicates that a horizontal crack provides better protection from particle penetration than incline cracks. Gravitational sedimentation is the dominant particle deposition mechanism for micron-sized particles (≥ 1 μm), while Brownian diffusion is a significant or dominates deposition of submicron-sized particles (< 1 μm).

Visual examination indicated that both inertial impaction and entrance cut off were not significant for typical residential building conditions.

Particle penetration through typical cracks was investigated in an outdoor-indoor chamber. This study used a non-intrusive laser particle dynamic analyzer to measure particle concentrations at crack entrance and exit. The concentration ratio at crack exit over entrance was defined as P_p. Experimental results agreed reasonably with the particle penetration model. The deviations from theoretical penetration coefficients were mostly less than 5%. Nearly complete penetration was found for $H > 0.406$ mm and $L < 30$ mm cracks.

ACKNOWLEDGEMENT

The accomplishment of this thesis must be attributed to many contributors. In the beginning, I would like to express my great respect to my supervisor, Dr. Warren B. Kindzierski, and my co-supervisor, Dr. Daniel W. Smith, for their encouragement and patient instruction during the past five years. I also would like to express my sincere appreciation to my Examining Committee Members, Dr. Grant Allen, Dr. Brian Fleck and Dr. Mark Loewen. Your critical comments not only improve the quality of the thesis, but also extend the scope of this research.

I would like to thank the Toxcon HSRC Inc. for their support during my aerosol generator study as well. Especially, I appreciate Dr. Robert E. Rogers for his generosity and kindly help during my research.

Finally, I would like to thank those friends who accompanied me through this period of time. Of course, I must thank my parents and all family members. Your encouragement guided me through this challenge.

It is time to go on another journey. I will always remember those who help me in the past.

LIST OF SYMBOL

A = Stack coefficient

a = Area, m^2

B = Wind coefficient

C = Dimensionless particle concentration, c/c_0

C_b = Empirical constant for the orifice flow equation

C_c = Cunningham slip coefficient

C_d = Drag coefficient

C_i = Indoor pollutant concentration, mg/m^3

C_o = Outdoor pollutant concentration, mg/m^3

C_z = Discharge coefficient

c = Particle concentration, $No./m^3$

c_o = Particle concentration at the entrance of a crack, $No./m^3$

D = Particle diffusivity, m^2/s

D_i = Dilution ratio

D_j = Nozzle diameter, m

d_a = Particle aerodynamic diameter, 10^{-6} m (i.e. μm)

d_p = Particle diameter, 10^{-6} m (i.e. μm)

D_h = Hydraulic diameter. $D_h \sim 4h$ for narrow cracks, m

F = Force, Newton

F_b = Buoyancy force, Newton

F_d = Drag force, Newton

F_g = Gravity force, Newton

f = Volume fraction of microspheres in stock suspension

f_d = Frequency of Doppler bursts, s^{-1}

GSD = Geometric standard deviation

g = Gravitational acceleration, m/s^2

H = Crack height, m

h = Half-height of a crack, $h = H/2$, m

I/O = Ratio of indoor to outdoor pollutant concentration

K = Boltzmann's constant

k = Particle deposition velocity, m/s

L = Crack length, m

L_e = Entrance length, m

M = Number of horizontal grids

m = Mass, kg

N = Number of vertical grids

NMD = Number mean diameter, μm

NP = Dimensionless differential pressure parameter

NQ = Dimensionless Reynolds number expressed with infiltration flow rate

n = Empirical constant for the orifice flow equation

P_p = Particle penetration coefficient

Pe = Peclet number

ΔP = Differential pressure across a crack, Pa

$p(z)$ = Probability of finding z microspheres in a droplet

q = Infiltration flow rate, m^3/s

R = Ratio of singlet microspheres

Re = Reynolds number

S = Indoor source emission rate, 10^{-6} kg/s

s = Stopping distance, m

Stk = Stock number

T = Absolute temperature, °K

t = Time, second

U = Dimensionless fluid velocity

u = Fluid velocity, m/s

u_m = Average fluid velocity, m/s

v = Particle velocity, m/sec

V = Advection velocity, m/s

V_i = House volume, m^3

VMD = Volume median diameter of droplets, 10^{-6} m (i.e. μm)

V/N = Ratio of vapor mass concentration over nuclei cncentration.

v_s = Terminal settling velocity, m/s

W = Crack width, m

x, y = Horizontal and vertical axis

X, Y = Dimensionless horizontal and vertical axis

z = Number of microspheres in a droplet

$\bar{z}$ = Average number of microspheres in a droplet population

Greek Letters

α = Level of significance, 5%

β = Coefficient for the dimensional analysis infiltration model

δ = Intersect angle of two laser beams, degree

λ = Wavelength of laser beams, nm

γ = Coefficient for the dimensionless infiltration model

μ = Absolute viscosity of air, 18.24×10^{-6} N·s/m^2

θ = Crack incline angle, degree

ϕ = Dimensionless entrance length

ϕ_b = Brewster angle, degree

Φ = Phase shift, degree/μm

ν = Kinematic viscosity of air, 15.7×10^{-6} m^2/s

σ_g = Geometric standard deviation of a particle population

σ_x = Dimensionless parameters for the Taulbee model

σ_y = Dimensionless parameters for the inclined crack model

ρ_f = Density of air at atmospheric pressure and 20°C, 1.164 kg/m^3

ε = The portion of particles deposit inside a crack

Subcripts

f = Fluid

p = Particle

h = Horizontal crack

i = Grid number in horizontal axis

j = Grid number in vertical axis

v = Vertical crack

x = x-axis component

y = y-axis component

TABLE OF CONTENTS

CHAPTER 1. GENERAL INTRODUCTION.....1

1.1 BACKGROUND 1

1.2 AIR INFILTRATION 5

1.3 OUTDOOR-INDOOR PARTICLE PENETRATION 8

1.3.1 Indoor/Outdoor Ratio 8

1.3.2 IAQ Model 9

1.3.3 Particle Dynamics Modeling Approach 10

1.4 PARTICLE DEPOSITION MECHANISMS 11

1.4.1 Gravitational Sedimentation 12

1.4.2 Inertial Impaction 12

1.4.3 Brownian Diffusion 13

1.5 OBJECTIVES AND SCOPES 14

1.6 REFERENCES 15

CHAPTER 2. RATIONAL APPROACH FOR AIR INFILTRATION MODELING.....22

2.1 INTRODUCTION 22

2.2 THEORY 24

2.2.1 Infiltration Flow Model 24

2.2.2 Infiltration Flow Field 25

2.2.3 Laminar Velocity Profiles for Parallel Plate Flow 26

2.3 MATERIALS AND METHOD 26

2.3.1 Chamber 27

2.3.2 Crack Sandwiches 28

2.3.3 Driving Force Control 29

2.3.4 Flow Measurement 30

2.4 RESULTS AND DISCUSSION 30

2.4.1 Crack Infiltration 30

2.4.2 Infiltration Flow Field 31

2.5 CONCLUSION 32

2.6 REFERENCES 44

CHAPTER 3. MODELING PARTICLE PENETRATION THROUGH HORIZONTAL CRACKS 46

3.1 INTRODUCTION 46

3.2 THEORETICAL BACKGROUND 47

3.2.1 Air Infiltration Theory 47

3.2.2 Particle Deposition Modeling 48

3.2.3 The Fuchs Model 48

3.2.4 The Licht Model 49

3.2.5 The Taulbee Model 50

3.3 MODEL DEVELOPMENT 52

3.3.1 Modeling Parameters 52

3.3.2 Dimensionless Modeling Approach 52

3.3.3 Numerical Method 54

3.4 RESULTS AND DISCUSSION 54

3.4.1 Particle Penetration Curves 54

3.4.2 Concentration Contour 57

3.4.3 Validating the Taulbee Model Using the IAQ Modeling Approach 58

3.5 CONCLUSION 61

3.6 REFERENCES 71

CHAPTER 4. MODELING PARTICLE PENETRATION THROUGH INCLINED CRACKS 73

4.1 INTRODUCTION 73

4.2 THEORETICAL BACKGROUND 74

4.2.1 Air Infiltration Modeling 74

4.2.2 Particle Dynamics 75

4.2.3 Numerical Method 76

4.3 RESULTS AND DISCUSSION 77

4.3.1 Effects of Incline Angle 77

4.3.2 Concentration Contours 79

4.4 CONCLUSION 80
4.5 REFERENCES 90

CHAPTER 5. GENERATION OF MONODISPERSE AEROSOLS 91

5.1 INTRODUCTION 91
5.2 EXPERIMENTAL MATERIALS 93
5.2.1 Joint Vapor/Nuclei Type Generator 93
5.2.2 TSI Aerosol Diluter and Aerodynamic Diameter Sizer (APS) 95
5.3 EXPERIMENTAL METHOD 95
5.3.1 Factorial Design Experiment 95
5.3.2 Tests for Generator Stability, Repeatability, and Response 98
5.3.3 Homogeneous/Heterogeneous Condensation 98
5.4 RESULTS AND DISCUSSION 99
5.4.1 Factorial Design Experiment 99
5.4.2 Aerosol Size Adjustment 102
5.4.3 Generator Stability 103
5.4.4 Canola Oil as An Alternative Aerosol Material 104
5.4.5 Roles of Atomizer on Generator Performance 105
5.5 CONCLUSION 107
5.6 REFERENCES 126

CHAPTER 6. RATIONAL APPROACH FOR STANDARD PARTICLE GENERATION 129

6.1 INTRODUCTION 129
6.2 THEORY 132
6.2.1 Dilution of Microsphere Suspensions 132
6.2.2 Estimate Sizes of Residual Particles 133
6.2.3 Aerodynamic Diameter 133
6.3 MATERIALS AND METHOD 134
6.3.1 The Atomization/Evaporation Method 134
6.3.2 The TSI APS 3320 135
6.3.3 The Dantec PDA 136

6.4 RESULTS AND DISCUSSION 138
6.4.1 Validate the Performance of APS 138
6.4.2 Validate/Calibrate Performance of PDA 140
6.5 CONCLUSION 141
6.6 REFERENCES 153

CHAPTER 7. RATIONAL APPROACH FOR PARTICLE PENETRATION MODELING 154

7.1 INTRODUCTION 154
7.2 EXPERIMENTAL MATERIALS AND METHOD 157
7.2.1 Infiltration Control and Aerosol Generator 157
7.2.2 Traverse System 158
7.2.3 Operation Theory of the Particle Dynamic Analyzer (PDA) 159
7.2.4 PDA Setup 162
7.2.5 Particle Deposition Pattern Tests 164
7.3 RESULTS AND DISCUSSION 165
7.3.1 Entrance Cut Off Analysis 165
7.3.2 Visual Examination of Particle Deposition Pattern 166
7.3.3 Validation of Particle Penetration Models 167
7.3.4 Real House Penetration Behavior 170
7.4 CONCLUSION 174
7.5 REFERENCES 195

CHAPTER 8. GENERAL CONCLUSION AND RECOMMENDATION 196

8.1 GENERAL OVERVIEW 196
8.2 CONCLUSION 198
8.3 RECOMMENDATION 202
8.4 REFERENCES 204

LIST OF TABLES

Table 2-1 Crack dimensions and differential pressures tested in the infiltration study....33

Table 3-1 Summary of the modeling parameters in the particle penetration modeling....63

Table 5-1 High and low levels of the four factors selected in the 2^4 factorial design experiment....109

Table 5-2 Main effects and interactions derived from the factorial design experiment....110

Table 5-3 Significant factors that control number mean diameter (NMD) and geometric standard deviation (GSD) of product aerosols....111

Table 5-4 Particle statistics of output aerosols for combinations of DEHS temperature, condensation chimney, and atomizer flow rate....112

Table 5-5 Power-law models for number mean diameter (NMD) of product aerosols and atomizer flow rate, Q....113

Table 5-6 System stabilization time and particle statistics for stability tests....114

Table 5-7 Regression analysis and hypothesis test for stability tests....115

Table 5-8 Particle statistics of output aerosols, using canola oil and 25 mm condensation chimney....116

Table 5-9 Concentration of primary droplets and output aerosols for a series of atomizer flow rates (aerosols produced using the 25 mm condensation chimney)....117

Table 6-1 Theoretical and APS measured aerodynamic diameters for the standard polystyrene microspheres....143

Table 6-2 Setup of the PDA optical system....144

Table 6-3 Setup of the signal processor of the Dantec Particle Dynamic Analyzer (PDA)....145

Table 6-4 Aerosol flow and sheath flow of the Aerodynamic Particle Sizer (APS) measured using a mini-BUCK bubble meter....146

Table 7-1 Summary of test parameters for the particle penetration experiment....176

Table 7-2 Parameter settings of the PDA's transmitting and receiving optic 177
Table 7-3 Parameter settings for the PDA's signal processor 178

LIST OF FIGURES

Figure 2-1 Definitions of rectangular and L-shaped cracks 34

Figure 2-2 Schematic diagram of the experimental setup for the infiltration study.....35

Figure 2-3 Explode diagram of the test chamber (not to scale).....36

Figure 2-4 Explode diagram of the rectangular crack sandwiches (not to scale).....37

Figure 2-5 Explode diagram of the L-shaped crack sandwich (not to scale) 38

Figure 2-6 Infiltration flow rate for the L = 60 mm rectangular cracks 39

Figure 2-7 Infiltration flow rate for the L = 30 mm rectangular cracks 40

Figure 2-8 Infiltration flow rate for the L = 60 mm L-shaped cracks.....41

Figure 2-9 Entrance length ratio (L_e/L) for the L = 60 mm rectangular cracks 42

Figure 2-10 Entrance length ratio (L_e/L) for the L = 30 mm rectangular cracks 43

Figure 3-1 Boundary conditions and grid layout for the numerical analysis 64

Figure 3-2 Theoretical particle penetration coefficients versus dimensionless parameters X and σ_y, which correspond to crack length L = 10 to 50 mm, crack height H = 100 to 1000 mm, and differential pressure ΔP = 1 to 12 Pa.....65

Figure 3-3 Particle concentration contours for $\sigma_y = 10^2$ (simulated using the Taulbee model, σ_y of this order represents particles approximately 1 μm in diameter). 66

Figure 3-4 Particle concentration contours inside a crack for σ_y = 0.1 (simulated using the Taulbee model, σ_y of this order represents particles approximately 0.1 μm in diameter).....67

Figure 3-5 Particle concentration contours inside a crack for σ_y =10 (simulated using the Taulbee model, σ_y of this order represents particles of approximately 0.7 μm in diameter).....68

Figure 3-6 Comparison between the Taulbee model and experimental particle penetration coefficients for submicron-sized particles published by Mosley *et al.* (2001).....69

Figure 3-7 Comparison between the Taulbee model and experimental particle penetration coefficients for micron-sized particles published by Mosley *et al.* (2001) 70
Figure 4-1 Schematic diagram of an inclined crack 82
Figure 4-2 Boundary conditions and grid layout for numerical analysis 83
Figure 4-3 Simulated particle penetration coefficient for 2.5 μm particles (modeling conditions: incline angle $|\theta| \leq 90°$, differential pressure from 1 to 12 Pa, crack length L = 60 mm, and crack height H = 0.305 mm). 84
Figure 4-4 Simulated particle penetration coefficient for 1.0 μm particles (modeling conditions: incline angle $|\theta| \leq 90°$, differential pressure from 1 to 12 Pa, crack length L = 60 mm, and crack height H = 0.305 mm). 85
Figure 4-5 Simulated particle penetration coefficient for 0.1 μm particles (modeling conditions: incline angle $|\theta| \leq 90°$, differential pressure from 1 to 12 Pa, crack length L = 60 mm, and crack height H = 0.305 mm) 86
Figure 4-6 Concentration contours for 2.5 μm particles (modeling conditions: differential pressure ΔP = 2 Pa, crack length L = 60 mm, and crack height H = 0.305 mm) 87
Figure 4-7 Concentration contours for 1.0 μm particles (modeling conditions: differential pressure ΔP = 2 Pa, crack length L = 60 mm, and crack height H = 0.305 mm) 88
Figure 4-8 Concentration contours for 0.1 μm particles (modeling conditions: differential pressure ΔP = 2 Pa, crack length L = 60 mm, and crack height H = 0.305 mm) 89
Figure 5-1 Schematic diagram of the modified Rapaport-Weinstock generator 118
Figure 5-2 Schematic diagram of the atomizer nozzle 119
Figure 5-3 Half-normal plots of the factorial design experiment 120
Figure 5-4 Dependence of number mean diameter (*NMD*) on atomizer flow rate for DEHS 121

Figure 5-5 Sequential number mean diameter (*NMD*), geometric standard deviation (*GSD*), and particle concentration for the stability tests using 25 mm condensation chimney and DEHS 122
Figure 5-6 Relationship between number mean diameter (*NMD*) of particles and atomizer flow rate for canola oil 123
Figure 5-7 Sequential number mean diameter (*NMD*), geometric standard deviation (*GSD*), and particle concentration for the stability tests using 25 mm condensation chimney and canola oil 124
Figure 5-8 Size distribution of primary droplets and product aerosols using DEHS as aerosol material 125
Figure 6-1 Schematic diagram of the TSI Aerodynamic Particle Sizer (adapted from operation manual, TSI Inc.) 147
Figure 6-2 Experimental setup for the experiment using PSL microsphere to validate performance of the Aerodynamic Particle Sizer (APS) 148
Figure 6-3 Typical particle size distribution histogram of the 1.020 μm PSL microspheres measured by the Aerodynamic Particle Sizer (APS) 149
Figure 6-4 Typical particle size distribution histogram of the 2.504 μm PSL microspheres measured by the Aerodynamic Particle Sizer (APS) 150
Figure 6-5 Typical Particle size distribution histogram of the 1.020 μm PSL microspheres measured by the Dantec Particle dynamic Analyzer (PDA) 151
Figure 6-6 Typical Particle size distribution histogram of the 2.504 μm PSL microspheres measured by the Dantec Particle dynamic Analyzer (PDA) 152
Figure 7-1 Schematic diagram of the experimental setup for particle penetration study 179
Figure 7-2 Measurement volume of two intersect laser beams (after Dantec Measurement Technology A/S) 180
Figure 7-3 Fringe Model for velocity measurement (after Dantec Measurement Technology A/S) 181
Figure 7-4 Schematic diagram showing measurement of particle diameter using phase shift (after Dantec Measurement Technology A/S) 182

Figure 7-5 Schematic diagram of using two pairs of photodetectors to solve the 2π ambiguity (after Dantec Measurement Technology A/S) 183
Figure 7-6 Schematic diagram of the Dantec PDA system 184
Figure 7-7 Schematic diagram of particle scattering modes (After Dantec Measurement Technology A/S) 185
Figure 7-8 Schematic diagram of a one-component forward scattering PDA system (after Dantec Measurement Technology A/S) 186
Figure 7-9 Deposition pattern for the rectangular crack of $H = 0.305$ mm, $L = 60$ mm, $\Delta P = 8$ Pa, and $d_p = 1.4$ μm (8 hours experimental time) 187
Figure 7-10 Deposition pattern for the rectangular crack of $H = 0.305$ mm, $L = 60$ mm, $\Delta P = 8$ Pa, and $d_p = 1.4$ μm (8 hours experimental time) 188
Figure 7-11 Deposition pattern for the L-shaped crack of $H = 0.305$ mm, $L = 60$ mm, $\Delta P = 8$ Pa, and $d_p = 1.4$ μm (8 hours experimental time) 189
Figure 7-12 Particle penetration coefficient for the $L = 60$ mm rectangular crack, $d_p = 1.4$ μm 190
Figure 7-13 Particle penetration coefficient for the $L = 30$ mm rectangular crack, $d_p = 1.4$ μm 191
Figure 7-14 Particle penetration coefficient for the $L = 60$ mm L-shaped crack, $d_p = 1.4$ μm 192
Figure 7-15 Comparisons between theoretical and experimental particle penetration coefficients for rectangular cracks 193
Figure 7-16 Comparisons between theoretical and experimental particle penetration coefficients for L-shaped cracks 194

LIST OF APPENDICES

Appendix A Summary of Particle Dynamic Parameters (Hinds, 1982) 206

Appendix B Derivation of the Dimensionless Air Infiltration Flow Field 209

Appendix C Derivation of the Laminar Infiltration Flow Field 211

Appendix D Derivation of the Licht Particle Penetration Model 214

Appendix E Derivation of the Fuchs Particle Penetration Model 219

Appendix F The TK-Solver® Program Codes for the Taulbee Model (Dimensionless Model) 221

Appendix G The TK-Solver® Program Codes for the Inclined Crack Model (Dimensional Model) 230

Appendix H Summary of Air Infiltration Data 240

Appendix I Summary of Aerosol Generator Data 246

Appendix J Summary of APS & PDA Validation Data 253

Appendix K Summary of Particle Penetration Data For Rectangular Cracks 256

Appendix L Summary of Particle Penetration Data For L-shaped Cracks 261

CHAPTER 1. GENERAL INTRODUCTION

1.1 BACKGROUND

In the past, ambient air pollution regulation was directed toward setting source emission limits and ambient air quality standards. The efforts did improve ambient air quality. However, people are not continuously exposed to ambient air all of the time. The current primary air quality standards of the National Ambient Air Quality Standards (NAAQS) have long been questioned in protecting general public. As more and more time budget research found that people spend more than 80 to 90% of time indoors (Farrow *et al.*, 1997; Jenkins and Philips, 1988; Robinson and Nelson, 1995), it is logical to speculate that current ambient air quality standards may not be appropriate for indoor air quality regulations. Actually the most susceptible population spends almost 100% of their time indoors (Yocom, 1982). Indoor air quality regulations must take these findings into consideration so as to protect public health. Canada is a pioneer in indoor air quality regulation. In 1987, the Department of National Health and Welfare published Exposure Guidelines for Residential Indoor Air Quality (Department of Health and Welfare Canada, 1987). These guidelines are based on acceptable long-term and short-term exposure ranges.

Since buildings are surrounded by ambient air, indoor air quality interacts with outdoor air pollutants. Efforts have been devoted to investigate the outdoor-indoor air quality relationship since 1970s. It was found by other researchers that the reactivity and physical properties of air pollutants along with ventilation measures affect pollutant penetration efficiency. Yocom (1982) pointed out that gaseous pollutants could readily penetrate into indoor environments with infiltration air. However, because of indoor

sources and reactivity of pollutants, indoor pollutant levels might be quite different from outdoors. For inert pollutants, such as carbon monoxide (CO), Yocom (1982) found the long-term indoor to outdoor concentration ratio (*I/O*) approached unity, while the short-term *I/O* might far exceed unity because of the contribution from indoor combustion sources. Take tobacco smoking as an example, Elliot and Rowe (1975) found tobacco smoking greatly increased indoor CO levels during public gathering in an arena, *I/O* reached 4.8. Moschandreas *et al.* (1981) investigated the effect of a gas stove on indoor CO levels. In comparison with a control test in an office building that had no combustion source, Moschandreas *et al.* (1981) found the *I/O* ratios were 1.64 and 1.05 for a gas stove operating house and the office building, respectively. The results suggested that a gas stove was an important indoor CO source.

Reactive gaseous pollutants have quite a different penetration story. Although reactive gaseous pollutants can readily penetrate indoors as inert gaseous pollutants do, they are subject to rapid chemical depletion in the transport process. As a result, lower indoor levels were found when there was no significant indoor source (Anderson, 1972; Spengler *et al.* 1979). Take ozone (O_3) as an example, Thompson *et al.* (1973) and Sabersky *et al.* (1973) found indoor O_3 level have similar diurnal pattern as outdoors, which suggested that there was a close relationship between indoor and outdoor O_3 levels. Indoor O_3 levels were consistently lower than outdoors, indicating O_3 losses in the transport process. Thompson *et al.* (1973) found the *I/O* ratio for O_3 was approximately 0.5.

For particulate matter (PM), the outdoor-indoor relationship is much more complex than gaseous pollutants because of the mobility differences between PM and air.

Contrary to gaseous pollutants that can be readily transported with infiltration air, PM tends to settle out of air because of gravity and other deposition mechanisms. Particle size, infiltration flow rate and geometry of infiltration channel all affect particle penetration efficiency. Indoor sources further complicate the scenario. Several studies found that tobacco smoking is the major source of indoor respirable particulate matter (RPM). Tobacco smoking could raise *I/O* for RPM up to 3.34 to 11.6 (Ozkaynak *et al.*, 1993; Leaderer and Hammond, 1991; Santanam *et al.*, 1990; NAS, 1986; Dockery and Spengler, 1978; Spengler *et al.*, 1981; Repace and Lowrey, 1980). For other indoor combustion sources, RPM contributions are not consistent in literature. Some research found that fireplaces and cooking increases indoor RPM levels, others not (Ozkaynak *et al.*, 1993; Kamens *et al.*, 1991; Moschandreas *et al.*, 1978). Moschandreas *et al.* (1991) attributed the inconsistent result to the fact that *I/O* relationship is dependent on indoor activities.

Another investigation approach, based on a mass-balance model, has been used to estimate PM penetration efficiency (P_p). This model considered particle deposition velocity and source emission rate to account for the effects of indoor activities. Using the model, the US EPA PTEAM study found $P_p \approx 1$ for PM10 particles (Koutrakis *et al.*, 1992). Thatcher and Layton (1995) found particles up to 25 μm could readily penetrate into a two-story house in California. Other research that investigated sheltering efficiency against airborne radioisotope particles found building envelopes provide a filtration effect to protect residents from PM exposure (Englemann, 1992; Brown, 1988; Kocher, 1980). The latter studies investigated the penetration of radioisotope labeled outdoor PM. Their study designs could distinguish outdoor PM from those generated indoors. As a result,

the isotope labeling technique probably provided a better estimation of particle penetration efficiency. Kocher (1980) used the mass-balance model to estimate a dose reduction factor (*DRF*) of a building for the Three-Mile Island accident. The definition of *DRF* is actually the same as the *I/O* ratio. Under typical air change rates (0.5 to 1.5 hr^{-1}), *DRF* of a model building ranged from 0.2 to 0.8 for PM. Englemann (1992) used the model to estimate *DRF* using 2 μm particles to represent respirable plutonium in another study. The study found that all simulated buildings significantly reduce indoor PM levels, including office buildings, well-constructed houses, old houses, and industrial buildings. In addition to theoretical modeling, experimental investigations conducted during the Three-Mile-Island and the Chernobyl accident also found buildings did provide protection from outdoor radioactive PM (Fogh *et al.*, 1997; Roed and Cannell, 1987). Fogh *et al.* (1997) and Roed and Cannell (1987) reported that *DRF* = 0.5 and 0.37 for particulate iodine, respectively.

The above discrepancies in particle penetration efficiencies suggest that the mass balance models inherit some uncertainties. An alternative modeling approach is required to identify outdoor-to-indoor particle penetration efficiency. In 1999, Liu and Nazaroff focused on specific idealized cracks to estimate P_p. This model combined an air infiltration model and particle deposition models. Although the modeling approach could not be applied on actual houses readily, it provides information to examine particle transport mechanisms and avoids the confounding factors induced from indoor activities. The current study applied the same idea and used an alternative model to investigate outdoor-to-indoor particle penetration. This model provides information to examine

particle deposition mechanisms. In addition, it can deal with both rectangular cracks and L-shaped cracks.

1.2 AIR INFILTRATION

According to the ASHRAE Fundamental Handbook (American Society of Heating, Refrigerating, and Air Conditioning Engineers, Inc., 1989), three ventilation modes: forced ventilation, natural ventilation, and infiltration are used in building ventilation. Forced ventilation uses mechanical forces to draw fresh outdoor air indoors. A filtration system is designed to remove ambient air pollutants. Because mechanical ventilation systems create a positive pressure indoors, outdoor air pollutants cannot penetrate indoors. In this ventilation mode, particle penetration is determined by the efficiency of filtration systems.

Natural ventilation is defined as ventilation through manually controlling the opening of doors, windows, and other building components (ASHRAE, 1989). Natural ventilation is the major ventilation mode to adjust indoor temperature, humidity and other environmental conditions. Because such openings are relatively large, air pollutants can readily be transported indoors. Nearly 100% penetration efficiency is expected (Yocom and McCarthy, 1991).

For infiltration flow, although its flow rate is much less than natural ventilation, two reasons attract research interest on infiltration penetration. First, infiltration flow is the major ventilation mode when ambient air is polluted. For example, when a smoke plume from a forest fire or a plume from a nuclear power plant accident covers a city, residents tends to close doors and windows to prevent pollutants from penetrating indoors. Infiltration flow through unintentional openings, such as the perimeters of door and window frames, is the only air leakage source. As a result, several studies focused on

infiltration penetration to examine the protection from building sheltering (Englemann, 1992; Gross, 1981). Second, because more and more energy efficient houses have been built due to the increasing energy costs, there is a great need to investigate infiltration flow in order to balance energy conservation, living comfort, and residence heath (Proskiw, 1995; Yocom and McCarthy, 1991; Forest *et al.*, 1990; Elmroth *et al.*, 1982; Wanner, 1982).

The ASHRAE Fundamental Handbook defines infiltration as "uncontrolled airflow through cracks and interstices, and other unintentional openings." (ASHRAE, 1989). Wind pressure and stack effect, induced from temperature differences, are the driving forces of infiltration flow. Since the energy crisis era, several empirical and semi-empirical models have been developed to estimate infiltration flow using the driving force terms (Etheridge, 1998; ASHRAE, 1989; Baker et al, 1987; Goldschmidt, 1986; Gross, 1981). Among these models, the ASHRAE Fundamental Handbook used an empirical one to calculate infiltration flow from wind velocity and temperature difference:

$$Q_I = a\left(A\Delta T + BV^2\right)^{0.5} \times 10^{-3} \qquad (1\text{-}1)$$

where Q_I is airflow rate (m^3/s), a is effective leakage area (cm^2), A is stack coefficient, ΔT is average temperature difference between outdoor-indoor (°C), B is wind coefficient, and V is average wind speed (m/s). The ASHRAE Fundamental Handbook provides tables of effective leakage area for typical building components and the coefficients A and B as a basis to estimate whole house infiltration (ASHRAE, 1989).

These models were used to estimate infiltration flow for a whole house, while other models focused on infiltration through specific cracks. Hopkins and Hansford

(1974) found residential cracks could be treated as pairs of parallel plates. Based on parallel plate theory, several empirical and semi-empirical models have been proposed. For example, the orifice flow models and dimensional analysis models have been used in passive ventilation and fire safety studies (Hopkins and Hansford, 1974; Etheridge, 1977; Gross and Haberman, 1989; Walker and Wilson, 1990; Wilson and Walker, 1991; Baker *et al.*, 1987).

The empirical orifice flow model simulates infiltration as air flow through an orifice plate. Infiltration flow rate can be predicted from differential pressure with a power law equation:

$$q = C_b(\Delta P)^n \tag{1-2}$$

where C_b and n are empirical constants, q is infiltration flow rate, and ΔP is differential pressure across a crack. Gross and Haberman (1989) and Wilson and Walker (1991) suggested that the exponent n = 0.5 for air infiltration through sharp edged holes and n = 1.0 for laminar flow through long, thin rectangular cracks. This suggests that laminar infiltration flow is linearly dependent on the differential pressure across a rectangular crack. This model, although widely used in infiltration studies, is not dimensionally homogenous and conflicts with the principle of similarity with respect to the Reynolds number. In addition, turbulent orifice flow is quite different from the flow fields in residential crack infiltration, which tend to be laminar or in a transition between turbulent and laminar flow fields for long, thin cracks.

Other research used dimensionless analysis to derive a semi-empirical model as shown (Hopkins and Hansford, 1974):

$$\frac{1}{C_z} = \beta \frac{L}{D_h} \cdot \frac{1}{\mathrm{Re}} + \gamma \qquad (1\text{-}3)$$

where C_z is discharge coefficient, L is crack length, D_h is hydraulic diameter of a crack, and β and γ are coefficients. Theoretically, $\beta = 96$ for ideal rectangular cracks (Hopkins and Hansford, 1974). In practice, β and γ are derived from experimental data. Etheridge (1977) and Baker *et al.* (1987) used regression analysis to obtain the coefficients β and γ for rectangular cracks, L-shaped cracks, and double-bend cracks.

Gross and Haberman (1989) proposed another model to simulate parallel plate flow. The model was used in this study to estimate infiltration flow for both rectangular cracks and L-shaped cracks. Details of the model are presented in Chapter 2.

When uniformly distributed flow enters a crack, because of the boundary layer effect, infiltration flow gradually develops into laminar flow. Schlichting (1979) and Sparrow *et al.* (1967) solved the flow field in the flow development region for tube flow and parallel plate flow. They proposed a dimensionless entrance length parameter to estimate the length of the flow development region. The model indicated that infiltration flow field could be assumed laminar for long-narrow cracks. The velocity profile of fully developed laminar flow is parabolic. It can be derived from the Navier-Stokes equation and the continuity equation (Schlichting, 1979; Kay, 1957).

1.3 OUTDOOR-INDOOR PARTICLE PENETRATION

1.3.1 Indoor/Outdoor Ratio

Since Yocom (1982) reviewed the major outdoor-indoor air quality research conducted in the 1970s, additional literature has been published for outdoor-to-indoor particle penetration. One of the methods used to examine P_p was based on the ratio of indoor to outdoor particle concentrations (I/O). However, the I/O ratio is a function of

indoor source emission rate, air change rate, and particle deposition rate. If particulate matter is not labeled to distinguish from those generated indoors, *I/O* cannot represent the actual particle penetration coefficient. Furthermore, because these three factors are dependent on indoor activities, field studies found the *I/O* ratio varied widely for different experimental settings. Some studies reported the *I/O* ratio to be less than 1.0 and concluded that building barriers prevent outdoor particles from entering indoors (Anderson, 1972; Alzona *et al.*, 1979; Li, 1994). Others found the *I/O* ratio varied widely and might be far greater than 1.0 (Dockery and Spengler, 1981; Sinclair *et al.*, 1992; Tung *et al.*, 1999). These studies attributed the wide variation in *I/O* ratio to the influence of indoor activities. Consequently, using an *I/O* ratio to represent particle penetration efficiency may not be appropriate.

1.3.2 IAQ Model

Another approach to estimate particle penetration efficiency is based on a mass balance model, usually called the indoor air quality model (IAQ model). This model considers particle deposition rates (k), and indoor source emission rates (S) to account for the contribution from indoor activities (Roed and Cannell, 1987; Thatcher and Layton, 1995; Wallace, 1996; Tung *et al.*, 1999). The IAQ model assumes that outdoor pollutant concentration is in equilibrium with indoor microenvironment and indoor air is completely mixed. As a result, the mass balance equation with respect to the indoor environment can be written as shown (Shair and Heitner, 1974; Nazaroff and Cass, 1989; Yocom and McCarthy, 1991):

$$V_i \frac{dC_i}{dt} = S + qP_pC_0 - kA_iC_i - qP_pC_i \qquad (1\text{-}4)$$

where V_i is house volume, C_o and C_i are pollutant concentrations in the outdoor and indoor environments, q is infiltration flow rate, k is particle deposition velocity, A_i is indoor surface area, and P_p is particle penetration coefficient.

In steady state, indoor concentration (C_i) is constant and equation 1-4 becomes:

$$C_i = \frac{S + qP_pC_0}{qP_p + kA_i} \tag{1-5}$$

Particle penetration efficiency P_p can be estimated from equation 1-5 since other terms can be measured experimentally. In application, source emission rate, pollutant deposition rate, and infiltration flow rate are measured under controlled experimental conditions. The derived parameters do not represent the dynamic fluctuations in residential conditions. As a result, using the IAQ model to predict particle penetration coefficient is subject to the confounding effects of these factors. In addition, complete mixing assumption is not valid for most residential conditions.

1.3.3 Particle Dynamics Modeling Approach

An alternative approach to avoid the above experimental confounding is to estimate particle penetration by examining particle concentrations at crack entrance and exit. Liu and Nazaroff (1999) evaluated particle penetration based on particle deposition models that considered both Brownian diffusion and gravitational sedimentation. This modeling approach considered crack geometry, particle diameter, and the differential pressure across a crack to predict P_p. Because typical crack dimensions and target particle sizes can be measured, the only other factor that affects particle penetration driving force is related to difference pressure across a crack. Although indoor activities have significant effects on difference pressures between indoor and outdoor environments, their effects can be accounted for by measuring typical difference pressures for

residential conditions, which is reported to be less than 10 Pa for ordinary conditions (Wilson and Walker, 1992). As a result, human activity factor is included in this modeling approach and confounding induced from indoor activities are avoided. However, a limitation of this modeling approach is how to apply it on actual house cracks. For actual cracks, there is no appropriate instrument to measure crack height directly. This limitation can be solved by an infiltration test method. The ASTM Test Method E1242 describes a chamber design to measure effective leakage area of building components. Using the measured effective leakage area, crack dimensions can be estimated so that this modeling approach can be used to estimate a particle penetration coefficient (Kehrli, 1995).

1.4 PARTICLE DEPOSITION MECHANISMS

Particle trajectory analysis is one of the models that have been used to simulate particle deposition in a crack infiltration journey (Liu and Nazaroff, 1999; Mosley *et al.*, 2001). If a particle deposits on a crack surface, it is assumed removed from infiltration stream. Particle trajectory models are based on the equation of motion. According to the Newton's Law, the net forces on a particle is equal to the product of particle mass and acceleration rate:

$$m_p \frac{d\vec{u}}{dt} = \sum \vec{F} \qquad (1\text{-}6)$$

where m_p is particle mass, $\vec{u}$ is velocity vector, t is time, and $\vec{F}$ is the vector of driving forces. Since driving forces can be estimated from particle deposition mechanisms, the equation of motion can be integrated to obtain particle velocity function. Integrating the velocity function gives the particle's trajectory (Wang 1975).

1.4.1 Gravitational Sedimentation

For micron-sized particles, gravitational sedimentation is a significant deposition mechanism (Hinds, 1982). When a particle is released in air, three forces determine its trajectory: gravity, buoyancy force, and drag force. The equation of motion can be written as (Licht 1980):

$$m_p \frac{d\vec{u}}{dt} = \overrightarrow{F_g} + \overrightarrow{F_b} + \overrightarrow{F_d} = m_p \vec{g} + m_f \vec{g} + \frac{C_d}{2} \rho_f a \vec{u}^2 \tag{1-7}$$

where $\overrightarrow{F_g}$ is gravity force, $\overrightarrow{F_b}$ is buoyancy force, $\overrightarrow{F_d}$ is drag force, ρ_f is gas density, a is particle projection area, and C_d is drag coefficient. For two-dimensional motion, the equation can be written as component equations in x and y directions:

$$x\text{-component: } m_p \frac{du_x}{dt} = -F_{d_x} \tag{1-8}$$

$$y\text{-component: } m_p \frac{du_y}{dt} = g(m_p - m_f) - F_{d_y} \tag{1-9}$$

Integrating the equations can derive particle trajectory.

1.4.2 Inertial Impaction

Inertial impaction might be an important particle deposition mechanism for the 90° bend in L-shaped and double-bend cracks. It has been investigated theoretically and experimentally on aerosol separation processes, such as inertial impactors and virtual impactors. When flow direction changes, particles with sufficient inertia deviate from the streamlines and impact on channel wall. The Stokes number, or impaction parameter, governs impaction efficiency (Hinds, 1982). It is defined as the ratio of particle stopping distance (at the average nozzle exit velocity, U) to nozzle radius ($D_j/2$) (Davies and Aylward 1951; Ranz and Wong 1952; Licht 1980):

$$Stk = \frac{s}{D_j/2} = \frac{\rho_p d_p^2 u C_c}{9\mu D_j} \quad (1\text{-}10)$$

where s is stopping distance, D_j is nozzle diameter, ρ_p is particle density, u is flow velocity, C_c is Cunningham slip correction factor, and other terms are defined previously. Stopping distance and Cunningham slip correction factors are particle size dependent, as shown in Appendix A. For residential crack infiltration, Liu and Nazaroff (1999) found the Stk number was less than 0.36. Inertial impaction was not a significant particle deposition mechanism.

1.4.3 Brownian Diffusion

Brownian motion is induced from random bombardment of gas molecules on particles. The probability of random bombardment is proportional to aerosol concentration. As a result, Brownian diffusion causes a net movement of particles from a high concentration area to low concentration area. The potential of Brownian diffusion deposition is characterized by particle diffusivity D, which can be calculated from the Stokes-Einstein equation (Hinds, 1982):

$$D = \frac{KTC_c}{3\pi\mu d_p} \quad (1\text{-}11)$$

where K is Boltzmann's constant, T is absolute temperature, and μ is absolute viscosity of air. The equation suggests that particle diffusivity is inversely proportional to particle size. Generally speaking, Brownian diffusion is not an efficient deposition mechanism for micron-sized particles. However, it has significant particle deposition efficiency for submicron-sized particles when particle transport distances are small. For particles smaller than 0.1 μm, Brownian diffusion is a major deposition mechanism (Hinds, 1982). Appendix A lists particle diffusivity for a series of particles.

The aforementioned particle trajectory analysis fails to simulate the wiggling trajectory induced from Brownian motion. Particle penetration must be simulated using a mass transport equation, as shown in equation 1-12 (Tan and Hsu, 1972; Taulbee and Yu, 1975):

$$\nabla \cdot (c\vec{v}) = D\nabla^2 c \qquad (1\text{-}12)$$

where c is particle concentration, $\vec{v}$ is particle velocity vector, and D is particle diffusivity. This study used the mass transport equation to formulate a particle penetration model that considers both gravitational sedimentation and Brownian diffusion.

1.5 OBJECTIVES AND SCOPES

Although efforts have been devoted to investigate the outdoor-indoor air quality relationship, there are discrepancies among published studies. The IAQ model has inherent confounding factors induced from indoor activities, which lead to discrepancies among particle penetration research. As a result, it is necessary to use other modeling approaches to validate these key points. In addition, deposition mechanisms that govern particle penetration efficiency need to be identified. The objective of this study was to derive mathematical models to estimate particle penetration efficiency through rectangular cracks and L-shaped cracks in typical residential conditions. Experimental investigations were also conducted to validate the models. The scope of research activities of this study included:

1. Screening an air infiltration model to estimate infiltration flow rate, and to determine the flow fields (Chapter 2);

2. Deriving particle penetration models for horizontal cracks, and to examine the differences among these models (Chapter 3);
3. Deriving a particle penetration model for cracks of arbitrary incline angle. The model is to be used for L-shaped cracks (Chapter 4);
4. Developing a suitable aerosol generator for the study. Effects of controlling parameters were examined (Chapter 5);
5. Applying an atomization/evaporation methodology to generate standard particles for instrument calibration/validation (Chapter 6);
6. Validating the particle penetration models in a test chamber (Chapter 7).

1.6 REFERENCES

Alzona, J., Cohen, B. L., Rudolph, H., Jaw, H. N., and Frohliger, J. O. (1979). Indoor-Outdoor Relationships for Airborne Particulate Matter of Outdoor Origin. *Atmos. Environ.* 13:55-60.

Anderson, I. (1972). Technical Notes: Relationships Between Outdoor and Indoor Air Pollution. *Atmos. Environ.* 6:275-278.

ASHRAE (1989). *Fundamental Handbook.* American Society of Heating, Refrigerating, and Air-Conditioning, Atlanta, GA.

Baker, P. H., Sharples S., and Ward, I. C. (1987). Air Flow Through Cracks. *Build. Environ.* 22:293-304.

Brown, J. (1988). The Effectiveness of Sheltering as a Countermeasure in the Event of an Accident. *Radiological Protection Bulletin.* No. 97:9-15.

Department of Health and Welfare Canada (1987). *Exposure Guidelines for Residential Indoor Air Quality*. Environmental Health Directorate, Health Protection Branch, Health and Welfare Canada, Ottawa, Canada.

Dockery, D. W., and Spengler, J. D. (1978). Indoor-Outdoor Respirable Particulate and Sulfate Relationships in Four Communities. *74th Annual Meeting of the Air Pollution Control Association*, Houston, TX. Paper 78-60.5.

Dockery, D. W., and Spengler, J. D. (1981). Indoor-Outdoor Relationships of Respirable Sulfates and Particles. *Atmos. Environ.* 15:335-343.

Elliot, L. P., and Rowe, D. R. (1975). Air Quality During Public Gathering. *J. Air Pollut. Control Assoc.* 25:635-636.

Elmroth, A., Forslund, J., and Rolen, C. (1982). Effects of Energy Conservation Measures in Existing Buildings. *The 2nd AIC Conference*. Air Infiltration Center. Stockholm, Sweden. pp19-37.

Engelmann, R. J. (1992). Sheltering Effectiveness Against Plutonium Provided by Buildings. *Atmos. Environ.* 26A:2037-2044.

Etheridge, D. W. (1977). Crack Flow Equations and Scale Effect. *Build. Environ.* 12:181-189.

Etheridge, D. W. (1998). A Note on Crack Flow Equations for Ventilation Modeling. *Build. Environ.* 33:325-328.

Farrow, A., Taylor, H., and Golding, J. (1997). Time Spent in the Home by Different Family Members. *Environ. Technol.* 18:605-614.

Fogh, C. L., Byrne, M. A., Roed, J., and Anthony, J. H. G. (1997). Size Specific Indoor Aerosol Deposition Measurement and Derived I/O Concentration Ratios. *Atmos. Environ.* 31:2193-2203.

Forest, T. W., Walker, I. S., and Checkwitch, K. (1990). *Moisture Accumulation in a Building Envelope*. Report No. 80. Department of Mechanical Engineering, University of Alberta, Edmonton, Alberta, Canada.

Goldschmidt, V. W. (1986). Average Infiltration Rates in Residence: Comparison of Electric and Combustion Heating Systems. *Measured Air Leakage of Buildings*. Ed:Trechsel, H. R. *et al.*, Symposium: Performance of Building Construction, Philadelphia, PA. April 1984. pp61-69.

Gross, D., and Haberman, W. L. (1989). *Fire Safety Science: Proceedings of the Second Symposium*. The Second International Symposium on Fire Safety Science, International Association for Fire Safety Science, Tokyo, Japan.

Gross, D. (1981). A Review of Measurements, Calculations and Specifications of Air Leakage Through Interior Door Assemblies. *Building Standards*. L/2:11-16.

Hinds, W. C. (1982). *Aerosol Technology*. John Wiley & Sons, Inc., New York, N. Y.

Hopkins, L. P., and Hansford, B. (1974). Air Flow Through Cracks. *Build. Serv. Engr.* 42:123-131.

Jenkins, P. L., and Philips, T. J. (1988). The California Resource Board Indoor Air Quality and Personal Exposure Program. The 81st Annual Meeting of the Air Pollution Control Association, 20-24 June 1988, Dallas, TX.

Kay, J. M. (1957). *An Introduction to Fluid Mechanics and Heat Transfer*. Pitman Press, Bath. New York, N. Y.

Kamens, R., Lee, C. T., Weiner, R., and Leith, D. (1991). A Study to Characterize Indoor Particles in Three Non-Smoking Homes. *Atmos. Environ.* 25:939-948.

Kehrli, D. W. (1995). A Description of the New ASTM Test Method E1242, Used for Measuring Fenestration Air Leakage at Different Temperatures and Pressures. *Airflow Performance of Building Envelopes, Components, and Systems*. Ed: Modera, M. P., and Persily, A. K. American Society for Testing and Materials. Philadelphia, PA. pp81-89.

Koch, J. and Tadmor J. (1988). Sheltering--A Protective Measure Following an Accidental Atmospheric Release from a Nuclear Power Plant. *Health Physics.* 54:659-667.

Kocher, D. C. (1980). Effects of Indoor Residence on Radiation Doses from Routine Releases of Radionuclides to the Atmosphere. *Nuclear Technology*. 48:171-179.

Koutrakis, P., Briggs, S. L. K., and Leaderer, B. P. (1992). Source Apportionment of Indoor Aerosols in Suffolk and Onondaga Counties, New York. *Environ. Sci. Technol.* 26:521-527.

Leaderer, B. P., and Hammond, S. K. (1991). Evaluation of Vapor Phase Nicotine and Respiable Suspended Particle Mass as Markers for Environmental Tobacco Smoke. *Environ. Sci. Technol.* 25:770-777.

Li, C.-S. (1994). Relationships of Indoor/Outdoor Inhalable and Respirable Particles in Domestic Environment. *The Sci. of the Total Environ.* 151:205-211.

Licht, W. (1980). *Air Pollution Control Engineering*. Marcel Dekker, Inc., New York, N.Y.

Liu, D. L., and Nazaroff, W. W. (1999). Modeling Particles Penetration Through Cracks in Building Envelopes, *Proceedings: 8th Int. Conference on Indoor Air Quality and Climate.* Edinburg, Scotland, 4:1055-1059.

Moschandreas, D. J., Zabransky, J., and Pelton, D. J. (1981). *Comparison of Indoor and Outdoor Air Quality*. Electric Power Research Institute, Report EA-1733, Palo Alto, CA.

Mosley, R. E., Greenwell, D. J., Sparks, L. E., Guo, Z., Tucker, W. G., Fortmann, R., and Whitfield, C. (2001). Penetration of Ambient Fine Particles into Indoor Environment. *Aerosol Sci. Technol.* 34:127-136.

National Academic Sciences (1986). *Environmental Tobacco Smoke: Measuring Exposure and Assessing Health Effects*. National Academic Press. Washington, DC.

Nazaroff, W.W. and Cass, G. R. (1989). Mathematical Modeling of Indoor Aerosol Dynamics. *Environ. Sci. Technol.* 23:157-165.

Ozkaynak, H., Spengler, J. D., Xue, J., Koutrakis, P., Pellizzari, E. D., and Wallace, L. A. (1993). Sources and Factors Influencing Personal and Indoor Exposure to Particles: Findings from the Particle TEAM Pilot Study. *Indoor Air '93: Proceedings of the 6th International Conference on Indoor Air Quality and Climate*. 3:457-462.

Proskiw, G. (1995). An analysis of Moisture Accumulation in the Roof Cavities of Manufactured Housing. *Airflow Performance of Building Envelopes,*

Components, and Systems. Ed: Modera, M. P., and Persily, A. K. American Society for Testing and Materials. Philadelphia, PA. pp156-176.

Repace, D. W., and Lowrey, A. H. (1980). Indoor Air Pollution, Tobacco Smoke, and Public Health. *Science*. 208:464.

Robinson, J., and Nelson, W. C. (1995). *National Human Activity Pattern Survey Data Base*. U.S. EPA, Research Triangle Park, NC.

Roed, J. and Cannell, R. J. (1987). Relationship Between Indoor and Outdoor Aerosol Concentration Following the Chernobyl Accident. *Radiation Protection Dosimetry*. 21:107-110.

Sabersky, R. H., Sinema, D. A., and Shair, F. H. (1973). Concentrations, Decay Rates and Removal of Ozone and Their Relation to Establishing Clean Indoor Air. *Environ. Sci. Technol.* 7:347-353.

Santanam, S., Spengler, J. D., and Ryan, P. B. (1990). Particulate Matter Exposures Estimated from an Indoor-Outdoor Source Apportionment Study. *Indoor Air '90: Proceedings of the 5th International Conference on Indoor Air Quality and Climate*. Ottawa, Canada.2:583-588.

Schlichting, H. (1979). *Boundary-Layer Theory*. McGraw-Hill, New York, N. Y.

Sinclair, J. D., Psota-Kelty, L. A., and Peins, G. A. (1992). Indoor/Outdoor Relationships of Airborne Ionic Substances: Comparison of Electronic Equipment Room and Factory Environment. *Atmos. Environ.* 26A:871-882.

Shair, F. H. and Heitner, K. L. (1974). Theoretical Model for Relating Indoor Pollutant Concentration. *Environ. Sci. Technol.* 8:444-451.

Sparrow, E. M., Hixon, C. W., and Shavit, G. (1967). Experiments on Laminar Flow Development in Rectangular Ducts. *Transactions of the ASME.* pp161-164.

Spengler, J. D., Ferris, Jr. B. G., Dockery, D. W. (1979). Sulfur Dioxide, Nitrogen Dioxide Levels Inside and Outside of Home and the Implications on Health Effects Research. *Environ. Sci. Technol.* 13:1276-1280.

Spengler, J. D., Dockery, D. W. and Turner, W. A. (1981). Long-Term Measurements of Respirable Sulfate and Particles Inside and Outside Homes. *Atmos. Environ.* 15:22-30.

Tan, C. W., and Hsu, C. J. (1972). Mass Transfer of Aerosols with Axial Diffusion in Narrow Rectangular Channels. *Appl. Sci. Res.* 25:295-312.

Taulbee, D. B., and Yu, C. P. (1975). Simultaneously Diffusion and Sedimentation of Aerosols in Channel Flows. *J. Aerosol Sci.* 6:433-441.

Thatcher, T. L., and Layton, D. W. (1995). Deposition, Resuspension, and Penetration of Particles within a Residence. *Atmos. Environ.* 29:1487-1497.

Thompson, C. R., Hensel, E. G., and Katz, G. (1973). Outdoor-Indoor Levels of Six Pollutants. *J. Air Pollut. Control Assoc.* 23:881.

Tung, T. C. W., Chao, C. Y. H., and John, B. (1999). A Methodology to Investigate the Particulate Penetration Coefficient through Building Shell. *Atmos. Environ.* 33:881-893.

Walker, I. S., and Wilson, D. J., (1990). *The Alberta Air Infiltration Model.* Report 71. Department of Mechanical Engineering, University of Alberta, Edmonton, Alberta, Canada.

Wallace, L. (1996). Indoor Particles: A Review. *J. Air & Waste Manage.* 46:98-126.

Walton, W. H. (1954). Theory of Size Classification of Airborne Dust Clouds by Elutriation. *British Journal of Applied Physics.* (Supplement No. 3):S29-S40.

Wang, C. (1975). Gravitational Deposition of Particles from Laminar Flows in Inclined Channels. *J. Aerosol Sci.* 6:191-204.

Wanner, H. U. (1982). Indoor Air Quality and Minimum Ventilation. *The 2nd AIC Conference*. Air Infiltration Center. Stockholm, Sweden. 13-18.

Wilson, D. J., and Walker, I. S. (1991). *Passive Ventilation to Maintain Indoor Air Quality*. Report 81. Department of Mechanical Engineering, University of Alberta, Edmonton, Alberta, Canada.

Yocom, J. E. (1982). Indoor-Outdoor Air Quality Relationships: A Critical Review. *J. Air Pollut. Control Assoc.* 32:500-519.

Yocom, J. E. and McCarthy, S. M. (1991). *Measuring Indoor Air Quality, A Practical Guide*. John Wiely & Sons Ltd. Weat Sussex, UK.

CHAPTER 2. RATIONAL APPROACH FOR AIR INFILTRATION MODELING

2.1 INTRODUCTION

The relationship between infiltration air and pollutants is similar to that of vehicles and passengers. Infiltration flow acts as a vehicle to transport passengers, i.e. (air pollutants), from outdoor to indoor environment. In the infiltration journey, some pollutants get off the vehicle because of certain deposition mechanisms; others remain airborne and are transported into the indoor environment. As a result, indoor air quality research cannot be separated from ventilation theories. Fortunately, there has been great advancement in infiltration studies since the energy crisis in 1970s. During that period of time, infiltration studies focused on energy conservation applications, leading to the development of tighter buildings. Many infiltration test methods and infiltration models have been established to estimate infiltration flow through building envelopes (Palmiter, 1995; Kehrli, 1995; ASTM, 2001; Hopkins and Hansford, 1974; Gross and Haberman, 1989). The advancement in infiltration research provides a foundation for indoor air quality research. Some of the developed infiltration models have been used to facilitate indoor air quality research and modeling (Liu and Nazaroff, 1999; Fogh *et al.*, 1997; Thatcher and Layton, 1995; Olcerst, 1994).

Similar to indoor air quality research, infiltration test methods and models can be categorized into two groups. One of them focused on measuring whole house infiltration, while the other focused on infiltration behaviors for individual cracks (or individual building components). For whole house infiltration study, the fan pressurization test and several tracer test methods have been developed since the 1970s (Kehrli, 1995; ASTM, 2001). Both test methods were primarily used in building comfort

and building energy efficiency research. Recently, the test methods have been used in indoor air quality research. For example, the tracer test methods have been used to measure air movement inside buildings to trace pollutant movement and penetration (Nazaroff and Cass, 1989; Thatcher and Layton, 1995).

The second group of infiltration research models focused on infiltration through individual cracks to investigate the behavior and flow field of infiltration flow. Hopkins and Hansford (1974) did a survey on some residential houses and found most residential cracks were geometrically analogous to the combination of pairs of parallel plates. The Parallel plate theories, as used in fluid mechanics research, were thus adapted to develop infiltration models for rectangular cracks, L-shaped cracks, and double-bend cracks (Baker *et al.* 1987; Etheridge, 1977; Gross and Haberman, 1989). In addition to infiltration flow rate, flow field is also important in some applications, e.g. the pollutant penetration research. Sparrow (1962) and Schlicting (1989) used boundary-layer theory to examine flow development through rectangular ducts and proposed an entrance length parameter (L_e) to estimate the length of flow development region. For long-narrow cracks, infiltration flow could be assumed laminar throughout the cracks. The parabolic velocity profiles of laminar flow have been mathematically derived using the Navier-Stoke and continuity equations (Schlicting, 1979; Kay 1957).

This chapter uses a semi-empirical infiltration model proposed by Gross and Haberman (1989) to estimate infiltration flow through pairs of parallel plates. A controlled chamber was designed to test the validity of the model. Table 2-1 presents the crack dimensions and differential pressures tested in this study. The differential pressures were chosen from 0 to 15 Pa to cover typical residential infiltration conditions (0 to10 Pa). The

test crack dimensions were crack length L = 30 and 60 mm, crack width W = 100 mm, and crack height H from 0.203 to 0.508 mm. Figure 2-1 illustrates the definition of crack length L, crack width W, and crack height H for rectangular and L-shaped cracks. The crack dimensions were designed to simulate typical cracks of tighter building designs. To validate the infiltration model, this study measured infiltration flow rates from 0 to 15 Pa, with step increments of approximately 0.5 Pa. The same procedures were repeated three times. Experimental results indicate that the adapted model could predict infiltration through these cracks reasonably well. Using this infiltration model, the study further examined the validity of assuming laminar flow across the cracks. It indicates that the ratio of entrance length over crack length (L_e/L) was usually less than 5% for typical residential conditions ($\Delta P \leq 10$ Pa). The laminar flow assumption was generally valid. This chapter summarizes the infiltration models and flow field equations. Detailed model derivation and information are presented in Appendix B.

2.2 THEORY

2.2.1 Infiltration Flow Model

Several empirical and semi-empirical models have been proposed to predict infiltration flow through pairs of parallel plates and L-shaped cracks. This study used the dimensionless model proposed by Gross and Haberman (1989) to estimate infiltration flow rate. The model has been validated using the experimental data reported by Hopkins and Hansford (1974). The model validation indicated that the model could be used for both rectangular cracks and L-shaped cracks at low Reynolds numbers, which is typical for residential infiltration conditions. This infiltration model is comprised of three regions

according to the magnitude of a dimensionless difference pressure parameter, *NP*. The model is shown in equations 2-1 to 2-3.

$$NQ = 0.01042NP, \quad NP \le 250 \tag{2-1}$$

$$NQ = -3.305 + 0.2915NP^{0.5} + 0.01665NP^{0.75} + 0.0002749NP, \quad 250 < NP < 10^6 \tag{2-2}$$

$$NQ = 0.555NP^{0.5}, \quad NP \ge 10^6 \tag{2-3}$$

NP and NQ are defined in equations 2-4 and 2-5:

$$NP = \left(\frac{\Delta p D_h^2}{\rho_f \nu^2}\right)\left(\frac{D_h}{L}\right)^2 \tag{2-4}$$

$$NQ = \frac{qD_h}{W\nu L} \tag{2-5}$$

where ΔP is differential pressure across a crack, D_h is hydraulic diameter of a crack ($D_h \approx 2H$ for fine cracks), ρ_f is air density, ν is kinematic viscosity of air, q is infiltration flow rate, W is crack width, and L is crack length.

2.2.2 Infiltration Flow Field

Based on the infiltration flow model described previously, Han (1960) and Sparrow (1962) used an entrance length parameter (L_e) to verify whether infiltration flow could be assumed laminar for rectangular crack flow. Entrance length was defined as the channel length required for uniform flow to develop into laminar flow. If an entrance length were much shorter than the corresponding crack length, assuming laminar flow throughout the crack would be reasonable. Schlichting (1979) proposed a dimensionless entrance length ϕ to estimate the flow development region for parallel plate flow, as shown in equation 2-6:

$$\phi = \frac{L_e}{D_h \,\mathrm{Re}} \tag{2-6}$$

where Re is Reynolds number, and D_h is hydraulic diameter of a crack. Schlichting (1979) found when $\phi = 0.01$, crack infiltration flow could fully develop into laminar flow.

The entrance length L_e physically represents the length of the flow development region. If L_e is much smaller than total crack length L, infiltration flow can be assumed to be laminar throughout the crack.

2.2.3 Laminar Velocity Profiles for Parallel Plate Flow

Because residential cracks are mostly long and narrow, infiltration flow is believed to be laminar shortly after entering a crack. The velocity profile of fully developed laminar flow is parabolic, with the fastest moving region in the center and gradually decreasing to zero at crack walls. The parabolic velocity profile can be derived from the Navier-Stokes equation and the continuity equation, as shown in equation 2-7 (Kay 1957):

$$u = 6u_m\left(\frac{y}{H} - \left(\frac{y}{H}\right)^2\right) \tag{2-7}$$

where u_m is average infiltration velocity, H is crack height, and y is vertical position inside a crack.

2.3 MATERIALS AND METHOD

Figure 2-2 illustrates a schematic diagram of the infiltration flow test system. A crack sandwich that simulates typical building crack dimensions was installed between the indoor and outdoor chamber. A vacuum pump was used to draw air through the indoor chamber so as to create a differential pressure across the crack. The differential pressure was controlled by the precision needle valve V4 and monitored using the

differential pressure transducer, P1. Depending on infiltration flow rate, three gas mass flow meters, F1 to F3, were used to measure infiltration flow rate. Each flow meter has an on/off valve, V1 to V3, to select a flow meter with appropriate ranges. The following sections provide the specifications of the test chambers, crack sandwiches, and control/monitoring instruments.

2.3.1 Chamber

Figure 2-3 illustrates an exploded diagram of the acrylic test chamber. The chamber was composed of an indoor compartment and an outdoor compartment. The four pieces on the left-hand-side of Figure 2-3 comprised the outdoor compartment. It was made of a half-cut circular column of 220 mm I.D. Its top and bottom were sealed with two semi-circular plates. This assembly unit was then sealed with a binding plate to combine with the indoor chamber using bolts and nuts. There were three extension tubes manufactured on the top plate of the outdoor chamber. Two of them were used to hold a thermometer and a differential pressure transducer, while the third was an air inlet port. This port was connected to an aerosol generator to provide aerosol flow in a later particle penetration study. In addition to these openings, there was an outlet port at the bottom of the chamber so that aerosol flow could continuously flush through the chamber. In current infiltration study, these two aerosol ports were opened to atmosphere.

The right-hand-side chamber in Figure 2-3 is the indoor compartment. It is basically the same dimensions as the outdoor one, however it has only an outlet port. This port was connected to a vacuum pump to drive infiltration flow through the crack sandwich.

Between the outdoor and indoor compartments, there was a separation plate to hold a crack sandwich. The separation plate isolated these two chambers so that the differential pressures across the crack could be adjusted.

2.3.2 Crack Sandwiches

Two types of cracks were made as sandwiches in this study. They were straight-through rectangular cracks, and L-shaped cracks. The dimensions of the test cracks were chosen to simulate typical cracks for tighter buildings. Hopkins and Hansford (1974) measured typical crack dimensions in some residential houses. Their survey indicated that typical cracks were from 10 mm to 50 mm in length (L) and from 0.5 mm to 10 mm in height (H). As a result of the survey, this study chose crack length L = 30 mm and 60 mm, and crack width was 100 mm. However, the test cracks were made finer than the aforementioned crack heights since particle penetration models indicate that almost 100 % of particles penetrate through cracks if H is greater than 0.5 mm. Consequently, this experiment selects crack height H = 0.203 mm, 0.305 mm, 0.406 mm, and 0.508 mm. Because crack width was 200 to 500 times of to crack heights, the test cracks could be assumed to be pairs of parallel plates.

The narrow test cracks that simulate tighter structures are not extraordinary with the popularity of energy efficient buildings, as well as emergency shelters and buildings required in certain areas. One of the examples is the emergency planning zones (EPZ) of nuclear power plants. Originally, evacuation was deemed the major emergency response to protect people in the EPZ in case of power plant core meltdown or containment rupture. However, several modeling works and field research for the Three-Mile Island event and the Chernobyl accident found building envelops provided protection from exposure to airborne radio nuclides (Kocher, 1979; Brown, 1988; Roed and Cannell,

1988; Englemann, 1992). In light of the protection from building shells, tighter houses and emergency shelters are required in certain areas. The finer crack designs would mimic these cases.

Figure 2-4 illustrates an exploded diagrams of the L = 60 mm and L = 30 mm rectangular crack sandwiches. Each crack was made of two acrylic blocks, two stainless steel plates, and a pair of spacers. Several spacers of different thickness were used to make different crack height H. To ensure accurate crack heights H, thickness of the spacers was measured using a micrometer (0 to1 inch Mitutoyo Co., Kanagawa, Japan). The resolution of the micrometer is 0.0001 inch (2.5 μm). In practice, it was found that the tightness of bolts and nuts affected crack thickness significantly. As a result, a filler gauge (General Tools, Montreal, Canada) was used to determine actual crack height. The filler gauge has 26 gauge leaves, whose thickness covers from 38 μm to 0.635 mm. The step thickness between two leaves is 0.001 inch (25.4 μm). Crack thickness was defined by the thickest leaf gauge that could slide freely within the crack.

The same sandwich design was used to assemble the L-shaped cracks, as illustrated in Figure 2-5. The L-shaped crack was made by attaching a side plate to a rectangular sandwich forming a vertical crack channel. The length of the vertical channel was made the same as the horizontal one. In this study, only one crack length was made for the L-shaped crack. Both the horizontal and vertical channels were 30 mm in length. The overall crack length L = 60 mm.

2.3.3 Driving Force Control

This study used a vacuum pump to draw air from the indoor chamber to produce differential pressures between the indoor and outdoor chambers. The

magnitude was controlled by the needle valve V4 and monitored by the differential pressure transducer P1 (Setra 2641, Setra, Boxborough, MA). The full range of the micromanometer was 0 to 25 Pa, with accuracy of ±1% full scale. The micrometer was connected to a data logger (Lakewood, Edmonton, Alberta, Canada) to record a 4 to 20 mA signal output. The micronmanometer was calibrated using a laboratory made calibrator. This calibrator used the same operation theory as a Microtector (Model 1430, Dwyers Instruments, Inc.).

2.3.4 Flow Measurement

According to the target crack dimensions and differential pressures, equations 2-1 to 2-3 were used to estimate infiltration flow rates. It indicates that infiltration flow covers from ~0 to 1785.3 mL/min. Three gas mass flow meters, with full ranges of 0 to 100, 0 to 500, and 0 to 2000 mL/min, were used to cover the measurement range (FMA 3303, FMA 3305, and FMA 3307, Omega, Laval, Quebec). The flow meters were delivered with NIST certificates. To ensure no damage during shipment, a mini-Buck bubble meter (A. P. Buck, Orlando, FL) was used to validate their performance. The Lakewood data logger was used to record the 0 to 5 V signal output.

2.4 RESULTS AND DISCUSSION

2.4.1 Crack Infiltration

Figures 2-6 to 2-8 illustrate theoretical and experimental air infiltration flow rates for the L = 60 mm, L = 30 mm rectangular cracks; and the L = 60 mm L-shaped crack, respectively. In this study, infiltration flow rates were measured three times from 0 to 15 Pa, with step increment of approximately 0.5 Pa. Generally, the infiltration model agree with experimental results well. Significant deviation between experimental results and model predictions were found on the H = 0.508 mm and H = 0.305 mm cracks when

$\Delta P \geq 6$ to 8 Pa. However, the deviations were less than 5% from model predictions. Experimental results indicate that infiltration flow rates were generally linearly dependent on differential pressure for all crack assemblies, which suggested infiltration flow probably was laminar, according to the orifice flow model. However, high percentage error from model prediction was also observed at low differential pressure (< 3-4 Pa). This might be induced from the precision needle valve used in this study. At lower end, this valve was not proportional to its dial knob. As a result, when adjusted the valve to low flow rate to create low differential pressure, sudden drop was observed, and could not be controlled precisely.

2.4.2 Infiltration Flow Field

Figures 2-9 and 2-10 illustrate the percentage ratio of L_e/L for the L = 60 mm and 30 mm cracks, respectively. The figures indicate that the thicker the crack height, and the shorter the crack length, the L_e/L ratio will be greater. Within the test infiltration conditions, Figure 2-9 indicates that L_e/L were less than 3% for L = 60 mm cracks, when $\Delta P < 10$ Pa (typical differential pressure for residential conditions). Infiltration flow could be assumed laminar throughout the cracks.

For the L = 30 mm cracks, Figure 2-10 indicates that L_e/L are less than 8% when $\Delta P < 10$ Pa. For most cases, L_e/L were less than 5%. The laminar flow assumption was judged appropriate for residential crack infiltration modeling. This finding greatly simplifies particle penetration modeling because laminar flow field can be estimated using equation 2-7. Since the flow field is know, particle dynamic theories can be applied to simulate particle behavior, and thus particle penetration efficiency can be estimated.

2.5 CONCLUSION

This study used a semi-empirical infiltration model to estimate infiltration flow through rectangular and L-shaped cracks. A chamber was designed to validate the infiltration model. Using the modeling results, an entrance length parameter was used to validate the assumption of laminar flow across the crack. This study found:

1. Infiltration flow was linearly dependent on differential pressure under typical residential conditions (1 to 15 Pa). It suggests that infiltration flow fields were laminar.
2. Experimental results indicate that the model could predict infiltration through these cracks reasonably well. The infiltration flow rate for the test conditions ranged from ~0 to 1785.3 mL/min.
3. Using modeling results, the laminar infiltration flow field assumption was validated using the entrance length parameter. It indicates that L_e/L was, for the most part, less than 5% for typical differential pressure. Laminar flow assumption was generally valid.
4. Entrance length ratio (L_e/L) is proportional to differential pressure and crack height, and inversely proportional to crack length. For short/thick cracks, the infiltration flow field may not be laminar. Generally speaking, if $H < 0.5$ mm and $L > 30$ mm, the laminar flow assumption was valid.

Table 2-1 Crack dimensions and differential pressures tested in the infiltration study

Parameter	Symbol	Unit	Test conditions
Crack length	L	mm	Rectangular cracks: 30, 60 L-shaped crack: 60
Crack width	W	mm	100
Crack height	H	mm	0.203, 0.305, 0.406, 0.508
Differential Pressure	ΔP	Pa	0-15

(1) Rectangular Crack

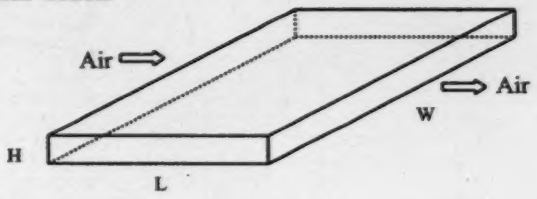

(2) L-shaped Crack

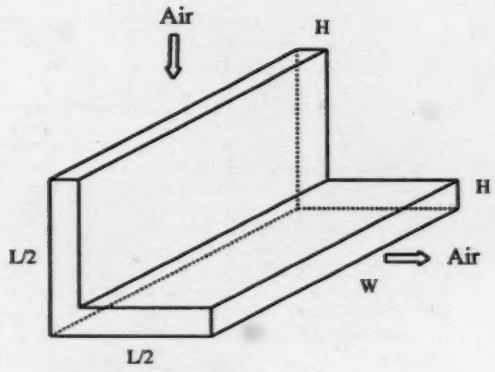

Figure 2-1 Definitions of rectangular and L-shaped cracks

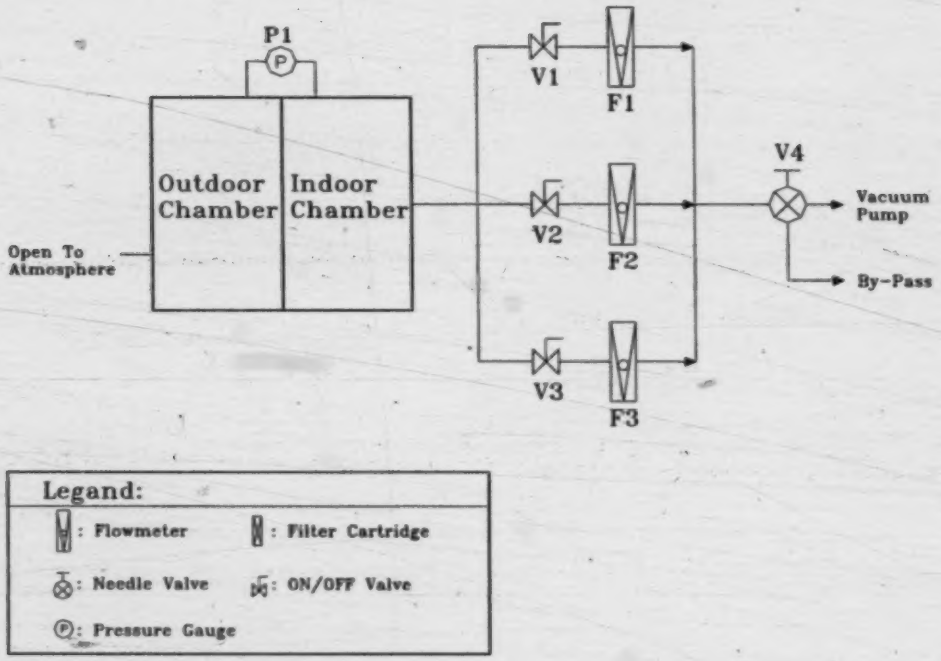

Figure 2-2 Schematic diagram of the experimental setup for the infiltration study

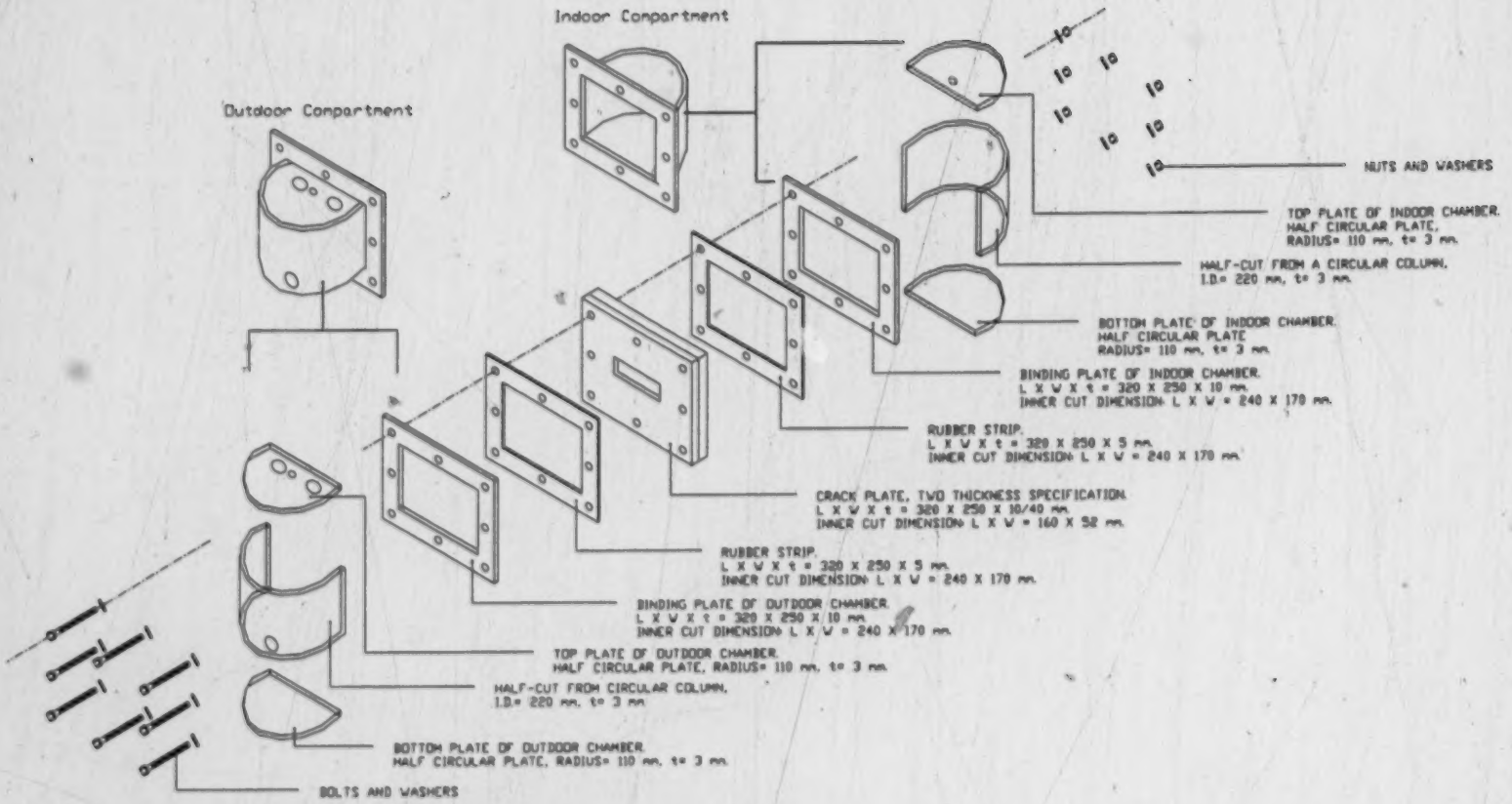
Indoor Compartment
Outdoor Compartment
NUTS AND WASHERS
TOP PLATE OF INDOOR CHAMBER.
HALF CIRCULAR PLATE.
RADIUS= 110 mm, t= 3 mm.
HALF-CUT FROM A CIRCULAR COLUMN.
I.D.= 220 mm, t= 3 mm.
BOTTOM PLATE OF INDOOR CHAMBER.
HALF CIRCULAR PLATE
RADIUS= 110 mm, t= 3 mm.
BINDING PLATE OF INDOOR CHAMBER.
L X W X t = 320 X 250 X 10 mm.
INNER CUT DIMENSION L X W = 240 X 170 mm.
RUBBER STRIP.
L X W X t = 320 X 250 X 5 mm.
INNER CUT DIMENSION L X W = 240 X 170 mm.
CRACK PLATE, TWO THICKNESS SPECIFICATION.
L X W X t = 320 X 250 X 10/40 mm.
INNER CUT DIMENSION L X W = 160 X 52 mm.
RUBBER STRIP.
L X W X t = 320 X 250 X 5 mm.
INNER CUT DIMENSION L X W = 240 X 170 mm.
BINDING PLATE OF OUTDOOR CHAMBER.
L X W X t = 320 X 250 X 10 mm.
INNER CUT DIMENSION L X W = 240 X 170 mm.
TOP PLATE OF OUTDOOR CHAMBER.
HALF CIRCULAR PLATE, RADIUS= 110 mm, t= 3 mm.
HALF-CUT FROM CIRCULAR COLUMN.
I.D.= 220 mm, t= 3 mm.
BOTTOM PLATE OF OUTDOOR CHAMBER.
HALF CIRCULAR PLATE, RADIUS= 110 mm, t= 3 mm.
BOLTS AND WASHERS

Figure 2-3 Explode diagram of the test chamber (not to scale)

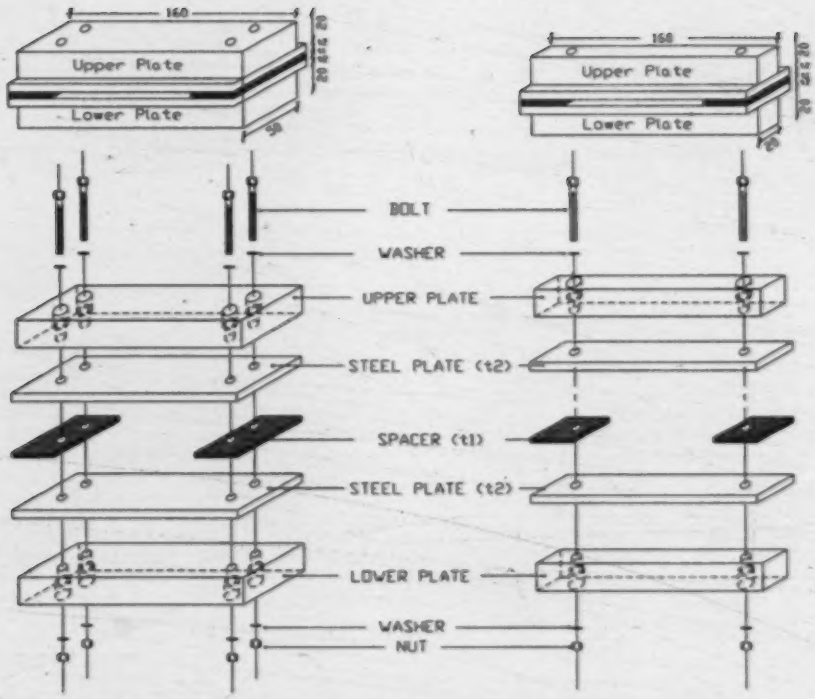

Figure 2-4 Explode diagram of the rectangular crack sandwiches (not to scale)

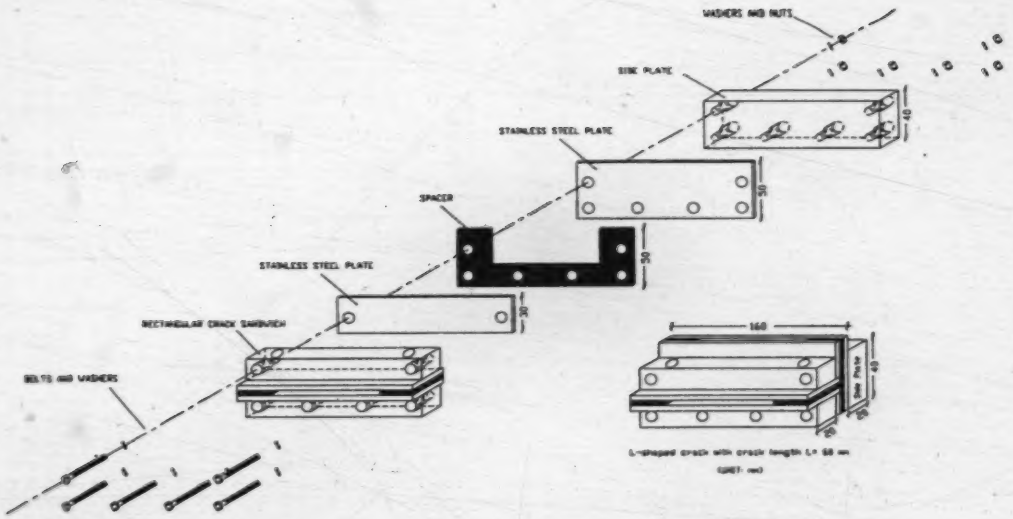

Figure 2-5 Explode diagram of the L-shaped crack sandwich (not to scale)

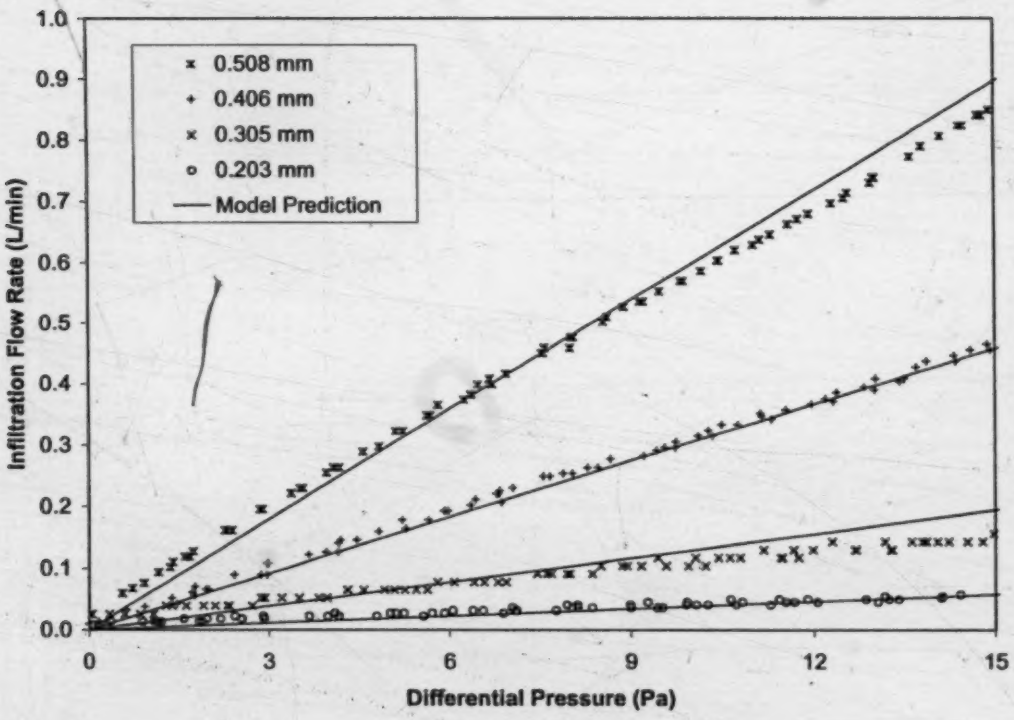

Figure 2-6 Infiltration flow rate for the $L = 60$ mm rectangular cracks

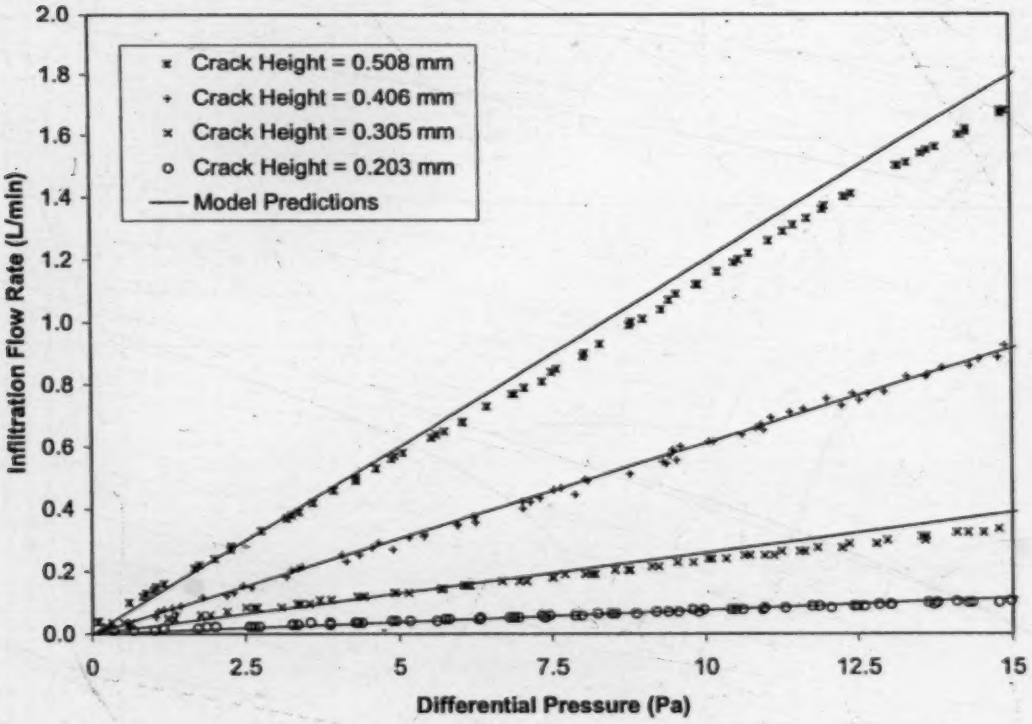

Figure 2-7 Infiltration flow rate for the $L = 30$ mm rectangular cracks

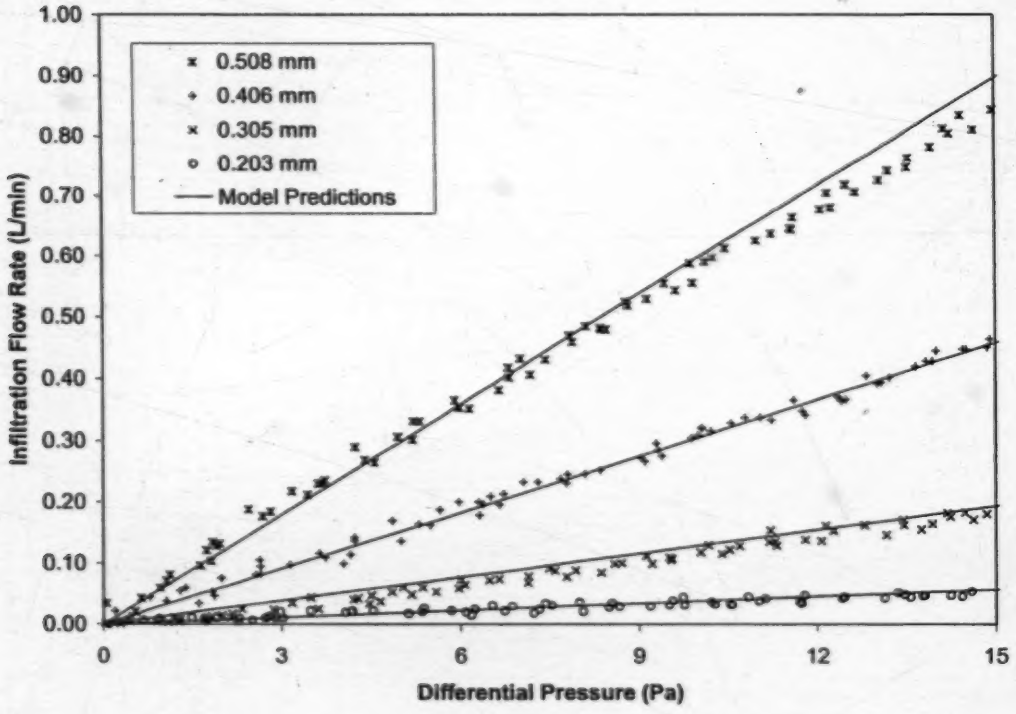

Figure 2-8 Infiltration flow rate for the L = 60 mm L-shaped cracks

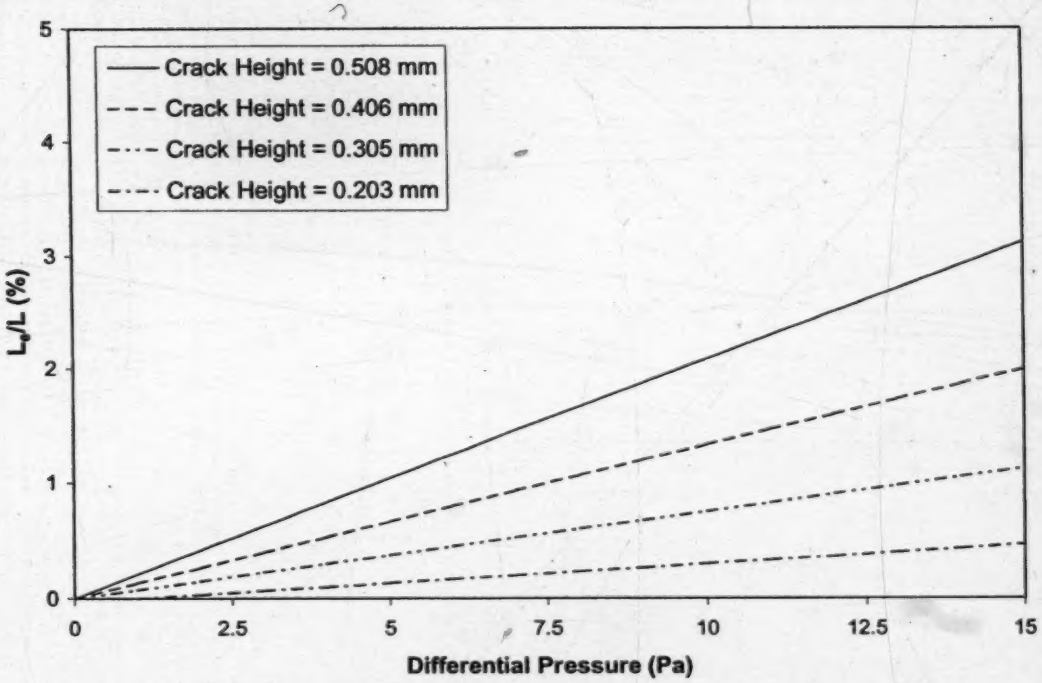

Figure 2-9 Entrance length ratio (L_e/L) for the L = 60 mm rectangular cracks

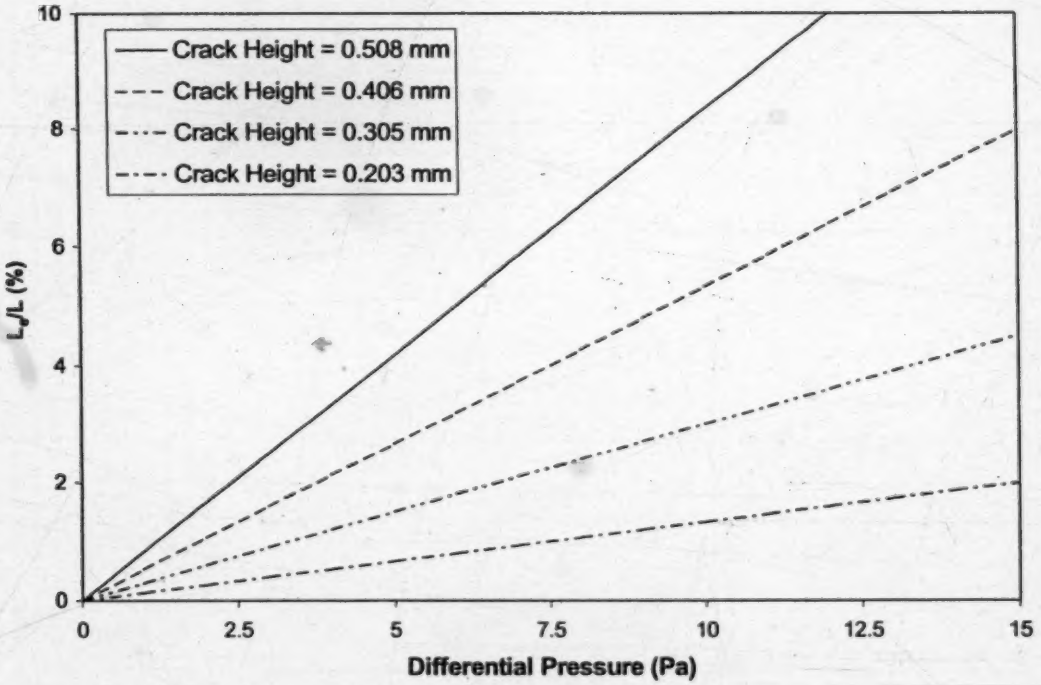

Figure 2-10 Entrance length ratio (L_e/L) for the L = 30 mm rectangular cracks

2.6 REFERENCES

ASTM E741-00 (2001). Standard Test Method for Determining Air Change in a Single Zone by Means of a Tracer Gas Dilution. American Society for Testing and Materials. West Conshohocken, PA.

Baker, P. H., Sharples S., and Ward I. C. (1987). Air Flow Through Cracks. *Build. Environ.* 22:293-304.

Etheridge, D. W. (1977). Crack Flow Equations and Scale Effect. *Build. Environ.* 12:181-189.

Fogh, C. L., Byrne, M. A., Roed, J., and Anthony, J. H. G. (1997). Size Specific Indoor Aerosol Deposition Measurement and Derived I/O Concentration Ratios. *Atmos. Environ.* 31:2193-2203.

Gross, D., and Haberman, W. L. (1989). *Fire Safety Science: Proceedings of the Second International Symposium.* The Second International Symposium on Fire Safety Science, International Association for Fire Safety Science, Tokyo, Japan.

Han, L. S. (1960). Hydraulic Entrance Lengths for Incompressible Laminar Flow in Rectangular Ducts. *J. Appli. Mech.* Sep:403-409.

Hopkins, L. P., and Hansford, B. (1974). Air Flow Through Cracks. *Build. Serv. Engr.* 42:123-131.

Kehrli, D. W. (1995). A Description of the New ASTM Test Method E1242, Used for Measuring Fenestration Air Leakage at Different Temperatures and Pressures. *Airflow Performance of Building Envelopes, Components, and Systems.* Ed: Modera, M. P., and Persily, A. K. American Society for Testing and Materials. Philadelphia, PA. pp81-89.

Kay, J. M. (1957). *An Introduction to Fluid Mechanics and Heat Transfer.* Pitman Press, Bath. New York, N. Y.

Liu, D. L., and Nazaroff, W. W. (1999). Modeling Particles Penetration Through Cracks in Building Envelopes, *Proceedings: 8th Int. Conference on Indoor Air Quality and Climate.* Edinburgh, Scotland, 4:1055-1059.

Liu, D. L., and Nazaroff, W. W. (2001). Modeling Pollutant Penetration Across Building Envelopes. *Atmos. Environ.* 4:

Nazaroff, W.W. and Cass, G. R. (1989). Mathematical Modeling of Indoor Aerosol Dynamics. *Environ. Sci. Technol.* 23:157-165.

Olcerst, R. (1994). Quantification of an Indoor Population by Means of Air Exchange Rates and Carbon Dioxide Gas Concentrations. *Am. Ind. Hyg. Assoc. J.* 55:1080-1083.

Palmiter, L. (1995). Uncertainties in Fan Pressurization Measurements. *Airflow Performance of Building Envelopes, Components, and Systems*. Ed: Modera, M. P., and Persily, A. K. American Society for Testing and Materials. Philadelphia, PA. pp266-283.

Schlichting, H. (1979). *Boundary-Layer Theory*. McGraw-Hill, New York, N. Y.

Sparrow, E. M., Hixon, C. W., and Shavit, G. (1967). Experiments on Laminar Flow Development in Rectangular Ducts. *Transactions of the ASME.* pp116-164.

Thatcher, T. L., and Layton, D. W. (1995). Deposition, Resuspension, and Penetration of Particles within a Residence. *Atmos. Environ.* 29:1487-1497.

Wang, Y. L., and Longwell, P. A. (1964). Laminar Flow in the Inlet Section of Parallel Plates. *A.I.Ch.E. J.* 10:323-329.

CHAPTER 3. MODELING PARTICLE PENETRATION THROUGH HORIZONTAL CRACKS

3.1 INTRODUCTION

Liu and Nazaroff (1999) proposed a particle penetration model for horizontal cracks. Their model assumed that a rectangular crack was analogous to a pair of parallel plates. This modeling combined an infiltration model with particle deposition models to estimate particle penetration coefficient (P_p). Liu and Nazaroff (1999) assumed that the flow field across a crack was laminar and considered gravitational sedimentation and Brownian diffusion to simulate particle penetration coefficient. These two mechanisms were assumed independent. The overall penetration coefficient $P_p = P_g \times P_d$, where P_g and P_d were penetration coefficients calculated from the models that considered gravitational sedimentation and Brownian diffusion, respectively. For gravitational sedimentation, Liu and Nazaroff used the penetration model for particle elutriator to calculate P_g (Fuchs, 1964). As for Brownian diffusion, the diffusion battery theory was used (Hinds, 1982). Mosley *et al.* (2001) and Liu and Nazaroff (2001) have validated the modeling approach experimentally. Both studies found the trends of experimental data agreed well with theoretical models for the surrogates of ideal rectangular cracks.

Instead of modeling gravitational sedimentation and Brownian diffusion separately, this study adapted a particle mass transport equation to estimate particle penetration coefficient. This modeling approach combined infiltration flow field with gravitational sedimentation and Brownian diffusion to construct the mass transport model. The derived particle transport equation is a two-dimensional partial differential equation. It was solved numerically using Newton's method of tangents. The advantage of the particle mass transport model is it not only estimates particle penetration

coefficient, but also provides concentration contours inside cracks. The concentration contours visualize the concentration distribution inside cracks. This information helps identifying the dominant particle deposition mechanisms. This study also compared the performance of the model with two other models that considered particle deposition induced from gravitational sedimentation. The comparison indicated that the mass transport model was applicable to micron-sized and submicron-sized particles. The model was validated using experimental data reported by Mosley *et al.* (2001). It indicates that this model agreed well with experimental results for both micron-sized and submicron-sized particles.

3.2 THEORETICAL BACKGROUND

Because particles are transported by infiltration air to penetrate through building envelopes, particle penetration modeling cannot be independent from air infiltration modeling. This study considered a residential crack as a pair of parallel plates and used an infiltration model to estimate infiltration flow and its flow field. The information was combined with particle deposition models to estimate particle penetration coefficients. The following sections discuss the derivation of the particle penetration models.

3.2.1 Air Infiltration Theory

Three questions need to be defined for a crack infiltration flow: (1) what is the flow rate? (2) is the flow field laminar? and (3) what is the velocity profile? The answers to these questions for rectangular cracks have been derived from theory of parallel-plate flow, which has been discussed and experimentally validated in Chapter 2. It indicates that the model proposed by Gross and Haberman (1989) predicted infiltration flow rate reasonably well. In addition, entrance length analysis suggested that crack infiltration flow could be assumed laminar for long narrow cracks. The velocity profile of the

laminar flow field is a parabolic distribution function. It has been derived from the Navier-Stokes equation and the continuity equation (Kay, 1957). This chapter incorporates the infiltration field function into a particle mass transport function to simulate particle penetration behavior.

3.2.2 Particle Deposition Modeling

Assuming laminar infiltration flow, three particle penetration models that consider gravitational sedimentation and/or Brownian diffusion have been developed for rectangular channels (Licht, 1980, Fuchs, 1964, Taulbee and Yu, 1975). Two of the models were proposed by Licht (1980) and Fuchs (1964) for particle elutriators. These two models considered gravitational sedimentation as the particle deposition mechanism. The modeling approach was based on particle trajectory analysis. They are termed the "Licht model" and the "Fuchs model". The third model considered both gravitational sedimentation and Brownian diffusion. It was proposed by Taulbee and Yu (1975) and Tan and Hsu (1972) to simulate particle penetration through diffusion batteries. This model used a mass transport equation to predict particle penetration coefficients. It has the advantage of providing concentration contours to visualize particle penetration behavior. This model is called the "Taulbee model" herein. This chapter summarizes the three particle penetration models. Detailed derivation procedures are provided in Appendices D and E.

3.2.3 The Fuchs Model

Fuchs (1964) applied the concept of flow function to derive a particle penetration model that considered gravitational sedimentation. Fuchs (1980) calculated the trajectory of a particle in a laminar flow field based on the Newton's law of motion. If

the trajectory of a particle reached crack walls before it exited a crack, it was assumed removed. Several assumptions were made to develop this model (Fuchs, 1964):

1. particles are homogeneously and uniformly distributed at crack entrance;
2. buoyancy force is neglected since density of air is much less than that of particles;
3. particles instantly adjust their horizontal velocity to fluid velocity, i.e. very short relaxation time; and
4. particles accelerate rapidly to their terminal settling velocity in the vertical direction.

Using Newton's law of motion, the Fuchs model is presented in equation 3-1 (Fuchs, 1964; and Wang, 1975):

$$P_p = 1 - \frac{L}{H}\frac{v_s}{u_m} \tag{3-1}$$

Walton (1954) and Pich (1972) also used the concepts of flow tube and limiting trajectory analysis to simulate particle deposition caused by gravitational sedimentation. Both studies derived the same particle penetration model.

3.2.4 The Licht Model

Licht (1980) proposed another model to calculate the trajectory of a particle in a laminar flow field based on the Newton's law of motion. If the trajectory of a particle reached crack walls before it exited a crack, it was assumed removed. The Licht model is shown in equation 3-2 (Licht, 1980):

$$3\varepsilon^2 - 2\varepsilon^3 = \frac{L}{H}\frac{v_s}{u_m}, \tag{3-2}$$

where ε is the portion of particles that deposit inside a crack, L is crack length, H is crack height, v_s is particle terminal settling velocity, and u_m is average fluid velocity. As a result, particle penetration coefficient $P_p = 1 - \varepsilon$.

3.2.5 The Taulbee Model

When both gravitational sedimentation and Brownian diffusion are considered in particle dynamics, particle trajectory analysis fails to simulate the wiggling motion induced from Brownian diffusion. Taulbee and Yu (1975) and Tan and Hsu (1972) used a mass transport equation to simulate particle penetration for diffusion batteries. The steady state mass transport equation was written as shown in equation 3-3:

$$\nabla \cdot (c\vec{v}) = D\nabla^2 c \qquad (3\text{-}3)$$

where c is particle concentration, $\vec{v}$ is a particle velocity vector, and D is particle diffusivity. For a two-dimensional parallel-plate flow, equation 3-3 can be written as:

$$u\frac{\partial c}{\partial x} + v_s\frac{\partial c}{\partial y} = D\left(\frac{\partial^2 c}{\partial x^2} + \frac{\partial^2 c}{\partial y^2}\right) \qquad (3\text{-}4)$$

Axial advection term — Sedimentation term — Axial diffusion term — Traverse diffusion term

where u is fluid velocity and other terms have been defined previously.

Tan and Hsu (1972) used Peclet Number to determine the relative importance of the advection terms and the diffusion terms. Peclet Number is defined as $Pe = 2hV/D$, where V is advection velocity, and h is crack half-height ($H/2$). Tan and Hsu (1972) suggested that a diffusion term is negligible relatively to an advection term when $Pe >> 1$.

For the sedimentation and traverse diffusion terms in equation (3-4), the magnitude of crack height was on the order of 10^{-4} m, Peclet Number falls on the order of 10^{-1}, 10^{2}, and 10^{3} for 0.1 μm, 1.0 μm, and 3.0 μm particles, respectively. It suggests that both gravitational sedimentation and radial diffusion must be considered for submicron-sized particles. As a result, both the sedimentation term and traverse diffusion term were

retained in the model. As for the significance of axial advection and axial diffusion terms, it was found that Peclet Numbers are generally far greater than one for our test conditions. As a result, the axial diffusion term was neglected. The mass transport equation can be rewritten as equation 3-5:

$$u\frac{\partial c}{\partial x}+v_s\frac{\partial c}{\partial y}=D\frac{\partial^2 c}{\partial y^2} \tag{3-5}$$

This is a two-dimensional, second-order partial differential equation. Two boundary conditions are required to solve the model. The first boundary condition was derived from the assumption that particles were uniformly distributed at crack entrance, i.e. $c(0,y)=c_0$. The second boundary condition considered that particles were removed when they deposit on crack surface. As a result, particle concentrations at crack surfaces are zero, i.e. $c(x,\pm h)=0$.

Equation 3-5 was transformed into a dimensionless form by choosing the following five dimensionless groups:

$$X=\frac{2x}{hPe},\ Y=\frac{y}{h},\ \sigma_s=\frac{hv_s}{D},\ C=\frac{c}{c_0},\ U=\frac{u}{u_m} \tag{3-6}$$

When these dimensionless groups are substituted into equation 3-5, the dimensionless mass transport equation becomes:

$$U\frac{\partial C}{\partial X}+\sigma_s\frac{\partial C}{\partial Y}=\frac{\partial^2 C}{\partial Y^2} \tag{3-7}$$

The corresponding dimensionless boundary conditions are $C(0,Y)=1$, and $C(X,\pm 1)=0$.

3.3 MODEL DEVELOPMENT

3.3.1 Modeling Parameters

Three independent parameters were required to execute the crack infiltration models and the particle penetration models: (1) the differential pressure across a crack, (2) overall crack dimensions, and (3) aerodynamic diameter of a particle. Table 3-1 lists the simulated parameters in this study. Differential pressures from 1 to 10 Pa were chosen to simulate typical residential conditions (Walkers and Wilson, 1972). Particles from 0.1 to 2.5 μm were investigated, given their potential adverse health characteristics. In addition, it is believed that the dominant particle deposition mechanisms are different for micro-sized and submicron-sized particles.

As for crack dimensions, the overall dimensions of rectangular cracks from 10 to 50 mm in length (L), and 200 to 1000 μm in height (H) were chosen in this study. These cracks are narrower than typical residential cracks. As discussed in Chapter 2, the selected narrow cracks are to simulate tighter building designs. Such tighter structures are not extraordinary with the popularity of energy efficient buildings, as well as the emergency shelters and buildings required in certain area that are subject to potential air pollution episodes.

3.3.2 Dimensionless Modeling Approach

Combinations of the three modeling parameters produce a wide range of infiltration situations. Modeling them by changing one parameter at a time is an inefficient and complex task. As a result, the two dimensionless parameters X and σ_y, derived in the Taulbee model, were chosen to simplify this task. Since every combination of the three modeling parameters maps to a unique set of X and σ_y, these two parameters represent all infiltration situations.

In order to compare the performance of the three particle penetration models, X and σ_y were adapted into the Licht model and the Fuchs model so that the three particle penetration models could be compared. When X and σ_y are substituted into equation 3-1, the dimensionless Fuchs model becomes:

$$P_p = 1 - \frac{X \cdot \sigma_y}{2} \tag{3-8}$$

Similarly, the dimensionless Licht model is:

$$3\varepsilon^2 - 2\varepsilon^3 = \frac{X \cdot \sigma_y}{2} \tag{3-9}$$

These two equations indicate that $X \cdot \sigma_y$ determines the particle penetration coefficient for these two models. This is reasonable because the $X \cdot \sigma_y$ term eliminates particle diffusivity term, which is not considered in these two models.

The physical meanings of X and σ_y must be clarified to facilitate explanation of the results. According to the definition of σ_y, it is related to crack height (h) and particle size (as related to D and v_s). Equation 3-6 suggests that a larger σ_y relates to a larger particle diameter (lower D and higher v_s), and a wider crack. As a result, the larger the σ_y, the more significant the role of gravitational sedimentation will be. Because the magnitude of h is on the order of 10^{-4} m, $\sigma_y > 10^2$ represents particles larger than 1.0 μm in aerodynamic diameter; σ_y on the order of 10^0 represents particles of approximately 0.5 μm; while $\sigma_y \sim 10^{-1}$ represents particles of approximately 0.1 μm. Thus, σ_y can be deemed as a dimensionless particle size parameter for a given order of crack height. When the modeling parameters: d_p, L, H and ΔP are considered, Table 1 indicates that the magnitudes of σ_y and X fall on the order of 10^{-1} to 10^4 and 10^0 to 10^{-7}, respectively.

3.3.3 Numerical Method

The Taulbee Model is a two-dimensional, second-order partial differential equation. It was solved numerically by dividing a crack into $M \times N$ grids, where M is the grid number in horizontal axis and N is the grid number in vertical axis. This chapter chose $M = 20$ and $N = 10$ in the modeling. Modeling results form a 20×10 concentration matrix, as shown in Figure 3-1. This study used the backward finite difference method to define the above differential terms:

$$\frac{\partial C}{\partial X} = \frac{C_{i,j} - C_{i-1,j}}{\Delta X} \tag{3-10}$$

$$\frac{\partial C}{\partial Y} = \frac{C_{i,j} - C_{i,j-1}}{\Delta Y} \tag{3-11}$$

$$\frac{\partial^2 C}{\partial Y^2} = \frac{C_{i,j-1} - 2 \cdot C_{i,j} + C_{i,j+1}}{\Delta Y^2} \tag{3-12}$$

where i and j are gird numbers in x and y axis; ΔX and ΔY are grid length. In this study $i = 1$ to 20 and $j = 1$ to 10. The backward finite difference method transformed equation 3-7 into a set of 200 algebraic equations. The equation set was solved using the Newton's method of tangents. This study used the *TK-Solver*™ software to solve the equation set. The program codes are attached in Appendix F.

3.4 RESULTS AND DISCUSSION

3.4.1 Particle Penetration Curves

Figure 3-2 illustrates the particle penetration curves predicted from the Licht, Fuchs, and Taulbee models. This figure reveals some interesting points among the test models. For the Fuchs model and the Licht model, both models consider gravitational deposition as the particle deposition mechanism. The figure indicates that when $X \cdot \sigma_y \geq 1$,

both models predict consistent particle penetration coefficients. The Licht model predicts slightly higher particle penetration than the Fuchs model. However, the difference is not discernable. P_p was found to decrease from 0.5 to 0 when $X\cdot\sigma_y$ changes from 1.0 to 2.0. At $X\cdot\sigma_y = 1.0$, both models estimate $P_p = 0.5$, i.e., 50% of particles penetrate through cracks. For $X\cdot\sigma_y < 1$, the Licht model estimated lower particle penetration coefficients than the Fuchs model. The modeling differences range from 0 to approximately 0.1. It was also found that the Licht model predicts lower penetration coefficient than the Taulbee model. This discrepancy is disputable because the Taulbee model considers both gravitational sedimentation and Brownian diffusion. Theoretically, the Licht model should always predict a higher particle penetration coefficient than the Taulbee model. This discrepancy needs to be investigated to prove model validity.

Another finding observed from Figure 3-2 is the effects of Brownian diffusion, which can be recognized by comparing the particle penetration coefficients predicted from the Fuchs model and the Taulbee model. For example, in the case of $\sigma_y > 10^2$, both models predict consistent particle penetration coefficients. As discussed previously, $\sigma_y > 10^2$ represents particles larger than 1.0 μm. For particles of this size range, Brownian diffusion is less effective than gravitational deposition, relatively. As a result, both models predict consistent particle penetration efficiency. However, the Taulbee model predicts a lower P_p. The difference is possibly induced from Brownian diffusion. These results suggest that Brownian diffusion removes some particles when $\sigma_y > 10^2$, however, only a very minor portion.

Brownian diffusion significantly reduces particle penetration when σ_y is on (or less than) the order of 10^1, which is characterized by submicron-sized particles. In the

case of $\sigma_y = 10$ and $\log X = -1$, the Taulbee model predicts $P_p = 0.45$, while the Fuchs model predicts 0.5. Brownian diffusion deposition causes approximately 5% of particles to deposit inside the crack. This suggests that using the Fuchs model or the Licht model is not appropriate when $\sigma_y \leq 10$. As a result, when $\sigma_y \leq 10^1$, both Brownian diffusion and gravitational sedimentation must be considered in particle penetration modeling. The Taulbee model should be used instead of the other two when $\sigma_y \leq 10^1$.

Finally, the case of $\sigma_y = 10^{-1}$ is examined, which is characterized by particles approximately 0.1 μm in aerodynamic diameter. Figure 3-2 indicates that both the Licht model and the Fuchs model estimate higher particle penetration coefficients than those predicted by the Taulbee model. For example, when $\log X = 0$, the Taulbee model predicts $P_p = 0.15$, which is over 70% lower the Licht model and the Fuchs model (0.85 and 0.95, respectively). Because Brownian diffusion governs particle deposition behavior for particles ≤ 0.1 μm, the Taulbee model is the appropriate model.

From the above discussion, the Taulbee model was suitable for the whole range of X and σ_y because it considers both gravitational sedimentation and Brownian diffusion. On the other hand, the Fuchs model and the Licht model are only suitable for $\sigma_y > 10^2$ because they consider gravitational sedimentation only. Modeling results indicated that predictions using the Licht model are not consistent with the other two models. Further experimental investigation is required to verify the validity of the Licht models. If the Licht model is excluded for now, a rule can be used as a guideline to choose an appropriate particle penetration model: For particles larger than 1.0 μm (micron-sized particles), both the Fuchs model and the Taulbee model are appropriate to model outdoor-to-indoor particle penetration. Because the Fuchs model is much simpler in execution, it

is an appropriate model. However for submicron particles, the Taulbee model should be used since Brownian diffusion is a significant mechanism for particle removal.

3.4.2 Concentration Contour

The Taulbee model provides more information than predicting particle penetration coefficients. The modeling results can be illustrated as concentration contours to examine the dominant particle deposition mechanisms. Figures 3-3 to 3-5 illustrate typical contours for the diagnosis.

Figure 3-3 illustrates the concentration contours for $\sigma_y = 10^2$, which represents particles approximately 1.0 μm in aerodynamic diameter. These figures indicate the concentration contours are downward tilted, suggesting that particle behavior is influenced by gravitational force. As a result, particles are mostly deposited on the bottom crack walls. Except for gravitational force, the effect of infiltration velocity on particle penetration behavior is substantial. Figure 3-3 (a) to (c) illustrates the concentration contours for $X = 5\times10^{-2}$, 2.5×10^{-2} and 10^{-3}, respectively. According to equation 3-6, the smaller the X parameter, the higher the difference pressure across a crack and thus the higher the infiltration velocity. A higher infiltration velocity means a shorter residence time inside the cracks. As a result, more particles are swept out of the crack. The hypothesis is supported by the predicted particle penetration coefficients, which are 0.002, 0.079, and 0.946 for $X = 5\times10^{-2}$, 2.5×10^{-2}, and 10^{-3}, respectively.

Figure 3-4 illustrates the concentration contours for 0.1 μm particles ($\sigma_y = 0.1$). The concentration contours are symmetric to crack centerlines. Although these contours slightly tilt downward, this effect is not discernable. This suggests that non-directional

Brownian diffusion dominates particle deposition behavior. Particle penetration coefficients for $X = 10$, 1 and 0.1 are 0, 0.151, and 0.768, respectively.

Figure 3-5 illustrates the concentration contours for $\sigma_y = 10$, which represents particles of approximately 0.5 μm in diameter. These concentration contours indicate that both gravitational sedimentation and Brownian diffusion are effective particle deposition mechanisms since the tilted extent lies between the above two cases. The significant tilted extent suggests that gravitational deposition is the major particle deposition mechanism. Particle penetration coefficients for $X = 0.5$, 10^{-1} and 10^{-2} are 0.006, 0.452, and 0.920, respectively.

3.4.3 Validating the Taulbee Model Using the IAQ Modeling Approach

This study used experimental results published by Mosley *et al.* (2001) to validate the Taulbee model. Mosley *et al.* designed a chamber to measure particle penetration for horizontal slits. The study used a two-compartment chamber, each 19 m^3 to simulate indoor and outdoor environments. A slit assembly, composed of 140 rectangular slits, was placed between the two compartments to simulate cracks of building envelopes. The slit dimensions were $H = 0.508$ mm, $L = 102$ mm, and $W = 433$ mm. The total effective leakage area equaled to 0.03 m^2. Mosley *et al.* used an aerosol generator to produce oil particles from 0.05 to 5 μm. Aerosols were released in the outdoor chamber to simulate outdoor particles. Particle concentrations in the indoor and outdoor chambers were measured by an electrical low pressure impactor (ELPI) and an aerodynamic particle sizer (APS) to estimate P_p using the IAQ model. The estimated P_p's for submicron-sized and micron-sized particles were adapted to validate the Taulbee model.

Figure 3-6 compares the Taulbee model and experimental penetration coefficients (Mosley *et al.*, 2001) for submicron-sized particles. The diamonds, circles, cubes, and triangles represent the measured mean particle penetration coefficients for difference pressures of 2, 5, 10, and 20 Pa, respectively. The means and standard deviations were calculated from 7 to 12 observations reported by Mosley *et al.* (2001). The solid lines represent theoretical particle penetration coefficient estimated by the Taulbee model. Figure 3-6 indicates that the H = 0.508 mm slits did not provide much protection from submicron-sized particles; more than 90% of particles penetrated through the slits. When differential pressure was higher than 10 Pa, the measured mean particle penetration coefficients were even higher than 1.0. Because particle concentrations in the indoor compartment should always be less than or equal to the outdoor compartment, the $P_p > 1.0$ results may be the results of experimental errors. If experimental error is taken into account, the Taulbee model satisfactorily estimates particle penetration coefficients for submicron-sized particles.

Figure 3-7 compares the Taulbee model and experimental penetration coefficients for micron-sized particles. When the differential pressure across the slit assembly is 2 Pa, the rectangular slits effectively remove particles larger than 2.5 μm; particle penetration coefficients are close to zero. Experimental results show higher penetration for small particles. For those from 1 to 2.5 μm, particle penetration coefficient ranges from 0.66 to 0.

When ΔP = 5 Pa, the slits effectively filter out particles larger than 3 μm; theoretical particle penetration coefficients are less than 0.17. As for particles from 1 μm to 2.5 μm, particle penetration coefficient decreased from 0.86 to 0.3. Model deviations

are usually less than 0.1 from the mean particle penetration coefficients. For ΔP = 10 Pa, the theoretical particle penetration coefficient decreases from 0.93 to 0.04 for particles from 1 to 5 μm in aerodynamic diameter.

The comparisons made in Figures 3-6 and 3-7 indicates that the Taulbee model reasonably predicted the mean particle penetration coefficients for 1, 2, and 5 μm particles. However, the measured particle penetration coefficients for 3 and 4 μm particles are much lower than the Taulbee model. The mean deviations are approximately 0.2 and 0.15, respectively. When the difference pressure across the slit assembly was 20 Pa, the Taulbee model reasonably predicted particle penetration coefficient except for 5 μm particles. Modeling results indicate that particle penetration coefficient decreases from 0.97 to 0.30 for particles from 1 to 5 μm in aerodynamic diameter. Model deviations are always less than 0.1. However, experimental penetration coefficients underestimated P_p by approximately 0.2 for 5 μm particles.

This model validation indicates that the Taulbee model estimated particle penetration for submicron-sized particles and micron-sized (PM2.5) particles reasonably well. Deviations from mean experimental results for submicron-sized particles were mostly less than 10%. For micron-sized particles, the Taulbee model predicted the trends reasonably well. However, the standard deviations of experimental observations could amount to 20%. In attempting to explain model deviation, it is necessary to take experimental errors into account. Mosley *et al.* (2001) used a mass conservation model to calculate P_p. This model is intrinsically the same as the IAQ model discussed previously. For this type of modeling approach, experimental error in air exchange rate, particle deposition rate, and particle concentration measurement will propagate through to the

estimated particle penetration coefficient. Although Mosley *et al.* took a great effort in chamber design to minimize experimental errors. They estimated approximately 35% uncertainty in the calculated particle penetration coefficient. Mosley *et al.* pointed out the sources of experimental error include uncertainties in air exchange rate measurements, particle concentration measurements, incomplete chamber mixing, and particle deposition rate measurements. In consideration of these potential error sources, model validation indicated that the Taulbee model satisfactorily estimated experimental results. Model deviations were mostly less than 10%, with some situations approaching 20%. However, these deviations were well below the 35% experimental uncertainty reported by Mosley *et al.* (2001).

3.5 CONCLUSION

This study incorporated an infiltration model into particle deposition models to simulate particle penetration for rectangular cracks. Trajectory analysis was used to estimate particle penetration induced from gravitational sedimentation (the Licht model and the Fuchs model), and a mass transport equation was used when both gravitational sedimentation and Brownian diffusion were considered (the Taulbee model). The results of the modeling found:

1. Comparison among these three models indicates that the Taulbee model is universally applicable for both micron-sized particle and submicron-sized particles. This model has the advantage of providing concentration contours to diagnose particle deposition mechanisms.
2. For particles larger than 1.0 μm in aerodynamic diameter, gravitational sedimentation governs particle deposition behavior. All three models can be used to estimate

particle penetration. However, it is found that the Licht model deviated from the other two models.

3. For submicron-sized particles, Brownian diffusion is the major or significant deposition mechanism. Only the Taulbee model should be used to simulate particle penetration.
4. The Taulbee model was validated using experimental data published by Mosley *et al.* (2001). The validation work indicates that the Taulbee agree well with the trends of experimental data for both submicron-sized and micro-sized ($\leq$ 5 μm) particles. It indicates that the 0.508 mm slits could not effectively retard submicron-sized particles from penetrating indoors. As for micron-sized particles, both particle diameter and differential pressure determine particle penetration efficiency.

Table 3-1 Summary of the parameters in the particle penetration modeling

Parameter	Symbol	Unit	Range	
			Minimum	Maximum
Particle aerodynamic diameter	D_p	μm	0.1	2.5
Crack length	L	mm	10	50
Crack height	H	μm	200	1000
Pressure drop	ΔP	Pa	1	10
Dimensionless parameter X	X	-	10^{0}	10^{-7}
Dimensionless parameter σ_y	σ_y	-	10^{-1}	10^{4}

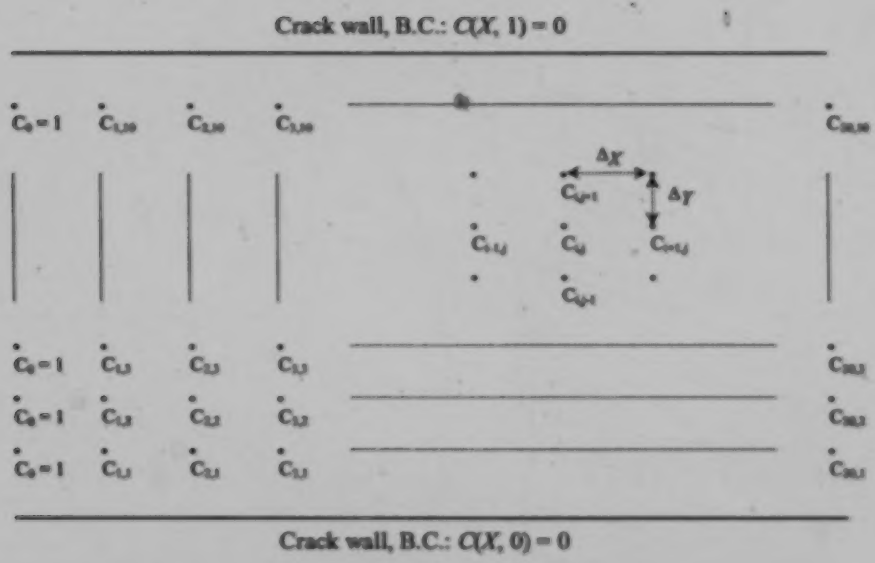

Figure 3-1 Boundary conditions and grid layout for the numerical analysis

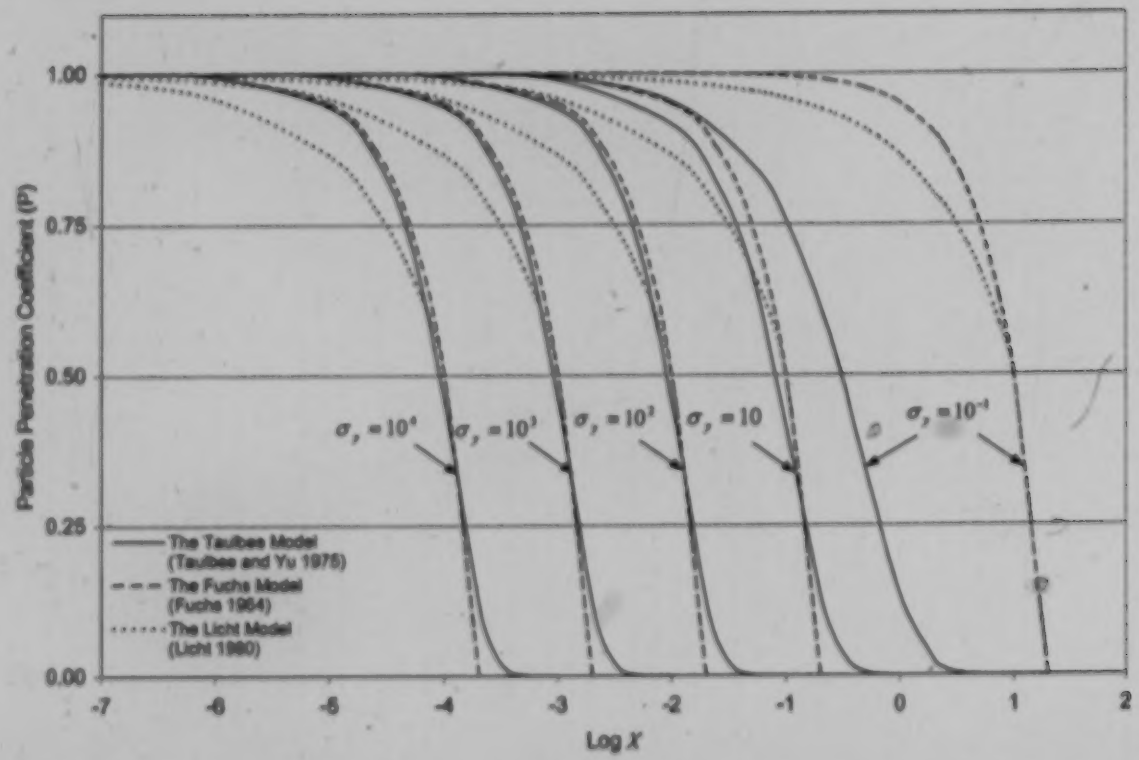

Figure 3-2 Theoretical particle penetration coefficients versus dimensionless parameters X and σ_y, which correspond to crack length L = 10 to 50 mm, crack height H = 100 to 1000 mm, and differential pressure ΔP = 1 to 12 Pa.

(a) $X = 5 \times 10^{-2}$

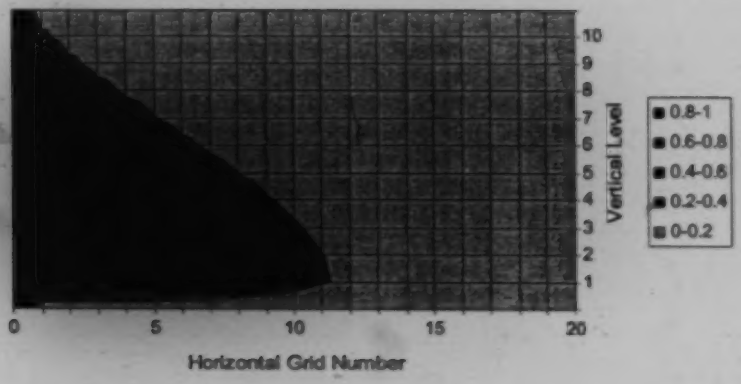

(b) $X = 2.5 \times 10^{-2}$

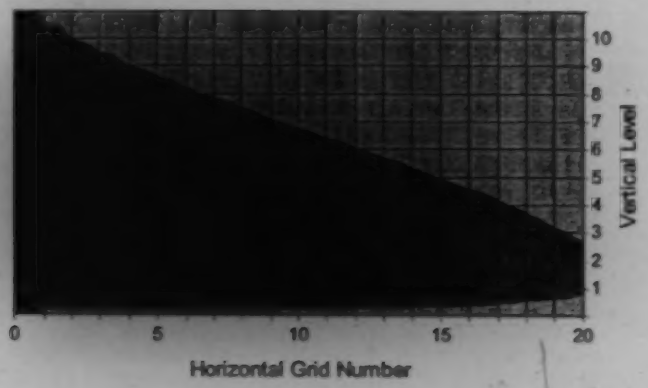

(c) $X = 10^{-3}$

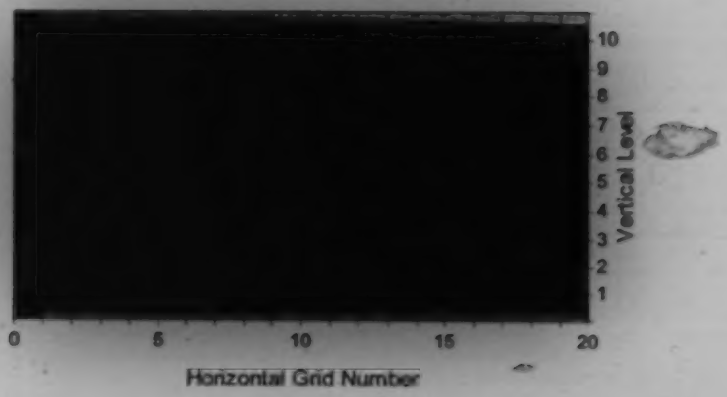

Figure 3-3 Particle concentration contours for $\sigma_y = 10^2$ (simulated using the Taulbee model, σ_y of this order represents particles approximately 1 μm in diameter).

(a) $X = 10$

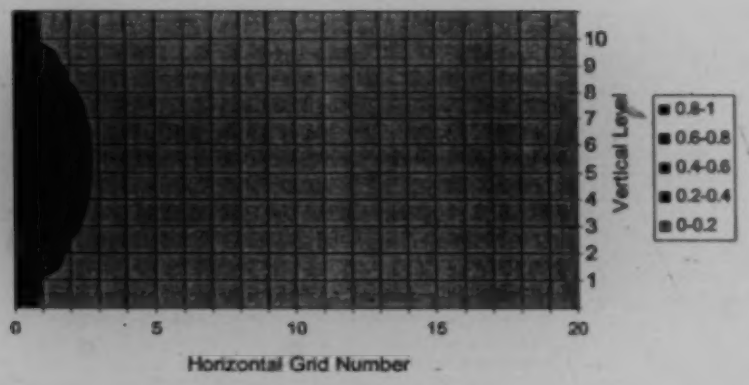

(b) $X = 1$

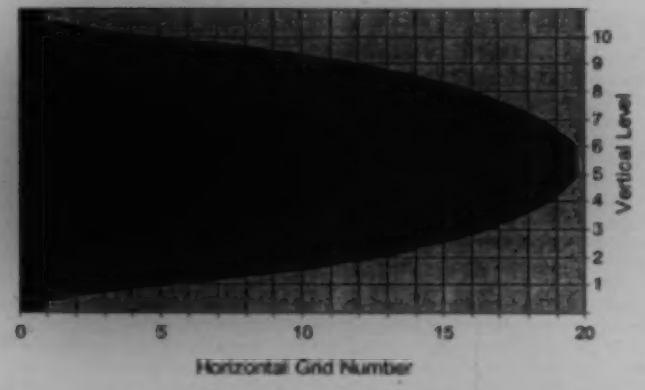

(c) $X = 0.1$

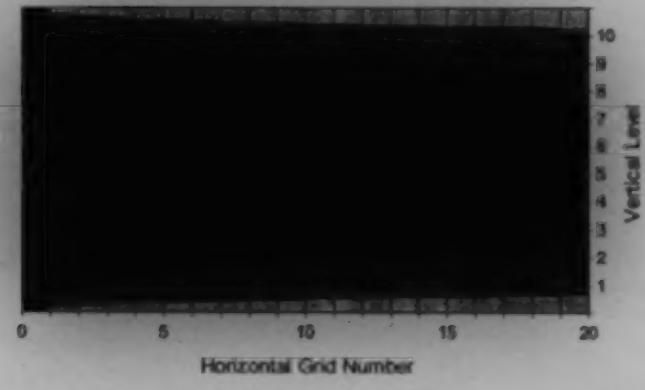

Figure 3-4 Particle concentration contours inside a crack for $\sigma_y = 0.1$ (simulated using the Taulbee model, σ_y of this order represents particles approximately 0.1 μm in diameter).

(a) $X = 0.5$

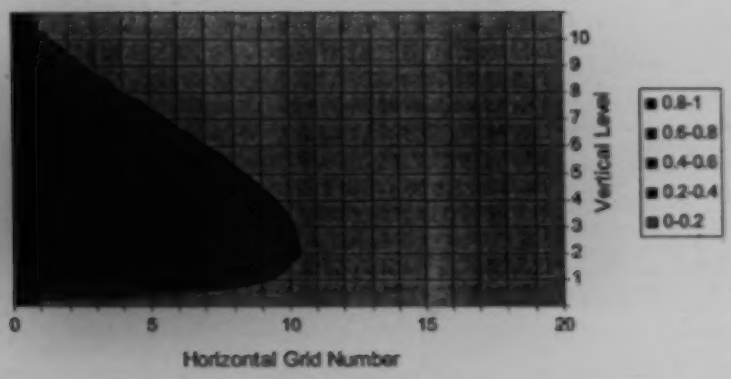

(b) $X = 10^{-1}$

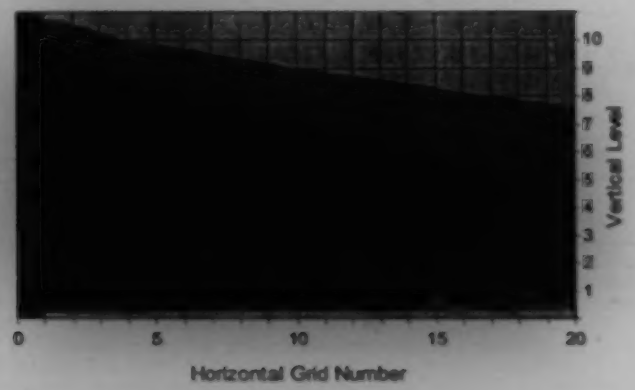

(c) $X = 10^{-2}$

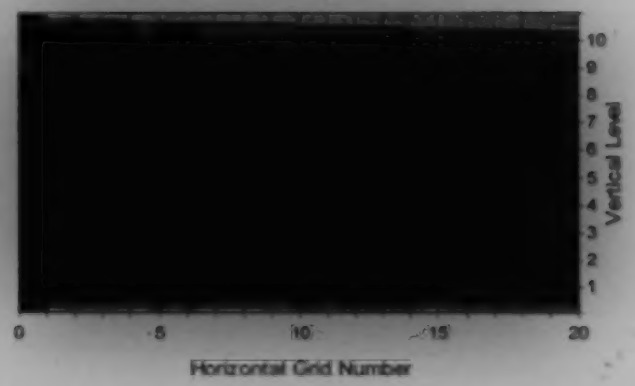

Figure 3-5 Particle concentration contours inside a crack for σ_y =10 (simulated using the Taulbee model, σ_y of this order represents particles of approximately 0.7 μm in diameter).

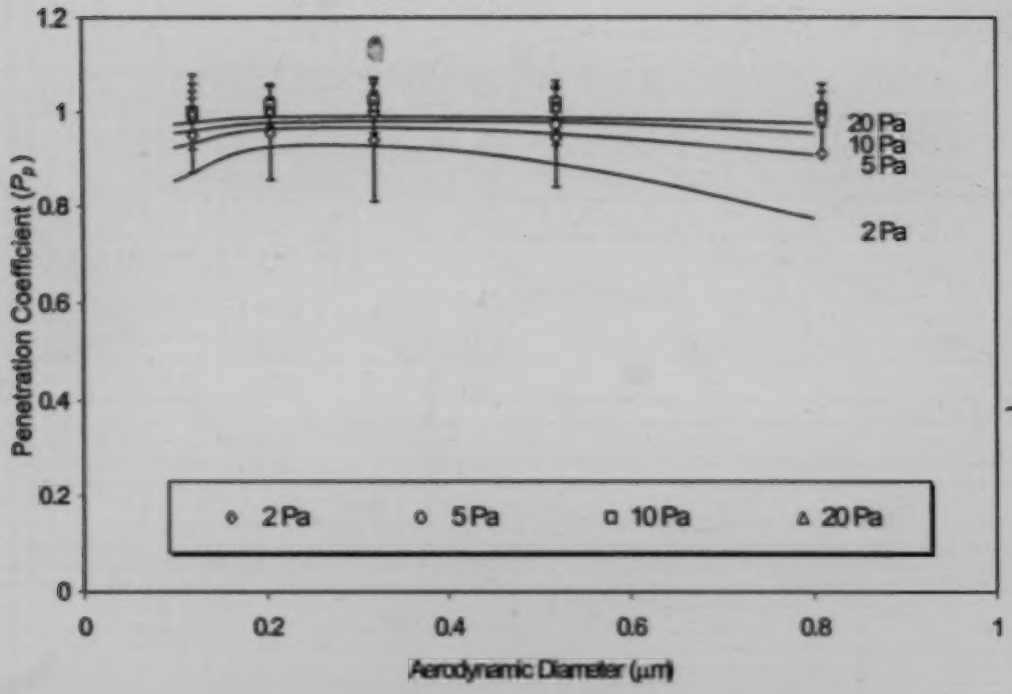

Figure 3-6 Comparison between the Taulbee model and experimental particle penetration coefficients for submicron-sized particles published by Mosley *et al.* (2001)

Note: Solid lines represent the Taulbee model. Symbols represent experimental results of Mosley *et al.* (2001). Error bars represent standard deviations.

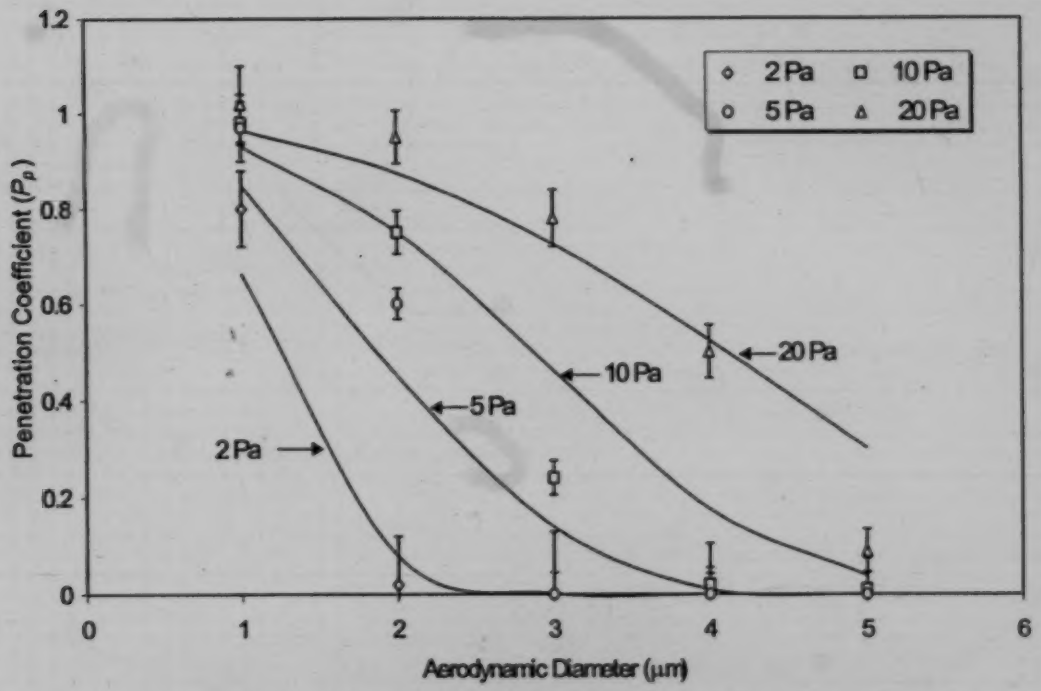

Figure 3-7 Comparison between the Taulbee model and experimental particle penetration coefficients for micron-sized particles published by Mosley *et al.* (2001)

Note: Solid lines represent the Taulbee model. Symbols represent experimental results of Mosley *et al.* (2001). Error bars represent standard deviations.

3.6 REFERENCES

Clement, C. F. (1995). Aerosol Penetration through Capillaries and Leaks: Theory. *J. Aerosol Sci.* 26:369-385.

Fuchs, N. A. (1964). *The Mechanics of Aerosols*. Army Chemical Warfare Laboratories, Army Chemical Center, Maryland, U. S.

Gross, D., and Haberman, W. L. (1989). Fire Safety Science: Proceedings of the Second International Symposium. The Second International Symposium on Fire Safety Science, International Association for Fire Safety Science, Tokyo, Japan.

Hinds, W. C. (1982). *Aerosol Technology*. John Wiley & Sons, Inc., New York, N. Y.

Licht, W. (1980). *Air Pollution Control Engineering*. Marcel Dekker, Inc., New York, N.Y.

Liu, D. L., and Nazaroff, W. W. (1999). Modeling Particles Penetration Through Cracks in Building Envelopes, *Proceedings: 8th Int. Conference on Indoor Air Quality and Climate.* Edinburgh, Scotland, 4:1055-1059.

Liu, D. L., and Nazaroff, W. W. (2001). Particle Penetration Through Building Cracks: Effect of Materials, *20th Annual AAAR Conference.* October 15-19, 2001. Portland, OR, p264.

Louis, M. J., and Nelson, P. E. (1995). Extraneous Air Leakage from Window Perimeters. *Airflow Performance of Building Envelops, Components, and Systems, ASTM STP 1255*, Mark P. M., and Andrew K. P., American Society for Testing and Materials, Philadelphia, PA, 108-122.

Mayo, T. (1992). *Air Leakage Characteristics of Various Rough-opening Sealing Methods for Windows and Doors*. Canada Center for Mineral and Energy Technology Branch, Ottawa, ON, Canada.Mitchell, J. P., Edwards, R. T. and Ball, M. H. E. (1990) The Penetration of Aerosols Through Fine Capillaries. *Int. J. Radioactive Materials Transport (RAMTRANS)* 1:101-116.

Morton, D. A. V. and Mitchell, J. P. (1995). Aerosol Penetration through Capillaries and Leaks: Experimental Studies on the Influence of Pressure. *J. Aerosol Sci.* 26:353-367.

Mosley, R. E., Greenwell, D. J., Sparks, L. E., Guo, Z., Tucker, W. G., Fortmann, R., and Whitfield, C. (2001). Penetration of Ambient Fine Particles into Indoor Environment. *Aerosol Sci. Technol.* 34:127-136.

Pich, J. (1972). Theory of Gravitational Deposition of Particles from Laminar Flows in Channels. *J. Aerosol Sci.* 3:351-361.

Tan, C. W., and Hsu, C. J. (1972). Mass Transfer of Aerosols with Axial Diffusion in Narrow Rectangular Channels. *Appl. Sci. Res.* 25:295-312.

Taulbee, D. B., and Yu, C. P. (1975). Simultaneously Diffusion and Sedimentation of Aerosols in Channel Flows. *J. Aerosol Sci.* 6:433-441.

Walker, I. S., and Wilson, D. J., (1990). *The Alberta Air Infiltration Model.* Report 71. Department of Mechanical Engineering, University of Alberta, Edmonton, Alberta, Canada.

Walton, W. H. (1954). Theory of Size Classification of Airborne Dust Clouds by Elutriation. *British Journal of Applied Physics.* (Supplement No. 3):S29-S40.

Wang, C. (1975). Gravitational Deposition of Particles from Laminar Flows in Inclined Channels. *J. Aerosol Sci.* 6:191-204.

CHAPTER 4. MODELING PARTICLE PENETRATION THROUGH INCLINED CRACKS

4.1 INTRODUCTION

Outdoor-indoor particle penetration modeling for horizontal cracks has been investigated by Liu and Nazaroff (1999) and Mosley *et al.* (2001). However, horizontal cracks only account for a portion of residential cracks. There are also L-shaped and multiple-bend cracks typically found in building envelops. It is necessary to propose a model that can deal with these cracks. Liu and Nazaroff (1999) discussed the effects of inertial impaction on L-shaped cracks and double-bend cracks. Given the low infiltration velocity for typical residential conditions, it was found that the Stokes Number was less than 0.36 for typical residential conditions. Inertial impaction did not enhance particle deposition. This finding suggests that an alternative modeling approach that considers a L-shaped crack as the combination of a horizontal section and a vertical section may be applicable. Because infiltration flow can be assumed laminar for long narrow cracks, particle deposition behaviors in the horizontal and vertical sections probably can be assumed independent for these two sections. As a result, the overall particle penetration coefficient $P_p = P_h \times P_v$, where P_h and P_v are penetration coefficients in the horizontal and vertical sections. If a particle penetration model can deal with cracks of arbitrary incline angles, particle penetration coefficients for L-shaped and multiple-bend cracks can be estimated.

The objective of this chapter was to derive a model to estimate particle penetration coefficient for inclined cracks. The incline crack model is an extension of the Taulbee model. It combines infiltration modeling with particle mass transport modeling to estimate a particle penetration coefficient. The derived model is a two-dimensional,

second-order partial differential equation. It can be transformed into a set of algebraic equations using finite difference methods. The algebraic equation set can be solved using the Newton's method of tangent. The solution to the equation set is a concentration matrix inside a crack. It helps identify particle deposition mechanisms.

The incline crack model requires three input parameters: aerodynamic diameter, crack geometry, and differential pressure. In this study, the differential pressure parameter was chosen from 0 to 12 Pa to cover typical residential conditions (Walker and Wilson, 1990). Both submicron-sized (0.1 μm) and micron-sized (1.0 μm, and 2.5 μm) particles were investigated, given their potential adverse health characteristics and respiratory deposition efficiency. In addition, the dominant deposition mechanisms for submicron-sized and micron-sized particles were identified. For crack geometry, this study chose an $H = 0.305$ mm, and $L = 60$ mm crack in the model simulation. Modeling results were used to examine the effects of incline angle, differential pressure, and particle size on particle penetration coefficient.

4.2 THEORETICAL BACKGROUND

4.2.1 Air Infiltration Modeling

The infiltration model proposed by Gross and Haberman (1989), discussed in Chapter 3, was adapted to estimate crack infiltration flow. An advantage of this model is it can deal with both rectangular and L-shaped cracks. This enables the incline crack model to be used in L-shaped crack penetration modeling. It is expected that infiltration behavior through inclined cracks is the same as horizontal ones, and the flow field can be assumed laminar for typical residential conditions.

4.2.2 Particle Dynamics

Figure 4-1 illustrates a particle traveling through a rectangular channel of height H, and length L. The channel inclines at an angle θ, v_s is terminal settling velocity of the particle, and $u(y)$ is fluid velocity. For typical residential crack infiltration, the flow field $u(y)$ is assumed laminar and can be described by equation 2-7. Let the x-axis and y-axis be the axial and traverse coordinates along the crack. The laminar fluid flow velocity $u(y)$ is parallel to the x-axis, while terminal settling velocity (v_s) can be divided into an axial and a traverse velocity components, i.e. $\bar{v}_s = v_{sx}\bar{i} + v_{sy}\bar{j}$, where v_{sx} and v_{sy} are component terminal settling velocities in x and y directions. The mass transport equation is shown in equation 4-1 (Taulbee and Yu, 1975; Tan and Hsu, 1972):

$$\nabla \cdot (c\vec{v}) = D\nabla^2 c \qquad (4\text{-}1)$$

where c is particle concentration, $\vec{v}$ is particle velocity vector, and D is particle diffusivity. For two-dimensional parallel-plate flow, the particle velocity vector is $\bar{v} = \bar{u} + \bar{v}_s$, where $\bar{u}$ is fluid velocity and $\bar{v}_s$ is terminal settling velocity of a particle. As a result, equation 4-1 can be written as:

$$(u + v_{sx})\frac{\partial c}{\partial x} + v_{sy}\frac{\partial c}{\partial y} = D\left(\frac{\partial^2 c}{\partial x^2} + \frac{\partial^2 c}{\partial y^2}\right) \qquad (4\text{-}2)$$

where $v_{sx} = -\, v_s \sin\theta$ and $v_{sy} = -\, v_s \cos\theta$ for a crack inclined at an angle θ, and v_{sy} is effective particle deposition velocity.

Two boundary conditions are required to solve equation 4-2. First, the particle concentration is assumed uniformly distributed at crack entrance, i.e. $c(0, y) = c_0$. Second, particles are assumed removed when they deposit on crack surfaces. As a result, particle concentration on crack surface equals to zero, i.e. $c(x,0) = c(x, H) = 0$.

Equation 4-2 can be transformed into a dimensionless form by choosing four of the dimensionless parameters (X, Y, C, and U) used in Chapter 3. The σ_y used in Chapter 3 was divided into two terms ($\sigma_y \cdot cos\theta$ and $\sigma_y \cdot sin\theta$) because the current model considered two dimensions. When these dimensionless groups are substituted into equation 4-2, the dimensionless mass transport equation is:

$$(U - \frac{2\sigma_x}{Pe})\frac{\partial C}{\partial X} - \sigma_y \frac{\partial C}{\partial Y} = \left(\frac{2}{Pe}\right)^2 \frac{\partial^2 C}{\partial X^2} + \frac{\partial^2 C}{\partial Y^2} \qquad (4\text{-}3)$$

The corresponding dimensionless boundary conditions are: $C(0,Y) = 1$ and $C(X,0) = C(X,1) = 0$.

4.2.3 Numerical Method

The particle penetration model is a two-dimensional, second-order partial differential equation. It can be solved numerically by dividing a crack into $M \times N$ grids, where M and N are grid number in the horizontal axis and vertical axis. This study chose $M = 20$ and $N = 10$, forming a 20×10 concentration matrix, as shown in Figure 4-2. The backward finite difference method was used to define the above differential terms as shown in the following:

$$\frac{\partial C}{\partial X} = \frac{C_{i,j} - C_{i-1,j}}{\Delta X} \qquad (4\text{-}4)$$

$$\frac{\partial C}{\partial Y} = \frac{C_{i,j} - C_{i,j-1}}{\Delta Y} \qquad (4\text{-}5)$$

$$\frac{\partial^2 C}{\partial X^2} = \frac{C_{i-1,j} - 2 \cdot C_{i,j} + C_{i+1,j}}{\Delta X^2} \qquad (4\text{-}6)$$

$$\frac{\partial^2 C}{\partial Y^2} = \frac{C_{i,j-1} - 2 \cdot C_{i,j} + C_{i,j+1}}{\Delta Y^2} \qquad (4\text{-}7)$$

where i = 1 to 20 and j = 1 to 10 are gird numbers in x and y axis, and ΔX and ΔY are grid lengths. The backward finite difference method transformed equation 4-4 into a set of 200 algebraic equations. It was solved using the *TK-Solver*™ software. The program codes are attached in Appendix G.

4.3 RESULTS AND DISCUSSION

This study chose micron-sized (1 and 2.5 μm) and submicron-sized (0.1 μm) particles to simulate the effect of inclined angle and differential pressure on particle penetration coefficient. The simulated crack incline angles (θ) ranged from –90° to 90°. A positive θ represents an upward incline crack and vise versa. The simulated crack geometries were L = 60 mm and H = 0.305 mm, and typical differential pressures (ΔP) from 1 to 12 Pa were chosen in the modeling.

4.3.1 Effects of Incline Angle

Figure 4-3 illustrates the effects of incline angle on particle penetration coefficient for 2.5 μm particles. The penetration curves indicate that particle penetration coefficients are symmetric to θ = 0°, which suggests that incline orientation (upward and downward inclination) does not affect particle penetration coefficient. For any differential pressure, particle penetration coefficient increases monotonously with $|\theta|$. A horizontal crack provides the best protection to retard particles from penetrating through a crack. The finding can be explained from the effect of incline angle on the effective particle deposition velocity ($v_{sy} = -v_s \cos \theta$). When $|\theta|$ increases from 0° to 90°, cos θ decreases from 1 to 0 monotonously. The decreased effective particle deposition velocity reduces particle deposition induced from gravitational sedimentation. As a result, P_p increases monotonously with $|\theta|$. At 90°, the effective particle deposition velocity v_{sy}

equals to zero. Brownian diffusion is the only particles deposition mechanism. Figure 4-3 indicates that Brownian diffusion does not enhance particle deposition for the 2.5 μm particles. Complete penetration occurs for all simulated differential pressures. The figure also indicates that P_p increases monotonously with differential pressure for all incline angles. A greater differential pressure increases infiltration velocity, which reduces particle residence time such that more particles are swept out of the crack. Take $\theta = 0°$ as an example, particle penetration coefficient increases from 0 to 0.49 when ΔP increases from 1 to 12 Pa.

Figure 4-4 illustrates the effects of incline angle on particle penetration coefficient for 1.0 μm particles. Similar to 2.5 μm particles, the effect of incline angle on P_p is symmetric to $\theta = 0°$. For any differential pressure, particle penetration coefficient increases monotonously with $|\theta|$, which suggests that a horizontal crack provides the best protection to retard particles from penetrating through a crack. For horizontal cracks, P_p increases from 0.18 to 0.91 for ΔP from 1 to 12 Pa. As for vertical cracks, $v_{sy} = 0$, Brownian diffusion is the only particle deposition mechanism. Because Brownian diffusion is not an efficient deposition mechanism for micron-sized particles, the simulated particle penetration coefficients are higher than 0.95. Comparisons between Figure 4-3 and Figure 4-4 indicate that particle penetration coefficients for 1 μm particles are always higher than those of 2.5 μm particles. The difference in P_p is related to the difference in terminal settling velocity.

Figure 4-5 illustrates the effects of incline angle on particle penetration coefficient for 0.1 μm particles. Compared to the results of 1.0 and 2.5 μm particles, incline angle did not show any effect on particle penetration coefficient. The distinct

feature indicates that particle penetration is induced from non-directional Brownian diffusion. As a result, crack inclination does not affect particle deposition. For all inclined angles, P_p increases from 0.55 to 0.92 when ΔP increases from 1 to 12 Pa.

4.3.2 Concentration Contours

Figure 4-6(a) to (d) illustrate the concentration contours of 2.5 μm particles for incline angles θ = 0°, 45°, 60°, and 90°. The simulated differential pressure is 2 Pa, which corresponds to the infiltration velocity of 13.7 mm/sec. For θ = 0°, 45°, and 60°, the figures indicates that concentration contours tilt downward, which suggests that gravitational sedimentation is the dominant particle deposition mechanism. Because effective particle deposition velocity v_{sy} is inversely proportional to $|\theta|$, particle penetration coefficient increases accordingly with the absolute value of the incline angle. The effect can be observed from the increasingly stretched contours from θ = 0° to 60°. For vertical cracks (θ = 90°), concentration contours are symmetric to crack centerline and nearly complete penetration occurs. The finding suggests that non-directional Brownian diffusion is the dominant particle deposition mechanism. Because Brownian diffusion is not a significant deposition mechanism for micron-sized particles, only a minor fraction deposits inside the crack, $P_p \sim 1.0$.

Figure 4-7(a) to (d) illustrate the concentration contours of 1.0 μm particles for incline angles θ = 0°, 45°, 60°, and 90°, respectively. The simulated differential pressure was 2 Pa. Similar to Figure 4-6, the downward tilted concentration contours suggest that gravitational sedimentation governs particle deposition for θ = 0°, 45°, and 60°. When θ = 90°, concentration contours are symmetric to crack centerline. It indicates that non-directional Brownian diffusion dominates particle deposition. Because

Brownian diffusion is not a significant deposition mechanism for micron-sized particles, only a minor fraction deposits inside the crack, $P_p = 0.95$.

Figure 4-8(a) and (b) illustrate the concentration contours of 0.1 μm particles for incline angles $\theta = 0°$ and 90°. The simulated differential pressure is 2 Pa. Different from previous cases, concentration contours are symmetric to crack centerline for both incline angles and their concentration contours are independent of $|\theta|$. The finding indicates that non-directional Brownian diffusion dominates deposition behavior for submicron-sized particles, $P_p = 0.92$.

4.4 CONCLUSION

A numerical particle transport model was derived to simulate particle penetration coefficients for cracks of arbitrary incline angles. This model was used to examine how crack incline angle (θ), differential pressure (ΔP), and particle size affect the particle penetration coefficient for the simulated crack geometry. This study found:

1. For micron-sized particles, gravitational sedimentation is the dominant particle deposition mechanism. Modeling results indicate that horizontal cracks ($\theta = 0°$) provide the best protection to prevent micron-sized particles from penetrating through cracks.
2. Upward and downward crack inclination has the same effect on particle penetration coefficient. P_p increased monotonously with the absolute value of incline angle, $|\theta|$. An inclined crack reduces effective particle deposition velocity (v_{sy}); as a result, particle penetration efficiency is proportional to $|\theta|$.
3. Brownian diffusion is the dominant particle deposition mechanism for submicron-sized particle. Because Brownian diffusion is a non-directional deposition mechanism,

incline angle does not affect particle penetration efficiency for submicron-sized particles.

4. For a specific crack geometry and particle size, particle penetration efficiency is proportional to differential pressure. An increased difference pressure increased infiltration velocity such that more particles are swept out of the crack.
5. Brownian diffusion is the dominant particle deposition mechanism for vertical cracks. For micron-sized particles because Brownian diffusion is not a significant deposition mechanism, nearly complete penetration occurs for vertical cracks. As for submicron-sized particles, because Brownian diffusion is a non-directional deposition mechanism, particle penetration coefficient is independent of incline angles.

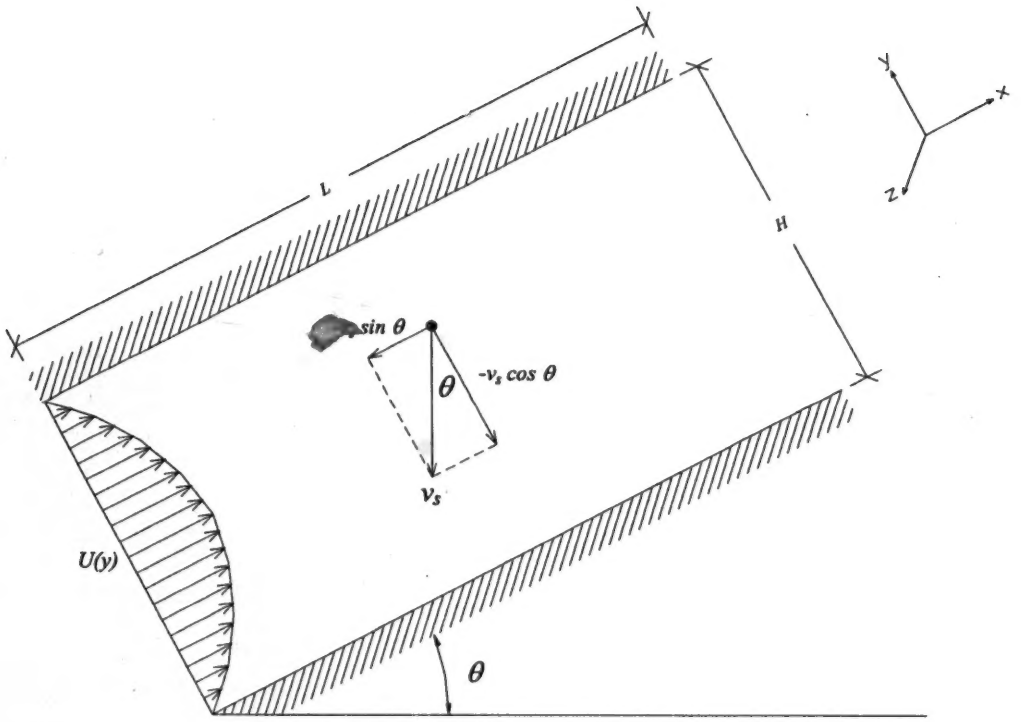

Figure 4-1 Schematic diagram of an inclined crack

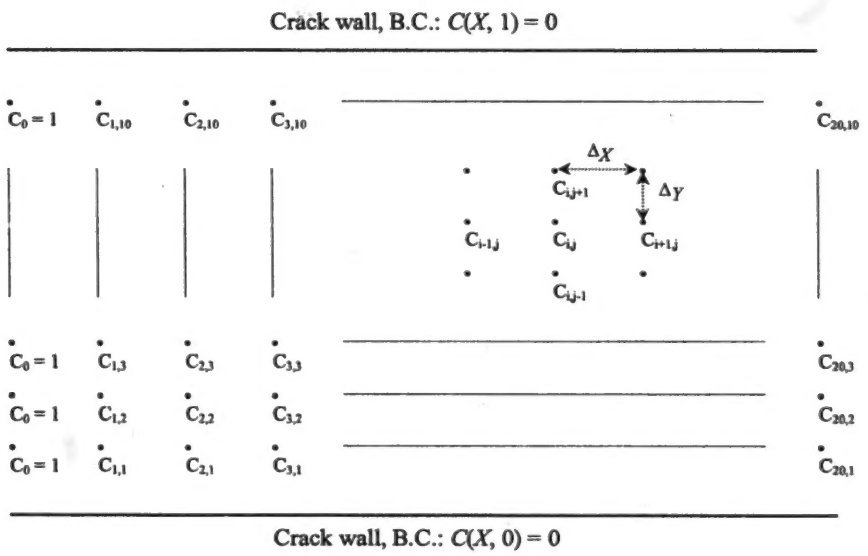

Figure 4-2 Boundary conditions and grid layout for numerical analysis

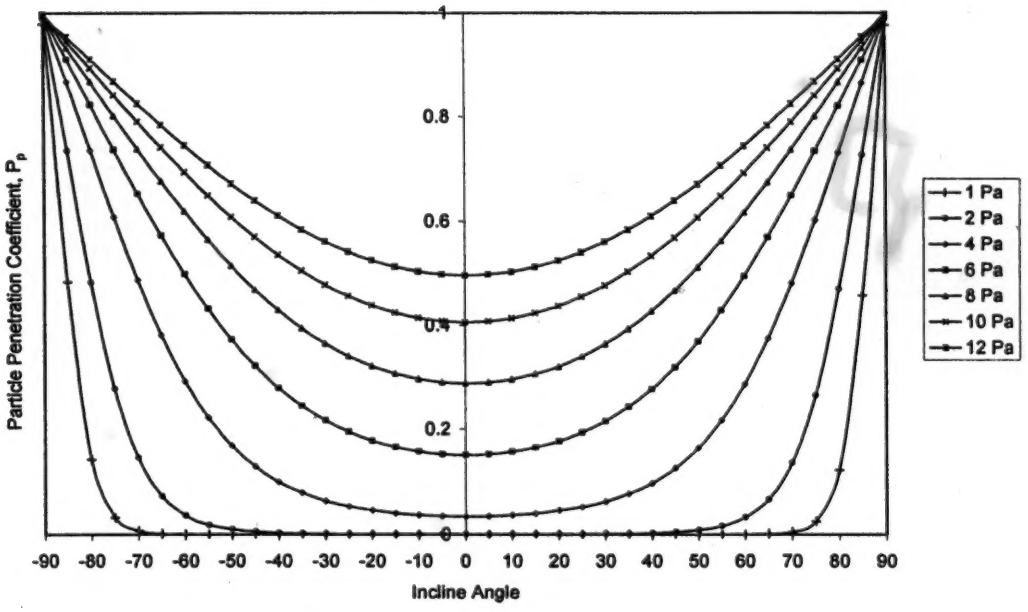

Figure 4-3 Simulated particle penetration coefficient for 2.5 μm particles (modeling conditions: incline angle $|\theta| \leq 90°$, differential pressure from 1 to 12 Pa, crack length L = 60 mm, and crack height H = 0.305 mm)

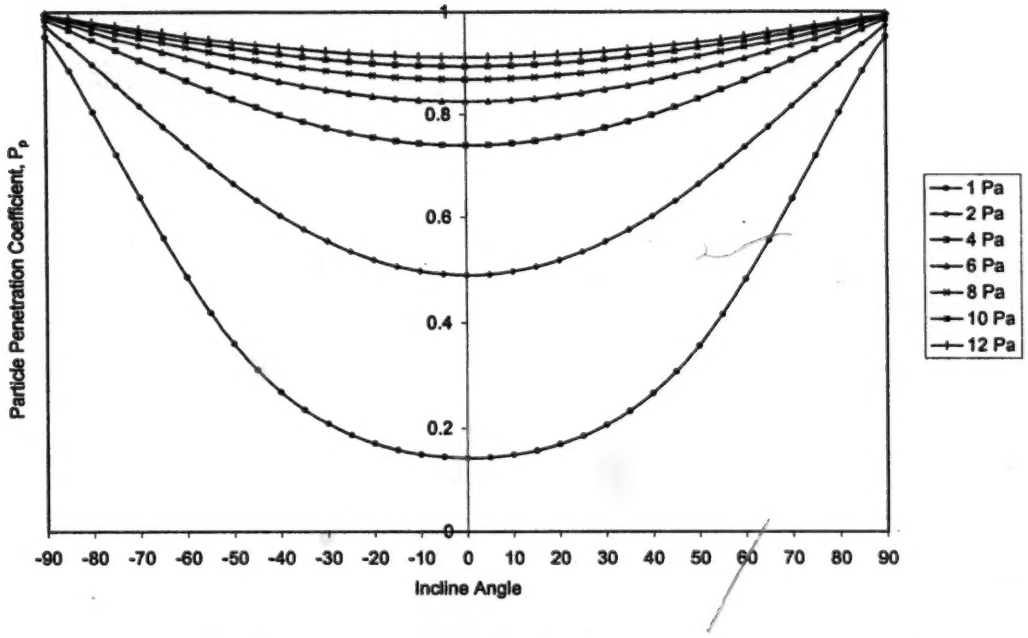

Figure 4-4 Simulated particle penetration coefficient for 1.0 μm particles (modeling conditions: incline angle $|\theta| \leq 90°$, differential pressure from 1 to 12 Pa, crack length $L = 60$ mm, and crack height $H = 0.305$ mm)

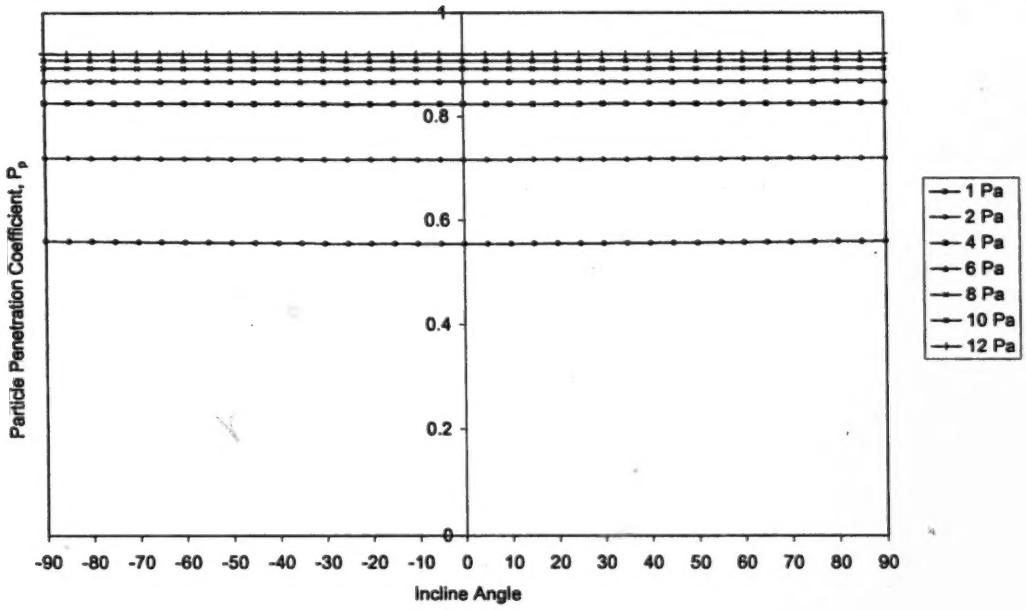

Figure 4-5 Simulated particle penetration coefficient for 0.1 μm particles (modeling conditions: incline angle $|\theta| \leq 90°$, differential pressure from 1 to 12 Pa, crack length L = 60 mm, and crack height H = 0.305 mm)

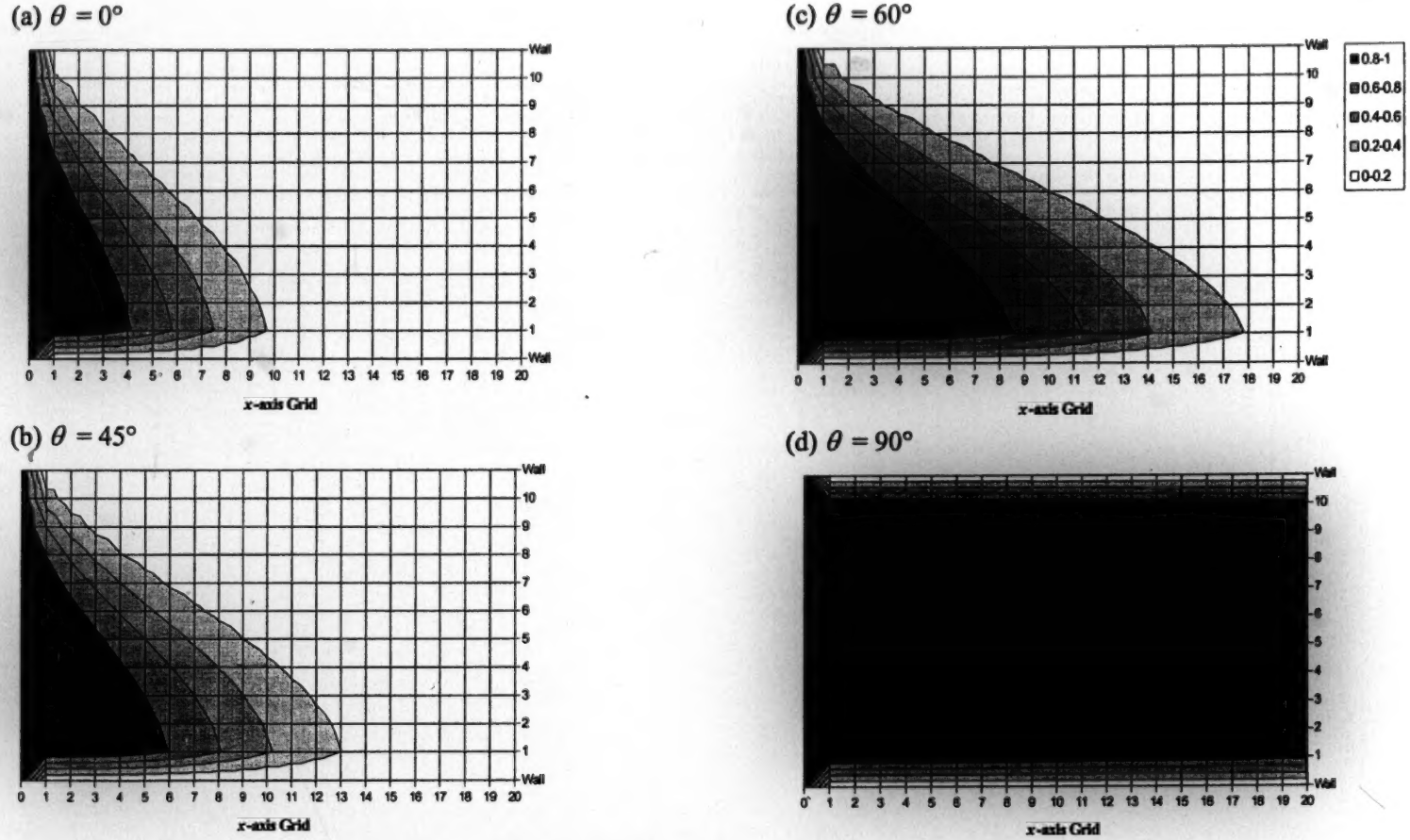

Figure 4-6 Concentration contours for 2.5 μm particles (modeling conditions: differential pressure $\Delta P = 2$ Pa, crack length $L = 60$ mm, and crack height $H = 0.305$ mm)

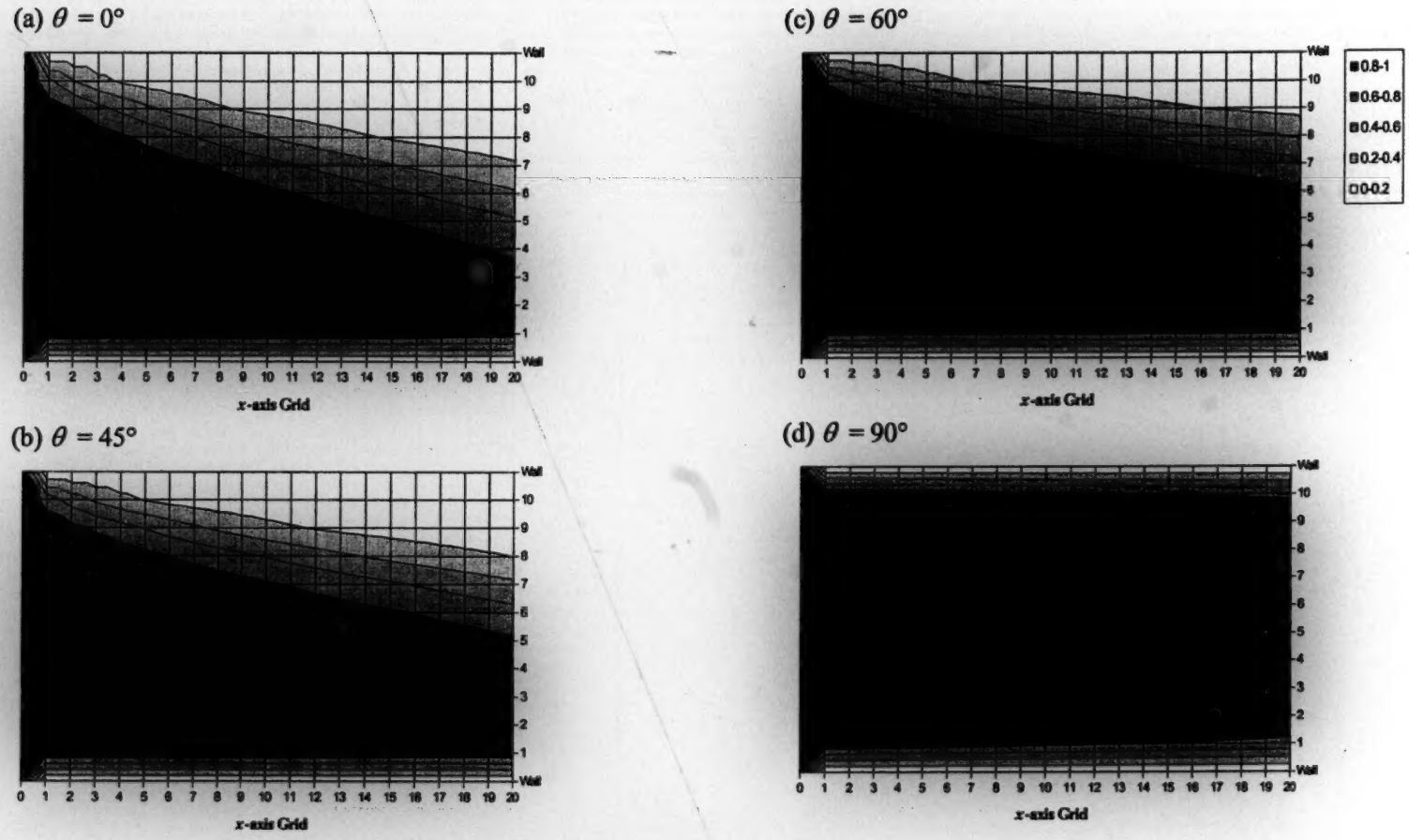

Figure 4-7 Concentration contours for 1.0 μm particles (modeling conditions: differential pressure $\Delta P = 2$ Pa, crack length $L = 60$ mm, and crack height $H = 0.305$ mm)

(a) $\theta = 0°$

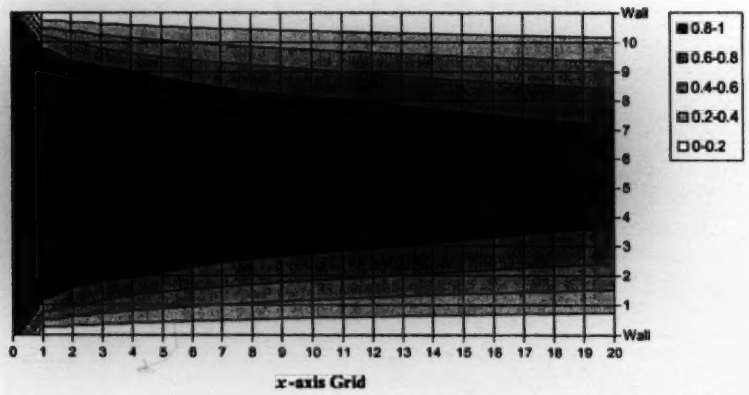

(b) $\theta = 90°$

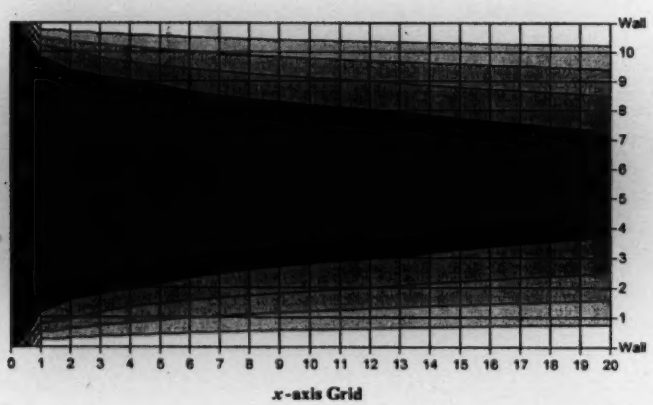

Figure 4-8 Concentration contours for 0.1 μm particles (modeling conditions: differential pressure $\Delta P = 2$ Pa, crack length $L = 60$ mm, and crack height $H = 0.305$ mm)

4.5 REFERENCES

Gross, D., and Haberman, W. L. (1989). *Fire Safety Science: Proceedings of the Second International Symposium.* The Second International Symposium on Fire Safety Science, International Association for Fire Safety Science, Tokyo, Japan.

Liu, D. L., and Nazaroff, W. W. (1999). Modeling Particles Penetration Through Cracks in Building Envelopes, *Proceedings: 8th Int. Conference on Indoor Air Quality and Climate.* Edinburgh, Scotland, 4:1055-1059.

Mosley, R. E., Greenwell, D. J., Sparks, L. E., Guo, Z., Tucker, W. G., Fortmann, R., and Whitfield, C. (2001). Penetration of Ambient Fine Particles into Indoor Environment. *Aerosol Sci. Technol.* 34:127-136.

Tan, C. W., and Hsu, C. J. (1972). Mass Transfer of Aerosols with Axial Diffusion in Narrow Rectangular Channels. *Appl. Sci. Res.* 25:295-312.

Taulbee, D. B., and Yu, C. P. (1975). Simultaneously Diffusion and Sedimentation of Aerosols in Channel Flows. *J. Aerosol Sci.* 6:433-441.

Walker, I. S., and Wilson, D. J., (1990). *The Alberta Air Infiltration Model.* Report 71. Department of Mechanical Engineering, University of Alberta, Edmonton, Alberta, Canada.

CHAPTER 5. GENERATION OF MONODISPERSE AEROSOLS

5.1 INTRODUCTION

Condensation-type aerosol generators have been widely used in aerosol research as sources of monodisperse aerosols. The generators produce aerosols through homogeneous condensation and heterogeneous condensation. The former means that aerosols are produced by self-nucleation of aerosol vapor, while the latter by condensation of aerosol vapor onto condensation nuclei. The competition between these two condensation phenomena is determined by the availability of condensation nuclei and mass concentration of aerosol vapor. Homogeneous condensation dominates over heterogeneous condensation when there is a very high vapor mass concentration and very low nucleus concentration. Research on Sinclair-LaMer type generators suggests that concentration of condensation nuclei must be higher than approximately 10^5 to 10^6 No./cm^{-3} so that heterogeneous condensation can suppress homogeneous condensation (Ristovski *et al.*, 1998). It was also found that heterogeneous condensation produces monodisperse aerosols, while homogeneous condensation produces polydisperse aerosols (Ristovski *et al.*, 1998; Peters and Altmann, 1993; Horton *et al.*, 1991). In order to produce monodisperse aerosols, most condensation-type aerosol generators are designed to operate under heterogeneous condensation conditions. For which cases, the ratio of vapor mass concentration to nucleus concentration (V/N ratio) determines how much aerosol vapor a condensation nucleus can share. As a result, the V/N ratio is a key parameter controlling both size distribution and monodispersity of output aerosols (Liu *et al.*, 1966).

According to the generation mechanisms of condensation nuclei and aerosol vapor, condensation-type generators can be categorized into two types. One of them uses

two independent sources to produce condensation nuclei and aerosol vapor. The Sinclair-LaMer type generator is a typical example of this generator (Sinclair and LaMer, 1949). This type of generator can control nucleus concentration and aerosol vapor mass concentration independently. It is more flexible in operation and has a wider operational range. The other type of generator uses a joint vapor/nuclei source, usually an atomizer or a nebulizer, to produce polydisperse aerosol droplets as the source of both condensation nuclei and aerosol vapor. Because there is a trace amount of nonvolatile impurity in aerosol material, when a droplet evaporates, the residue of impurity serves as a condensation nucleus. This generator was proposed by Rapaport and Weinstock (1955) and was named after them. Because both condensation nuclei and aerosol vapor come from the same source, the joint vapor/nuclei type aerosol generator cannot control nucleus concentration and aerosol vapor independently. This aerosol generator is less flexible in performance than the Sinclair-LaMer type generator. A prototype Rapaport-Weinstock generator only produces aerosols up to 1.2 μm.

The objective of this study was to assemble a joint vapor/nuclei type generator for the particle penetration study. A two-level, four-factor (2^4) factorial design approach was adapted to investigate the controlling parameters of this generator and its performance. This study also did a preliminary investigation to examine how concentration of primary droplets affects homogeneous/heterogeneous condensation, and the relationship between size distribution of primary droplets and number mean diameter (*NMD*) of output aerosols. Because this generator can be assembled in a laboratory, it provides an economic alternative to generate monodisperse aerosols.

5.2 EXPERIMENTAL MATERIALS

5.2.1 Joint Vapor/Nuclei Type Generator

Figure 5-1 illustrates a schematic diagram of the joint vapor/nuclei type generator assembled for this study. Similar to the prototype (Rapaport and Weinstock, 1955), the aerosol generator is composed of an atomizer, an evaporator, and a condensation chimney. The atomizer is used to produce polydisperse droplets, called primary droplets, as the joint source of aerosol vapor and condensation nuclei. When primary droplets are carried into the evaporator, they are fully evaporated to produce aerosol vapor. The remaining residue particles serve as condensation nuclei. The combined vapor/nuclei flow then enters the condensation chimney, where temperature is cooled down to ambient forming a supersaturated environment to encourage heterogeneous condensation.

5.2.1.1 Atomizer

The atomizer used in this study was obtained from an atomizer assembly of a Perkin-Elmer Atomic Absorption Spectrometer. The atomizer was operated at 2.9 kPa using a nitrogen gas cylinder. A rotameter (P-03217-28, Cole-Parmer Instrument Co., Vernon Hills, IL) was used to measure atomizer flow rate. When nitrogen flow accelerates through an orifice section, it induces a backpressure on the rotameter. To account for the pressure induced change in nitrogen density, a pressure gauge (Minigauge, Ashcroft, Stratford, CT) was installed nearby the outlet of the rotameter. The measured atomizer flow rates were then calibrated to standard conditions and are presented in standard litre per minute (L/min).

5.2.1.2 Evaporator

The atomizer was connected to an evaporator to evaporate primary droplets. The evaporator was made of a Pyrex tube 25 mm in inner diameter and 300 mm in

length. It was heated by heating tape (Heavy Insulated Samox, Barnstead/Thermolyne, Dubuque, IA), keeping the temperature at 200° and 280°C when using di(2-ethylhexyl) sebacate (DEHS) (Sigma-Aldrich Canada, Oakville, ON) and canola oil as the aerosol materials, respectively. Temperature of the evaporator was controlled by a variable autotransformer (Variable-Voltage Controller, Cole-Parmer Instrument Company, Vernon Hills, IL) and was monitored by a thermal probe (Digi-Sense Type K Thermometer, Cole-Parmer Instrument Co., Vernon Hills, IL).

The evaporator was connected to a U-shaped tube to direct the vapor/nuclei flow downward. The downward-flow pattern balances the convective flow and thermal buoyancy flow forces, forming a flat condensation front. This measure improves monodispersity of output aerosols (Roth *et al.*, 1992; Swift, 1967; Liu *et al.*, 1966; Muir, 1965). To prevent premature condensation in the U-shaped tube, heating tape was wrapped around it and kept at the same temperature as that of the evaporator (Horton *et al.*, 1991).

5.2.1.3 Condensation Chimney

Downstream to the U-shaped tube is a condensation chimney. Two Pyrex condensation chimneys of different inner diameters were made for this generator. One of them was replicated from the prototype Rapaport-Weinstock generator. It is 25 mm in I.D. and 1200 mm in length. When using this condensation chimney, the generator was designed to have similar performance as the prototype generator. It was expected to produce aerosols up to 1.2 μm. In order to produce bigger aerosols, a bigger condensation chimney (75 mm I.D.) was made. The bigger condensation chimney has a lower surface-to-volume ratio, which reduces vapor wall loss so as to generate bigger aerosols (Japuntich *et al.*, 1992). A 20 mm I.D. sampling tube was designed for the 75 mm

condensation chimney to collect aerosols from the central part of the condensation chimney in order to sample aerosols with better monodispersity in the central region (Roth *et al.*, 1992).

Another modification to the prototype aerosol generator was to use heating tape to control the temperature of DEHS. Temperature affects the viscosity and surface tension of DEHS and was expected to alter size distribution of primary droplets, which may be a factor controlling the *NMD* of output aerosols.

5.2.2 TSI Aerosol Diluter and Aerodynamic Diameter Sizer (APS)

This study used the TSI Aerodynamic Particle Sizer (APS 3320, TSI Inc., St. Paul, MN) to measure size distribution of output aerosols. The APS is a single particle counter. It measures the time-of-flight of a particle to estimate its aerodynamic diameter. TSI Inc. uses a series of standard microspheres to obtain the calibration curve between time-of-flight and aerodynamic diameter. This instrument can size particles from 0.5 to 20 μm. For particles from 0.3 to 0.5 μm, the APS can detect them, however, without size resolution. The APS is designed to measure particle concentrations on the order of 10^3 No./cm^{-3} or less. In this study, because the test generator produces fog-like aerosols with concentrations on the order of 10^5 No./cm^{-3} (Ristovski *et al.*, 1998), an aerosol dilutor (Model 3302A, TSI Inc., St. Paul, MN) with 1:100 dilution ratio was used to dilute output aerosols upstream to the APS. Detailed information of the APS is discussed in Chapter 6.

5.3 EXPERIMENTAL METHOD

5.3.1 Factorial Design Experiment

This study used a factorial design experiment to do a preliminary investigation on the aerosol generator. A factorial design approach is characterized by its excellent

investigation efficiency and the ability to detect the interactions between (or among) the investigated factors. Although it cannot explore a problem in detail, it provides a map to the investigated problem and guides an experimenter for detailed exploration. A two-level, four-factor (2^4) factorial design experiment was used to investigate the performance of the laboratory-assembled aerosol generator. There were four factors investigated in this study, and two levels were assigned to each factor. As a result, there were 2^4 treatments to be investigated. The four factors chosen in this experiment were: (A) atomizer flow rate, (B) use of a flow straightener, (C) inner diameter of a condensation chimney, and (D) temperature of aerosol material (DEHS). Table 5-1 summarizes the high and low levels used for these factors.

Atomizer flow rate was chosen in this study because it was expected to have an effect on the size of output aerosols. A joint vapor/nuclei type generator assumes that one primary droplet produces one condensation nucleus. As a result, the bigger the size distribution of primary droplets, the higher the ratio of aerosol vapor mass concentration to nucleus concentration (V/N) ratio will be. A higher V/N ratio means that each condensation nucleus can share more aerosol vapor and thus was expected to produce bigger output aerosols (Altmann and Peters, 1992; Japuntich *et al.*, 1992; Liu *et al.*, 1966). To select the appropriate high and low settings, the DEHS suction rate (mL/min) was measured to determine the atomizer's operational range. Experimental results indicated that the maximum DEHS suction rate occurred at 3.17 L/min. When atomizer flow rate was lower than 2.69 L/min, the suction pressure could not effectively draw up DEHS. As a result, these two flow rates were chosen as the high and low settings.

The second investigated factor was presence/absence of a flow straightener at the entrance of the condensation chimney. The flow straightener was used to condition the flow field such that all output aerosols have similar growth history. This factor was expected to have an effect on aerosol monodispersity (Japuntich *et al.*, 1992). This study used a stainless steel wire mesh as the flow straightener. The diameter of steel wires was approximately 100 μm and there were four wires per millimeter.

Inner diameter of the condensation chimney was chosen in this study because it affects the available vapor mass concentration in condensation chimneys. For a constant boundary layer thickness of wall condensation, the surface-to-volume ratio of a condensation chimney determines the amount of vapor wall loss and was expected to have an effect on aerosol size (Japuntich *et al.*, 1992; Roth *et al.*, 1992). This study used a 25 mm condensation chimney as the low setting and a 75 mm condensation chimney as the high setting. The 75 mm condensation chimney has a lower surface-to-volume ratio and was expected to produce bigger output aerosols.

The last factor in the factorial design experiment was temperature of aerosol material (DEHS). Selection of this factor was based on the Sinclair-LaMer type generators. For these generators, aerosol material is heated in a bath to produce aerosol vapor. Temperature of the bath determines the saturation vapor pressure and the amount of vapor available for aerosol generation (Perry and Smaldone, 1985). As for the joint vapor/nuclei type generator, this factor was expected to play a different role. The viscosity and surface tension of DEHS is a function of temperature. When temperature of DEHS is changed, size distributions of primary droplets and output aerosols would change in response. As a result, size distribution of output aerosols can be adjusted by

DEHS temperature. This study chose the high and low settings to be 22°C (room temperature) and 120°C.

5.3.2 Tests for Generator Stability, Repeatability, and Response

Because the particle penetration study uses a particle dynamic analyzer to measure particle concentration at the crack entrance and exit alternatively to estimate particle penetration coefficient. The particle concentration in the test outdoor-indoor chamber must be stable so that the alternatively measured concentrations can be compared. The stability and repeatability of the aerosol generator are key factors determining success of this project. Repeatability of the generator can be assessed from repetitive experiments. As for the generator's stability, several 1-hour experiments were conducted to examine the sequential changes in *NMD*, geometric standard deviation (*GSD*), and particle concentration. In this investigation, the generator was set at a homogeneous condensation condition in advance. The atomizer flow rate was then adjusted to 2.69 L/min to produce monodisperse aerosols. Simultaneously, the APS was turned on to measure *NMD*, *GSD*, and concentration of product aerosols. The APS was set to an automatic operation mode to collect sequential particle size distributions. Each test lasted for one hour after generator output was stabilized. This study defined a system stabilization time to determine the generator's response to atomizer flow rate. System stabilization time was defined as the time required to obtain a stable monodisperse population when atomizer flow rate is changed from a homogeneous condensation condition to an intended generation condition.

5.3.3 Homogeneous/Heterogeneous Condensation

For a joint vapor/nuclei type generator, both condensation nuclei and aerosol vapor are produced from the atomizer. This study initially examined how size distribution

of primary droplets affects homogenous condensation and heterogeneous condensation. Figure 5-2 illustrates the structure of the atomizer used in this generator. It is made up of an atomizer needle, a needle adjustment mechanism and a nozzle orifice. When nitrogen gas flows through the orifice throat, the stream is accelerated causing a negative pressure on the atomizer needle. The negative pressure draws up aerosol material forming a jet. The liquid jet is broken up by the high-speed nitrogen flow to produce primary droplets. There are two parameters to control size distribution of primary droplets: (1) the relative location between the needle tip and the orifice throat, and (2) atomizer flow rate. The relative location of the needle tip to the orifice throat can be adjusted using the adjustment nut and a positioning spring, as shown in Figure 5-2. Because flow speed is the highest in the orifice throat, when the tip of the atomizer needle is located in the throat region, the suction pressure will be the highest. In this position, the maximum atomization rate produces maximum mass of primary droplets. By measuring suction rates (mL/min) of di(2-ethylhexyl) sebacate (DEHS), this study fixed the atomizer needle at the maximum atomization efficiency and used atomizer flow rate to control size distribution of primary droplets. To examine the relationship between size distributions of primary droplets and product aerosols, their size distributions were measured with respect to a series of atomizer flow rates to characterize the atomizer's roles on homogeneous condensation and heterogeneous condensation.

5.4 RESULTS AND DISCUSSION

5.4.1 Factorial Design Experiment

This study used the table of signs to calculate the main effects and interactions for the factorial design experiment after Box *et al.* (1978). Because high and low settings were chosen to be +1 and –1, the calculated main effects and interactions represent the

change in *NMD* and *GSD* per two units of change (i.e. +1 to -1) in the investigated factors. Table 5-2 summarizes the results of the analysis. They are plotted on two half-normal plots to discriminate the significant main effects and interactions that affected the generator's performance. On half-normal plots, the main effects or interactions that lie on a straight line are induced from random variation and have no real effect on the generator's performance. Only outliers to the straight line have significant effects on the generator's performance (Box *et al.*, 1978).

Figure 5-3(a) illustrates the half-normal plot for *NMD* of output aerosols. The figure indicates that only factors A and D have significant main effects on the *NMD* of output aerosols, and there is no significant interaction between or among the investigated factors. Table 5-3 summaries that the main effect induced from atomizer flow rate and DEHS temperature. It indicates the main effect induced from atomizer flow rate is –0.64 μm when atomizer flow rate was increased from 2.69 to 3.17 L/min. If the main effect was linearly dependent on atomizer flow rate, *NMD* would decrease approximately 0.6 μm for every increase of 1.0 L/min in atomizer flow rate. As for DEHS temperature, *NMD* of output aerosols increases 0.47 μm when DEHS temperature increases from 22°C to 120°C, which is equivalent to approximately 0.05 μm per 10°C increase if the main effect is linear.

Figure 5-3(b) illustrates the half-normal plot for *GSD* of output aerosols. It indicates that factor C, diameter of condensation chimney, is the only significant factor affecting the monodispersity of output aerosols. Contrary to our expectation, Factor B, use of a flow straightener, did not show a significant effect on aerosol monodispersity. This is contradictory to what was proposed by Japuntich *et al.* (1992), who stated that

using a flow straightener could improve aerosol monodispersity. An explanation may be due to the flow field inside the condensation chimneys, which can be characterized by the hydraulic entrance length of tube flow. The hydraulic entrance length of tube flow is defined as the distance for uniformly distributed flow to develop into stable laminar flow. If the vapor/nuclei flow cannot develop into stable flow shortly after entering the condensation chimney, condensation behavior at different parts of the chimney will be different, and particle sizes will vary widely. In such a case, using a flow straightener can dampen flow to produce uniform flow inside the condensation chimney so as to improve monodispersity. According to the entrance length model proposed by Sparrow *et al.* (1964), the entrance length to form stable flow is approximately 150 mm for the 25 mm condensation chimney. Because the evaporator, the U-shaped tube, and the 25 mm condensation chimney are of the same diameter and the former two tubes have a total length of approximately 600 mm, the flow should have stabilized before entering the condensation chimney. Using a flow straightener would not have a significant effect on aerosol monodispersity. On the other hand, when using the 75 mm condensation chimney, the sudden expansion from the U-shaped tube to the condensation chimney (25 to 75 mm) would require a distance to stabilize the flow field. As a result, use of a flow straightener should have an effect on aerosol monodispersity for this arrangement. However, factorial experimental results indicated that the flow straightener did not improve aerosol monodispersity. This may be a result of eddies observed downstream in the 75 mm condensation chimney. Eddies would increase the probability of particle collisions and degrade aerosol monodispersity.

5.4.2 Aerosol Size Adjustment

Since the factorial design experiment indicated that atomizer flow rate was the most important factor that controls the *NMD* of output aerosols, further investigation was undertaken to assess the suitability of using it as an adjustment parameter. According to the main effect estimated from the factorial design experiment, if the relationship between atomizer flow rate and the *NMD* of output aerosols is linear, the change in *NMD* will be -0.6 μm per unit increase in atomizer flow rate. Such a relationship is useful when using atomizer flow rate as an adjustment factor to control aerosol size. To examine whether the above hypothesis is valid, additional atomizer flow rates were tested to derive prediction models. Table 5-4 presents particle statistics of output aerosols for this investigation. The aerosols were generated using the 25 mm condensation chimney and the 22°C and 120°C DEHS. For the test conditions, the output aerosols ranged from 1.42 to 2.77 μm in *NMD*. The geometric standard deviations (*GSD*) of output aerosols were less than 1.2.

Figure 5-4 illustrates the relationship between atomizer flow rate and *NMD* of output aerosols. It indicates that *NMD* decreases monotonously with atomizer flow rate. The trends are not linear, but better described by power-law models, as summarized in Table 5-5. For both generation conditions, R-squares for the derived models were above 0.95, suggesting that the power-law models can estimate the *NMD* of output aerosols.

Further experiments outside the above flow ranges were undertaken to examine if the power-law models could be extrapolated to a wider range. Experimental observations indicated that when atomizer flow rate was higher than 4.42 L/min, the *GSD* of output aerosols was greater than 1.5. On the other hand, when atomizer flow rate was less than 2.45 L/min, homogeneous condensation dominates over heterogeneous

condensation, resulting in polydisperse aerosol populations. These findings suggest that atomizer flow rates between 2.45 to 4.42 L/min are the operational range of the generator, for which flow rates the *NMD* of output aerosols are between 3.1 and 1.42 μm.

5.4.3 Generator Stability

The previous section suggests that the laboratory-assembled aerosol generator has good reproducibility. Another important feature for this generator is its stability. These two features (reproducibility and stability) determine if the generator can be used in the particle penetration study. Figure 5-5 illustrates the sequential *NMD*, *GSD*, and particle concentration for the generator using the 25 mm condensation chimney. The particle statistics of output aerosols are summarized in Table 5-6. Because some of these tests appeared to have visible trends of increase in *NMD*, linear regression was used to estimate the temporal change in *NMD*. Slopes of the trend lines were tested using one-tailed hypothesis tests to conclude if *NMD* increased with time. The null hypothesis used was the slope of trend line equals zero, i.e. aerosol size is independent of operation time. The alternative hypothesis was the slope of trend line is greater than zero, i.e. *NMD* of output aerosols increases with time of operation.

Figure 5-5(a) illustrates the time profiles of 1 hour operation using the 22°C DEHS and the 25 mm condensation chimney. It indicates that the generator stabilization time was less than 2 minutes and the *GSD* of output aerosols was quite stable throughout the 1-hour operation period. However, *NMD* had a visible trend of increasing with time of operation, from 2.21 to 2.31 μm. The average incremental rate was 4.5% per hour. To examine if the incremental trend was statistically significant, trend line analysis and hypothesis tests were investigated. Table 5-7 summaries the trend line equations for the

NMD of output aerosols. For a level of significance (α) = 5 percent, the hypothesis test rejected the null hypothesis. It suggests that the slope of the trend line was significantly greater than zero, i.e. *NMD* of output aerosols increase with time of operation. However, this incremental rate was very minor, only approximately 0.1 μm per hour. Because a particle penetration experiment can be finished within an hour, this variation in aerosol size was considered acceptable.

Figure 5-5(b) illustrates the time profiles of a continuous 1 hour operation using 120°C DEHS and the 25 mm condensation chimney. Similar to Figure 5-5(a), the system stabilization time was less than 2 minutes. The figure indicates that output aerosols had a very stable GSD, and *NMD* slightly fluctuated around 2.70 μm during the test period. Table 5-7 summaries the trend line equations for the *NMD* of output aerosols. For a level of significance (α) = 5 percent, the hypothesis testing accepted the null hypothesis. It suggests that the *NMD* of output aerosols did not increase with time of operation. It is speculated that the fluctuations in *NMD* were induced from random errors.

5.4.4 Canola Oil as An Alternative Aerosol Material

Canola oil was tested to see if the generator could extend the *NMD* of product aerosols. Table 5-8 summarizes the *NMD*, *GSD*, and particle concentration data of output aerosols for the canola oil tests. It indicates that the output aerosols of canola oil cover a lower size range than DEHS. The *NMD* of output aerosols ranges from 0.79 to 1.57 μm. Aerosols larger than 1.0 μm are monodisperse, with *GSD* less than 1.15. On the other hand, for aerosols ranged from 0.79 to 1.0 μm, they were less monodisperse. *GSD* ranged from 1.16 to 1.31. Figure 5-6 illustrates the relationship between *NMD* of output aerosols and atomizer flow rates. Similar to the DEHS tests, a power-law model, as presented in

Table 5-5, can be used to estimate *NMD* of output aerosols. The R-square of the model was 0.959.

A stability test was conducted on the canola oil test to examine the stability of using it to produce monodisperse aerosols. Figure 5-7 illustrates the time profiles of *NMD*, *GSD*, and particle concentration of output aerosols. It indicates that the generator stabilization time was less than two minutes and output aerosols have an incremental trend in *NMD*. In this one-hour operation, *NMD* increases from 1.19 to 1.23 μm. The average incremental rate was 3.4% per hour. Hypothesis testing, as shown in Table 5-7, rejected the null hypothesis, suggesting that the slope of the trend line was significantly greater than zero. However, the incremental rate was very low, only 0.04 μm/hr.

5.4.5 Roles of Atomizer on Generator Performance

5.4.5.1 Homogeneous/Heterogeneous Condensation

Table 5-9 summarizes the concentrations of primary droplets and output aerosols for a series of atomizer flow rates. The aerosols were generated using the 25 mm condensation chimney and 120°C DEHS. It indicates that concentrations of primary droplets for atomizer flow rates of 2.28, 2.45, and 2.69 L/min were 1.9×10^4, 4.0×10^4, and 9.3×10^4 No./cm^{-3}, and the corresponding total concentrations of output aerosols were 2.1×10^5, 7.3×10^4, and 9.7×10^4 No./cm^{-3}, respectively. The paired concentrations indicate that a concentration of approximately 10^5 No./cm^{-3} is a criterion that determines the significance of homogeneous condensation and heterogeneous condensation. When atomizer flow rates were 2.28 and 2.45 L/min, the concentrations of primary droplets were less than 10^5 No./cm^{-3} and output aerosols formed bimodal distributions. The total aerosol concentration is much higher than that of primary droplets. Since one primary

droplet produces one heterogeneously condensed aerosol, the increased aerosol particles may be generated from homogeneous condensation. This suggests that homogeneous condensation plays an important role when concentration of primary droplets (i.e. condensation nuclei) is less than 10^5 No./cm^{-3}.

5.4.5.2 Effect of Size Distribution of Primary Droplets

Figure 5-8(a) illustrates the size distributions of primary droplets using 120°C DEHS as the aerosol material. This figure and Table 5-9 both indicate that when atomizer flow rate increases, the corresponding concentration of primary droplets also increases. The figure indicates that the concentrations of smaller primary droplets increases much more significantly when atomizer flow rate increases. The simultaneous increases in droplet concentration and decreases in droplet size distribution suggest that the V/N ratio is inversely proportional to atomizer flow rate. A decreased V/N ratio suggests that a higher atomizer flow rate will produce smaller output aerosols.

Figure 5-8(b) illustrates the size distributions of output aerosols for a series of atomizer flow rates. The aerosols were produced using the 25 mm condensation chimney and 120°C DEHS. This figure indicates that when atomizer flow rate is 2.28 L/min, output aerosols form a bimodal distribution. The modes of the two aerosol populations are 1.0 and 3.3 μm, respectively. Their geometric standard deviations (*GSD*s) indicate that the major aerosol population, with mode nearby 1.0 μm, is a polydisperse population; while the right-hand-side aerosol population although minor, is monodisperse. Its *GSD* is 1.15. When atomizer flow rate increases to 2.45 L/min, the bimodal distribution still exists. However, the polydisperse aerosol population is not very significant. The dominant aerosol population is monodisperse with *NMD* equal to 3.1 μm.

When atomizer flow rate further increases to 2.69 L/min or higher, only one monodisperse population forms.

The above examination suggests that size distribution of primary droplets can be used to predict the trend of *NMD*. Generally, the bigger the size distribution of primary droplets, the bigger the *NMD* of the monodisperse population. However, no quantitative model was formulated between the *NMD* of primary droplets and monodisperse output aerosols because a large portion of primary droplets was smaller than the lower sizing limit of the APS (< 0.52 μm). These findings only qualitatively suggest that size distribution of primary droplets can be used as a guide to choose an appropriate atomizer. Further investigation is needed to examine the relationship between the *NMD* of primary droplets and output aerosols. This may be difficult because vapor wall loss in the condensation chimney is hard to quantify.

5.5 CONCLUSION

This study used a factorial design experiment to investigate a laboratory assembled aerosol generator. Using the results, detail investigation on the stability and adjustment of the generator were examined. This study found:

1. The generator used in these experiments produces monodisperse aerosols from 0.79 (using canola oil) to 3.1 μm (using DEHS) in *NMD*. This size range is ideal for outdoor-to-indoor penetration studies.
2. The generator has good stability and reproducibility. These two features are very important for the particle penetration studies.
3. Factorial design experiments indicate that atomizer flow rate and DEHS temperature have significant effects on the *NMD* of output aerosols. Both factors suggest that size

distribution of primary droplets may be the key parameter that controls the *NMD* of output aerosols. Choosing an atomizer that produces an appropriate size distribution of primary droplets is a key to optimize the performance of a joint vapor nuclei type generator.

4. The generator has a rapid, reproducible response to atomizer flow rate. It can be used as an adjustment factor to control *NMD* of output aerosols. Several power-law models were derived for the generator.
5. The concentration of primary droplets determines the significance of homogeneous condensation and heterogeneous condensation. Experimental results suggest that the concentration of primary droplets must exceed 10^5 No./cm^{-3} so that heterogeneous condensation dominates over homogeneous condensation. However, further investigation is required to measure size distribution of primary droplets that are smaller than the lower sizing limit of the APS (0.52 μm).
6. Size distribution of primary droplets determines the V/N ratio in the condensation chimney, which in turn determines the *NMD* of output aerosols. However, the exact relationship between the *NMD* of primary droplets and output aerosols is hard to define because vapor wall loss cannot be quantified.

Table 5-1 High and low levels of the four factors selected in the 2^4 factorial design experiment

Factor	Parameter	Unit	High Level (+1)	Low Level (-1)
A	Atomizer flow rate	L/min	2.69	3.17
B	Flow straightener (Stainless steel mesh)	layer	1	0
C	Diameter of condensation chimney	mm	75	25
D	Temperature of DEHS	℃	120	22

Table 5-2 Main effects and interactions derived from the factorial design experiment

Factor	Main Effect/Interaction	
	NMD	*GSD*
A	-0.64	0.01
B	0.05	-0.03
C	-0.08	0.05
D	0.47	-0.02
AB	-0.04	0.02
AC	0	-0.01
AD	-0.05	-0.01
BC	-0.07	-0.04
BD	0.04	-0.03
CD	0.05	0.03
ABC	0.05	0.02
ABD	-0.01	0.02
ACD	0.02	-0.03
BCD	-0.01	-0.02
ABCD	-0.03	-0.02

Table 5-3 Significant factors that control number mean diameter (*NMD*) and geometric standard deviation (*GSD*) of product aerosols

Significant Factors	**Main Effect**
***NMD* (Number Mean Diameter)**	
(A) Atomizer flow rate	-0.6 μm per increase of 1.0 L/min
(D) Temperature of DEHS	+0.05 μm per increase of 10°C
***GSD* (Geometric Standard Deviation)**	
(C) Diameter of condensation chimney	+0.05 from low to high settings

Table 5-4 Particle statistics of output aerosols for combinations of DEHS temperature, condensation chimney, and atomizer flow rate

Temperature of DEHS	Particle Statistics[a]	Atomizer Flow Rate (L/min)			
		2.69	3.17	3.73	4.42
22°C	*NMD* (μm)[b]	2.22 (0.03)	1.87 (0.02)	1.56 (0.02)	1.42 (0.02)
	GSD	1.15	1.14	1.16	1.18
	Concentration[c]	1.4×10^5	3.2×10^5	4.6×10^5	4.6×10^5
120°C	*NMD* (μm)	2.77 (0.04)	2.37 (0.02)	1.97 (0.01)	1.72 (0.01)
	GSD	1.09	1.10	1.13	1.14
	Concentration	1.0×10^5	2.5×10^5	3.7×10^5	4.4×10^5

a. *NMD* = number mean diameter; *GSD* = Geometric standard deviation. All particle statistics are calculated from four experimental runs. Each run collects five consecutive 10-second samples after the generator is stabilized.

b. Mean (Standard Deviation).

c. Particle concentration (No./cm^{-3}).

Table 5-5 Power-law models for number mean diameter (*NMD*) of product aerosols and atomizer flow rate (*Q*)

Aerosol Material	Power-Law Formula[a, b]	R-square
DEHS @22°C	$NMD = 5.437\ Q^{-0.920}$	0.978
DEHS @120°C	$NMD = 7.321\ Q^{-0.981}$	0.996
Canola oil @22°C	$NMD = 9.194\ Q^{-2.027}$	0.959

a. *Q* is atomizer flow rate (L/min).

b. Each power law formula is calculated based on four flow rates, as shown in Table 5-4. Four replication runs are done on each flow rate.

Table 5-6 System stabilization time and particle statistics for stability tests

Aerosol Material	System Stabilization Time[a] (minute)	Particle Statistics[b]		
		NMD[c] (μm)	*GSD*	Concentration (No./cm^{-3})
DEHS @22°C	< 2	2.26 (0.04)	1.12	1.9×10^5
DEHS @120°C	< 2	2.70 (0.03)	1.09	1.3×10^5
Canola oil @22°C	< 2	1.20 (0.01)	1.12	3.4×10^5

a. System stabilization time means the length of time to obtain stable output aerosols after the atomizer flow rate is adjusted to 2.69 L/min.

b. *NMD* = number mean diameter; *GSD* = Geometric standard deviation. All particle statistics are calculated from four experimental runs. Each run consecutively collects five 10-second samples after system is stabilized.

c. Mean (Standard Deviation).

Table 5-7 Regression analysis and hypothesis test for stability tests

Aerosol Material	Trendlines of *NMD*[a] (t = operation time [hour])	Hypothesis Test on Slope of Trendline		
		t-value	P-value	Conclusion[c] ($\alpha = 5\%$)
DEHS @22°C	$NMD = (0.0899 \pm 0.0065)\,t + (2.2142 \pm 0.0058)$[b]	13.8	~0	Reject H_o
DEHS @120°C	$NMD = (0.0212 \pm 0.0107)\,t + (2.7050 \pm 0.0083)$	1.97	0.055	Accept H_o
Canola oil @22°C	$NMD = (0.0152 \pm 0.0047)\,t + (1.1961 \pm 0.0027)$	3.22	0.003	Reject H_o

a. *NMD* = number mean diameter. Trendline and statistical values are calculated from stabilized data, i.e. data after stabilization time (20 minutes) is used.

b. Mean ± Standard Deviation.

c. H_o (null hypothesis): Slope of trendline equals to zero.

Table 5-8 Particle statistics of output aerosols, using canola oil and 25 mm condensation chimney

Particle Statistics [a,b]	Atomizer Flow Rate (L/min)				
	2.45	2.69	2.98	3.17	3.46
NMD[c] (μm)	1.57 (0.03)	1.21 (0.03)	0.94 (0.02)	0.86 (0.02)	0.79 (0.01)
GSD	1.13	1.12	1.16	1.21	1.31
Concentration[d]	1.4×10^5	4.0×10^5	4.7×10^5	4.7×10^5	4.6×10^5

a. Particles generated using 25 mm condensation chimney.

b. *NMD* = number mean diameter; *GSD* = Geometric standard deviation. All particle statistics are calculated from four experimental runs. Each run collected five consecutive 10-second samples after system is stabilized.

c. Mean (Standard Deviation).

d. Particle concentration (No./cm^{-3}).

Table 5-9 Concentration of primary droplets and output aerosols for a series of atomizer flow rates (aerosols produced using the 25 mm condensation chimney)

Atomizer Flow Rate (L/min)	Concentration of Primary Droplet[a] ($No./cm^{-3}$)	Concentration of Output Aerosol[a] ($No./cm^{-3}$)		
		Polydisperse Population	Monodisperse Population	Total Concentration
2.28	1.9×10^{4}	1.9×10^{5}	1.8×10^{4}	2.1×10^{5}
2.45	4.0×10^{4}	3.5×10^{4}	3.7×10^{4}	7.3×10^{4}
2.69	9.3×10^{4}	-	9.7×10^{4}	9.7×10^{4}
3.17	2.5×10^{5}	-	2.5×10^{5}	2.5×10^{5}
3.73	3.9×10^{5}	-	3.7×10^{5}	3.7×10^{5}
4.42	4.9×10^{5}	-	4.4×10^{5}	4.4×10^{5}

a. Mean of five replication runs.

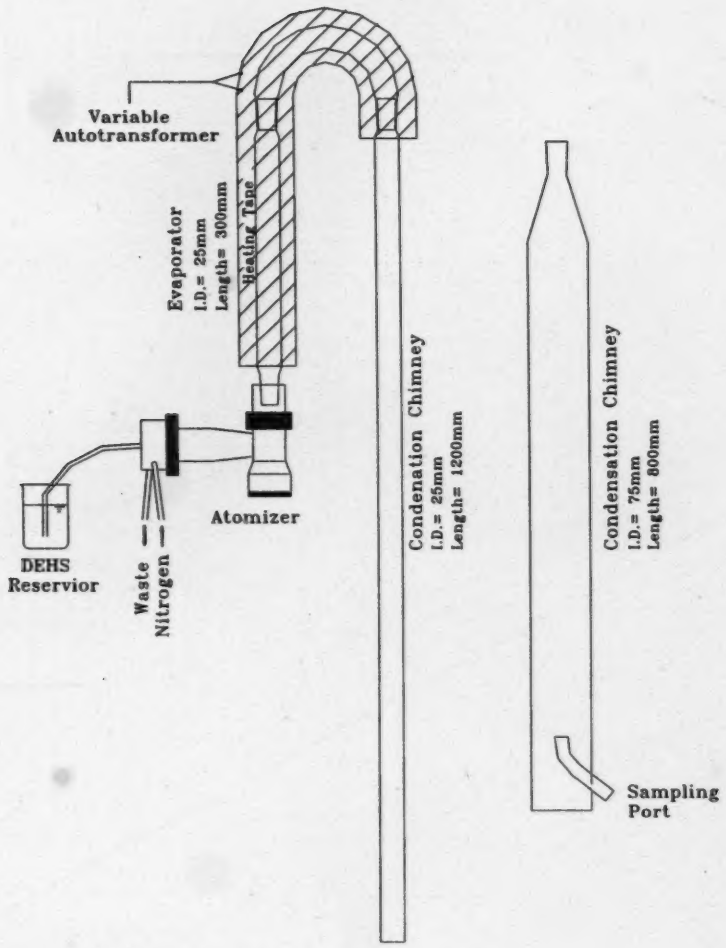

Figure 5-1 Schematic diagram of the modified Rapaport-Weinstock generator

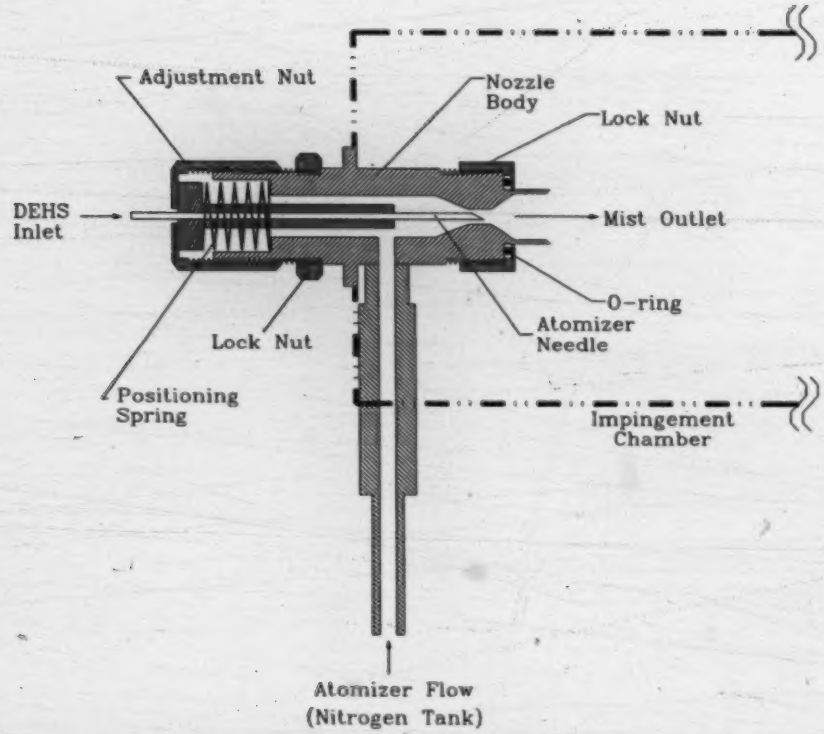

Figure 5-2 Schematic diagram of the atomizer nozzle

(a) Half-normal plot of *NMD*

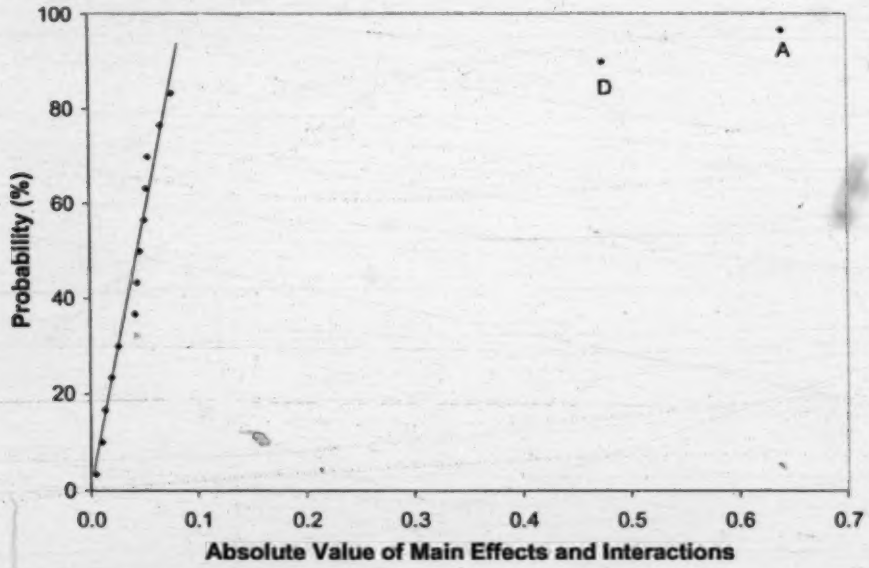

(b) Half-normal plot of *GSD*

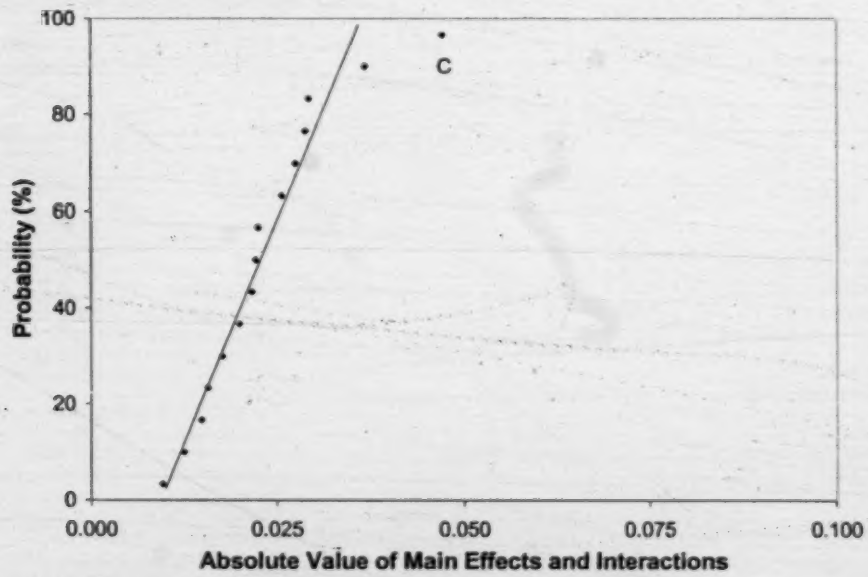

Figure 5-3 Half-normal plots of the factorial design experiment

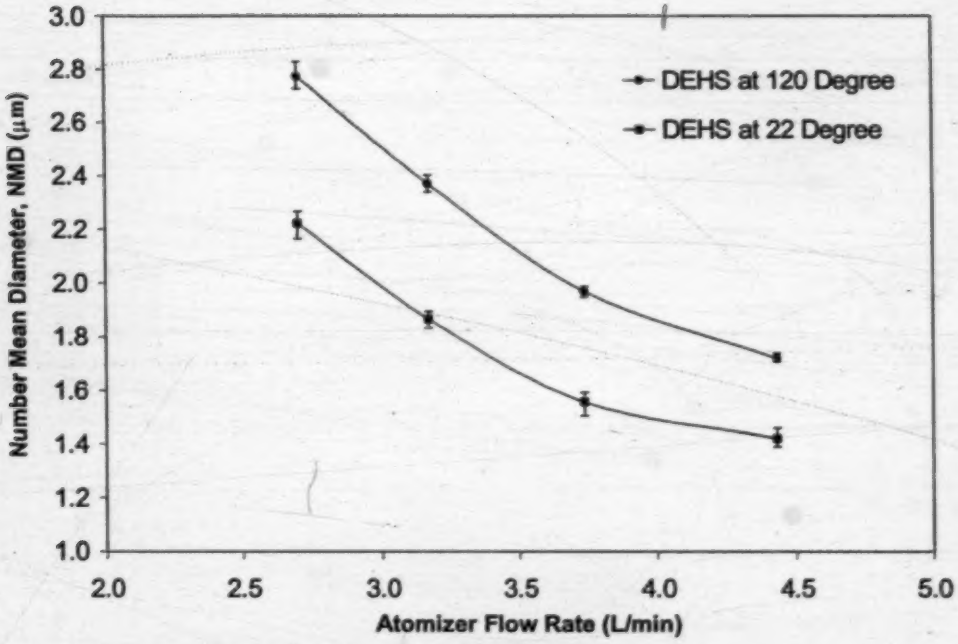

Figure 5-4 Dependence of number mean diameter (*NMD*) on atomizer flow rate for DEHS

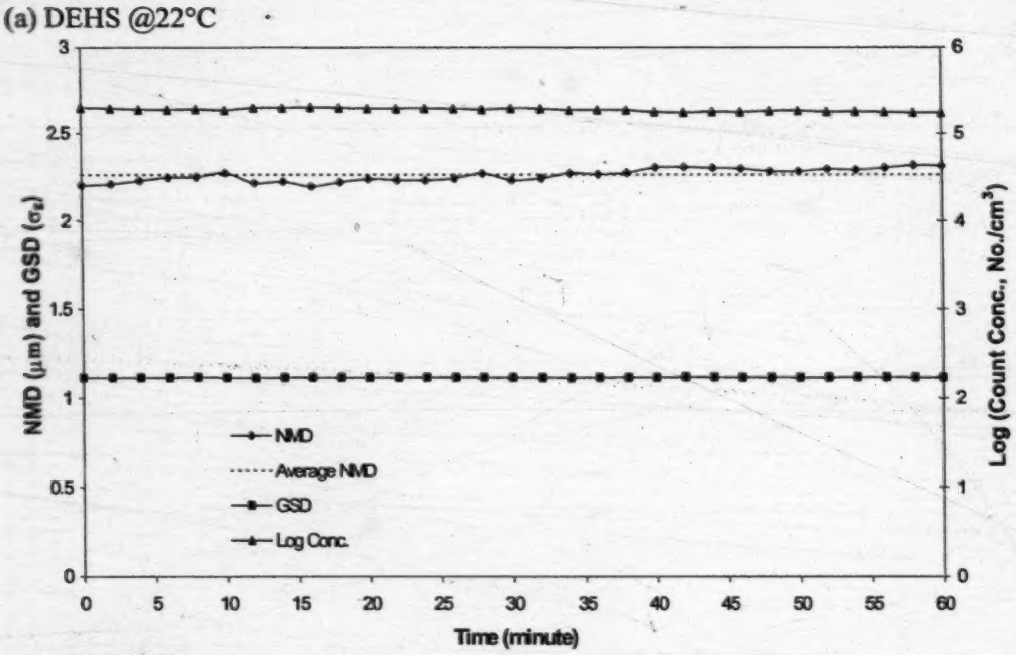

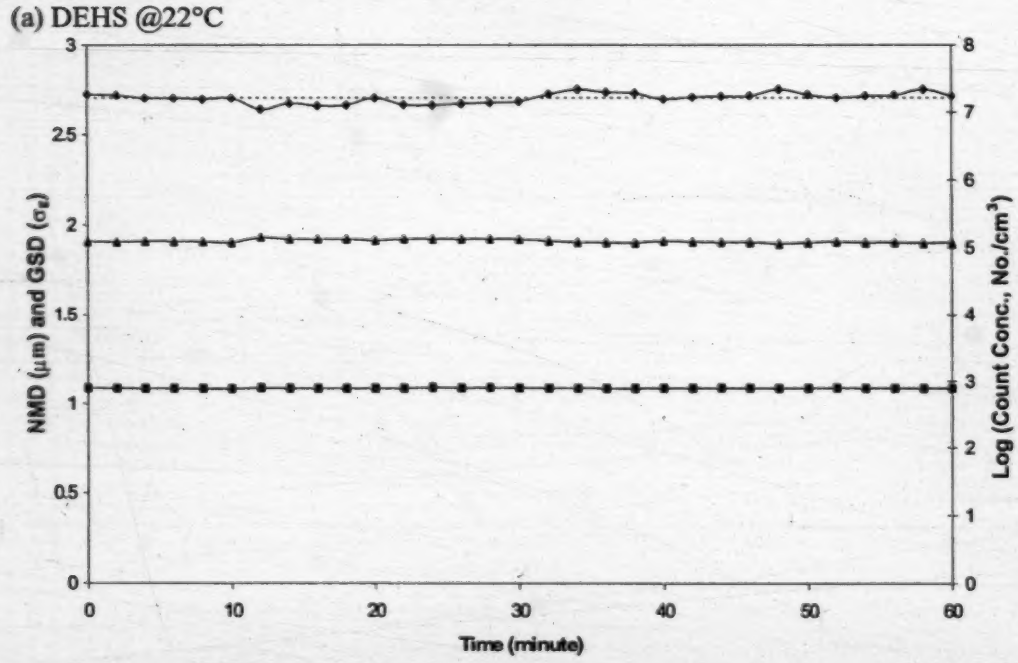

Figure 5-5 Sequential number mean diameter (*NMD*), geometric standard deviation (*GSD*), and particle concentration for the stability tests using 25 mm condensation chimney and DEHS

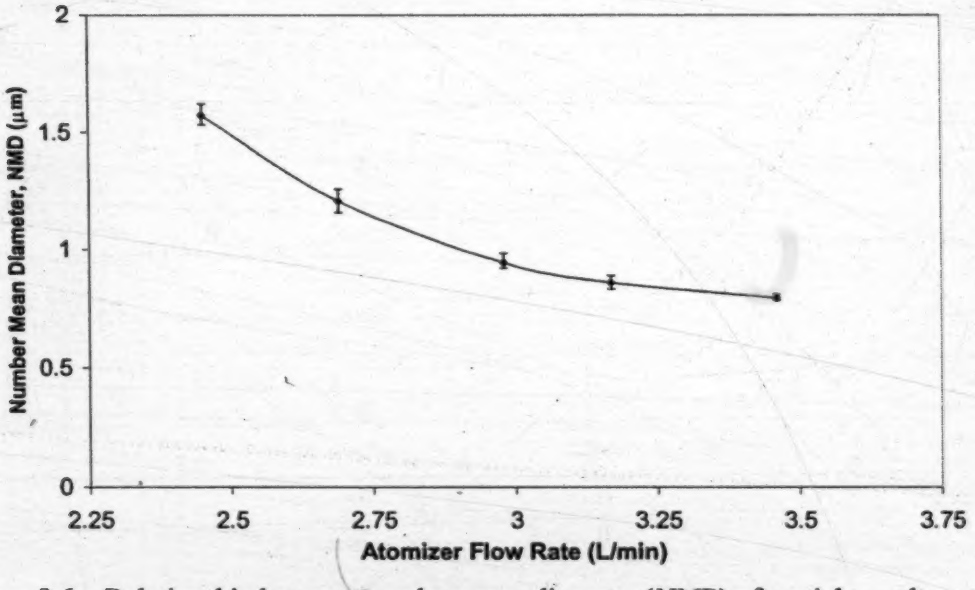

Figure 5-6 Relationship between number mean diameter (*NMD*) of particles and atomizer flow rate for canola oil

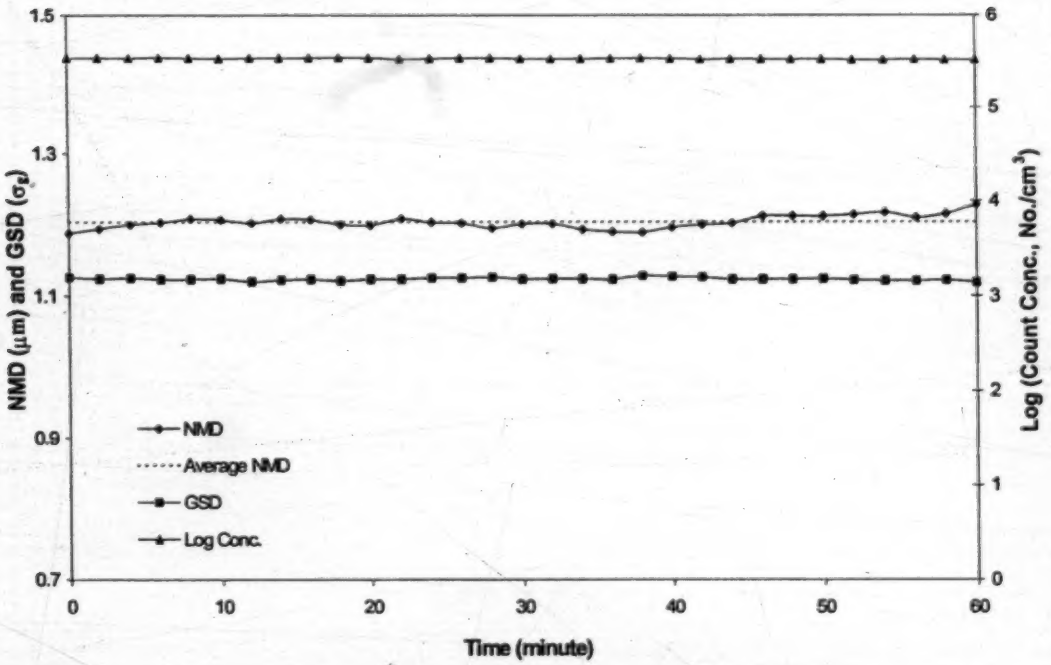

Figure 5-7 Sequential number mean diameter (*NMD*), geometric standard deviation (*GSD*), and particle concentration for the stability tests using 25 mm condensation chimney and canola oil

(a) Size distribution of primary droplets.

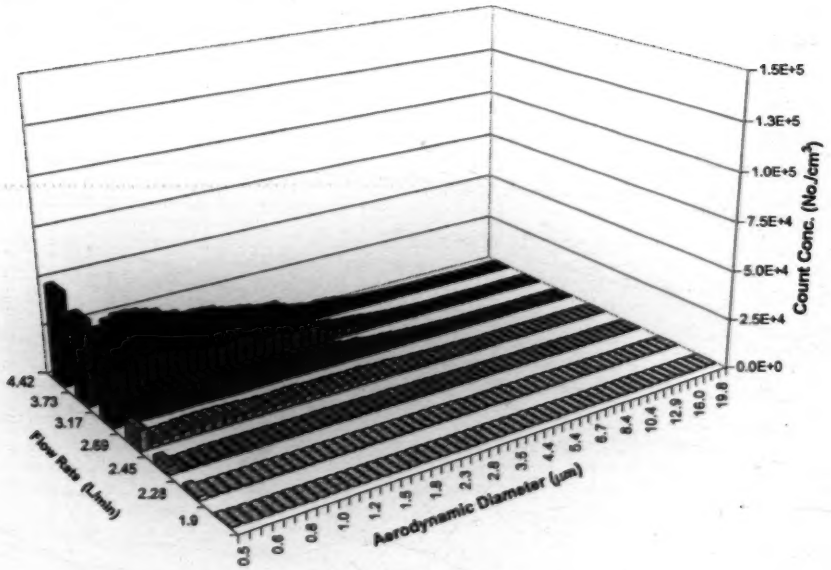

(b) Size distribution of output aerosols, using the 25 mm condensation chimney.

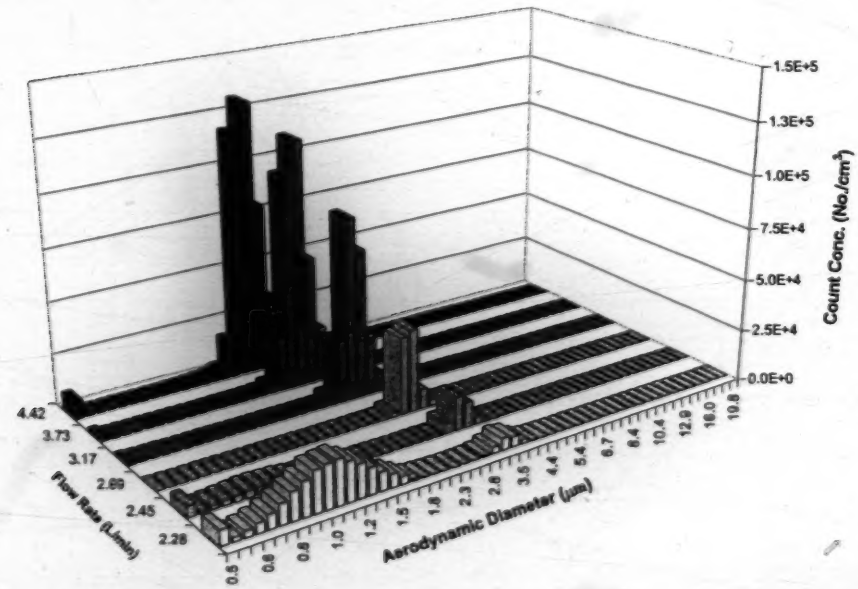

Figure 5-8 Size distribution of primary droplets and product aerosols using DEHS as aerosol material

5.6 REFERENCES

Altmann, J. and Peters, C. (1992). The Adjustment of the Particle Size at a Sinclair-La Mer-Type Aerosol Generator. *J. Aerosol Sci.* **23**(Suppl. 1), S277-S280.

Box, G. E. P., Hunter, W. G. and Hunter, J. S. (1978). *Statistics for Experimenters: An Introduction to Design, Data Analysis, and Model Building*. New York, N. Y., John Wiley & Sons.

Davies, E. J. (1983). Transport Phenomena with Single Aerosol Particles. *Aerosol Sci. Technol.* **2,** 121-144.

Davies, E. J. and Liao, S. C. (1975). The Growth Kinetics and Polydispersity of Condensational Aerosols. *J. Colloid Interface Sci.* **50**(3), 488-502.

Horton, K. D., Miller, R. D. and Mitchell, J. P. (1991). Characterization of a Condensation-Type Monodisperse Aerosol Generator (MAGE). *J. Aerosol Sci.* **22**(3), 347-363.

Japuntich, D. A., Stenhouse, J. I. T. and Liu, B. Y. H. (1992). An Aerosol Generator for High Concentrations of 0.5-5 Microns Solid Particles of Practical Monodispersity. *Aerosol Sci. Technol.* **16,** 246-254.

Japuntich, D. A., Stenhouse, J. I. T. and Liu, B. Y. H. (1992). A Monodisperse Aerosol Generator for High Concentrations of 0.5-5 Microns Solid Particles. *J. Aerosol Sci.* **23** (Suppl. 1), S177-S180.

Liu, B. Y. H., Whitby, K. T. and Yu, H. H. S. (1966). A Condensation Aerosol Generator for Producing Monodispersed Aerosols in the Size Range, 0.036 μm to 1.3 μm. *Journal de Recherché Atmospheriques.* **2,** 397-406.

Mercer, T. (1973). Production and Characterization of Aerosols. *Arch. Int. Med.* **131,** 39-50.

Muir, D. C. F. (1965). The Production of Monodisperse Aerosols by a LaMer-Sinclair Generator. *Ann. Occup. Hyg.* **8,** 233-238.

Perry, D. G. and Smaldone, G. C. (1985). Factors Affecting Aerosol Production from a Modified Sinclair-La Mer Aerosol Generator. *J. Aerosol Sci.* **16**(5), 427-436.

Pesthy, A. J., Flagan, R. C. and Seinfeld, J. H. (1981). The Effect of a Growing Aerosol on the Rate of Homogeneous Nucleation of a Vapor. *J. Colloid Interface Sci.* **82**(2), 465-479.

Pesthy, A. J., Flagan, R. C. and Seinfeld, J. H. (1983). Theory of Aerosol Formation and Growth in Laminar Flow. *J. Colloid Interface Sci.* **91**(2), 525-546.

Peters, C. and Altmann, J. (1993). Monodisperse Aerosol Generation with Rapid Adjustable Particle Size for Inhalation Studies. *J. Aerosol Medicine* **6**(4), 307-315.

Rapaport, E. and Weinstock, S. G. (1955). A Generator for Homogeneous Aerosols. *Experimentia* **11**, 363-367.

Ristovski, Z. D., Morawska, L. and Bofinger, N. D. (1998). Investigation of a Modified Sinclair-LaMer Aerosol Generator in the Submicrometer Range. *J. Aerosol Sci.* **29**(7), 799-809.

Roth, C., Gebhart, J. and Reisert, W. (1992). The Production of High-Concentrated Monodisperse Aerosols with Variable Size Distribution. *J. Aerosol Sci.* **23**(Suppl. 1), S185-S188.

Sher, E. and Sokolov, M. (1980). Size Distribution of Droplets Created by Vapour Condensation Through a Cooled Pipe. *Chem. Engr. Sci.* **35**, 1399-1403.

Sinclair, D. and LaMer, V. (1949). Light Scattering as a Measure of Particular Size in Aerosols. *Chem. Rev.* **44**, 245-267.

Sparrow, E. M., Lin, S. H. and Lundgren, T. S. (1964). Flow Development in the Hydrodynamic Entrance Region of Tubes and Ducts. *The Physics of Fluids* **7**(3), 338-347.

Swift, D. L. (1967). A Study of the Size and Monodispersity of Aerosols Produced in a Sinclair-LaMer Generator. *Ann. Occup. Hyg.* **10**, 337-348.

Willeke, K. and Baron, P. A. (1993). *Aerosol Measurement: Principle, Techniques, and Applications.* Van Nostrand Reinhold, New York, N.Y.

Fuchs, N. A. and Sutugin, A. G. (1966). Chapter I. Generation and Use of Monodisperse Aerosols. *Aerosol Science*. Davies C. N., Academic Press, London and New York.

Horton, K. D., Miller, R. D. and Mitchell, J. P. (1991). Characterization of a Condensation-Type Monodisperse Aerosol Generator (MAGE). *J. Aerosol Sci.* **22**(3), 347-363.

Liu, B. Y. H., Whitby, K. T. and Yu, H. H. S. (1966). A Condensation Aerosol Generator for Producing Monodispersed Aerosols in the Size Range, 0.036 μm to 1.3 μm. *J. Rech. Atmos.* **2,** 397-406.

Mercer, T. (1973). Production and Characterization of Aerosols. *Arch. Int. Med.* **131**: 39-50.

Muir, D. C. F. (1965). The Production of Monodisperse Aerosols by a LaMer-Sinclair Generator. *Ann. Occup. Hyg.* **8,** 233-238.

Perry, D. G. and Smaldone, G. C. (1985). Factors Affecting Aerosol Production from a Modified Sinclair-LaMer Aerosol Generator. *J. Aerosol Sci.* **16**(5), 427-436.

Peters, C. and Altmann, J. (1993). Monodisperse Aerosol Generation with Rapid Adjustable Particle Size for Inhalation Studies. *J. Aerosol Medicine* **6**(4), 307-315.

Rapaport, E. and Weinstock, S. G. (1955). A Generator for Homogeneous Aerosols. *Experimentia* **11,** 363-367.

Ristovski, Z. D., Morawska, L. and Bofinger, N. D. (1998). Investigation of a Modified Sinclair-LaMer Aerosol Generator in the Submicrometer Range. *J. Aerosol Sci.* **29**(7), 799-809.

Roth, C., Gebhart, J. and Reisert, W. (1992). The Production of High-Concentrated Monodisperse Aerosols with Variable Size Distribution. *J. Aerosol Sci.* **23**(Suppl. 1), S185-S188.

Stahlhofen, W., Gebhart, J. and Roth, C. (1976). Generation and Properties of a Condensation Aerosol of di-2-ethylhexyl-sebacate (DES)-III: Experimental Investigation into the Process of Aerosol Formation. *J. Aerosol Sci.* **7,** 223-231.

CHAPTER 6. RATIONAL APPROACH FOR STANDARD PARTICLE GENERATION

6.1 INTRODUCTION

Particle sizing instruments require periodical validation and calibration using primary size standards. An appropriate primary size standard must be monodisperse, with known size, and reliable (Keady and Nelson 1984). In the past, several technologies have been developed to produce monodisperse aerosols of primary standard quality. Each of these methods is applicable to a certain size range. For example, the electrical mobility classifier can produce nano to submicron-sized standards, while the vibration orifice aerosol generator is applicable for micron-sized standards up to 10^2 μm (Liu 1975; Keady and Nelson 1984). This chapter discusses an atomization/evaporation method to produce NIST certified size standards using microsphere suspensions for calibration purpose. This method is comprised of two steps: atomization of microsphere suspension and evaporation of droplets. Limited by the size distribution of droplets generated from most nebulizers, this method is generally useful to generate standard microspheres up to 4 μm (Keady and Nelson 1984).

The atomization/evaporation method was first used by microbiologists to generate bacterial aerosols. It became important in aerosol research when Dow Chemical Co. produced spherical polymer microspheres and classified them to specific size ranges (Davies, 1966). The microspheres have been used to calibrate aerosol instruments, also used in filter penetration study and clean room research. Nowadays, several suppliers provide microspheres of a variety of materials. The available sizes range from 10^{-2} to 10^3 μm. The products are available in aqueous suspensions or dry bulk material. For instrument

calibration, microspheres of a few micrometers are usually supplied in aqueous suspensions. The suspension is further diluted so that most of the nebulized droplets contain one microsphere. The droplets are then evaporated to obtain airborne microspheres for calibration purpose. As for bigger particles (> 4 μm) the atomization/evaporation method is not applicable because most atomizers do not generate droplets large enough to accommodate them. For these larger microspheres, dry products are used for calibration. For example, the TSI Inc. (2001) used a brush to scratch microspheres from a microsphere coating plate to calibrate an aerodynamic particle sizer (APS). However, significant aggregation was observed.

In using the atomization/evaporation method to generate microsphere size standards, one of the challenges is how to reproduce individual airborne microspheres with least multiplets. Multiplets are clusters of microspheres after droplets are evaporated. The atomization/evaporation method uses an atomizer to produce droplets from microsphere suspensions. The probability of finding more than one microsphere in a droplet depends on size distribution of droplets, concentration of suspension, and the relative size of microspheres to droplets. Raabe (1968) used Poisson probability distribution to estimate the required dilution ratio to generate a desired ratio of singlet microsphere. This model provides a preliminary guide to determine the dilution ratio for a stock suspension. In practice, because microsphere suppliers add surfactants in microsphere suspensions to avoid aggregation, the calculated dilution ratio predicted from the Raabe's model may be too low occasionally. As a result, air blow bubbles inside the atomizer. When the bubbles burst, lots of residue particles and multiplets were observed. Further dilution solved the bubbling problem.

A high dilution ratio alleviates multiplet interference; however, more empty droplets are generated, which interfere with calibration as well. Empty droplets means droplets that do not contain any microsphere. Ideally, empty droplets will totally evaporate if the suspension is composed of pure water and microspheres. However, because of the impurity of dilution water and the additives impregnated in stock suspension, residue particles were always found after evaporation (Whitby and Liu 1968). Without careful control, they will overlap with the microsphere population and interfere with instrument calibration. Use ultra-clean dilution water can partly solve the residue particle problem. However, the additives in microsphere suspensions are unavoidable. Because the concentration of additives is very low, residue particles are always in submicron or nanometer scale. With proper dilution, the microsphere population can be separated from residue particle population. In examining calibration results, these two particle populations are quite different. The microsphere population is a narrow monodisperse population, while the later is polydisperse. This provides evidence to distinguish them. There is another possible problem induced from solvent impurity. For those droplets containing singlet microspheres, the impurity will coat a thin layer on microspheres after evaporation. The coating causes positive error on the size of microspheres. Fortunately, because impurity concentration is always very low, the deviation is not detectable for most instruments (Keady and Nelson 1984).

In this study, two NIST certified polystyrene latex (PSL) size standards were used to validate and/or calibrate a TSI Aerodynamic Particle Sizer (APS) and a Dantec Particle Dynamic Analyzer (PDA). The atomization/evaporation procedures successfully produced singlet microspheres for the calibration. The APS detected part of the residue

particles. They were mostly smaller than the sizing limit of the APS. On the other hand, the PDA did not detect residue particles, possibly, because the light scattering characteristics of residue particles were different from transparent PSL microspheres.

6.2 THEORY

6.2.1 Dilution of Microsphere Suspensions

Raabe (1968) assumed that the droplets generated from a nebulizer are log-normally distributed and the probability of a microsphere being found in a droplet is given by the Poisson probability distribution. He derived an empirical formula to estimate the required dilution to generate a certain ratio (R) of singlet microspheres. Raabe (1968) assumed the microspheres were randomly dispersed in suspensions and were much smaller than droplet size. The probability of finding a microsphere in a droplet was given by the Poisson probability distribution:

$$p(z) = \frac{\bar{z}^z \cdot e^{-\bar{z}}}{z!} \tag{6-1}$$

where z is number of microspheres in a droplet, $p(z)$ is probability of finding z microspheres in a droplet, and $\bar{z}$ is average number of microspheres in the droplets.

An empirical formula was derived to estimate the dilution ratio required to generate a desired ratio (R) of singlet using a nebulizer, whose σ_g is less than 2.1 (Raabe, 1968):

$$D_i \cong \frac{f \cdot (VMD)^3 e^{4.5 \ln^2 \sigma_g}}{(1-R) d_p^3} \left[1 - \frac{e^{\ln^2 \sigma_g}}{2} \right] \tag{6-2}$$

where D_i is dilution ratio, f is volume fraction of microspheres in stock suspension, VMD is volume median diameter of droplet population, σ_g is geometric standard deviation of droplet population, R is singlet ratio, and d_p is diameter of microspheres.

6.2.2 Estimate Sizes of Residual Particles

Ideally no residue particles are expected from the microsphere generation procedures. However, because of the impurity in dilution water and additives in stock suspensions, residue particles are unavoidable. If the sizes of residue particles can be estimated, it is possible to adjust the dilution ratio so as to separate the residue particle population from the microsphere population. If the impurity and additives in the microsphere suspensions are non-volatile, based on mass balance theory, sizes of residue particles can be estimated from droplet size and impurity concentration, as shown in the following equation (Raabe 1975):

$$d_p = \left(\frac{\rho_l \cdot C}{\rho_p} \right)^{1/3} \cdot d_l \qquad (6\text{-}3)$$

where d_p and d_l are diameters of residue particle and droplet, ρ_p and ρ_l are density of residue particles and microsphere suspension, and C is impurity concentration.

6.2.3 Aerodynamic Diameter

The TSI Aerodynamic Particle Sizer (APS) measures aerodynamic diameters of particles. Aerodynamic diameter is defined as the diameter of a particle that has the same terminal settling velocity as a unit density sphere. In using the NIST certified PSL microsphere to validate the APS's performance, the physical diameter of microspheres must be corrected to aerodynamic diameter because the density of PSL is not unity. For spherical particles, the equivalent aerodynamic diameter relates to particle density and the Cunningham slip correction factor. The relationship is given by equation 6-4 (Willeke and Baron, 1993):

$$\rho_p C_c^{d_p} d_p^2 = C_c^{d_a} d_a^2 \qquad (6\text{-}4)$$

where ρ_p is particle density, d_p is visual diameter of the particle, d_a is the equivalent aerodynamic diameter, and $C_c^{d_p}$ and $C_c^{d_a}$ are Cunningham slip correction factors for the particle and the particle with equivalent aerodynamic diameter. Because density of PSL microspheres is close to unity, 1.05 g/No./cm^3, the adjustment with respect to the Cunningham slip correction factor can be neglected. The aerodynamic diameter of a particle thus is proportional to the square root of particle density. Table 6-1 lists the theoretical aerodynamic diameters of the 1.020 μm and 2.504 μm PSL microspheres. They are 1.045 μm and 2.566 μm, respectively.

6.3 MATERIALS AND METHOD

6.3.1 The Atomization/Evaporation Method

This study used NIST certified polystyrene latex (PSL) size standards to validate/calibrate the APS and the PDA. The 1.020 ± 0.022 μm and 2.504 ± 0.025 μm PSL microspheres suspensions were used in the calibration/validation tests (Duke Scientific Corporation, Palo Alto, CA.). These two standard microspheres were supplied in aqueous suspensions with microsphere contents of 1% and 0.5% (v/v), respectively. The surfactants and preservatives are less than 0.6%. To avoid the multiplet problem, the stock suspensions were further diluted. An Up-Draft Marc II Neb-U-Mist Model 1732 (Hudson Respiratory Care, Inc., Temecula, CA) was used to generate droplets that contain microsphere(s). The nebulizer was connected to an evaporator to dry water content. The evaporator is the same as the one used in the Rapaport-Weinstock generator (Chapter 5). The temperature was kept at 100°C.

The volume median diameter (*VMD*) and geometric standard deviation (σ_g) of the droplets generated by the T-UpDraft II nebulizer was approximately 5 μm and 2.0,

respectively (Finlay *et al.* 2000). According to this information, equation 6-2 estimated the required dilution ratios to be 1000 and 41 for the 1.020 μm and the 2.504 μm stock suspensions, respectively. However, a pretest found the dilution ratio for the 2.504 μm suspension was not enough such that supply air blew bubbles inside the nebulizer. Burst bubbles generated a significant amount of residual particles that overlapped with the PSL population. To prevent the problem, the PSL stock suspensions were diluted with 5 to 6 drops per 250 mL of ultra-pure water (18.5 mΩ, Elga Maxima, High Wycombe, Bukes, England).

6.3.2 The TSI APS 3320

The TSI Aerodynamic Particle Sizer (APS 3320, TSI Inc., St. Paul, MN) is a single particle counter. It measures the time-of-flight of a particle to estimate its aerodynamic diameter. The measurement theory is based on the relationship between aerodynamic diameter and particle inertia. In an accelerating stream, because of inertia, smaller particles accelerate faster, while bigger particles lag behind flow. Figure 6-1 illustrates a schematic diagram of the APS. It uses an internal vacuum pump to draw air from the inlet at 5.0 L/min. Air is split into a sample flow through the inner nozzle; and a sheath flow through the outer nozzle. The sheath flow is filtered and reunited with the sample flow to confine sample air in the central stream and accelerate it through the accelerating orifice nozzle to approximately 1.5 m/sec. The orifice nozzle was aligned to the measurement volume of two partly overlapped laser beams. When a particle passes through the measurement volume, two scattering signals were detected. The time between the two signals is called time-of-flight, which is used to calculate the aerodynamic diameter from a calibration curve. The TSI Inc. uses a series of standard

microspheres to obtain the calibration curve between time-of-flight and aerodynamic diameter. It can size particles from 0.5 to 20 μm. For particle from 0.3 to 0.5 μm, the APS can detect them, however without size resolution.

This study used a mini-Buck bubble meter (A. P. Buck Inc., Orlando, FL) to validate the sample flow rate and the sheath flow rate, which should be within 1.00 ± 0.05 L/min, and 4.00 ± 0.05 L/min, respectively, as recommended by the manufacturer. If any flowrates are out of range, users can adjust the potentiometer on the PC board to the target range (TSI Inc., 2001). Flow check ensures the flow control system is in working conditions. To ensure the laser optical system and signal processor works properly, the above two PSL size standards were used to validate instrument sizing ability.

Figure 6-2 illustrates the experimental setup of the APS validation test. The T-Updraft II nebulizer was operated at 6.0 L/min. It was connected to the evaporator to dry the droplets. The inlet of the APS was positioned at the evaporator outlet to collect airborne PSL microspheres. Consecutive 21 and 9 samples of 60 seconds were collected to validate the measured particle sizes for the 1.020 and 2.504 μm size standards, respectively.

6.3.3 The Dantec PDA

The Dantec Particle Dynamic Analyzer (PDA) used three photomultiplier detectors to examine the phase shifts of scattered signals to measure particle size. Proper alignment of the optical system and proper setup of the photomultipliers determine accurate particle sizing results and counting efficiency. In this study, the transmitting optics and the receiving optics were aligned according to operation manual. Then, the 1.020 μm PSL size standards were shot through the measurement volume as a standard to fine-tune the system. After fine-tuning the system, the 2.504 μm microsphere suspension was used to validate the setup. Table 6-2 lists the aligned optical parameters for the

transmitting and receiving optics. Detail information of the PDA will be discussed in Chapter 7. Because the PDA can measure particles from μm to several mm for different optical setups, this study aligned the system so that it was in the PDA's lower measurement range. As a result, the shortest focal length, 310 mm, was chosen for the transmitting and receiving optics; the widest beam spacing, 75 mm, was adjusted for the dual laser beams; and the micrometer was set at 2.0 mm. For PSL microspheres, the refractive index is 1.59. A Lorenz-Mie scattering plot in the operational manual of the Dantec PDA indicates that the light intensity of primary scattering is 5 orders of magnitude higher than reflection and secondary refractory for a 50 μm PSL particle at the Brewster angle (ϕ_b = 64.3°). As a result, forward scattering at 65° was selected. The optical setup could measure particles up to 42.2 μm. The phase factors of U_{12} and U_{13}, were 12.32 and 6.16 degree/μm. They were used to validate the sizing result. For a validated particle, the size measured from U_{12} was recorded by the PDA because it has better resolution than the phase factor U_{13}. The manufacturer recommends PDA particle sizing error to be ±0.5 to 1.0% full range.

Because PSL microspheres are perfect spheres, the 1.020 μm PSL microspheres were used as a standard to fine-tune the signal processor for accurate sizing results. Since they are spherical, the phase factors (U_{12} and U_{13}) between pairs of photomultipliers (U_1/U_2, U_1/U_3) should be the same. For a well-aligned system, the data acceptance ratio and spherical ratio should be near 100%. In addition, the PDA should measure correct particle diameters of the size standards. This study chose the maximum phase error to be 5° and spherical validation to be within 2%. Based on these validation parameters, the gains, bandwidth, and high voltage were fine-tuned for accurate sizing results. Table 6-3

lists the setup of the signal processor. These parameters were obtained from the validation experiment using the 1.020 μm PSL microspheres and were used throughout the validation/calibration study and the particle penetration study.

6.4 RESULTS AND DISCUSSION

6.4.1 Validate the Performance of APS

This study used a mini-Buck bubble meter to validate the APS's sample flow and sheath flow to ensure the air sampling system was in working conditions. Five readings were recorded for both flow paths, as shown in Table 6-4. All the measurements were within the ±0.05 L/min range, as recommended by the manufacturer. The flow control system of the APS was justified working properly. The APS was then validated using the 1.020 μm and 2.504 μm PSL microspheres.

Figure 6-3 illustrates a typical size distribution histogram of the 1.020 μm PSL size standard (d_a = 1.045 μm) measured by the APS. Except for the narrow microsphere population, there were residue particles in the < 0.52 μm channel. The PSL peak was very narrow, confirming generation of mostly singlet microspheres. The histogram indicates that the APS measures the PSL microspheres in the correct size channel. However, the distribution skews on the right-hand-side. These larger particles probably are multiplets.

Although this study used ultra-pure water as the dilution water, some residue particles were detected. The stock microsphere suspensions contain approximately 0.6% of additives in the stock suspension to prevent aggregation. According to the dilution model developed by Raabe (1968), the stock suspension must be diluted 1000 times to produce 90% singlet microspheres. This study used ultra-pure water to dilute the stock

suspension. The impurity in dilution water was negligible compared with the 0.6% additives in the stock suspensions. As a result, the additive concentration in the diluted suspension was approximately 0.0006%. According to equation 6-3, a 20 μm empty droplet would produce a 0.36 μm residue particle. Since the *VMD* of droplets was approximately 5 μm, it is expectable that there were more residue particles that were smaller than the lower detection limit of the APS (0.3 μm).

Figure 6-4 illustrates a typical size distribution of the 2.504 μm PSL microspheres (d_a = 2.566 μm) measured by the APS. Both residue particles and PSL microspheres were detected. The left-hand-side population clearly is from residue particles, while the narrowly distributed peak is for the 2.504 μm PSL microspheres. Because d_a = 2.57 μm is near the border between the 2.46 and 2.64 μm size bins, microspheres were registered in both size channels. Although large quantities of submicron-sized particles were detected, the peak for the 2.504 μm PSL microspheres was distinctively separated from each other. According to the histogram, the APS was judged in an acceptable condition.

The existence of residual particles is not extraordinary because the 2.504 μm PSL suspension was diluted only approximately 100 times. The additive concentration in the diluted suspension would be 0.006%. According to equation 6-3, a 10 μm empty droplet will form a 0.4 μm residue particle. As a result, more and bigger residue particles were detected than the 1.020 μm microsphere experiment.

Table 6-1 presents the aerodynamic diameters measured by the APS for the 1.020 μm and 2.504 μm PSL microspheres. This study used hypothesis tests to validate whether the APS correctly measures the aerodynamic diameters. The null hypothesis was

"the aerodynamic diameter measured by the APS is equal to the NIST certified aerodynamic diameter." For the 1.020 μm microspheres, the alternative hypothesis was "the aerodynamic diameter measured by the APS is not equal to the NIST certified aerodynamic diameter." For a level of significance (α) = 5 percent, the null hypothesis was accepted using a two-tailed hypothesis test (Table 6-1). It was concluded that the APS could measure the correct aerodynamic diameter of the 1.020 μm PSL microspheres.

For the 2.504 μm PSL microspheres, because the APS frequently overestimated PSL microsphere sizes, the alternative hypothesis used was "the aerodynamic diameter measured by the APS is larger than the NIST certified aerodynamic diameter." For a level of significance (α) = 5 percent, the null hypothesis was rejected using a one-tailed hypothesis test (Table 6-1). The APS statistically overestimated the aerodynamic diameter of the 2.504 μm PSL microspheres. However, the average positive deviation was very small, only +1.1% of the NIST certified diameter. This deviation was judged as an acceptable tolerance.

6.4.2 Validate/Calibrate Performance of PDA

Figures 6-6 and 6-7 illustrate typical size distribution histograms of PSL microspheres measured by the PDA system. The size bins were the same as those of the APS system. However, it was found that the PDA did not have such fine resolution such that some bins were always empty. The empty bins were not shown in the histogram so as to obtain continuous size distributions. Because the PSL particles are nearly perfect spheres and have a known diameter, this study used them as standards to fine-tune the setup of the PDA system. A well-aligned system should give the correct particle

diameters. In addition, the measurement results should have a high validation ratio and sphericity ratio. Figure 6-5 illustrates the size distribution histogram of the 1.020 μm PSL microspheres measured after fine-tuning the PDA. It indicates that 36.1% of mierospheres were registered in the 1.04 μm bin, and 22.7% and 24.6% of microspheres were registered in the 0.90 and 1.11 μm bins, respectively. Because size accuracy of the PDA system ranged from ±0.2 to ±0.4 μm, the results were judged an acceptable tolerance. For the setup, validation ratio and sphericity ratio were always higher than 99%.

After using the 1.020 μm PSL microspheres to fine-tune the PDA system, the 2.504 μm PSL microspheres were used to validate system setup. Figure 6-6 illustrates the size distribution histogram of the 2.504 μm PSL microspheres. A very narrow size distribution was registered by the PDA. There were 62.8% of microspheres being registered in the 2.46 μm bin, which covered from 2.37 to 2.55 μm size range. The validation ratio and sphericity ratio were always higher than 99%.

Both size distribution histograms did not record much evidence of residue particles. One possible reason the PDA could not see them is because of the optical characteristic of the residue particles. In this study the PDA was set at 65° forward scattering angle, which was commonly used for transparent organic droplets. However, the residue particles possibly are not transparent because they are composed of preservatives and surfactants. For these particles, the major scattering mode may be reflective scattering. As a result, the PDA would not detect them.

6.5 CONCLUSION

This chapter presents the methodology for atomization/evaporation of microsphere suspensions to generate particle size standards to validate and/or calibrate a

TSI APS, an aerodynamic diameter measurement instrument, and a Dantec PDA, a physical diameter measurement instrument. The atomization/evaporation method successfully generated singlet microspheres for calibration purpose. This study found:

1. The PSL suspensions were impregnated with preservatives and surfactants to avoid an aggregation problem. The dilution ratio estimated from the Raabe (1968) model was too low for the 2.504 μm microsphere suspension such that the atomizer blew bubbles inside. The burst bubbles produced residue particles and multiplet microspheres that interfered with instrument calibration. Further dilution with ultra-pure water solved this problem.
2. The APS validation test indicated that it was in good working condition. The APS correctly measured the aerodynamic diameter of the 1.020 and 2.504 μm PSL microspheres.
3. Because the PSL microspheres are perfect spheres, this study used the 1.020 μm PSL microspheres to calibrate the PDA system. After calibration, the PDA's validation ratio and sphericity ratio were > 99%. The PDA also correctly measured sizes of the microsphere size standards. Experimental results indicated that the PDA system was well aligned after the calibration/validation procedures.
4. Experimental results indicated that equation 6-3 could be used to estimate sizes of residue particles. Using the equation to calculate dilution ratio, the residue particle population could be separated from PSL size standards by proper dilution.

Table 6-1 Theoretical and APS measured aerodynamic diameters for the standard polystyrene microspheres.

Parameter	Unit	Standard PSL Microsphere	
		1.020 μm	2.504 μm
NIST certified mean diameter	μm	1.020 ± 0.022	2.504 ± 0.025
Density of microsphere	kg/m^3	1050	1050
Theoretical aerodynamic diameter	μm	1.045	2.566
APS measured aerodynamic diameter	μm	1.04 ± 0.004	2.59 ± 0.022
Sample number	No.	21	9
Percent error	%	-0.1%	+1.1%
t-statistic	-	1.63	3.68
$t_{critical}$	-	2.09	1.86
Hypothesis test conclusion ($\alpha = 5\%$)[a]	-	Accept H_o	Reject H_o

a. H_o: The aerodynamic diameter measured by the APS equals the NIST certified diameter.

Table 6-2 Setup of the Dantec Particle Dynamic Analyzer (PDA) optical system

PDA Components	Unit	Set-up Condition
Transmitting Optics		
Front lens focal length	mm	310
Laser beam spacing	mm	75
Fringe spacing	μm	2.14
Number of fringes	number	52
Frequency shift sign	-	Positive
Polarization	degree	0
Polarization orientation	-	Parallel to fringes
Laser wavelength	nm	514.5
Laser power	mW	300
Gaussian beam diameter	mm	0.82
Beam collimation	-	1.2
Beam expansion	-	1.85
Receiving Optics		
Front lens focal length	mm	310
Polarization	degree	0
Polarization orientation	-	Parallel
Scattering angle	degree	65 (Forward scattering)
Micrometer setting	mm	2.0
DEHS refractive index	-	1.59
Phase factor (U_{12})	deg/μm	12.32
Phase factor (U_{13})	deg/μm	6.16
Max diameter	μm	42.2

Table 6-3 Setup of the signal processor of the Dantec Particle Dynamic Analyzer (PDA)

Electronic Settings	Unit	Set-up Condition
Bandwidth		
Ux/Gain	MHz	0.4/High Gain
Burst detector bandwidth	MHz	0.1
Transit time resolution	μs	61.1
Arrival time resolution	μs	1
Optical frequency shift	MHz	40
Validation		
Validation level	dB	-3
Max phase error	degree	5
Max spherical deviation	%	2
High voltage		
U1	Volts	800
U2	Volts	744
U3	Volts	760

Table 6-4 Aerosol flow and sheath flow of the Aerodynamic Particle Sizer (APS) measured using a mini-BUCK bubble meter

Run Number	Aerosol Flow (L/min)	Sheath Flow (L/min)
1	1.030	4.032
2	1.025	4.035
3	1.032	4.044
4	1.039	4.018
5	1.028	4.019
Average	1.031	4.030
Standard Deviation	0.005	0.011

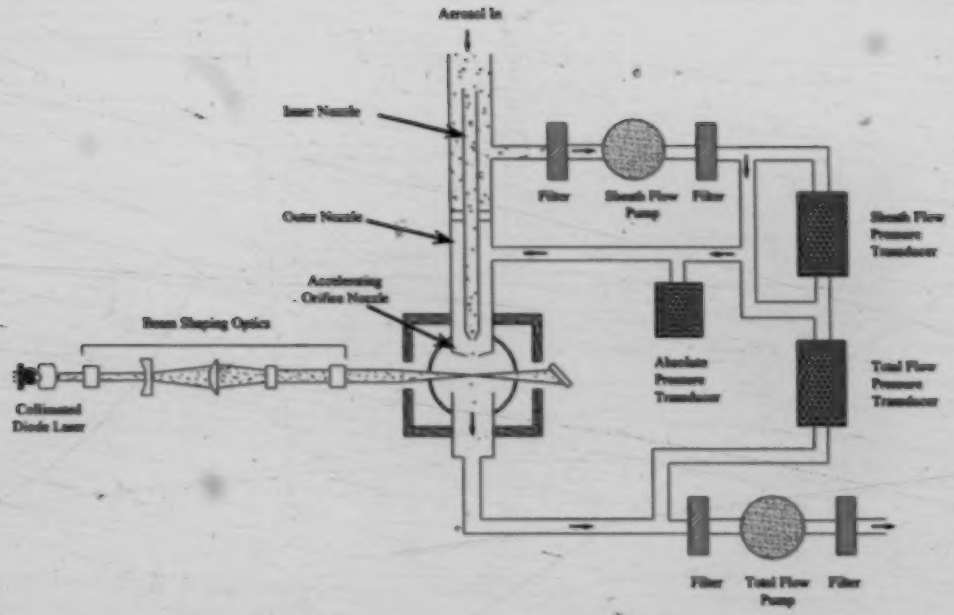

Figure 6-1 Schematic diagram of the TSI Aerodynamic Particle Sizer (adapted from operation manual, TSI Inc.)

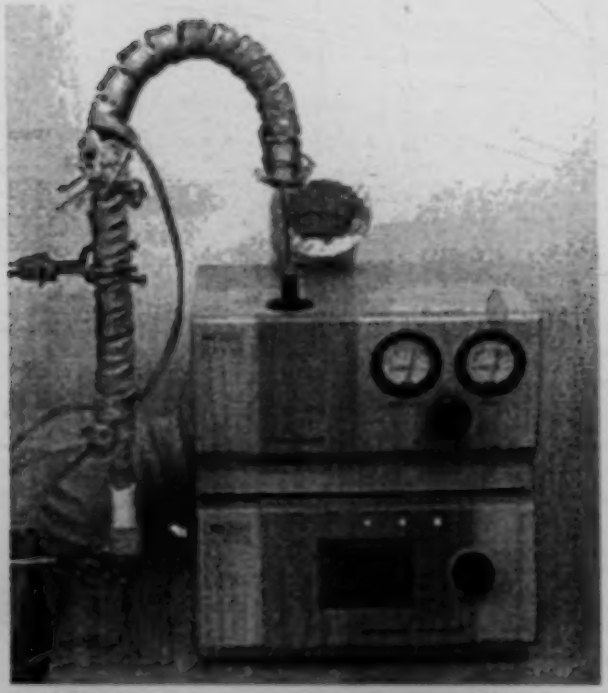

Figure 6-2 Experimental setup for the experiment using PSL microsphere to validate performance of the Aerodynamic Particle Sizer (APS)

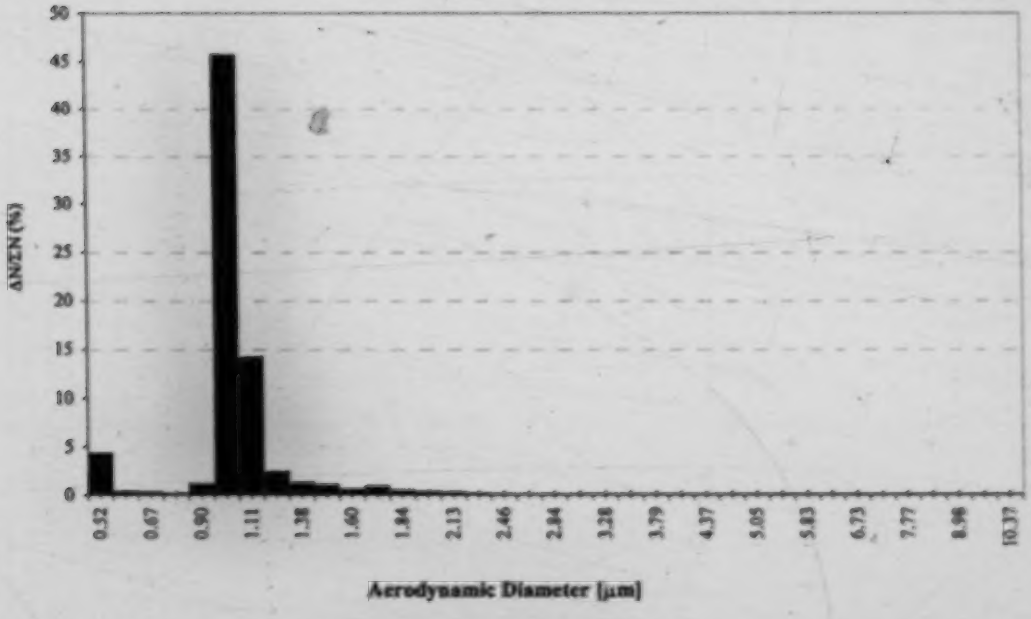

Figure 6-3 Typical particle size distribution histogram of the 1.020 µm PSL microspheres measured by the Aerodynamic Particle Sizer (APS)

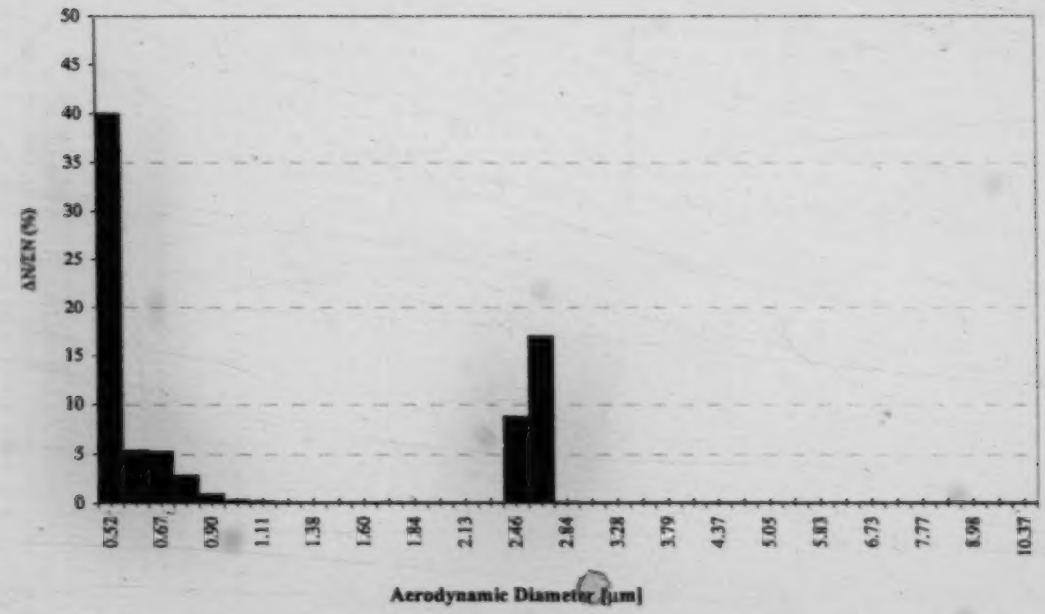

Figure 6-4 Typical particle size distribution histogram of the 2.504 μm PSL microspheres measured by the Aerodynamic Particle Sizer (APS)

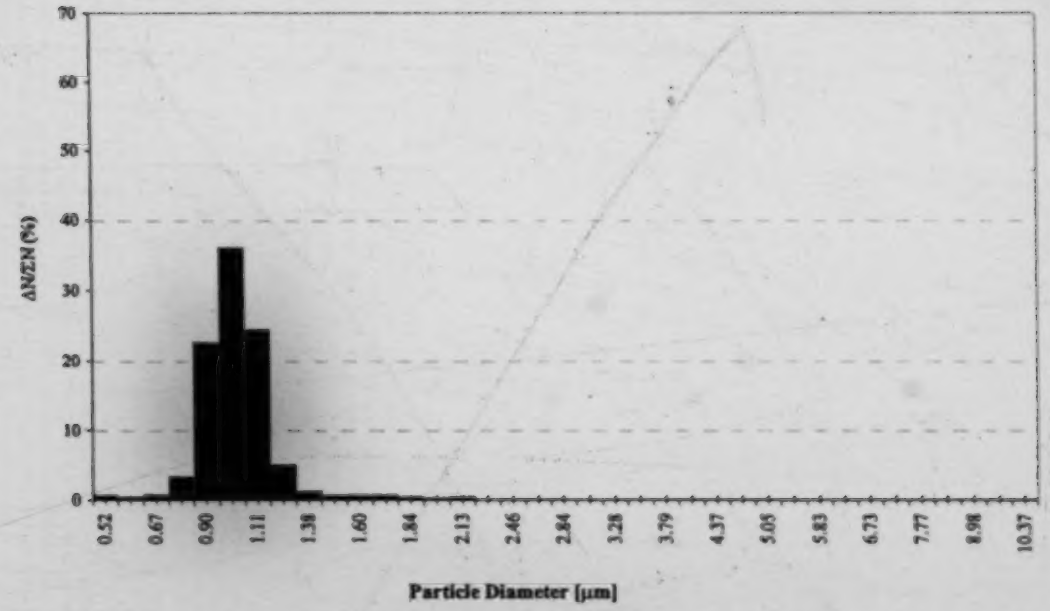

Figure 6-5 Typical Particle size distribution histogram of the 1.020 μm PSL microspheres measured by the Dantec Particle dynamic Analyzer (PDA)

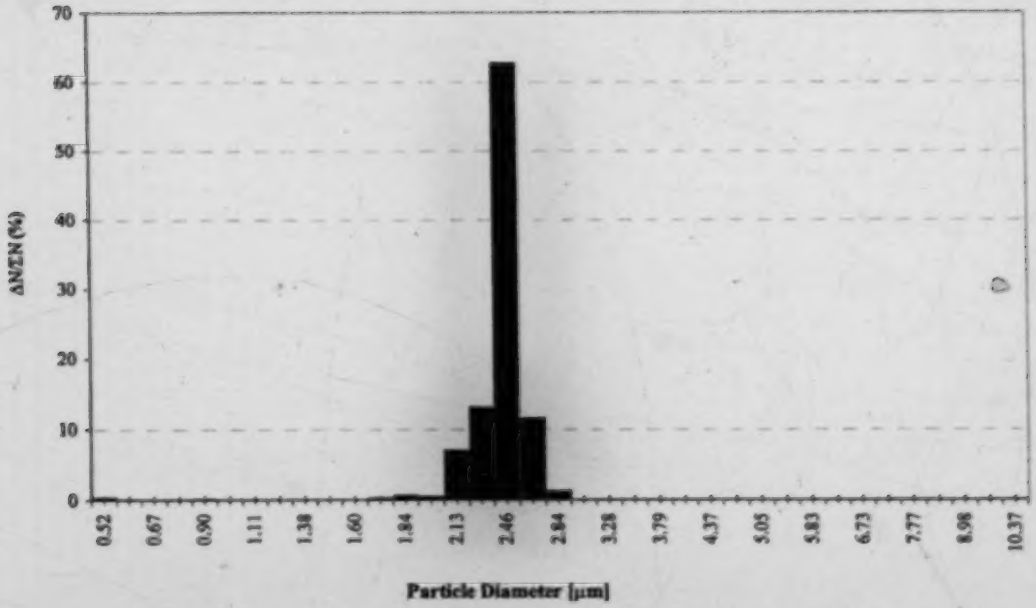

Figure 6-6 Typical Particle size distribution histogram of the 2.504 µm PSL microspheres measured by the Dantec Particle dynamic Analyzer (PDA)

6.6 REFERENCES

Berglund, R. N., and Liu, B. Y. H. (1973). Generation of Monodisperse Aerosol Standards. *Environ. Sci. Technol.* 7:147-153.

Davies C. N. (1966). *Aerosol Science*. Academic Press, London and New York.

Finlay, W. H., Lange, C. F., King, M., and Speert, D. P. (2000). Lung Delivery of Aerosolized Dextran. *Am. J. Respir. Crit. Care Med.* 161:91-97.

Fuchs, N. A., and Sutugin, A. G. (1966). Generation and Use of Monodisperse Aerosols. *Aerosol Science*. Ed. Davies, C. N. pp22-27.

Keady, P. B., and Nelson, P. A. (1984). Monodisperse Particle Generators for Calibrating Aerosol Instrumentation. 1984 Proceedings, 30th Annual Technical Meeting - Institute of Environmental Sciences: Environmental Integration Technology Today for a Quality Tomorrow. Orlando, Fla. Inst. of Environmental Sciences. pp94-100.

Liu, B. Y. H. (1975). Standardization and Calibration of Aerosol Instruments. Symposium on Fine Particles. Minneapolis, MN. *Fine Particles: Generation, Measurement, Sampling, and Analysis*. Ed. Liu, B. Y. H., Academic Press, Inc. pp40-53.

Raabe, O. G. (1975). The Generation of Aerosols of Fine Particles. Symposium on Fine Particles. Minneapolis, MN. *Fine Particles: Generation, Measurement, Sampling, and Analysis*. Ed. Liu, B. Y. H., Academic Press, Inc. pp57-110.

Raabe, O. G. (1968). The dilution of Monodisperse Suspensions for Aerosolization. *Am. Ind. Hyg. Assoc. J.* September-October: pp439-443.

TSI Inc. (2001) Calibrating the APS. Short Course: *Aerosol and Particle Measurement*. Department of Continuing Professional Education. University of Minnesota.

Whitby, K. T., and Liu, B. Y. H. (1968). Polystyrene Aerosols--Electrical Charge and Residue Size Distribution. *Atmos. Environ.* 2:103-116.

Willeke, K., and Baron, P. A. (1993). *Aerosol Measurement: Principle, Techniques, and Applications*. Van Nostrand Reinhold, New York, N.Y.

CHAPTER 7. RATIONAL APPROACH FOR PARTICLE PENETRATION MODELING

7.1 INTRODUCTION

Ever since Liu and Nazaroff (1999) proposed the modeling approach that simulates particle penetration coefficient (P_p) for individual cracks, only two experimental studies have been designed to examine its validity (Liu and Nazaroff, 2001, Mosley *et al.* 2001). Mosley *et al.* (2001) design a chamber study to validate the model using a stack of rectangular cracks. The experimental method was based on the IAQ model. Mosley *et al.* measured particle deposition rates and particle concentrations in the indoor and outdoor chambers to estimate P_p. The experimental results agreed well with the Taulbee model, as discussed in Chapter 3. However, there was very high variation in the measured particle penetration coefficients. Mosley *et al.* attributed the sources of experimental error to uncertainties in air exchange rate measurements, particle concentration measurements, incomplete chamber mixing, and particle deposition rate measurements. In consideration of these potential errors, the model validation in Chapter 3 indicated that the Taulbee model satisfactorily estimated experimental results of Mosley *et al.* Model deviations were mostly less than 10%, with some cases approaching 20%. However, these deviations were well below the 35% experimental uncertainty reported by Mosley *et al.* (2001).

In 2001, Liu and Nazaroff designed another experimental study to investigate how surface texture of crack materials affected particle deposition efficiency. The test crack materials included aluminum, brick, concrete, plywood, redwood, pine, and strand board. Among these materials, Liu and Nazaroff chose smoothly machined aluminum cracks as surrogates of ideal rectangular cracks. Experimental results indicated that the

measured particle penetration coefficients agreed well with model predictions for ideal cracks. For crack height H = 1.0 mm, complete particle penetration was observed for 0.1 to 1.0 μm particles. For other crack material, the measured deposition efficiency was 4 to 16% higher than model prediction. The enhanced deposition was attributed to surface roughness of the crack materials.

Experimental designs of Mosley *et al.* (2001) and Liu and Nazaroff (2001) were both based on concentrations measured in outdoor and indoor chambers. The experimental approaches inherited the same confounding factors, e.g. particle deposition, chamber mixing, etc, encountered in the IAQ modeling approach. Since the original modeling approach proposed by Liu and Nazaroff (1999) was based on the ratio of concentrations at crack entrance and exit, if particle concentrations can be measured at these two locations, it is possible to reduce experimental errors. In addition, this experimental idea also eliminates confounding factors of the IAQ model.

In addition to validate the Taulbee model, this chapter also examined the possibility of entrance cut-off. The particle penetration models discussed in Chapters 3 and 4 assume that particles are removed immediately when they deposit on crack surfaces. This assumption ensures no build-up inside cracks. However, in real-world situations, deposited particles will form protuberances that interfere with infiltration flow. If the protuberances are big enough, relative to crack channel, such that particles cannot follow streamlines, inertial impaction become significant. Inertial impaction enhances particle deposition on the upstream side of the protuberances. As a result, impaction deposition is mostly found at crack entrance, leading to what is called the entrance cut off (Morton and Mitchell, 1995; Williams, 1994). Clement (1995) and Mitchell *et al.* (1990)

developed theoretical models to predict entrance cut off. It was found that the significance of impaction deposition, gravitational deposition and Brownian diffusion were determined by capillary radius, capillary length, and fluid velocity. A larger capillary radius, shorter capillary length, or higher fluid velocity would reduce the significance of impaction deposition. Although the fine capillaries ($\sim 10^1$ μm), very high differential pressures ($\sim 10^2$ kPa), and high particle concentrations investigated by Morton and Mitchell (1995) and Clement (1995) are very different from typical residential conditions, it is necessary to verify if entrance cut-off would happen in tighter building designs. If entrance cut off is a significant deposition mechanism, cracks will be clogged in a short time. A clogged crack retards particles from penetrating through cracks, and reduces infiltration flow. On the other hand, if entrance inertial impaction is not important, particles will deposit uniformly across the cracks.

This study designed an alternative experimental approach that directly measured particle concentrations at crack entrance and exit to validate the Taulbee model and inclined crack model. A non-intrusive laser Doppler particle dynamic analyzer (PDA) was used in the particle penetration study. The APS focuses its measurement volume at crack entrance and exit to measure particle concentrations, which enables measurement without interfering infiltration flow field. This study designed an acrylic outdoor-indoor chamber so that the measurement volume of the two laser beams could be aligned at crack entrance and exit. The joint vapor/nuclei type aerosol generator, as discussed in Chapter 5, was used to provide stable particle flow in the outdoor chamber. A vacuum pump was used to draw infiltration air through the crack to simulate infiltration flow. Experimental results indicated that the Taulbee model agrees well with the measured

particle penetration coefficient. Visual examination on particle deposition patterns indicated that entrance cut off and inertial impaction are not significant deposition mechanisms for the current test conditions.

7.2 EXPERIMENTAL MATERIALS AND METHOD

The experimental setup of the particle penetration study was composed of four parts: an outdoor-indoor chamber, an infiltration control system, an aerosol generator, and a particle measurement system. Among these, the outdoor-indoor chamber and the flow control system were the same as the air infiltration study, which has been presented in Chapter 2, while the aerosol generator was presented in Chapter 5. As for the particle measurement system, this study used a Dantec Particle Dynamic Analyzer (PDA) to measure particle concentrations at crack entrance and exit to estimate particle penetration coefficient.

7.2.1 Infiltration Control and Aerosol Generator

Figure 7-1 illustrates a schematic diagram of the experimental setup. The infiltration control system was generally the same as the system used in Chapter 2. One modification to the infiltration system was the use of a second vacuum pump to draw aerosol flow through the outdoor chamber. The design was to maintain a stable particle concentration in the outdoor chamber such that the alternatively measured concentrations at crack entrance and exit can be used to calculate particle penetration efficiency. To achieve this purpose, aerosol flow into the outdoor chamber must be significantly higher than infiltration flow. According to the infiltration model discussed in Chapter 2, the test infiltration flow rates were less than 2.0 L/min. As a result, the aerosol flow into the outdoor chamber was set at 10 L/min, approximately. Because the condensation-type aerosol generator did not produce such a high aerosol flow, the sampled aerosols were

diluted with ambient air immediately at the sampling inlet. In this flow rate, the outdoor chamber reached a stable concentration in less than 10 minutes.

7.2.2 Traverse System

The experimental approach of this study requires measurement of particle concentrations at crack entrance and exit alternatively. It requires a traverse system to move the chamber such that the PDA's measurement volume can be aligned at crack entrance and exit. In addition, the chamber must be installed on a rotation platform so that the PDA can measure particle concentration at crack entrance and exit alternatively. To achieve the measurement requirement, a 2-D traverse system was coupled with a heavy-duty scissor jack to move the chamber in three dimensions. A rotation disk was installed on the scissor jack so as to rotate between the indoor and outdoor chambers alternatively. This study measured five pairs of particle concentrations at crack entrance/exit to derive five particle penetration coefficients for each test condition.

In alignment, this study used the scissor jack mechanism to align the PDA's measurement volume at the vertical elevation of the crack first. This was accomplished by adjusting the scissor jack up and down until the cross section (measurement volume) of the two laser beams was observed through the other side of the crack. Then, the chamber was moved toward laser beams horizontally until they directly illuminated on the edge of crack plates. The chamber was again moved away from laser beams slightly until laser beams just did not illuminate on crack plates. This alignment procedure ensured the measurement volume was aligned as close to the crack entrance/exit as possible. Because the Gaussian beam diameter (0.82 mm) was greater than crack height (< 0.508 mm), all particles at one plane that enter/exit the test crack can be detected by

the PDA. The ratio of particle concentration at crack exit to entrance was used to calculate penetration efficiency.

7.2.3 Operation Theory of the Particle Dynamic Analyzer (PDA)

The particle measurement system used in this study was a Dantec particle dynamic analyzer. The PDA is a non-intrusive measurement technology. It measures both particle velocity and concentration simultaneously. Particle velocity is measured from the frequency of Doppler burst, while particle size measurement is based on the phase shift of scattered signals detected by two pairs of photodetectors. This section discusses the measurement theories of the PDA system. Rational decisions on selecting system parameters are discussed as well.

7.2.3.1 The Fringe Theory (Velocity Measurement)

The Dantec PDA is an extension of laser Doppler anemometry. It measures particle velocity based on the frequency of Doppler bursts when a particle travels through the measurement volume. Figure 7-2 illustrates two laser beams of equal intensity intersecting each other at an angle δ. The laser beams interferer with each other, producing parallel planes of light and dark planes. The parallel planes are called fringes and the region of intersection is the measurement volume. When the intersect angle δ is selected, fringe space s can be calculated from the wavelength of laser beams (λ):

$$s = \frac{\lambda}{2\sin\left(\frac{\delta}{2}\right)} \qquad (7\text{-}1)$$

Figure 7-3 illustrate a particle travels through the measurement volume at velocity v. When the particle meets sequential light and dark fringes, it emits scattered

signals with periodical fluctuation in light intensity. The frequency of Doppler burst f_d can be related to particle traveling velocity v:

$$f_d = \frac{v}{s} \tag{7-2}$$

Combining equations 7-1 and 7-2, particle velocity can be calculated from the frequency of Doppler bursts. This is the fringe model (Devenport 1996):

$$f_d \lambda = 2v \sin\left(\frac{\delta}{2}\right) \tag{7-3}$$

The fringe planes produced by two identical beams are stationary; therefore, the light scattering frequency cannot indicate the direction of particle motion. To solve the directional ambiguity problem, the PDA system introduces a frequency shift on one of the incident laser beams such that fringe planes sweep through the measurement volume continuously. As a result, the frequency of Doppler bursts is modulated by the shift frequency. Particles moving in the same direction as fringe movement decreases the modulation frequency and vice versa. The Dantec PDA system uses a Bragg cell to produce a 40 MHz frequency shift on one of the incident laser beam to solve the directional ambiguity problem.

7.2.3.2 Phase Shift (Particle Size Measurement)

The Dantec PDA system measures particle size based on the phase shift of scattered signals detected by two pairs of photodetectors. When a particle passes through the measurement volume, a photodetector receives sequential light and dark signals at Doppler frequency. If two photodetectors, *U1* and *U2*, are aligned at different angles, the received signals will have a phase shift Φ between *U1* and *U2*, as shown in Figure 7-4. The phase shift Φ is proportional to the focal length of the particle. For spherical

particles, focal length is equal to particle diameter. As a result, particle diameter can be calculated from the measured phase shift.

Figure 7-4 illustrates a schematic diagram showing the size dependency of phase shifts observed from a pair of photodetectors *U1* and *U2*. For D_1 and D_2 particles, particle diameter is linearly dependent on phase shifts. However, for the D_3 particle, phase shift Φ_3 is over 2π such that the detector cannot tell whether particle size is D_3 or D'_3. This is called 2π ambiguity. The Dantec PDA system adds a third photodetector *U3* between *U1* and *U2*, as shown in Figure 7-5, to solve the 2π ambiguity. For the distant pair of detectors *U1* and *U2*, the slope of phase shift $\Phi_{1,2}$ to particle diameter is greater and thus has better size resolution. However, 2π ambiguity limits its useful size range. On the other hand, the slope for the close pair of detectors *U1* and *U3* is less steep. This pair can measure larger particles without the 2π ambiguity. However, its size resolution is worse. With the combination of the two pairs of photodetectors, the PDA system extends particle measurement range and improves size resolution simultaneously. In addition, the phase shifts of the two pair of photodetectors are compared as a validation tool. For spherical particles, theoretically, the sum of phase differences among the three photodetectors should be zero. However, it is not always the case because of measurement error. The PDA uses sphericity check criteria to discriminate the acceptable phase error. This study set the acceptable phase error to be 2° and used NIST certified PSL microspheres to fine-tune the PDA system. Because the PSL microspheres and DEHS droplets were perfect spheres, the fine-tuned system always had > 99% validation ratio.

7.2.4 PDA Setup

Figure 7-6 illustrates a schematic diagram of the Dantec PDA system. It was composed of four major components: an Ar-ion laser source, transmitting optics, receiving optics, and a signal processor. The system offers several optical accessories to measure particles of different scattering characteristics and size ranges. The following sections discuss the parameters chosen to optimize measurement conditions.

7.2.4.1 Scattering Angle

Figure 7-7 illustrates a laser beam from left-hand-side illuminating a spherical particle. There are three scattering modes frequently used in PDA measurement applications: reflection, first-order refraction, and second-order refraction. Because the phase factors of these three scattering modes are different, signals from the mixture of three modes may give rise to sizing errors. It is necessary to choose a scattering angle such that one scattering mode dominates over the others. The Lorenz-Mie analysis was used to calculate scattering intensity with respect to scattering angle. The scattering intensity curve of a 50 μm PSL microsphere indicates that forward refractory scattering mode is five orders of magnitude over the other scattering modes at the Brewster angle (64.3°). As a result, this study chose 65° forward scattering in the PSL study. The Dantec Measurement Technology A/S recommends using the same scattering angle to measure DEHS particles. The refractive index of DEHS is 1.49.

7.2.4.2 Laser Source and Optics Systems

The Dantec PDA system uses a 300 mW Ar-ion laser as the illuminating source. Inside the transmitting optics, a color separator divides the laser beam into a 514.5 nm green beam and a 488 nm blue laser beam so that the PDA can measure two velocity components. Each of the laser beams is further divided into two beams of identical

intensity by a beam splitter for 2-D measurement. To solve directional ambiguity, a Bragg cell is used to produce a 40 MHz frequency shift on one of the incident laser beam. The laser beams are then re-focused by a front lens to intersect at the measurement volume.

Although the Dantec PDA can measure two velocity components, this study used it in a one-component configuration to facilitate alignment (Figure 7-8). The PDA used two pairs of intersect laser beams to measure two velocity components of particles. They were aligned in the vertical (green beams) and horizontal planes (blue beams), respectively. In this study, because the measurement volume must be aligned as close to the crack entrance/exit as possible, it was found that the horizontal blue beams illuminated on crack plates when the measurement volume was close to crack entrance/exit. The reflective light overlaps the scattered signals such that the signal processor could not function properly. To solve the problem, the two blue beams were masked, and the PDA signal processor was set to 1-D configuration in the particle penetration study.

The Dantec PDA system can measure particles from 1.0 μm to several mm depends on the setup of its optical system and signal processor. In this study because the investigated size range was in μm scale, the system was aligned at the PDA's lowest measurement range. This was accomplished by increasing the intersect angle δ and the apertures of photomultipliers. As a result, the shortest focal length, 310 mm, was chosen for the transmitting and receiving optics, the beam spacing was adjusted to 75 mm, and the micrometer was set at 2.0 mm. Table 7-2 presents the setup of the transmitting and receiving optics. It indicates that the phase factor $\Phi_{1,2}$ and $\Phi_{1,3}$ were 12.76 degree/μm and

6.38 degree/μm, respectively. Φ_{1-2} and Φ_{1-3} are used to validate measurement results. Because the test DEHS droplets are spherical shaped, validation ratio should be nearly 100%. For a validated particle, Φ_{1-2} is used for particle size calculation because it has better size resolution. Using this setup, the PDA's maximum sizing range was 40.7 μm. Its lower detection limit was determined by the wavelength of laser beams, at approximately 0.5 μm. The parameters of the signal processor were determined from the PSL validation/calibration study, as shown in. Table 7-3.

7.2.5 Particle Deposition Pattern Tests

To examine the significance of dominant particle deposition mechanisms, this study visually examined the deposition patterns of 1.4 μm particle inside the $H = 0.305$ mm rectangular cracks and L-shaped cracks. According to the Taulbee model, it was expected that gravitational sedimentation would be the major deposition mechanism for rectangular cracks. For L-shaped cracks, inertial impaction was expected to be insignificant given the low residential infiltration velocity (Liu and Nazaroff, 1999). To examine the significance of these deposition mechanisms, this study visually examined the deposition patterns of 1.4 μm particle inside the $H = 0.305$ mm rectangular cracks and L-shaped cracks. The test differential pressure was 8 Pa and each penetration test lasted for 8 hours to deposit enough particles for visual examination. Under these test conditions, a visible DEHS film could be observed on crack plates. It provides evidence to qualitatively examine particle deposition mechanisms. Because a camera could not record the DEHS film clearly, this study applied color scenic sands on the deposition plates and then shook the plates lightly. Scenic sands would stick on where there was DEHS film. Using this method, this study found gravitational sedimentation was the

major deposition mechanism. There was no evidence of inertial impaction on the 90° bend of the L-shaped cracks. In addition, the uniform deposition pattern indicates that entrance cut-off was not significant for all test situations.

7.3 RESULTS AND DISCUSSION

7.3.1 Entrance Cut Off Analysis

This section uses a case study investigated by Clement (1995) to examine the possibility of entrance cut off for residential crack penetration. Clement (1995) investigated particle penetration through fine capillaries to predict entrance cut off using an impaction deposition model. Clement found when differential pressure across an L = 50 mm capillary was 100 kPa, impaction deposition was significant if the capillary radius was approximately 15 μm or less. Using this case study as a reference, this section used geometric factors and infiltration velocity to examine if impaction deposition was an important deposition mechanism for residential penetration. For crack geometric factors, the cracks tested in this study were L = 30 to 60 mm and 0.102 mm to 0.254 mm in hydraulic radius. The larger radius suggests that our modeling rectangular cracks are less likely to be cut off than the 15 μm capillary. Consequently, if infiltration velocity through the 15 μm capillary was less than those through our test cracks, impaction deposition might not be significant. Using the Hagen-Poiseuille law, the calculated velocity was 78 mm/sec for the 15 μm capillary. This velocity is at the lower end of our modeled infiltration velocity (3 to 470 mm/sec). When crack geometric factors and infiltration velocity are both taken into consideration, it was expected that impaction deposition would not be significant in this study. Possible exceptions are fine cracks (e.g.

the $H \leq 0.203$ mm cracks). Under low differential pressures, significance of impaction deposition should be examined for these fine crack dimensions.

7.3.2 Visual Examination of Particle Deposition Pattern

Figures 7-9 and 7-10 illustrate the photos of particle deposition patterns for $L = 30$ and 60 mm rectangular cracks, respectively. These figures indicate that particles only deposit on the bottom plates. Gravitational sedimentation is the dominant particle deposition mechanism. The photos indicate that there is no deposition on the upper plates, suggesting Brownian diffusion is not a significant deposition mechanism. Although the photo cannot show the uniformity of oil film, generally speaking, visual examination indicates that the original DEHS film was very uniform on the bottom plates. The uniform deposition pattern suggests that entrance inertial impaction was not significant. If it was, particles should predominately deposit at crack entrance.

Figure 7-11 illustrates the deposition pattern for the $L = 60$ mm L-shaped crack. As predicted from the inclined crack model, the vertical section does not show visible DEHS film because the effective particle deposition velocity $v_{sy} = 0$, and Brownian diffusion is not an efficient deposition mechanism for micron-sized particles. For the horizontal crack section, particles only deposit on the bottom plate. This suggests that gravitational deposition is the major deposition mechanism. The deposition film was very uniform throughout the horizontal section. The observation suggests that inertial impaction was not significant at the 90° bend. If it was, more particles should deposit at the entrance of the bottom plate. These results indirectly confirm that the infiltration flow became laminar soon after the 90° bend. If it was not, there should be turbulence at the

bend such that some particles deposit on both upper and bottom plates at the entrance of the horizontal channel.

Visual inspection indicates that the assumption "crack height remains constant" was generally acceptable. The crack height tested in this study was 0.203 to 0.508 mm, which was hundreds time of the diameter of test particles. Effect of build-up particles should be examined. As observed in this deposition pattern experiment, even operated in a foggy test environment for 8 hours, the test oil particles only formed a thin film on crack surfaces upon deposition. Thickness of the film was much smaller than crack height. The assumption that crack height remains constant was judged acceptable for this laboratory study. Section 7.3.4 will discuss the effect of build-up on real house penetration.

7.3.3 Validation of Particle Penetration Models

This study measured particle penetration for a series of crack dimensions and particle sizes, as shown in Table 7-1. This section illustrates experimental results of 1.4 μm particles in Figures 7-12 to 7-14 to illustrate the agreement between experimental results and theoretical modeling. Summary of all tests results are illustrated in Figures 7-15 and 7-16 for the rectangular crack and L-shaped crack tests, respectively,

Figure 7-12 illustrates particle penetration curves with respect to differential pressure for the L = 60 mm rectangular cracks and 1.4 μm particles. The diamonds, triangles, circles, and cubes represent the measured mean particle penetration coefficients for the H = 0.508 mm, 0.406 mm, 0.305 mm, and 0.203 mm cracks, respectively. The means and standard deviations were calculated from five observations and the solid lines represent theoretical penetration coefficients estimated from the Taulbee model. It was

found that the H = 0.203 mm crack provided the best protection from penetration of test particles; more than 50% of particles deposit inside the crack for the test differential pressures. When ΔP is less than 4 Pa, almost all particles deposit inside the cracks. Particle penetration coefficients are less than 0.05. When differential pressure was higher than 8 Pa, less than or approximately 20% of particles deposit inside the cracks. Generally speaking, this experimental approach provided better particle penetration data than the IAQ modeling approach used by Mosley *et al.* (2001). The Taulbee model satisfactorily estimates particle penetration coefficients.

Figure 7-13 illustrates particle penetration curves for the L = 30 mm rectangular cracks and 1.4 μm particles. The legends are the same as those in Figure 7-12. It indicates that the Taulbee model predicts the trends of particle penetration coefficients reasonably well. P_p is inversely proportional to crack length. The 30 mm cracks provide less protection from particle penetration than the L = 60 mm cracks. For the H = 0.305, 0.405, and 0.508 mm cracks particle penetration coefficients were higher than 0.8 for most differential pressures. For the H = 0.203 mm crack, when $\Delta P > 6$ Pa, particle penetration coefficient ranges from 0.72 to 0.85. When $\Delta P < 4$ Pa, particle penetration coefficients were less than 0.62.

Figure 7-14 illustrates particle penetration curves for L = 60 mm L-shaped cracks and 1.4 μm particles. This study assumed that a L-shaped cracks is composed of a horizontal section and a vertical section, and flow fields in both sections are laminar. Using the inclined crack model, particle penetration coefficients for these two sections can be estimated as P_h and P_v. The overall particle penetration coefficient $P_p = P_h \times P_v$. The figure suggests that the modeling approach predicted experimental results reasonably

well. For the 0.305 mm, 0.406 mm, and 0.508 mm cracks, particle penetration coefficients were higher than 0.8 for most differential pressures. As for the 0.203 mm crack, particle penetration coefficients were less than 0.78.

Comparison between Figures 7-12 and 7-14 indicate that, under the same infiltration conditions, a rectangular crack provides higher deposition efficiency than a L-shaped crack. The overall crack length for these two cracks were both 60 mm. According to the infiltration model, their infiltration flow rates are the same. Experimental results indicate that particle penetration coefficients for the rectangular cracks were lower. These results are consistent with visual examination of particle deposition patterns, as shown in Figure 7-11, where the vertical channel does not show significant deposition. As a result, the effective deposition length of a L-shaped crack is only half of a rectangular one. The finding suggests that a horizontal cracks provide better protection from micron-sized particle penetration.

Figure 7-15 summarizes theoretical Taulbee model and experimental results for all the rectangular crack tests. The horizontal and vertical coordinates are penetration coefficients predicted from the Taulbee model and the experimental results, respectively. The figure indicates that test results are quite consistent with model predictions. The deviation between experimental results and the Taulbee model is generally within ±10%. Experimental deviation from the Taulbee model was larger for low penetration coefficient. For these cases, because few particles penetrated through the cracks, the PDA's measurement volume was hard to be aligned. As a result, greater deviation from the Taulbee model was observed. When P_p was less than 0.1, alignment of the measurement volume was not possible. Experimental P_p was 0. For P_p greater than 0.9,

there were some experimental penetration efficiency greater than 1.0. The results were not reasonable since P_p should be less than or equal to 1.0. The deviation might be induced from experimental error. Possible sources of the deviation could be generator stability, chamber repositioning, and PDA measurement error. Among these, the generator stability test (Figure 5-5) indicates that concentration of product particle might fluctuate within ±5%. When rotating the chamber to align with PDA's measurement volume, alignment may contribute to certain amount of error. For PDA measurement error, 10-15% of error in particle concentration measurement is expected according to the operation manual. These factors led to experimental deviations. Figure 7-15 indicates that particle penetration coefficients are mostly higher than 0.9 for the test conditions. Generally speaking, complete particle penetration was observed for crack height $H \geq 0.406$ mm and $L \leq 30$ mm.

Figure 7-16 summarizes the theoretical Taulbee model and experimental results for the *L*-shaped crack tests. It indicates that experimental results were quite consistent with model predictions. Most of the experimental penetration coefficients are within ±10% of the Taulbee model. Complete penetration was observed for $H \geq 0.406$ mm cracks.

7.3.4 Real House Penetration Behavior

The present study made assumptions on crack geometry and particle behavior to simplify modeling considerations. In real house penetration, crack geometry, surface characteristics and particle behavior are much more complicated and need to be taken into account in future modeling. In addition, further studies would be needed to investigate the performance of such models. For the present, a discussion on factors that

affect real house particle penetration is presented to bridge the gap between modeling and penetration behavior for actual situations.

7.3.4.1 Crack Geometry and Surface Characteristics

Although geometry of most building cracks is similar to rectangular slits between two parallel plates, the dimensions and surface characteristics vary widely. A method is required to define this variation so that particle penetration models can be used to represent actual house particle penetration. Take crack geometry as an example: the present models assume cracks are rectangular-shaped and require crack length, width, and height to execute the infiltration and particle penetration models. Among these geometric parameters, crack length and width can be obtained using a measuring tape. However, no devices can satisfactorily measure crack height for real building components. This makes application of particle penetration models on real building components difficult. However, actual crack heights can be approximated using an effective crack height parameter, which can be derived from the infiltration model, as shown in equations 2-1 to 2-3. The infiltration model indicates that infiltration flow rate is a function of crack length, width, height, and the difference pressure across the crack. Because crack length and width can be measured, if infiltration flow rate for a specific difference pressure is measurable, the effective crack height of a test building component can be estimated. The infiltration flow rate test can be accomplished by sealing a building component inside a two-compartment chamber. Difference pressure between the two compartments can be controlled by a vacuum pump and the corresponding infiltration flow rate can be measured. In this manner, equivalent crack height can be derived and used to estimate P_p for a test building compartment. In addition, the test chamber can be designed to be temperature and humidity controlled. Then, contraction and expansion

effects induced from ambient temperature and humidity changes can be tested. Similar infiltration tests have been used in air ventilation studies to characterize the infiltration flow rate of real building components for energy conservation rating (Louis and Nelson, 1995; Mayo, 1992).

Surface characteristics of cracks and particles are other parameters that closely affect particle behavior but not considered in our modeling. Our particles were assumed to adhere or stick on a crack surface once they deposit inside a crack. In an actual situation, sticking efficiency depends on physical and chemical characteristics of the particle and crack surface. Particle size and shape, and surface texture and electrostatic charge of the particle and crack would affect particle sticking efficiency. Furthermore, relative humidity in ambient air will modify surface characteristics as well. These factors complicate particle deposition behavior.

7.3.4.2 Particle Deposition Behavior

Our modeling neglects bounce, re-entrainment, and build-up when particles deposit on crack surfaces. These assumptions ensure constant crack geometry and a stable infiltration flow field. In practice, when particles hit crack surfaces, kinetic energy deforms the particles and adheres them to crack surfaces. If the remaining kinetic energy overcomes the adhesive forces, particles will bounce into the fluid flow field. For particles that successfully deposit on crack surface, they may adhere with other particles to form aggregates, or they may be re-entrained into the fluid if the drag force and lift force induced by air current overlying them overcomes the adhesive forces. Hinds (1982) suggested that particles smaller than 10 μm are not likely to be dislodged by common forces, such as air current. This implies that when a PM2.5 particle deposits on crack surfaces, it is more likely to stick or form aggregates with other particles on the surface.

When the aggregates grow big enough such that removal forces overcome adhesive forces, they will be re-entrained into the fluid. Re-entrained particles in the form of aggregates are likely to settle down shortly after being blown into the indoor environment. Consequently, particle re-entrainment is more likely to be a dust nuisance instead of an inhalation issue. Re-entrainment ends a particle deposition cycle and starts another one. On the other hand, if air current is not fast enough to cause re-entrainment, the aggregates accumulate over time and form a porous structure that acts as a filter. The porous structure allows air to flow through but retards particles from entering indoors. Gradually, when more particles deposit, cracks will be totally blocked. In this case, the particle penetration process comes to an end if the crack is not cleaned.

Another mechanism that our modeling neglects is impaction deposition. We assumed particles to be immediately removed when they deposit on crack surfaces. This assumption ensures no build-up inside cracks. This simplification is contradictory to actual deposition behavior. When particles deposit on crack surfaces, build-up particles form a protuberance and interfere with fluid flow. If the protuberance is big enough such that particles cannot follow streamlines, inertial impaction will become significant. Inertial impaction enhances particle deposition at the upstream side of the protuberance. As a result, impaction deposition is mostly found at the entrance of cracks, which may lead to entrance cut off (Morton and Mitchell, 1995). Clement (1995) developed theoretical models to predict entrance cut off. He found that impaction deposition was much more significant than gravitational deposition and Brownian diffusion for vertical fine capillaries. However, for horizontal ones, analogous to our modeled rectangular cracks, he found that the significance of these three mechanisms was determined by

capillary radius, capillary length, and fluid velocity. A larger crack radius, shorter capillary length, or higher fluid velocity would reduce the significance of impaction deposition. Clement (1995) used a case study to validate an impaction deposition model. He found that when difference pressure across a 50 mm capillary was 100 kPa, impaction deposition was significant if the capillary radius was about 15 μm or less. Using geometric factors and fluid velocity conditions of this study as a reference, it is possible to check if impaction deposition will dominate particle deposition inside our modeled rectangular cracks. For crack geometric factors, the modeled rectangular cracks are 30 and 60 mm in length and 0.203 to 0.508 mm in hydraulic radius. The shorter length and larger radius suggests that our modeling rectangular cracks are less likely to be cut off than the 15 μm capillary radius. Consequently, if infiltration velocity of the 15 μm capillary is less than the modeled rectangular cracks, impaction deposition may not be significant. Using the Hagen-Poiseuille law, the calculated infiltration velocity is 7.8 cm/sec for the 15 μm capillary. The velocity is at the lower end of our modeled infiltration velocity (0.7 to 196 cm/sec). When crack geometric factors and infiltration velocity are both taken into consideration, it is expected that impaction deposition will not be significant for most of our modeling conditions. Possible exceptions are fine cracks (e.g. 0.1 or 0.2 mm cracks). Under low difference pressures, impaction deposition should be taken into consideration for these fine cracks.

7.4 CONCLUSION

This study used a Dantec particle dynamic analyzer to measure particle concentrations at crack entrance and exit to estimate particle penetration through cracks.

In addition, photographs of crack plates were made to examine the particle deposition pattern so as to identify the dominant particle deposition mechanisms. This study found:

1. Entrance cut off did not happen for the current test conditions. However, for crack $H < 0.203$ mm, entrance cut off needs to be examined further.
2. Visual examination indicated that particles uniformly deposit on the bottom plates for rectangular cracks. Gravitational sedimentation is the major deposition mechanism for the micron-sized particles used in these tests. Particle deposition patterns indicate that both entrance cut off and inertial impaction were not significant for the test conditions.
3. Particle penetration coefficient increases monotonously with respect to differential pressure and crack height; while decreased monotonously with respect to crack length. For $H > 0.305$ mm, and $L < 30$ mm cracks, particle penetration coefficient was higher than 0.8 for the test cracks. Generally speaking, for $H > 0.406$ mm cracks, complete penetration was observed for differential pressures of typical residential conditions.
4. The Taulbee model agreed well with experiments. The measured particle penetration coefficients were mostly within ±0.05 of theoretical modeling results.
5. L-shaped cracks can be simulated as a combination of a horizontal section and a vertical section. The overall particle penetration coefficient equals to the product of individual penetration coefficients. When compared with rectangular cracks of the same crack length, height, and differential pressure, higher penetration coefficients were observed for L-shaped cracks.

Table 7-1 Summary of test parameters for the particle penetration experiment

Parameter	Symbol	Unit	Range
Particle diameter	d_p	μm	1.0, 1.2, 1.4, 1.6, 1.8
Crack length	L	mm	Rectangular cracks: 30, 60 L-shaped cracks: 60
Crack height	H	mm	0.203, 0.305, 0.406, 0.508
Differential pressure	ΔP	Pa	2, 4, 6, 8, 10, 12

Table 7-2 Parameter settings for the PDA's transmitting and receiving optics

PDA Components	Unit	Set-up Condition
Transmitting Optics		
Front lens focal length	mm	310
Laser beam spacing	mm	75
Fringe spacing	μm	2.14
Number of fringes	number	52
Frequency shift sign	-	Positive
Polarization	degree	0
Polarization orientation	-	Parallel to fringes
Laser wavelength	nm	514.5
Laser power	mW	300
Gaussian beam diameter	mm	0.82
Beam collimation	-	1.2
Beam expansion	-	1.85
Receiving Optics		
Front lens focal length	mm	310
Polarization	degree	0
Polarization orientation	-	Parallel
Scattering angle	degree	65 (Forward scattering)
Micrometer setting	mm	2.0
DEHS refractive index	-	1.448
Phase factor (U_{12})	deg/μm	12.76
Phase factor (U_{13})	deg/μm	6.38
Max diameter	μm	40.8

Table 7-3 Parameter settings for the PDA's signal processor

Electronic Settings	Unit	Set-up Condition
Band Width		
Ux/Gain	MHz	0.4/High Gain
Burst detector bandwidth	MHz	0.1
Transit time resolution	μs	61.1
Arrival time resolution	μs	1
Optical frequency shift	MHz	40
Validation		
Validation level	dB	+3
Max phase error	degree	5
Max spherical deviation	%	2
High voltage		
U1	Volts	800
U2	Volts	744
U3	Volts	760

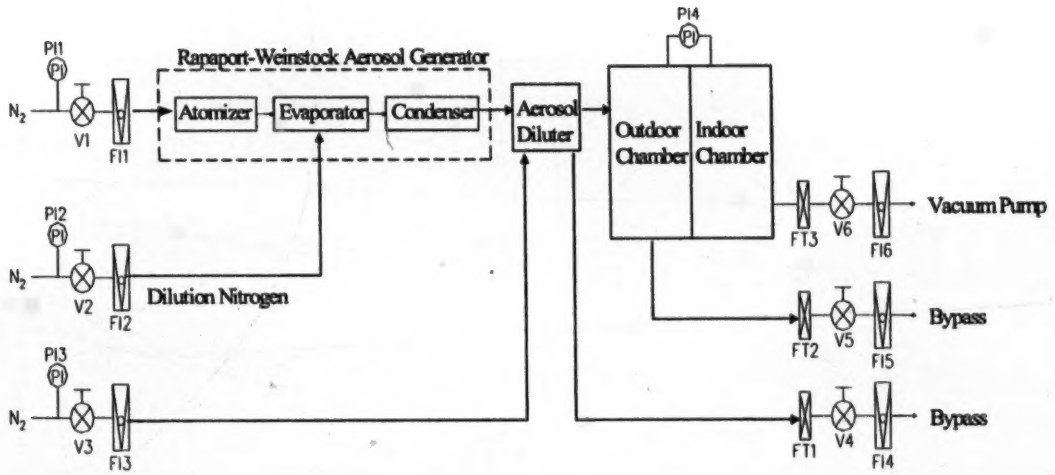

Figure 7-1 Schematic diagram of the experimental setup for particle penetration study

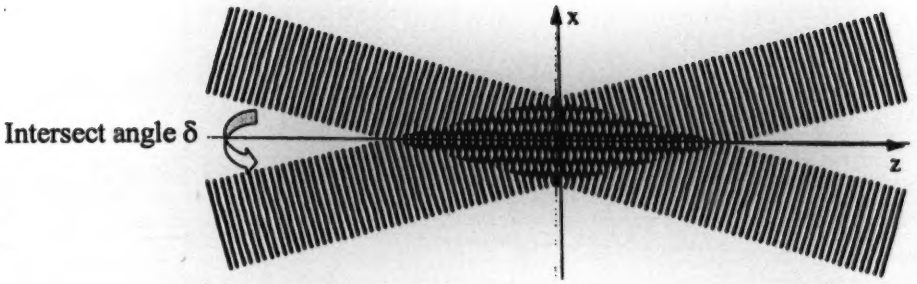

Figure 7-2 Measurement volume of two intersect laser beams (after Dantec Measurement Technology A/S)

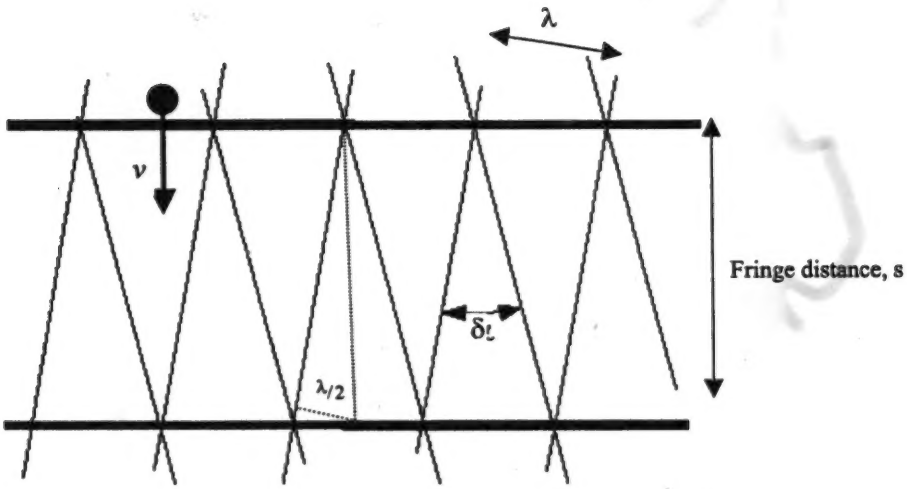

Figure 7-3 Fringe Model for velocity measurement (after Dantec Measurement Technology A/S)

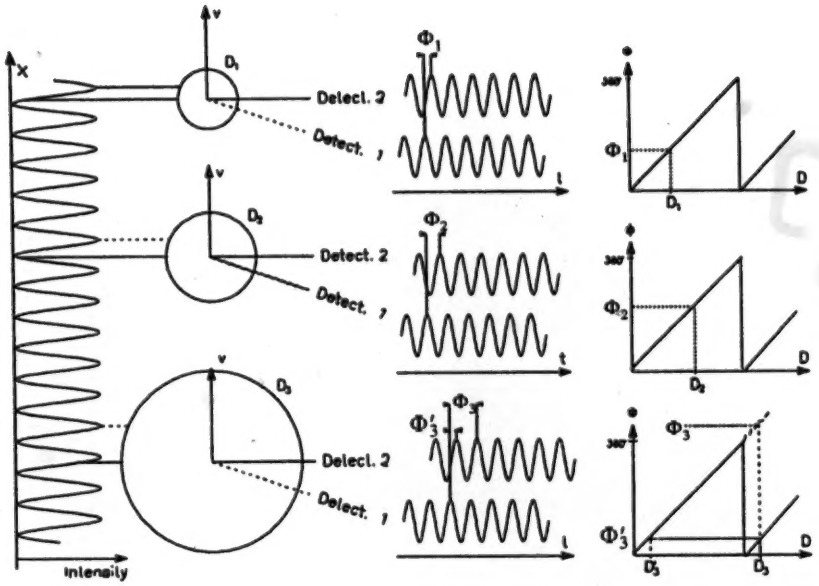

Figure 7-4 Schematic diagram showing measurement of particle diameter using phase shift (after Dantec Measurement Technology A/S)

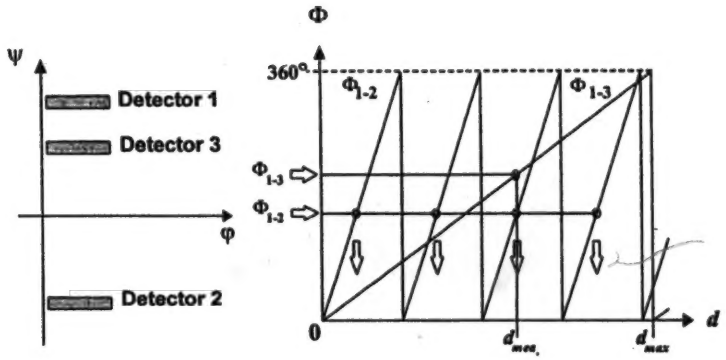

Figure 7-5 Schematic diagram of using two pairs of photodetectors to solve the 2π ambiguity (after Dantec Measurement Technology A/S)

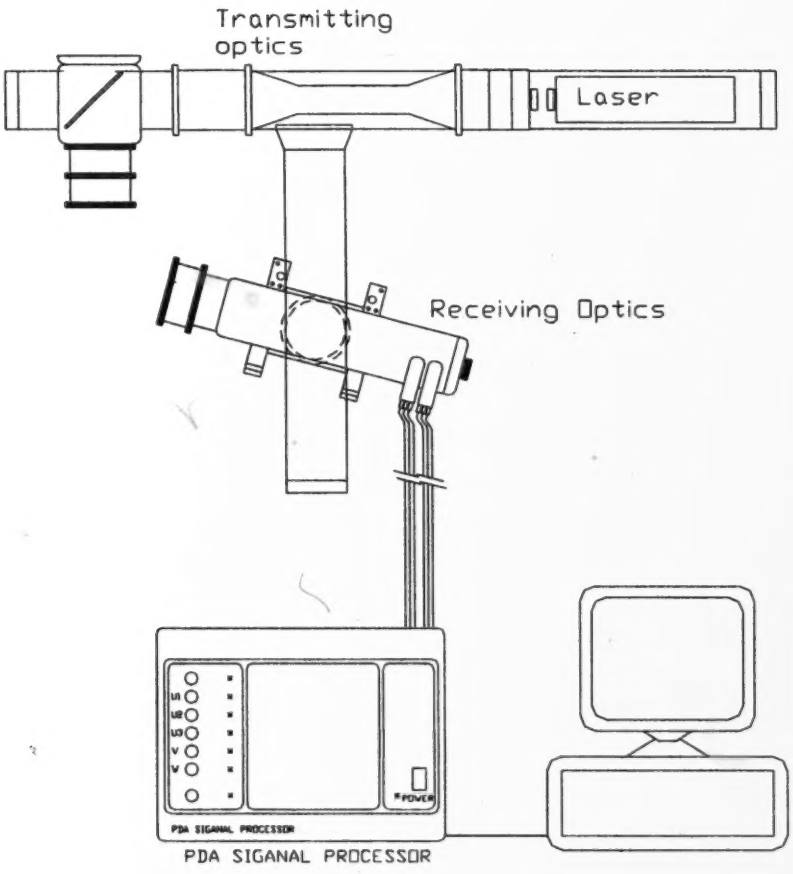

Figure 7-6 Schematic diagram of the Dantec PDA system

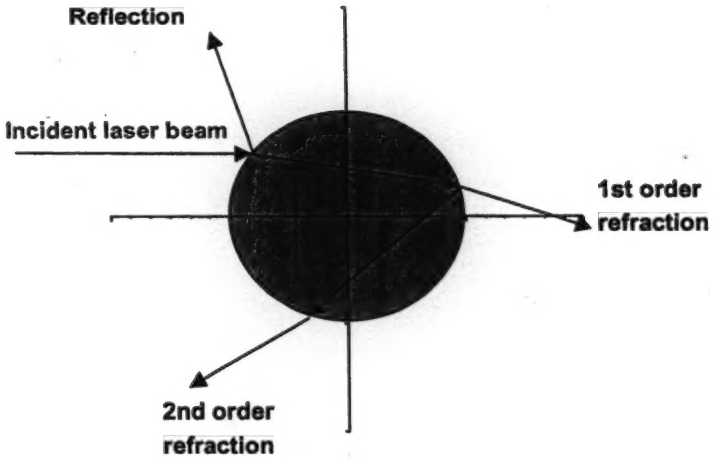

Figure 7-7 Schematic diagram of particle scattering modes (After Dantec Measurement Technology A/S)

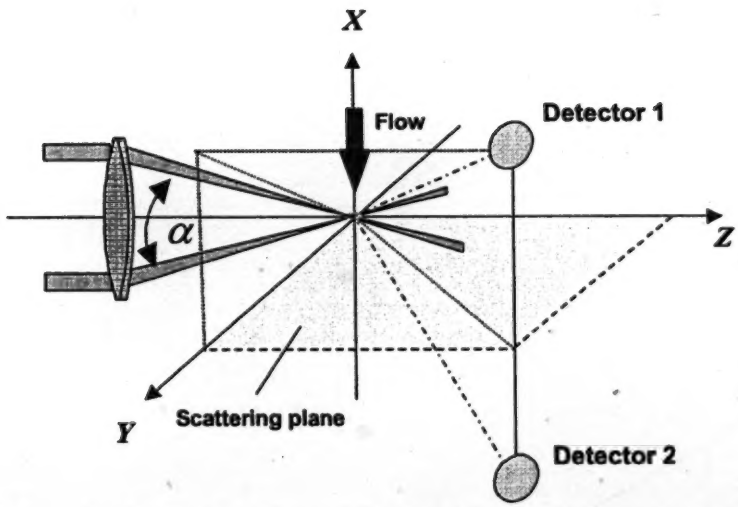

Figure 7-8 Schematic diagram of a one-component forward scattering PDA system (after Dantec Measurement Technology A/S)

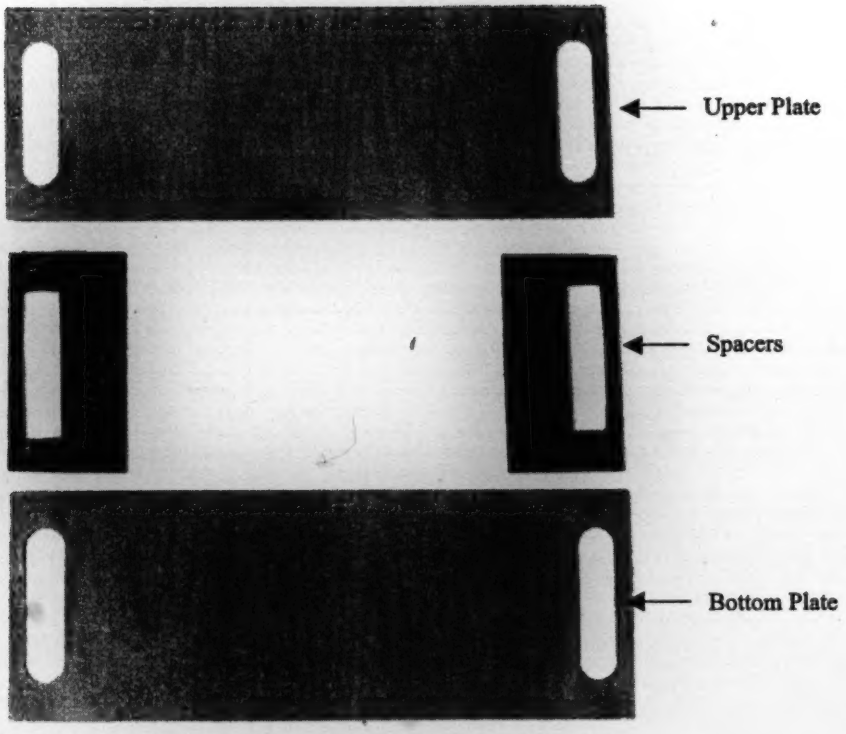

Figure 7-9 Deposition pattern for the rectangular crack of $H = 0.305$ mm, $L = 60$ mm, $\Delta P = 8$ Pa, and $d_p = 1.4$ μm (8 hours experimental time)

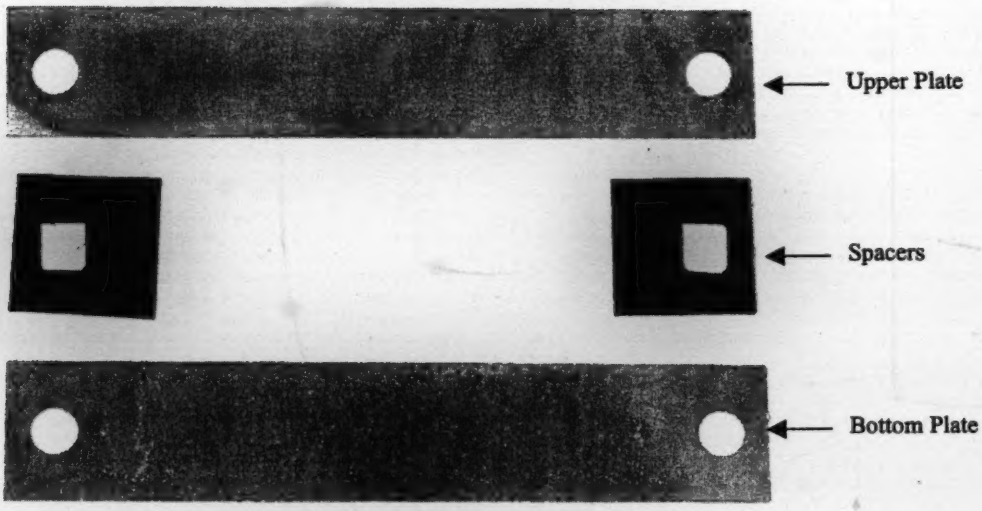

Figure 7-10 Deposition pattern for the rectangular crack of $H = 0.305$ mm, $L = 60$ mm, $\Delta P = 8$ Pa, and $d_p = 1.4$ μm (8 hours experimental time)

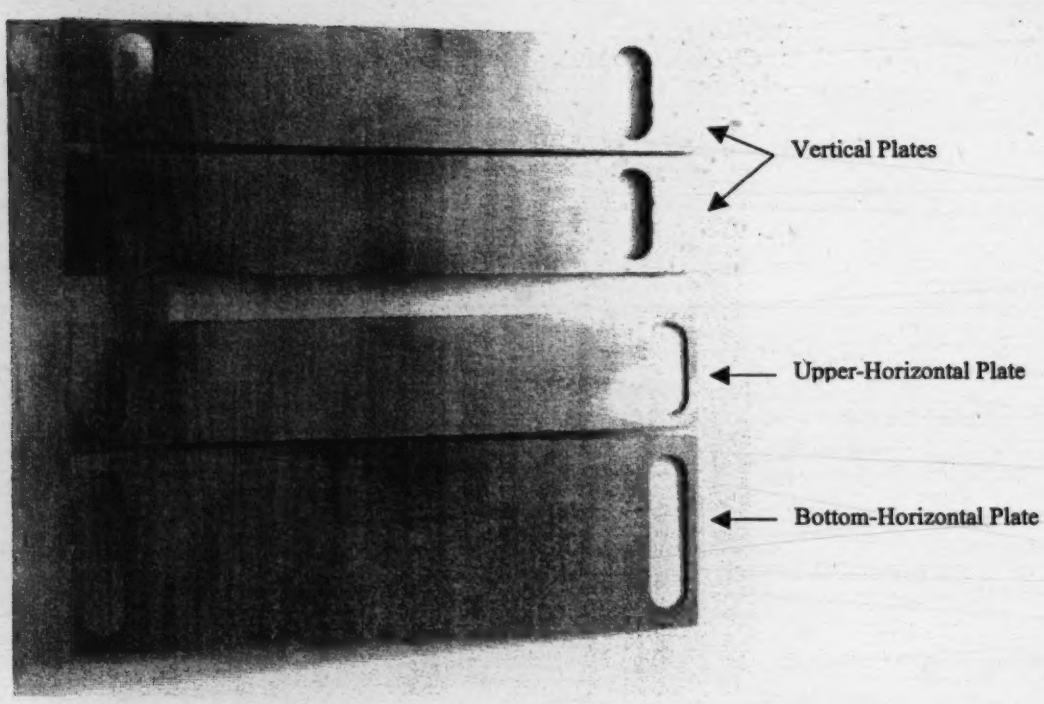

Figure 7-11 Deposition pattern for the L-shaped crack of $H = 0.305$ mm, $L = 60$ mm, $\Delta P = 8$ Pa, and $d_p = 1.4$ μm (8 hours experimental time)

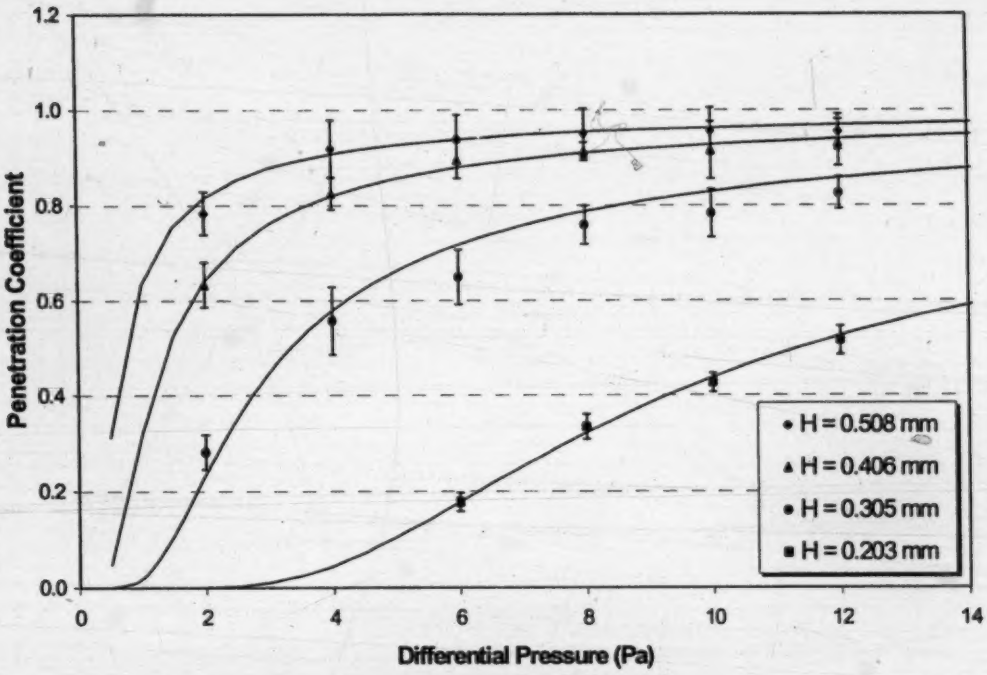

Figure 7-12 Particle penetration coefficient for the $L = 60$ mm rectangular crack, $d_p = 1.4$ μm

Note: Error bars represent standard deviations.

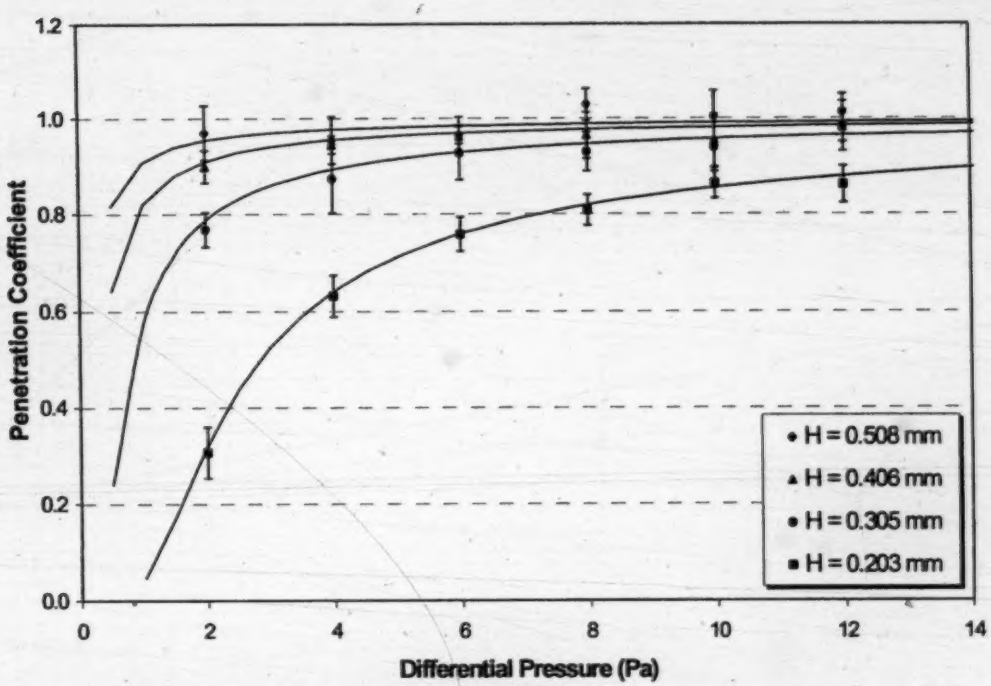

Figure 7-13 Particle penetration coefficient for the $L = 30$ mm rectangular crack, $d_p = 1.4$ μm

Note: Error bars represent standard deviations.

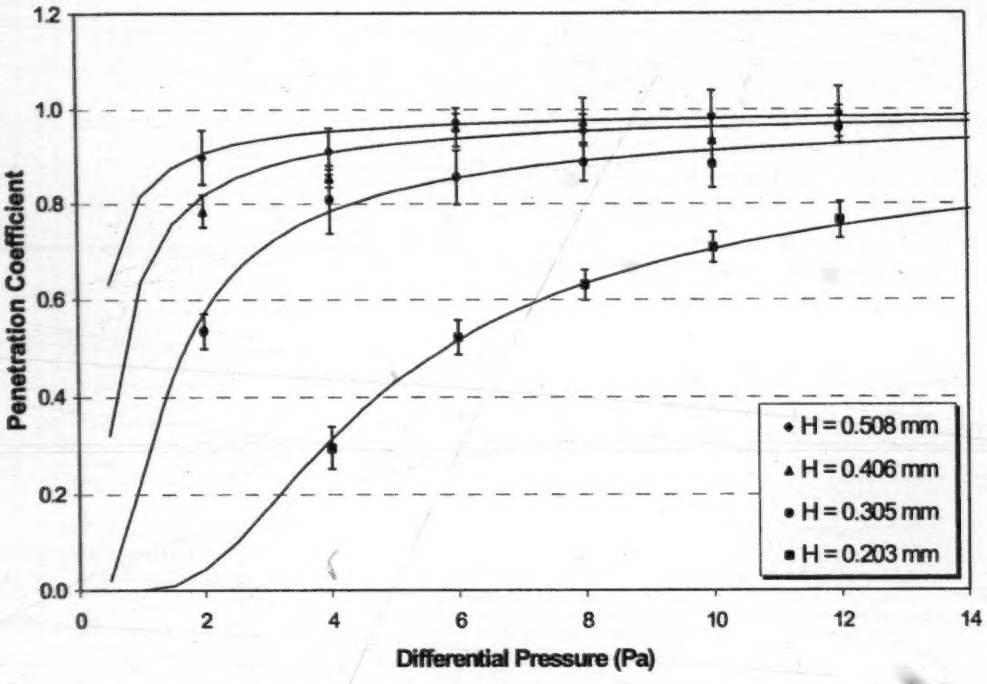

Figure 7-14 Particle penetration coefficient for the L = 60 mm L-shaped crack, d_p = 1.4 μm

Note: Error bars represent standard deviations.

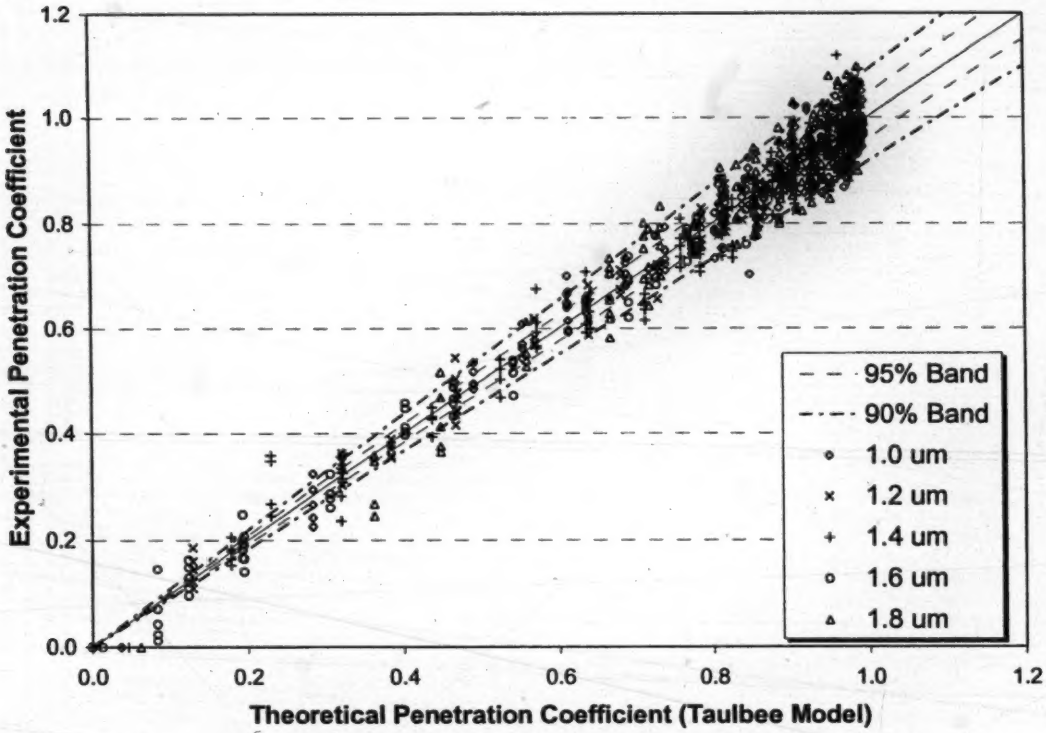

Figure 7-15 Comparisons between theoretical and experimental particle penetration coefficients for rectangular cracks

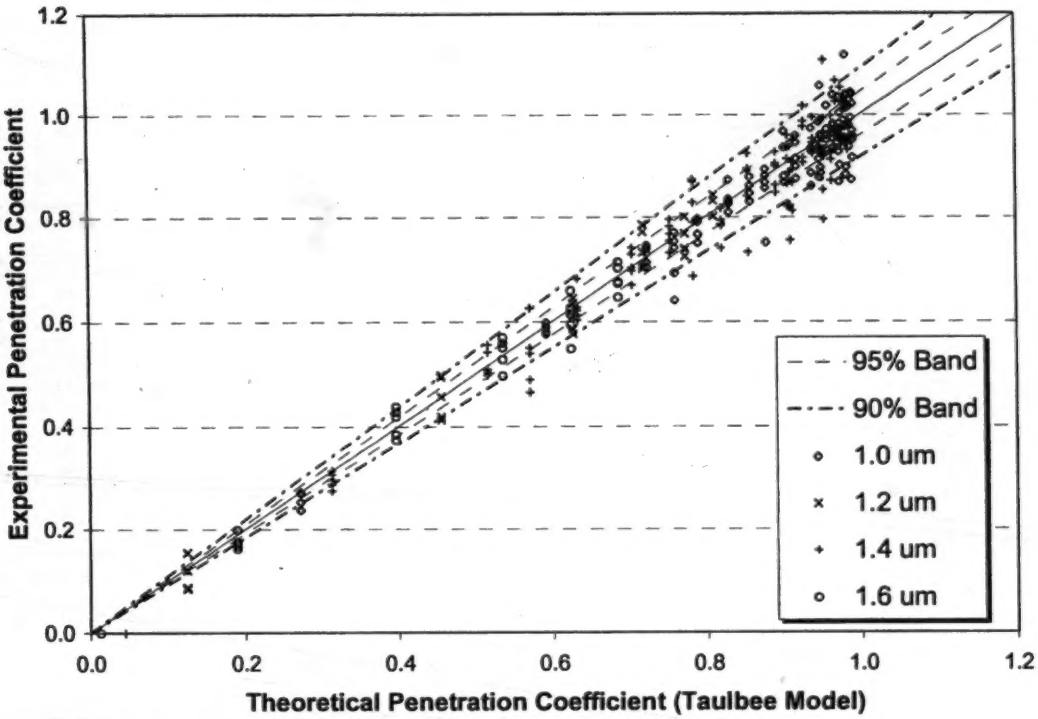

Figure 7-16 Comparisons between theoretical and experimental particle penetration coefficients for L-shaped cracks

7.5 REFERENCES

Clement, C. F. (1995). Aerosol Penetration through Capillaries and Leaks: Theory. *J. Aerosol Sci.* 26:369-385.

Gross, D., and Haberman, W. L. (1989). Fire Safety Science: Proceedings of the Second International Symposium. The Second International Symposium on Fire Safety Science, International Association for Fire Safety Science, Tokyo, Japan.

Liu, D. L., and Nazaroff, W. W. (1999). Modeling Particles Penetration Through Cracks in Building Envelopes, *Proceedings: 8th Int. Conference on Indoor Air Quality and Climate.* Edinburgh, Scotland, 4:1055-1059.

Liu, D. L., and Nazaroff, W. W. (2001). Particle Penetration Through Building Cracks: Effect of Materials, *20th Annual AAAR Conference.* October 15-19, 2001. Portland, OR, p264.

Mitchell, J. P., Edwards, R. T., and Ball, M. H. E. (1990). The Penetration of Aerosols Through Fine Capillaries. RAMTRANS. 1:101-116.

Mosley, R. E., Greenwell, D. J., Sparks, L. E., Guo, Z., Tucker, W. G., Fortmann, R., and Whitfield, C. (2001). Penetration of Ambient Fine Particles into Indoor Environment. *Aerosol Sci. Technol.* 34:127-136.

Williams, M. M. R. (1994) Particle Deposition and Plugging in Tubes and Cracks (With Special Reference to Fission Product Retention). *Progress in Nuclear Energy.* 28:1-60.

CHAPTER 8. GENERAL CONCLUSION AND RECOMMENDATION

8.1 GENERAL OVERVIEW

The investigation of outdoor-indoor particle penetration originated from the I/O ratio (Yocom, 1982) and IAQ modeling approaches (Thatcher and Layton, 1995; Koutrakis *et al.*, 1992). Both approaches are subject to confounding effects induced from indoor activities. In 1999, Liu and Nazaroff (1999) proposed an alternative approach to investigate particle penetration for horizontal cracks. This modeling approach estimated particle penetration coefficient from the ratio of particles that can penetrate through a crack. As a result, the confounding factors induced from indoor activities were avoided. This modeling approach combined infiltration models with particle deposition models to simulate a particle penetration coefficient. The model proposed by Liu and Nazaroff (1999) dealt with rectangular cracks only. However, because L-shaped and multiple bend cracks are commonly found in building envelops, it is necessary to develop models for these cracks.

Liu and Nazaroff (1999) investigated the role of inertial impaction for L-shaped cracks. It was found that inertial impaction was negligible because of the low infiltration velocity for typical residential conditions. This finding suggests that another modeling approach for L-shaped and multiple bend cracks may be possible. Because infiltration flow through the simulated horizontal cracks was found to be laminar for most residential conditions, a L-shaped crack can be simulated as the combination of a horizontal section and a vertical section. The overall particle penetration is thus equal to the product of individual penetration coefficients. If a model that deals with incline cracks can be developed, particle penetration through L-shaped cracks can be estimated. This study was

thus motivated to develop an inclined crack model for L-shaped and multiple bend cracks.

The major efforts of this study were directed to investigate the effects of crack geometry, particle size, and differential pressure on particle penetration through rectangular and L-shaped cracks. Because the modeling approach was composed of infiltration flow modeling and particle dynamic modeling, the first part of this study was to choose and validate an infiltration model (Gross and Haberman, 1982). Experimental investigation indicated that the chosen model agreed well with experimental results. Infiltration flow fields for long-narrow cracks can be assumed laminar for typical residential conditions. Using the model, this study derived a particle mass transport equation that considered both gravitational sedimentation and Brownian diffusion to establish a particle penetration model (Taulbee and Yu, 1975). A comparison with two other models (Licht, 1980; Fuchs, 1964) that considered gravitational sedimentation indicated that the Taulbee model could deal with both micron-sized and submicron-sized particle penetration. The model was later modified to deal with cracks of arbitrary incline angles. Using the latter model, particle penetration for both rectangular cracks and L-shaped cracks can be simulated.

The Taulbee model was validated with experimental results published by Mosley *et al.* (2001). The comparison indicated that experimental results agreed well with model predictions for both micron-sized and submicron-sized particles. However, the experimental design of Mosley *et al.* (2001) was subject to confounding induced from chamber mixing and particle deposition. To solve the problem, this study designed an outdoor-indoor chamber and used a non-intrusive particle dynamic analyzer to measure

particle penetration for individual cracks. It was found that gravitational sedimentation dominated particle deposition behavior for micron-sized particles. Both entrance cut-off and inertial impaction were not important particle deposition mechanisms for the conditions examined. The particle penetration model agreed well with experimental results. This experimental approach avoided the confounding factors induced from chamber mixing/deposition, as observed by Mosley *et al.* (2001).

For the particle penetration experiment, a condensation-type aerosol generator was constructed to generate monodisperse aerosols (Rapaport and Weinstock, 1955). The generator was suitable for the study because it had a high particle output concentration, excellent stability, and fast response to size adjustment. The liquid particles produced from the generator will not be not re-suspended upon deposition onto crack walls, which obeyed model assumptions. This study also used an atomization/evaporation method to produce standard PSL microspheres to calibrate/validate particle measurement instruments (Keady and Nelson, 1984). The known-size and perfect spherical characteristics were suitable to calibrate the particle dynamic analyzer and aerodynamic particle sizer. Validation/calibration results indicate that the aligned PDA system measured correct sizes of microsphere size standards. Data validation rate was nearly 100%.

8.2 CONCLUSION

Based on the particle penetration study, the followings major findings from both theoretical modeling and experimental investigations are reported:

Infiltration Modeling and Investigation

1. Infiltration flow rate is linearly dependent on differential pressure for the test cracks under typical residential conditions (1 to 10 Pa). Experimental results indicated that

the model agrees well with infiltration experiments. The infiltration flow rates for the test conditions ranged from ~0 to 1785.3 mL/min.

2. Entrance length analysis for the test cracks indicated that L_e/L were mostly less than 5% for typical differential pressures. The laminar flow assumption was validated for $H < 0.508$ mm and $L > 30$ mm cracks.

Condensation-Type Aerosol Generator

1. The generator constructed can produce monodisperse aerosols from 0.8 (using canola oil) to 3.1 μm (using di(2-ethylhexyl) sebacate; DEHS) in number mean diameter. This size range is suitable for respirable particle investigations.
2. The generator produced monodisperse aerosols with high output concentrations. It also had excellent stability and reproducibility. These characteristics are very suitable for particle penetration studies.
3. A preliminary investigation indicated that number concentration and size distribution of primary droplets have determinant effects on homogeneous/heterogeneous condensation and *NMD* of output aerosols. However, the aerodynamic particle sizer (APS) used in this study could not measure particles smaller than 0.5 μm. Additional investigation would be required to measure the whole size range of primary droplets.

Generation of Polystyrene Latex (PSL) Microspheres for Instrument Calibration

1. The dilution ratio estimated from the model proposed by Raabe (1968) might be too low for certain PSL stock suspensions, such that the atomizer blew bubbles inside. The burst bubbles produced residue particles and multiplet microspheres that interfere with instrument calibration. Further dilution with ultra-pure water solved this problem.

2. The known size and perfect spherical characteristics of PSL microspheres were suitable for instrument calibration. This study used 1.020 μm PSL microspheres to calibrate the PDA system. After calibration, the PDA's validation ratio and sphericity ratio were greater than 99%. The PDA also correctly measured the sizes of 2.504 μm microspheres. Experimental results indicated that the PDA system was well aligned after the calibration/validation procedures.
3. Experimental results indicated that sizes of residue particles could be estimated from the impurity concentration based on a mass conservation equation. Using the equation to calculate appropriate dilution ratios, the residue particle population could be separated from PSL size standards.

Particle Penetration Modeling (The Taulbee Model)

1. Comparison among the three particle penetration models indicated that the Taulbee model is universally applicable for both micro-sized particle and submicron-sized particles. This model is also advantageous in providing concentration contours to diagnose particle deposition mechanisms.
2. For micron-sized particles, gravitational sedimentation governs particle deposition behavior. All three models can be used to estimate particle penetration. However, it was found that the Licht model's predictions deviated from the other two. As for submicron-sized particles, Brownian diffusion is the major or significant deposition mechanism. Only the Taulbee model should be used to simulate particle penetration.
3. The Taulbee model was validated using experimental data published by Mosley *et al.* (2001). The validation work indicated that the Taulbee model agreed well with trends of experimental data for both submicron-sized and micro-sized (PM2.5) particles. This indicates that the 0.508 mm slits could not effectively retard submicron-sized particles

from penetrating indoors. As for micron-sized particles, both particle diameter and differential pressure determined particle penetration efficiency.

Particle Penetration Modeling (The Incline Crack Model)

1. Evaluation of an inclined crack model indicated that gravitational sedimentation is the dominant particle deposition mechanism for micron-sized particles. An inclined crack reduces effective terminal sedimentation velocity (v_{sy}) such that particle penetration efficiency increases monotonously with $|\theta|$. For the same crack geometries (L and H), modeling results indicated that horizontal crack ($\theta = 0°$) provides the best protection to prevent micron-sized particles from penetrating through cracks.
2. Brownian diffusion is the dominant particle deposition mechanism for submicron-sized particles. Because Brownian diffusion is a non-directional deposition mechanism, incline angle does not affect particle penetration efficiency.
3. Brownian diffusion is the dominant particle deposition mechanism for vertical cracks. For micron-sized particles, because Brownian diffusion is not a significant deposition mechanism, complete penetration is expected for vertical cracks. As for submicron-sized particle, particle penetration coefficient remains constant for all inclined angles.

Particle Penetration Experiment

1. Visual examination indicated that particles uniformly deposit on the bottom crack plates. Gravitational sedimentation is the major deposition mechanism for the test micron-sized particle. Both entrance cut-off and inertial impaction were not observed to occur in this investigation. However, for crack $H < 0.203$ mm, entrance cut off would need to be examined further.
2. The Taulbee model agrees well with experimental results. The measured particle penetration coefficients were mostly within ±0.05 of theoretical modeling results.

3. L-shaped cracks can be simulated as a combination of a horizontal and vertical section. The overall particle penetration coefficient equals to the product of penetration coefficients in these two sections.
4. Particle penetration coefficient is a function of crack geometry, particle size and differential pressure. For typical residential conditions and micron-sized particles, this study found 80% of particles can penetrate through $H > 0.305$ mm, and $L < 30$ mm cracks. As for $H > 0.406$ mm, and $L < 30$ mm cracks, complete penetration was observed.

8.3 RECOMMENDATION

This study provides a methodology to validate derived particle penetration models for typical residential conditions. Recommendation for future works include:

1. Limited by the sizing limit of the particle dynamic analyzer, this study did not investigate submicron-sized (< 1 μm) particle penetration. It is expected that Brownian diffusion is the major or significant deposition mechanism for these fine particles. The non-directional Brownian diffusion mechanism indicates that particles may deposit on both the upper and lower crack plates. Further investigation is required to validate this hypothesis and the particle penetration models.
2. The particle penetration models assume cracks are analogous to pairs of parallel plates. These models require crack length, width, and height to execute infiltration and particle penetration models. Among these geometric parameters, crack length and width can be obtained by measurement. However, no devices can satisfactorily measure crack height for real building components. This makes application of the present particle penetration models on real building components difficult. However,

actual crack heights can be estimated using an effective crack height parameter, which can be derived from the infiltration model, shown in equations 2-1 to 2-3. The infiltration model indicates that infiltration flow rate is a function of crack length, width, height, and differential pressure across a crack. Because crack length and width can be measured, if infiltration flow rate for a specific difference pressure is measurable, the effective crack height of a building component can be estimated. The ASTM Test Method E 1424 described a chamber test method that can be used to measure infiltration flow rate to estimate effective leakage area for specific building components (Kehrli, 1995). This provides a possibility to apply the present particle penetration models in building industry applications.

3. Building codes need to be revised in those areas that are subject to potential air pollution episodes. This study found complete penetration occurred for $H > 0.406$ mm, and $L < 30$ mm cracks. Because typical residential cracks are mostly wider than these dimensions (Hopkins and Hansford, 1974), buildings in these areas need to be built tighter so as to retard particles from penetrating indoors. In the case of an episode, if residents cannot be evacuated in time, they should be ordered to stay at homes or in emergency shelters.
4. Further investigation should be undertaken on building components that have cracks other than rectangular and L-shaped cracks. One of the examples is the widely-used brush-type door sweeps. For such building products, filter filtration models probably can be applied to simulate particle penetration. However, such products do not implant fibers uniformly throughout the crack. For such products, particles probably

can readily penetrate through the gap between bundles, while high deposition may be observed on the bundle fibers.

5. Penetration of reactive gaseous pollutant is another field of interest in outdoor-indoor penetration. Gaseous pollutants are readily transported indoors by infiltration air. However, they may react with crack surfaces in the infiltration channel such that < 100% pollutant penetration efficiency is expected. The whole process may be diffusion controlled or reaction controlled depending on the reactivity of pollutants, crack geometry, and crack materials. Further studies based on pollutant transport and reaction kinetics are required in this field of research.

8.4 REFERENCES

Fuchs, N. A. (1964). *The Mechanics of Aerosols*. Army Chemical Warfare Laboratories, Army Chemical Center, Maryland, U. S.

Gross, D., and Haberman, W. L. (1989). *Fire Safety Science: Proceedings of the Second Symposium*. The Second International Symposium on Fire Safety Science, International Association for Fire Safety Science, Tokyo, Japan.

Hopkins, L. P., and Hansford, B. (1974). Air Flow Through Cracks. *Build. Serv. Engr.* 42:123-131.

Keady, P. B., and Nelson, P. A. (1984). Monodisperse Particle Generators for Calibrating Aerosol Instrumentation. 1984 Proceedings, 30th Annual Technical Meeting - Institute of Environmental Sciences: Environmental Integration Technology Today for a Quality Tomorrow. Orlando, Fla. Inst. of Environmental Sciences. pp94-100.

Kehrli, D. W. (1995). A Description of the New ASTM Test Method E1242, Used for Measuring Fenestration Air Leakage at Different Temperatures and Pressures. *Airflow Performance of Building Envelopes, Components, and Systems*. Ed: Modera, M. P., and Persily, A. K. American Society for Testing and Materials. Philadelphia, PA. pp81-89.

Koutrakis, P., Briggs, S. L. K., and Leaderer, B. P. (1992). Source Apportionment of Indoor Aerosols in Suffolk and Onondaga Counties, New York. *Environ. Sci. Technol.* 26:521-527.

Licht, W. (1980). *Air Pollution Control Engineering*. Marcel Dekker, Inc., New York, N.Y.

Liu, D. L., and Nazaroff, W. W. (1999). Modeling Particles Penetration Through Cracks in Building Envelopes, *Proceedings: 8th Int. Conference on Indoor Air Quality and Climate.* Edinburgh, Scotland, 4:1055-1059.

Mosley, R. E., Greenwell, D. J., Sparks, L. E., Guo, Z., Tucker, W. G., Fortmann, R., and Whitfield, C. (2001). Penetration of Ambient Fine Particles into Indoor Environment. *Aerosol Sci. Technol.* 34:127-136.

Raabe, O. G. (1968). The dilution of Monodisperse Suspensions for Aerosolization. *Am. Ind. Hyg. Assoc. J.* September-October: pp439-443.

Rapaport, E. and Weinstock, S. G. (1955). A Generator for Homogeneous Aerosols. *Experimentia* **11,** 363-367.

Taulbee, D. B., and Yu, C. P. (1975). Simultaneously Diffusion and Sedimentation of Aerosols in Channel Flows. *J. Aerosol Sci.* 6:433-441.

Thatcher, T. L., and Layton, D. W. (1995). Deposition, Resuspension, and Penetration of Particles within a Residence. *Atmos. Environ.* 29:1487-1497.

Yocom, J. E. (1982). Indoor-Outdoor Air Quality Relationships: A Critical Review. *J. Air Pollut. Control Assoc.* 32:500-519.

Appendix A Summary of Particle Dynamic Parameters (Hinds, 1982)

(20°C, 1 atm, density = 1000 kg/m^3)

Particle Diameter (μm) / Parameter / Unit	Slip Correction Factor	Mobility	Relaxation Time	Terminal Settling Velocity	Diffusivity
	-	m/(N·sec)	second	m/sec	cm^2/sec
0.01	22.499	1.31E+13	6.85E-06	6.72E-08	5.29E-01
0.02	11.555	3.36E+12	1.41E-05	1.38E-07	1.36E-01
0.03	7.917	1.54E+12	2.17E-05	2.13E-07	6.21E-02
0.04	6.106	8.88E+11	2.98E-05	2.92E-07	3.59E-02
0.05	5.024	5.85E+11	3.83E-05	3.75E-07	2.36E-02
0.06	4.307	4.18E+11	4.72E-05	4.63E-07	1.69E-02
0.07	3.798	3.16E+11	5.67E-05	5.55E-07	1.28E-02
0.08	3.419	2.49E+11	6.66E-05	6.53E-07	1.01E-02
0.09	3.126	2.02E+11	7.71E-05	7.56E-07	8.17E-03
0.1	2.893	1.68E+11	8.81E-05	8.64E-07	6.81E-03
0.2	1.882	5.47E+10	0.000229	2.25E-06	2.21E-03
0.3	1.569	3.04E+10	0.000430	4.21E-06	1.23E-03
0.4	1.421	2.07E+10	0.000692	6.78E-06	8.35E-04
0.5	1.334	1.55E+10	0.001016	9.96E-06	6.28E-04
0.6	1.278	1.24E+10	0.001401	1.37E-05	5.01E-04
0.7	1.238	1.03E+10	0.001847	1.81E-05	4.16E-04
0.8	1.208	8.78E+09	0.002355	2.31E-05	3.55E-04
0.9	1.185	7.66E+09	0.002923	2.86E-05	3.10E-04
1	1.166	6.78E+09	0.003552	3.48E-05	2.74E-04
1.1	1.151	6.09E+09	0.004243	4.16E-05	2.46E-04
1.2	1.139	5.52E+09	0.004994	4.89E-05	2.23E-04
1.3	1.128	5.05E+09	0.005806	5.69E-05	2.04E-04
1.4	1.119	4.65E+09	0.006679	6.55E-05	1.88E-04
1.5	1.111	4.31E+09	0.007613	7.46E-05	1.74E-04
1.6	1.104	4.01E+09	0.008608	8.44E-05	1.62E-04
1.7	1.098	3.76E+09	0.009664	9.47E-05	1.52E-04
1.8	1.092	3.53E+09	0.010780	0.000106	1.43E-04
1.9	1.088	3.33E+09	0.011958	0.000117	1.35E-04
2	1.083	3.15E+09	0.013196	0.000129	1.27E-04
2.1	1.079	2.99E+09	0.014496	0.000142	1.21E-04
2.2	1.076	2.84E+09	0.015856	0.000155	1.15E-04
2.3	1.072	2.71E+09	0.017277	0.000169	1.10E-04
2.4	1.069	2.59E+09	0.018760	0.000184	1.05E-04
2.5	1.067	2.48E+09	0.020303	0.000199	1.00E-04
3	1.055	2.05E+09	0.028932	0.000284	8.27E-05
4	1.042	1.51E+09	0.050759	0.000497	6.12E-05
5	1.033	1.2E+09	0.078678	0.000771	4.86E-05
6	1.028	9.96E+08	0.112689	0.001104	4.03E-05
7	1.024	8.51E+08	0.152791	0.001497	3.44E-05
8	1.021	7.42E+08	0.198984	0.00195	3.00E-05
9	1.018	6.58E+08	0.251270	0.002462	2.66E-05
10	1.017	5.91E+08	0.309647	0.003035	2.39E-05
30	1.006	1.95E+08	2.756425	0.027013	7.88E-06
50	1.003	1.17E+08	7.[illegible]9851	0.074871	4.72E-06

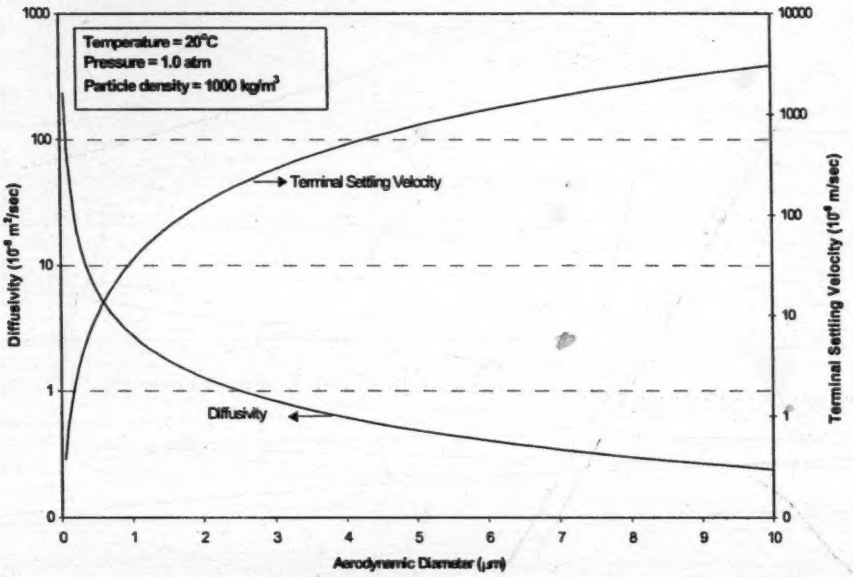

Figure A-1 Diffusivity and terminal settling velocity of airborne particles (20°C, 1 atm, density = 1000 kg/m^3)

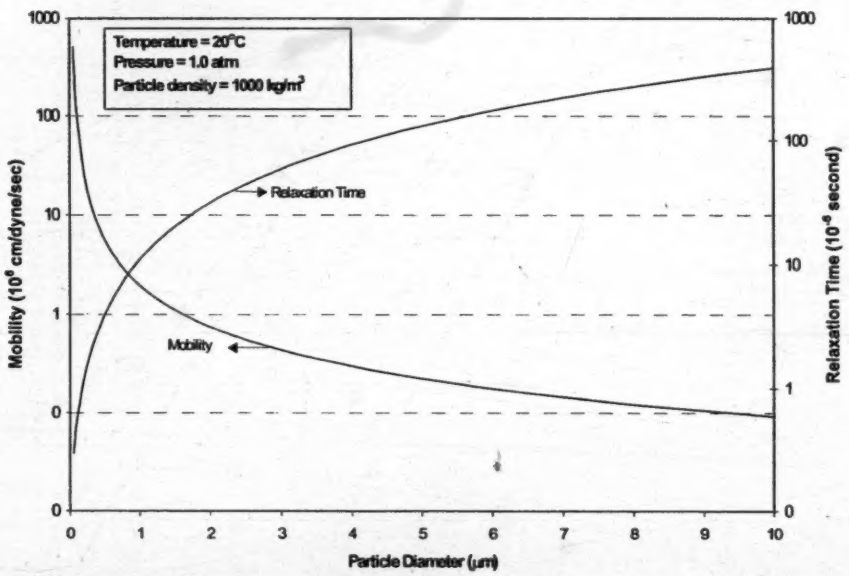

Figure A-2 Relaxation time and particle mobility of airborne particles (20°C, 1 atm, density = 1000 kg/m^3)

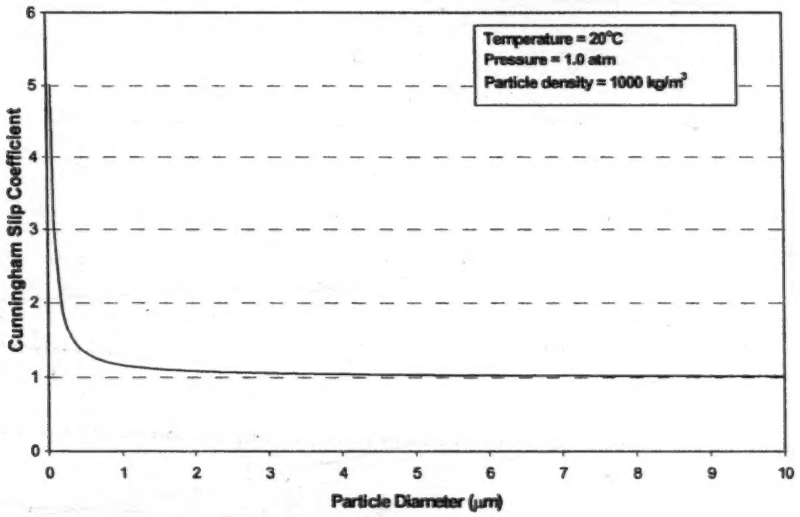

Figure A-3 Cunningham slip coefficient for airborne particles (20°C, 1 atm, density = 1000 kg/m^3)

Appendix B Derivation of the Dimensionless Air Infiltration Flow Field

For parallel-plate flow, Kay (1957) proposed six parameters and used dimensionless analysis to analyze infiltration flow. These parameters are $\Delta P, \rho_f, \mu, D_h, L,$ and u_m, which represent the differential pressure across a crack, the density and absolute viscosity of the fluid, the hydraulic diameter of the crack, the crack length, and the mean infiltration velocity, respectively. These parameters can be written in a flow function as shown in Eq. (B-1):

$$f(\Delta p, \rho_f, \mu, u_m, D_h, L) = 0 \tag{B-1}$$

Eq. (B-1) can be reduced to three dimensionless groups π_1, π_2, π_3. The three dimensionless groups represent three fundamental dimensions: length, mass and time. There are six variables and three fundamental dimensions (length, mass, and time) in the equation. According to the π theory, the infiltration flow function can be reduced to three dimensionless groups π_1, π_2, π_3. This paper selects ρ_f, u_m, and D_h as the primary quantities. π_1, π_2, π_3 were related to the remaining three parameters, $\Delta p, \mu$, and L.

Suppose π_1 represents the differential pressure through a crack, π_1 can be written as the combination of the three primary quantities, i.e. $\pi_1 = \dfrac{\Delta p}{\rho_f^k u_m^l D_h^m}$. Because π_1 is dimensionless, k, l, and m must be solved so that the dimensions of the parameter of pressure drop are cancelled. Dimensional analysis derives: $k = 1$, $l = 2$, and $m = 0$. Thus π_1 is shown in Eq. (B-2):

$$\pi_1 = \frac{\Delta p}{\rho_f u_m^2} \tag{B-2}$$

Suppose π_2 represents the parameter $\frac{\mu}{\rho_f^k u_m^l D_h^m}$, $k = 1$, $l = 1$, and $m = 1$ from dimensionless analysis. Eq. (B-3) indicates the π_2 parameter. It represents the Reynolds number, using hydraulic diameter as the characteristic length parameter.

$$\pi_2 = \frac{\mu}{\rho_f u_m D_h} \tag{B-3}$$

The parameter π_3 is derived with the same method. The result is shown in Eq. (B-4):

$$\pi_3 = L/D_h \tag{B-4}$$

The dimensionless infiltration flow equation is thus written as Eq. (B-5):

$$\frac{\Delta p}{\rho_f u_m^2} = \frac{L}{D_h} f(\mathrm{Re}) = 2C_z \frac{L}{D_h} \tag{B-5}$$

where C_z is skin coefficient. Eq. (B-5) can be further modified by choosing L/D_h as a geometric parameter of the crack so that it can be written as Eq. (B-6):

$$C_z = f(\mathrm{Re}, \frac{L}{D_h}) \tag{B-6}$$

Etheridge (1977) and Hopkins and Hansford (1974) used a linear regression method to formulate this function. They found the semi-empirical Eq. (B-7) could be correlated with their experimental data reasonably.

$$\frac{1}{C_z^2} = A\frac{L}{D_h R_e} + B \tag{B-7}$$

where A and B are empirical constants.

Appendix C Derivation of the Laminar Infiltration Flow Field

The velocity profile of a laminar crack flow can be derived from the Navier-Stokes equation and the continuity equation (Kay 1957; Etheridge 1977; Schlichting 1979). When laminar flow through a pair of parallel plates is considered, the fluid velocity components in y and z direction would be zero. As a result, the Navier-Stokes equation and the continuity equation can be written as:

$$\rho\left(\frac{\partial u}{\partial t}+u\frac{\partial u}{\partial x}\right)=-\frac{\partial p}{\partial x}+\mu\left(\frac{\partial^2 u}{\partial x^2}+\frac{\partial^2 u}{\partial y^2}+\frac{\partial^2 u}{\partial z^2}\right) \tag{C-1}$$

$$\frac{\partial u}{\partial x}=0 \tag{C-2}$$

Eq. (C-2) is the continuity equation. This equation implies that the fluid velocity u is independent of position x, i.e., $u = u(y,z,t)$. Because the parallel plates extend infinitely alone z-axis, u is also independent of z. If we assume steady state, u is a function of y only, and the Navier-Stokes Eq. (C-1) can be written as Eq. (C-3):

$$\frac{\partial p}{\partial x}=\mu\left(\frac{\partial^2 u}{\partial y^2}\right) \tag{C-3}$$

Because u is a function of y, if both sides of Eq. (C-3) are equivalent, Eq. (C-3) must be a constant. As a result, the left-hand-side, i.e. the pressure gradient in x direction, is assumed to be uniform throughout the crack. The gradient of differential pressure on the x axis is equal to the ratio of differential pressure to crack length, as defined in Eq. (C-4):

$$\frac{\partial p}{\partial x}=-\frac{\Delta p}{L} \tag{C-4}$$

If Eq. (C-4) is substituted into Eq. (C-3), the partial differential equation becomes an ordinary differential equation:

$$-\frac{\Delta p}{L} = \mu\left(\frac{d^2u}{dy^2}\right) \tag{C-5}$$

Because the laminar parabolic velocity profile is symmetric to the centerline of the crack, the first order derivative of u equals zero at the half-height position of the crack, i.e., $du/dy = 0$ at $y = H/2$. This is the boundary condition of Eq. (C-5). Integrating Eq. (C-5) with the corresponding boundary condition, the function of the velocity profile becomes a first order differential equation as shown in Eq. (C-6):

$$\frac{du}{dy} = \frac{\Delta p}{\mu L}\left(\frac{H}{2} - y\right) \tag{C-6}$$

According to the boundary layer theory, the fluid velocity at crack walls is zero. This comprise the boundary conditions for Eq. (C-6); i.e. $u(0) = 0$ and $u(H) = 0$. Integrating Eq. (C-6) with the boundary condition gives the laminar velocity profile for a parallel plate flow:

$$u = \frac{1}{2\mu}\frac{\Delta p}{L}\left(Hy - y^2\right) \tag{C-7}$$

The corresponding average infiltration velocity is defined by dividing the infiltration flow rate q over the cross sectional area of the crack.

$$u_m = \frac{q}{Area} = \frac{1}{H}\int_0^H u(y)dy \tag{C-8}$$

When Eq. (C-7) is substituted into Eq. (C-8), this equation can be integrated over the crack height to solve for the average infiltration velocity u_m. The average infiltration velocity is thus shown as Eq. (C-9):

$$u_m = \frac{1}{12}\frac{\Delta p \cdot H^2}{\mu L} \tag{C-9}$$

The function of the infiltration velocity profile can be written with respect to u_m by substituting Eq. (C-9) into Eq. (C-7):

$$u = 6u_m\left(\frac{y}{H} - \left(\frac{y}{H}\right)^2\right) \tag{C-10}$$

Appendix D Derivation of the Licht Particle Penetration Model

Particle trajectory analysis is used to simulate particle penetration behavior when considering gravitational sedimentation as the only particle deposition mechanism. When the flow field inside a pair of parallel plates is known, the trajectory of a particle can be calculated using Newton's law of motion, which states that a trajectory function is the derivation of a velocity function. When a particle is released at crack entrance, it is subject to the influences of fluid flow and gravitational force. In a laminar flow, the former affects the horizontal behavior of the particle, while the latter determines its vertical motion. Thus, a particle accelerates or decelerates because of drag and reaches an equilibrium state. A "relaxation time" parameter is defined as the time required for the velocity of a particle to be reduced by drag to 36.8% (1/e) of its initial velocity (Licht, 1980). This parameter is a property of a particle. For a small particle, the relaxation time is very short, e.g. the relaxation time for particles 0.1 to 3.0 μm in aerodynamic diameter was found to be in the order of 10^{-7} to 10^{-5} second (Hinds, 1982). As a result, the horizontal velocity component of a small particle is assumed to be the velocity of fluid flow, while the vertical component is equal to its terminal settling velocity. According to Newton's law of motion, the trajectory of a particle can be integrated from its velocity functions. If the trajectory of a particle reaches the crack walls before exiting a crack, it is assumed removed.

Figure D-1 illustrates particle trajectories in plug flow and laminar flow fields (after Licht, 1980). When the fluid flow field is a plug flow, a particle is subjected to a constant fluid velocity and a constant terminal settling velocity along its path. Thus, the velocity vector of the particle is always constant. As a result, the particle trajectory is a

straight line, as shown by the dashed line in Figure D-1. When the flow field is laminar, the velocity profiles are parabolic and symmetric to crack centerline. On its settling path, the particle is constantly subjected to a different fluid velocity. Particle trajectory is a curve. Licht (1980) and Fuchs (1964) used different trajectory analysis to solve the trajectory curve to estimate particle penetration through pairs of parallel plates.

Licht (1980) derived the trajectory of a particle in a laminar flow field based on Newton's law of motion. If a particle reaches crack walls before it exits a crack, the particle is assumed removed. Several assumptions were made to develop this model (Licht, 1980).

1. particles are homogeneously and uniformly distributed at the crack entrance;
2. buoyancy force is neglected since the density of air is much less than that of particles;
3. particles instantly adjust their velocity to fluid velocity as described previously; and
4. particles accelerate rapidly to their terminal settling velocity, as is defined in Eq. (D-1) according to Stoke's law:

$$v_s = \frac{gC_u}{18}\frac{(\rho_p - \rho_f)}{\mu}d_p^2 \qquad \text{(D-1)}$$

where g is gravitational acceleration, C_u is the Cunningham slip correction coefficient, and d_p is the aerodynamic diameter of a particle.

According to Newton's law of motion, the velocity function of a particle is equal to the derivative of its trajectory. The derivatives of $x(t)$ and $y(t)$ are the velocity functions of the particle, $v_x(t)$ and $v_y(t)$ in horizontal and vertical directions respectively. Because particles adjust their velocity to fluid velocity instantly, v_x is equal to the laminar fluid velocity function (u). Similarly, v_y is equal to the particle's terminal settling velocity (v_s):

$$\frac{dx}{dt} = v_x = u \tag{D-2}$$

$$\frac{dy}{dt} = v_y = v_s \tag{D-3}$$

where $x(t)$ and $y(t)$ are the horizontal and vertical trajectory functions of the particle. Substituting the laminar fluid flow function, u and dividing Eq. (D-2) by Eq. (D-3), the independent variable, time t, can be eliminated. Particle trajectory function becomes a function of x and y, as shown in Eq. (D-4). Since u_m, v_s, and H are known parameters, positions of the particle in x direction can be calculated as a function of position y:

$$\left(\frac{dx}{dy}\right) = -\frac{6u_m}{v_s}\left[\frac{y}{H} - \left(\frac{y}{H}\right)^2\right] \tag{D-4}$$

Eq. (D-4) can be transformed into a dimensionless equation with respect to u_m and H. The position functions x and y are divided by H to derive the dimensionless position functions: $x' = x/H$ and $y' = y/H$, while the terminal settling velocity v_s is divided by u_m to derive the dimensionless terminal settling velocity: $v'_s = v_s/u_m$. When these three dimensionless parameters are substituted into Eq. (D-4), a dimensionless particle trajectory function can be derived:

$$\frac{dx'}{dy'} = -\frac{6}{v'_s}\left(y' - y'^2\right) \tag{D-5}$$

Eq. (D-5) can be used to determine whether a particle deposits inside a crack or not. Particle penetration coefficient is simulated based on the ratio of particles that penetrate through the crack. However, it is impractical to repeat this procedure for one particle after another over a particle population to derive a statistically meaningful particle penetration coefficient. As a result, the concept of "critical particle trajectory" was introduced to use crack height to calculate the particle penetration coefficient (Licht,

1980). A critical particle trajectory is defined as the path of a particle which enters a crack at the height of ε and exactly deposits at the end of a crack. ε is defined as the critical entrance height. Because particles are assumed uniformly distributed at crack entrance, those entering the crack below ε will deposit inside the crack. The ratio ε/H is equal to the portion of particles that deposit inside the crack. ε/H is defined as a dimensionless critical entrance length ε'. As a result, the particle penetration coefficient $P_p = 1-\varepsilon'$.

Integrating Eq. (D-5) from (x', y') = (0, ε') to (x', y') = (L/H, 0) yields the trajectory of a particle that enters a crack at the height of ε and exactly deposits at the exit of the crack. The integration result is shown in Eq. (D-6). This equation can be solved by trial and error to derive ε'. The corresponding particle penetration coefficient P will be equal to $1-\varepsilon'$.

$$3\varepsilon'^2 - 2\varepsilon'^3 = \frac{L}{H}\frac{v_s}{u_m} \qquad \text{(D-6)}$$

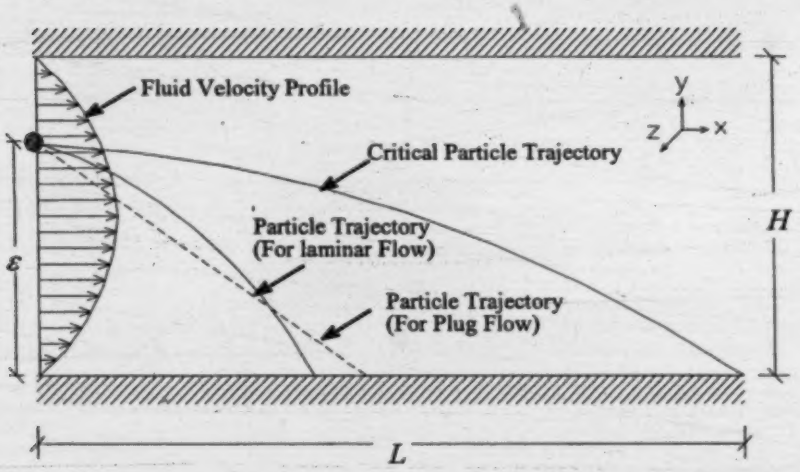

Figure D-1 Schematic Particle Trajectory in Plug Flow and Laminar Flow Fields

Appendix E Derivation of the Fuchs Particle Penetration Model

Fuchs (1964) applied the concept of flow function of laminar flow to derive a particle penetration model. A flow function is defined as the fluid flow rate per unit crack width from the bottom of a crack to a given height y. Using a flow function to calculate particle penetration coefficient is similar to the concept of using critical entrance height in the Licht model. Since particles are assumed to distribute uniformly at the entrance of a crack, if the critical flow function at the crack entrance can be calculated, the particle penetration coefficient can be derived.

The velocity field of a laminar flow defined by a flow function $\psi(y)$ was given by Fuchs (1964) and Wang (1975) as shown in Eq. (E-1) and (E-2):

$$u_x = \frac{\partial \psi}{\partial y} \tag{E-1}$$

$$u_y = -\frac{\partial \psi}{\partial y} \tag{E-2}$$

where u_x and u_y are the horizontal and vertical velocity functions of a fluid flow. According to Newton's law of motion, particle trajectory functions can be written as Eq. (E-3) and (E-4):

$$\frac{dx}{dt} = v_x = u_x \tag{E-3}$$

$$\frac{dy}{dt} = v_y = u_y - v_s \tag{E-4}$$

where v_x and v_y are the horizontal and vertical velocity functions of a particle and v_s is the terminal settling velocity of the particle. Similar to the derivation of the Licht model, fluid velocity functions are substituted into Eq. (E-3) and (E-4). Then Eq. (E-3) is divided by Eq. (E-4) to eliminate the independent variable, time t. The resulting particle trajectory function is shown in Eq. (E-5):

$$-\frac{dx}{\partial\psi/\partial y}=\frac{dy}{\partial\psi/\partial x+v_s} \tag{E-5}$$

Rearranging Eq. (E-5), it can be written as Eq. (E-6):

$$-v_s dx=\frac{\partial\psi}{\partial x}dx+\frac{\partial\psi}{\partial y}dy=d\psi \tag{E-6}$$

Integrating Eq. (E-6) with respect to ψ, from the crack entrance (x, ψ) = (0, ψ_0) to the crack exit (x, ψ) = (L, ψ_L), leads to a trajectory function, as shown in Eq. (E-7):

$$v_s L=\psi_0-\psi_L \tag{E-7}$$

where ψ_0 and ψ_L are the flow functions at the entrance and exit of a crack. The critical trajectory notation can be derived from Eq. (E-7) when ψ_L = 0. This physical condition refers to a critical trajectory at the exit of the crack above which particles are swept out of the crack. When $\psi_L = 0$ is substituted into Eq. (E-7), the corresponding flow function at the crack entrance is $\psi_0 = v_s L$, which represents the critical trajectory at the entrance of the crack. Because particles are assumed to distribute uniformly at the crack entrance, the ratio of the flow rate above the critical trajectory to the total infiltration flow rate is equal to the particle penetration coefficient. The total infiltration flow rate per unit crack width at the entrance of the crack is equal to the multiplication of the crack height and average infiltration velocity, i.e. $H \cdot u_m$. Thus, the particle penetration coefficient is derived as shown in Eq. (E-8):

$$P_p=1-\frac{L}{H}\frac{v_s}{u_m} \tag{E-8}$$

Walton (1954) and Pich (1972) used the concepts of flow tube and limiting trajectory analysis to develop particle penetration models considering particle deposition caused by gravitational sedimentation. Both of these authors derived the same results as in the Fuchs model, i.e. Eq. (E-8).

Appendix F The TK-Solver® Program Codes for the Taulbee Model (Dimensionless Model)

This study used the TK-Solver® software to solve the algebraic equation set of the Taulbee model. The TK-Solver® software used the Newton's method of tangent to find a converge answer to the equation set. This program code is comprised of two major worksheets: the variable sheet and the rule worksheet. The variable worksheet is used to declare the name and status of variables, while the rule sheet contains the equations that link these variables. For the Taulbee model, there are 200 equations for 200 unknown variables. The answer to a converged equation set is the concentration matrix C1 to C200. The concentration matrix is loaded into the Excel® software to analyze concentration contours and particle penetration coefficient. The following summarizes the layout of these two worksheets.

The Variable Worksheet

Nomenclature:

1. "St" column declares the status of the variables.
2. "I" declares the variable as an input variable, the user must give a value to the model.
3. "O" declares the variable as an Output variable, the software will give an answer if the model converges. If the model does not converge, a "*" will mark in the "St" column to notify the user.
4. "Gu" declares the variable as a Guess variable, the user must give an initial guess value to the model. The software will give an answer if the model converges. If the model does not converge, a "*" will mark in the "St" column to notify the user. In this study, initial guess is set to 1, i.e. the concentration inside the crack is the same as crack entrance.
5. C1 to C200 are the concentration matrix, which equals to the M x N = 20 X 10 concentration matrix defined in Chapter 3.

6. *xxx*: User need to give a value
7. *yyy*: The software will give an answer after model calculation.
8. AC1 to AC20 are the average concentration (flow weighted) at the levels M = 1 to 20, respectively. They are defined in the Rule sheet. AC20 is the average concentration at crack exit. It is equal to the particle penetration coefficient.

St	Input	Name	Output	Unit	Comment
I	*xxx*	Sigy			Sigma y (σ_y)
I	*xxx*	X			*X*
O		h	*yyy*		Dimensionless Grid width (Defined in Rule sheet)
O		k	*yyy*		Dimensionless Grid height (Defined in Rule sheet)
I	20	M			x grid number (M=20 in this modeling)
I	10	N			y grid number (N = 10 in this modeling)
O		V1	*yyy*		Fluid velocity of level N = 1 and 10 (Defined in Rule sheet)
O		V2	*yyy*		Fluid velocity of level N = 2 and 9 (Defined in Rule sheet)
O		V3	*yyy*		Fluid velocity of level N = 3 and 8 (Defined in Rule sheet)
O		V4	*yyy*		Fluid velocity of level N = 4 and 7 (Defined in Rule sheet)
O		V5	*yyy*		Fluid velocity of level N= 5 and 6 (Defined in Rule sheet)
O		S1	*yyy*		Model coefficient (Defined in Rule sheet)
O		K	*yyy*		Model coefficient (Defined in Rule sheet)
O		S2	*yyy*		Model coefficient (Defined in Rule sheet)
Gu	1	C1			Concentration of grid #1 (Level N =1)
Gu	1	C2			Concentration of grid #2 (Level N =1)
Gu	1	C3			Concentration of grid #3 (Level N =1)
Gu	1	C4			Concentration of grid #4 (Level N =1)
Gu	1	C5			Concentration of grid #5 (Level N =1)
.....					
.....					
.....					
Gu	1	C20			Concentration of grid #20 (Level N =1)
Gu	1	C21			Concentration of grid #21 (Level N =2)
Gu	1	C22			Concentration of grid #22 (Level N =2)
Gu	1	C23			Concentration of grid #23 (Level N =2)
.....					
.....					
.....					
Gu	1	C40			Concentration of grid #40 (Level N =2)
Gu	1	C41			Concentration of grid #41 (Level N =3)
Gu	1	C42			Concentration of grid #42 (Level N =3)
Gu	1	C43			Concentration of grid #43 (Level N =3)
.....					
.....					
.....					
Gu	1	C160			Concentration of grid #160 (Level N =8)
Gu	1	C161			Concentration of grid #161 (Level N =9)
Gu	1	C162			Concentration of grid #162 (Level N =9)
Gu	1	C163			Concentration of grid #163 (Level N =9)
.....					
.....					

St	Input	Name	Output	Unit	Comment
Gu	1	C180			Concentration of grid #180 (Level N =9)
Gu	1	C181			Concentration of grid #181 (Level N =10)
Gu	1	C182			Concentration of grid #182 (Level N =10)
Gu	1	C183			Concentration of grid #183 (Level N =10)
.....					
.....					
.....					
Gu	1	C200			Concentration of grid #200 (Level N =10)
O		AC1	*yyy*		Ave. conc. at Level M = 1 (Defined in Rule sheet)
O		AC2	*yyy*		Ave. conc. at Level M = 2 (Defined in Rule sheet)
O		AC3	*yyy*		Ave. conc. at Level M = 3 (Defined in Rule sheet)
O		AC4	*yyy*		Ave. conc. at Level M = 4 (Defined in Rule sheet)
O		AC5	*yyy*		Ave. conc. at Level M = 5 (Defined in Rule sheet)
O		AC6	*yyy*		Ave. conc. at Level M = 6 (Defined in Rule sheet)
O		AC7	*yyy*		Ave. conc. at Level M = 7 (Defined in Rule sheet)
O		AC8	*yyy*		Ave. conc. at Level M = 8 (Defined in Rule sheet)
O		AC9	*yyy*		Ave. conc. at Level M = 9 (Defined in Rule sheet)
O		AC10	*yyy*		Ave. conc. at Level M = 10 (Defined in Rule sheet)
O		AC11	*yyy*		Ave. conc. at Level M = 11 (Defined in Rule sheet)
O		AC12	*yyy*		Ave. conc. at Level M = 12 (Defined in Rule sheet)
O		AC13	*yyy*		Ave. conc. at Level M = 13 (Defined in Rule sheet)
O		AC14	*yyy*		Ave. conc. at Level M = 14 (Defined in Rule sheet)
O		AC15	*yyy*		Ave. conc. at Level M = 15 (Defined in Rule sheet)
O		AC16	*yyy*		Ave. conc. at Level M = 16 (Defined in Rule sheet)
O		AC17	*yyy*		Ave. conc. at Level M = 17 (Defined in Rule sheet)
O		AC18	*yyy*		Ave. conc. at Level M = 18 (Defined in Rule sheet)
O		AC19	*yyy*		Ave. conc. at Level M = 19 (Defined in Rule sheet)
O		AC20	*yyy*		Ave. conc. at Level M = 20 (Defined in Rule sheet)

The Rule Worksheet

Nomenclature

1. "Rules" are the equations linking the variables declared in the Variable sheet. The description after the ";" mark is the comments to the rule, which does not affect model execution. In the model, the comment "POINT XX" means the algebraic equation at the grid XX (XX = 1 to 200).
2. "St" column declares the status of the rule. After execution, if the model does not converge to a solution, there will be "*" marks in the "St" column to notify the user. If converged solution are derived, the "*" mark will disappear.

St	Rule
*	h=X/M
*	k=2/(N+1)
*	V1=1.5*(1-(9/11)^2)/h
*	V2=1.5*(1-(7/11)^2)/h
*	V3=1.5*(1-(5/11)^2)/h
*	V4=1.5*(1-(3/11)^2)/h
*	V5=1.5*(1-(1/11)^2)/h
*	S1=-1/k^2
*	S2=-Sigy/k-1/k^2
*	K=2/k^2+Sigy/k
*	(V1+K)*C1+S1*C21=V1 ;POINT 1
*	-V1*C1+(V1+K)*C2+S1*C22=0 ;POINT 2
*	-V1*C2+(V1+K)*C3+S1*C23=0 ;POINT 3
*	-V1*C3+(V1+K)*C4+S1*C24=0 ;POINT 4
*	-V1*C4+(V1+K)*C5+S1*C25=0 ;POINT 5
*	-V1*C5+(V1+K)*C6+S1*C26=0 ;POINT 6
*	-V1*C6+(V1+K)*C7+S1*C27=0 ;POINT 7
*	-V1*C7+(V1+K)*C8+S1*C28=0 ;POINT 8
*	-V1*C8+(V1+K)*C9+S1*C29=0 ;POINT 9
*	-V1*C9+(V1+K)*C10+S1*C30=0 ;POINT 10
*	-V1*C10+(V1+K)*C11+S1*C31=0 ;POINT 11
*	-V1*C11+(V1+K)*C12+S1*C32=0 ;POINT 12
*	-V1*C12+(V1+K)*C13+S1*C33=0 ;POINT 13
*	-V1*C13+(V1+K)*C14+S1*C34=0 ;POINT 14
*	-V1*C14+(V1+K)*C15+S1*C35=0 ;POINT 15
*	-V1*C15+(V1+K)*C16+S1*C36=0 ;POINT 16
*	-V1*C16+(V1+K)*C17+S1*C37=0 ;POINT 17
*	-V1*C17+(V1+K)*C18+S1*C38=0 ;POINT 18
*	-V1*C18+(V1+K)*C19+S1*C39=0 ;POINT 19
*	-V1*C19+(V1+K)*C20+S1*C40=0 ;POINT 20
*	S2*C1+(V2+K)*C21+S1*C41=V2 ;POINT 21
*	S2*C2-V2*C21+(V2+K)*C22+S1*C42=0 ;POINT 22
*	S2*C3-V2*C22+(V2+K)*C23+S1*C43=0 ;POINT 23
*	S2*C4-V2*C23+(V2+K)*C24+S1*C44=0 ;POINT 24
*	S2*C5-V2*C24+(V2+K)*C25+S1*C45=0 ;POINT 25
*	S2*C6-V2*C25+(V2+K)*C26+S1*C46=0 ;POINT 26
*	S2*C7-V2*C26+(V2+K)*C27+S1*C47=0 ;POINT 27
*	S2*C8-V2*C27+(V2+K)*C28+S1*C48=0 ;POINT 28
*	S2*C9-V2*C28+(V2+K)*C29+S1*C49=0 ;POINT 29
*	S2*C10-V2*C29+(V2+K)*C30+S1*C50=0 ;POINT 30
*	S2*C11-V2*C30+(V2+K)*C31+S1*C51=0 ;POINT 31
*	S2*C12-V2*C31+(V2+K)*C32+S1*C52=0 ;POINT 32
*	S2*C13-V2*C32+(V2+K)*C33+S1*C53=0 ;POINT 33
*	S2*C14-V2*C33+(V2+K)*C34+S1*C54=0 ;POINT 34
*	S2*C15-V2*C34+(V2+K)*C35+S1*C55=0 ;POINT 35
*	S2*C16-V2*C35+(V2+K)*C36+S1*C56=0 ;POINT 36
*	S2*C17-V2*C36+(V2+K)*C37+S1*C57=0 ;POINT 37
*	S2*C18-V2*C37+(V2+K)*C38+S1*C58=0 ;POINT 38
*	S2*C19-V2*C38+(V2+K)*C39+S1*C59=0 ;POINT 39
*	S2*C20-V2*C39+(V2+K)*C40+S1*C60=0 ;POINT 40
*	S2*C21+(V3+K)*C41+S1*C61=V3 ;POINT 41
*	S2*C22-V3*C41+(V3+K)*C42+S1*C62=0 ;POINT 42
*	S2*C23-V3*C42+(V3+K)*C43+S1*C63=0 ;POINT 43
*	S2*C24-V3*C43+(V3+K)*C44+S1*C64=0 ;POINT 44
*	S2*C25-V3*C44+(V3+K)*C45+S1*C65=0 ;POINT 45

St	Rule
*	S2*C26-V3*C45+(V3+K)*C46+S1*C66=0 ;POINT 46
*	S2*C27-V3*C46+(V3+K)*C47+S1*C67=0 ;POINT 47
*	S2*C28-V3*C47+(V3+K)*C48+S1*C68=0 ;POINT 48
*	S2*C29-V3*C48+(V3+K)*C49+S1*C69=0 ;POINT 49
*	S2*C30-V3*C49+(V3+K)*C50+S1*C70=0 ;POINT 50
*	S2*C31-V3*C50+(V3+K)*C51+S1*C71=0 ;POINT 51
*	S2*C32-V3*C51+(V3+K)*C52+S1*C72=0 ;POINT 52
*	S2*C33-V3*C52+(V3+K)*C53+S1*C73=0 ;POINT 53
*	S2*C34-V3*C53+(V3+K)*C54+S1*C74=0 ;POINT 54
*	S2*C35-V3*C54+(V3+K)*C55+S1*C75=0 ;POINT 55
*	S2*C36-V3*C55+(V3+K)*C56+S1*C76=0 ;POINT 56
*	S2*C37-V3*C56+(V3+K)*C57+S1*C77=0 ;POINT 57
*	S2*C38-V3*C57+(V3+K)*C58+S1*C78=0 ;POINT 58
*	S2*C39-V3*C58+(V3+K)*C59+S1*C79=0 ;POINT 59
*	S2*C40-V3*C59+(V3+K)*C60+S1*C80=0 ;POINT 60
*	S2*C41+(V4+K)*C61+S1*C81=V4 ;POINT 61
*	S2*C42-V4*C61+(V4+K)*C62+S1*C82=0 ;POINT 62
*	S2*C43-V4*C62+(V4+K)*C63+S1*C83=0 ;POINT 63
*	S2*C44-V4*C63+(V4+K)*C64+S1*C84=0 ;POINT 64
*	S2*C45-V4*C64+(V4+K)*C65+S1*C85=0 ;POINT 65
*	S2*C46-V4*C65+(V4+K)*C66+S1*C86=0 ;POINT 66
*	S2*C47-V4*C66+(V4+K)*C67+S1*C87=0 ;POINT 67
*	S2*C48-V4*C67+(V4+K)*C68+S1*C88=0 ;POINT 68
*	S2*C49-V4*C68+(V4+K)*C69+S1*C89=0 ;POINT 69
*	S2*C50-V4*C69+(V4+K)*C70+S1*C90=0 ;POINT 70
*	S2*C51-V4*C70+(V4+K)*C71+S1*C91=0 ;POINT 71
*	S2*C52-V4*C71+(V4+K)*C72+S1*C92=0 ;POINT 72
*	S2*C53-V4*C72+(V4+K)*C73+S1*C93=0 ;POINT 73
*	S2*C54-V4*C73+(V4+K)*C74+S1*C94=0 ;POINT 74
*	S2*C55-V4*C74+(V4+K)*C75+S1*C95=0 ;POINT 75
*	S2*C56-V4*C75+(V4+K)*C76+S1*C96=0 ;POINT 76
*	S2*C57-V4*C76+(V4+K)*C77+S1*C97=0 ;POINT 77
*	S2*C58-V4*C77+(V4+K)*C78+S1*C98=0 ;POINT 78
*	S2*C59-V4*C78+(V4+K)*C79+S1*C99=0 ;POINT 79
*	S2*C60-V4*C79+(V4+K)*C80+S1*C100=0 ;POINT 80
*	S2*C61+(V5+K)*C81+S1*C101=V5 ;POINT 81
*	S2*C62-V5*C81+(V5+K)*C82+S1*C102=0 ;POINT 82
*	S2*C63-V5*C82+(V5+K)*C83+S1*C103=0 ;POINT 83
*	S2*C64-V5*C83+(V5+K)*C84+S1*C104=0 ;POINT 84
*	S2*C65-V5*C84+(V5+K)*C85+S1*C105=0 ;POINT 85
*	S2*C66-V5*C85+(V5+K)*C86+S1*C106=0 ;POINT 86
*	S2*C67-V5*C86+(V5+K)*C87+S1*C107=0 ;POINT 87
*	S2*C68-V5*C87+(V5+K)*C88+S1*C108=0 ;POINT 88
*	S2*C69-V5*C88+(V5+K)*C89+S1*C109=0 ;POINT 89
*	S2*C70-V5*C89+(V5+K)*C90+S1*C110=0 ;POINT 90
*	S2*C71-V5*C90+(V5+K)*C91+S1*C111=0 ;POINT 91
*	S2*C72-V5*C91+(V5+K)*C92+S1*C112=0 ;POINT 92
*	S2*C73-V5*C92+(V5+K)*C93+S1*C113=0 ;POINT 93
*	S2*C74-V5*C93+(V5+K)*C94+S1*C114=0 ;POINT 94
*	S2*C75-V5*C94+(V5+K)*C95+S1*C115=0 ;POINT 95
*	S2*C76-V5*C95+(V5+K)*C96+S1*C116=0 ;POINT 96
*	S2*C77-V5*C96+(V5+K)*C97+S1*C117=0 ;POINT 97
*	S2*C78-V5*C97+(V5+K)*C98+S1*C118=0 ;POINT 98
*	S2*C79-V5*C98+(V5+K)*C99+S1*C119=0 ;POINT 99
*	S2*C80-V5*C99+(V5+K)*C100+S1*C120=0 ;POINT 100

St	Rule
*	S2*C81+(V5+K)*C101+S1*C121=V5 ;POINT 101
*	S2*C82-V5*C101+(V5+K)*C102+S1*C122=0 ;POINT 102
*	S2*C83-V5*C102+(V5+K)*C103+S1*C123=0 ;POINT 103
*	S2*C84-V5*C103+(V5+K)*C104+S1*C124=0 ;POINT 104
*	S2*C85-V5*C104+(V5+K)*C105+S1*C125=0 ;POINT 105
*	S2*C86-V5*C105+(V5+K)*C106+S1*C126=0 ;POINT 106
*	S2*C87-V5*C106+(V5+K)*C107+S1*C127=0 ;POINT 107
*	S2*C88-V5*C107+(V5+K)*C108+S1*C128=0 ;POINT 108
*	S2*C89-V5*C108+(V5+K)*C109+S1*C129=0 ;POINT 109
*	S2*C90-V5*C109+(V5+K)*C110+S1*C130=0 ;POINT 110
*	S2*C91-V5*C110+(V5+K)*C111+S1*C131=0 ;POINT 111
*	S2*C92-V5*C111+(V5+K)*C112+S1*C132=0 ;POINT 112
*	S2*C93-V5*C112+(V5+K)*C113+S1*C133=0 ;POINT 113
*	S2*C94-V5*C113+(V5+K)*C114+S1*C134=0 ;POINT 114
*	S2*C95-V5*C114+(V5+K)*C115+S1*C135=0 ;POINT 115
*	S2*C96-V5*C115+(V5+K)*C116+S1*C136=0 ;POINT 116
*	S2*C97-V5*C116+(V5+K)*C117+S1*C137=0 ;POINT 117
*	S2*C98-V5*C117+(V5+K)*C118+S1*C138=0 ;POINT 118
*	S2*C99-V5*C118+(V5+K)*C119+S1*C139=0 ;POINT 119
*	S2*C100-V5*C119+(V5+K)*C120+S1*C140=0 ;POINT 120
*	S2*C101+(V4+K)*C121+S1*C141=V4 ;POINT 121
*	S2*C102-V4*C121+(V4+K)*C122+S1*C142=0 ;POINT 122
*	S2*C103-V4*C122+(V4+K)*C123+S1*C143=0 ;POINT 123
*	S2*C104-V4*C123+(V4+K)*C124+S1*C144=0 ;POINT 124
*	S2*C105-V4*C124+(V4+K)*C125+S1*C145=0 ;POINT 125
*	S2*C106-V4*C125+(V4+K)*C126+S1*C146=0 ;POINT 126
*	S2*C107-V4*C126+(V4+K)*C127+S1*C147=0 ;POINT 127
*	S2*C108-V4*C127+(V4+K)*C128+S1*C148=0 ;POINT 128
*	S2*C109-V4*C128+(V4+K)*C129+S1*C149=0 ;POINT 129
*	S2*C110-V4*C129+(V4+K)*C130+S1*C150=0 ;POINT 130
*	S2*C111-V4*C130+(V4+K)*C131+S1*C151=0 ;POINT 131
*	S2*C112-V4*C131+(V4+K)*C132+S1*C152=0 ;POINT 132
*	S2*C113-V4*C132+(V4+K)*C133+S1*C153=0 ;POINT 133
*	S2*C114-V4*C133+(V4+K)*C134+S1*C154=0 ;POINT 134
*	S2*C115-V4*C134+(V4+K)*C135+S1*C155=0 ;POINT 135
*	S2*C116-V4*C135+(V4+K)*C136+S1*C156=0 ;POINT 136
*	S2*C117-V4*C136+(V4+K)*C137+S1*C157=0 ;POINT 137
*	S2*C118-V4*C137+(V4+K)*C138+S1*C158=0 ;POINT 138
*	S2*C119-V4*C138+(V4+K)*C139+S1*C159=0 ;POINT 139
*	S2*C120-V4*C139+(V4+K)*C140+S1*C160=0 ;POINT 140
*	S2*C121+(V3+K)*C141+S1*C161=V3 ;POINT 141
*	S2*C122-V3*C141+(V3+K)*C142+S1*C162=0 ;POINT 142
*	S2*C123-V3*C142+(V3+K)*C143+S1*C163=0 ;POINT 143
*	S2*C124-V3*C143+(V3+K)*C144+S1*C164=0 ;POINT 144
*	S2*C125-V3*C144+(V3+K)*C145+S1*C165=0 ;POINT 145
*	S2*C126-V3*C145+(V3+K)*C146+S1*C166=0 ;POINT 146
*	S2*C127-V3*C146+(V3+K)*C147+S1*C167=0 ;POINT 147
*	S2*C128-V3*C147+(V3+K)*C148+S1*C168=0 ;POINT 148
*	S2*C129-V3*C148+(V3+K)*C149+S1*C169=0 ;POINT 149
*	S2*C130-V3*C149+(V3+K)*C150+S1*C170=0 ;POINT 150
*	S2*C131-V3*C150+(V3+K)*C151+S1*C171=0 ;POINT 151
*	S2*C132-V3*C151+(V3+K)*C152+S1*C172=0 ;POINT 152
*	S2*C133-V3*C152+(V3+K)*C153+S1*C173=0 ;POINT 153
*	S2*C134-V3*C153+(V3+K)*C154+S1*C174=0 ;POINT 154
*	S2*C135-V3*C154+(V3+K)*C155+S1*C175=0 ;POINT 155

St	Rule
*	S2*C136-V3*C155+(V3+K)*C156+S1*C176=0 ;POINT 156
*	S2*C137-V3*C156+(V3+K)*C157+S1*C177=0 ;POINT 157
*	S2*C138-V3*C157+(V3+K)*C158+S1*C178=0 ;POINT 158
*	S2*C139-V3*C158+(V3+K)*C159+S1*C179=0 ;POINT 159
*	S2*C140-V3*C159+(V3+K)*C160+S1*C180=0 ;POINT 160
*	S2*C141+(V2+K)*C161+S1*C181=V2 ;POINT 161
*	S2*C142-V2*C161+(V2+K)*C162+S1*C182=0 ;POINT 162
*	S2*C143-V2*C162+(V2+K)*C163+S1*C183=0 ;POINT 163
*	S2*C144-V2*C163+(V2+K)*C164+S1*C184=0 ;POINT 164
*	S2*C145-V2*C164+(V2+K)*C165+S1*C185=0 ;POINT 165
*	S2*C146-V2*C165+(V2+K)*C166+S1*C186=0 ;POINT 166
*	S2*C147-V2*C166+(V2+K)*C167+S1*C187=0 ;POINT 167
*	S2*C148-V2*C167+(V2+K)*C168+S1*C188=0 ;POINT 168
*	S2*C149-V2*C168+(V2+K)*C169+S1*C189=0 ;POINT 169
*	S2*C150-V2*C169+(V2+K)*C170+S1*C190=0 ;POINT 170
*	S2*C151-V2*C170+(V2+K)*C171+S1*C191=0 ;POINT 171
*	S2*C152-V2*C171+(V2+K)*C172+S1*C192=0 ;POINT 172
*	S2*C153-V2*C172+(V2+K)*C173+S1*C193=0 ;POINT 173
*	S2*C154-V2*C173+(V2+K)*C174+S1*C194=0 ;POINT 174
*	S2*C155-V2*C174+(V2+K)*C175+S1*C195=0 ;POINT 175
*	S2*C156-V2*C175+(V2+K)*C176+S1*C196=0 ;POINT 176
*	S2*C157-V2*C176+(V2+K)*C177+S1*C197=0 ;POINT 177
*	S2*C158-V2*C177+(V2+K)*C178+S1*C198=0 ;POINT 178
*	S2*C159-V2*C178+(V2+K)*C179+S1*C199=0 ;POINT 179
*	S2*C160-V2*C179+(V2+K)*C180+S1*C200=0 ;POINT 180
*	S2*C161+(V1+K)*C181=V1 ;POINT 181
*	S2*C162-V1*C181+(V1+K)*C182=0 ;POINT 182
*	S2*C163-V1*C182+(V1+K)*C183=0 ;POINT 183
*	S2*C164-V1*C183+(V1+K)*C184=0 ;POINT 184
*	S2*C165-V1*C184+(V1+K)*C185=0 ;POINT 185
*	S2*C166-V1*C185+(V1+K)*C186=0 ;POINT 186
*	S2*C167-V1*C186+(V1+K)*C187=0 ;POINT 187
*	S2*C168-V1*C187+(V1+K)*C188=0 ;POINT 188
*	S2*C169-V1*C188+(V1+K)*C189=0 ;POINT 189
*	S2*C170-V1*C189+(V1+K)*C190=0 ;POINT 190
*	S2*C171-V1*C190+(V1+K)*C191=0 ;POINT 191
*	S2*C172-V1*C191+(V1+K)*C192=0 ;POINT 192
*	S2*C173-V1*C192+(V1+K)*C193=0 ;POINT 193
*	S2*C174-V1*C193+(V1+K)*C194=0 ;POINT 194
*	S2*C175-V1*C194+(V1+K)*C195=0 ;POINT 195
*	S2*C176-V1*C195+(V1+K)*C196=0 ;POINT 196
*	S2*C177-V1*C196+(V1+K)*C197=0 ;POINT 197
*	S2*C178-V1*C197+(V1+K)*C198=0 ;POINT 198
*	S2*C179-V1*C198+(V1+K)*C199=0 ;POINT 199
*	S2*C180-V1*C199+(V1+K)*C200=0 ;POINT 200
*	AC1=((C1+C181)*V1+(C21+C161)*V2+(C41+C141)*V3+(C61+C121)*V4+(C81+C101)*V5)/(V1+V2+V3+V4+V5)/2
*	AC2=((C2+C182)*V1+(C22+C162)*V2+(C42+C142)*V3+(C62+C122)*V4+(C82+C102)*V5)/(V1+V2+V3+V4+V5)/2
*	AC3=((C3+C183)*V1+(C23+C163)*V2+(C43+C143)*V3+(C63+C123)*V4+(C83+C103)*V5)/(V1+V2+V3+V4+V5)/2
*	AC4=((C4+C184)*V1+(C24+C164)*V2+(C44+C144)*V3+(C64+C124)*V4+(C84+C104)*V5)/(V1+V2+V3+V4+V5)/2
*	AC5=((C5+C185)*V1+(C25+C165)*V2+(C45+C145)*V3+(C65+C125)*V4+(C85+C105)*V5)/(V1+V2+V3+V4+V5)/2
*	AC6=((C6+C186)*V1+(C26+C166)*V2+(C46+C146)*V3+(C66+C126)*V4+(C86+C106)*V5)/(V1+V2+V3+V4+V5)/2
*	AC7=((C7+C187)*V1+(C27+C167)*V2+(C47+C147)*V3+(C67+C127)*V4+(C87+C107)*V5)/(V1+V2+V3+V4+V5)/2
*	AC8=((C8+C188)*V1+(C28+C168)*V2+(C48+C148)*V3+(C68+C128)*V4+(C88+C108)*V5)/(V1+V2+V3+V4+V5)/2
*	AC9=((C9+C189)*V1+(C29+C169)*V2+(C49+C149)*V3+(C69+C129)*V4+(C89+C109)*V5)/(V1+V2+V3+V4+V5)/2
*	AC10=((C10+C190)*V1+(C30+C170)*V2+(C50+C150)*V3+(C70+C130)*V4+(C90+C110)*V5)/(V1+V2+V3+V4+V5)/2
*	AC11=((C11+C191)*V1+(C31+C171)*V2+(C51+C151)*V3+(C71+C131)*V4+(C91+C111)*V5)/(V1+V2+V3+V4+V5)/2
*	AC12=((C12+C192)*V1+(C32+C172)*V2+(C52+C152)*V3+(C72+C132)*V4+(C92+C112)*V5)/(V1+V2+V3+V4+V5)/2
*	AC13=((C13+C193)*V1+(C33+C173)*V2+(C53+C153)*V3+(C73+C133)*V4+(C93+C113)*V5)/(V1+V2+V3+V4+V5)/2

St	Rule
•	AC14=((C14+C194)*V1+(C34+C174)*V2+(C54+C154)*V3+(C74+C134)*V4+(C94+C114)*V5)/(V1+V2+V3+V4+V5)/2
•	AC15=((C15+C195)*V1+(C35+C175)*V2+(C55+C155)*V3+(C75+C135)*V4+(C95+C115)*V5)/(V1+V2+V3+V4+V5)/2
•	AC16=((C16+C196)*V1+(C36+C176)*V2+(C56+C156)*V3+(C76+C136)*V4+(C96+C116)*V5)/(V1+V2+V3+V4+V5)/2
•	AC17=((C17+C197)*V1+(C37+C177)*V2+(C57+C157)*V3+(C77+C137)*V4+(C97+C117)*V5)/(V1+V2+V3+V4+V5)/2
•	AC18=((C18+C198)*V1+(C38+C178)*V2+(C58+C158)*V3+(C78+C138)*V4+(C98+C118)*V5)/(V1+V2+V3+V4+V5)/2
•	AC19=((C19+C199)*V1+(C39+C179)*V2+(C59+C159)*V3+(C79+C139)*V4+(C99+C119)*V5)/(V1+V2+V3+V4+V5)/2
•	AC20=((C20+C200)*V1+(C40+C180)*V2+(C60+C160)*V3+(C80+C140)*V4+(C100+C120)*V5)/(V1+V2+V3+V4+V5)/2

Appendix G The TK-Solver® Program Codes for the Inclined Crack Model (Dimensional Model)

This study used the TK-Solver® software to solve the algebraic equation set of the Inclined Crack model. The TK-Solver® software used the Newton's method of tangent to find a converge answer to the equation set. Different from Appendix F, this model is solved in a dimensional form. The model is design to calculate particle dynamic parameters automatically. The user need to input atmospheric pressure, temperature, particle size, crack geometries, and incline angle to solve the model. This program also incorporates the "List solving" function. "List solving" function enables the users to solve a series of modeling conditions in a run. It improves modeling efficiency. Please refer to the operation manual for details of the "List Solving" function. The followings summarize the variable sheet and the rule sheet for the inclined crack model.

The Variable Worksheet

Nomenclature:

1. "St" column declares the status of the variables.
2. "I" declares the variable as an input variable, the user must give a value to the model.
3. "O" declares the variable as an Output variable, the software will give an answer if the model converges. If the model does not converge, a "*" will mark in the "St" column to notify the user.
4. "LLGu" declares the variable as a LGuess variable for List solving function. The user must create a table for this variable such that TK-Solver recognizes it as a List Solving parameter. Users need to give an initial guess value to the variable as well. After model execution, the software will give an answer if the model converges. If the model does not converge, a "*" will mark in the "St" column to notify the user. In this study, initial guess is set to 1, i.e. the concentration inside the crack is the same as crack entrance.

5. C1 to C200 are the concentration matrix, which equals to the M x N = 20 X 10 concentration matrix defined in Chapter 3.
6. B20, B40, B60,....., B200 are concentration profile at crack exit. B1, B21, B41,....., B181 are concentration profile at crack entrance. This study assumes they are equal to 1, i.e. particles distributed uniformly at crack entrance.
7. AC1 to AC20 are the average concentration (flow weighted) at the levels M = 1 to 20, respectively. They are defined in the Rule sheet. AC20 is the average concentration at crack exit. It is equal to the particle penetration coefficient.
8. *xxx*: User need to give an input value
9. *yyy*: The software will give an answer if the model converges.
10. When crack incline angle ALPHA = 0, the model is the same as the Taulbee model.

St	Input	Name	Output	Unit	Comment
I	76	p			Atmosphere Pressure, cm-Hg
I	1.38E-16	KB			Boltzmann Constant, dyne-cm/K
I	20	T			Atmosphere Temperature, C
I	.0000182	u			Air absolute viscosity, N-Sec/m^2
I	1000	Dp			Air Density, kg/m^3
I	2	dp			Particle Aerodynamic Diameter, um
I	.00061	H			Crack height, m
I	.06	L			Crack length, m
I	0	ALPHA			Incline Angle, degree
L	.0821	V			Average fluid velocity, m/sec
O		T95	yyy		Relaxation Time, Second
O		B	yyy		Particle Mobility
O		B20	yyy		Exit Concentration profile
O		B40	yyy		Exit Concentration profile
O		B60	yyy		Exit Concentration profile
O		B80	yyy		Exit Concentration profile
O		B100	yyy		Exit Concentration profile
O		B120	yyy		Exit Concentration profile
O		B140	yyy		Exit Concentration profile
O		B160	yyy		Exit Concentration profile
O		B180	yyy		Exit Concentration profile
O		B200	yyy		Exit Concentration profile
L		AC20	yyy		Penetration Penetration Coefficient
O		C			Cunningham Correction Factor
O		D			Particle Diffisivity, m^2/sec
O		Vt			Particle terminal velocity, m/sec
I	1	B1			Entrance concentration profile
I	1	B21			Entrance concentration profile
I	1	B41			Entrance concentration profile
I	1	B61			Entrance concentration profile
I	1	B81			Entrance concentration profile
I	1	B101			Entrance concentration profile
I	1	B121			Entrance concentration profile
I	1	B141			Entrance concentration profile
I	1	B161			Entrance concentration profile
I	1	B181			Entrance concentration profile
O		d	yyy		Half-height of crack, m
O		SIG	yyy		
O		X	yyy		
O		PE	yyy		Peclet number, Pe=hv/D
O		h	yyy		Dimensionless Grid width h=X/20
O		k	yyy		Dimensionless Grid height k=2/(10+1)
O		V1	yyy		Fluid velocity of level 1, 10
O		V2	yyy		Fluid velocity of level 2, 9
O		V3	yyy		Fluid velocity of level 3, 8
O		V4	yyy		luid velocity of level 4, 7
O		V5	yyy		Fluid velocity of level 5, 6
O		S	yyy		Matrix coefficient
O		S1	yyy		matrix coefficient
O		P	yyy		matrix coefficient
O		K	yyy		Matrix coefficient
LGu	1	C1			Concentration of grid #1 (Level N =1)
LGu	1	C2			Concentration of grid #2 (Level N =1)
LGu	1	C3			Concentration of grid #3 (Level N =1)
LGu	1	C4			Concentration of grid #4 (Level N =1)

St	Input	Name	Output	Unit	Comment
LGu	1	C5			Concentration of grid #5 (Level N =1)
.....					
.....					
LGu	1	C20			Concentration of grid #20 (Level N =1)
LGu	1	C21			Concentration of grid #21 (Level N =2)
LGu	1	C22			Concentration of grid #22 (Level N =2)
LGu	1	C23			Concentration of grid #23 (Level N =2)
.....					
.....					
.....					
LGu	1	C40			Concentration of grid #40 (Level N =2)
LGu	1	C41			Concentration of grid #41 (Level N =3)
LGu	1	C42			Concentration of grid #42 (Level N =3)
LGu	1	C43			Concentration of grid #43 (Level N =3)
.....					
.....					
.....					
LGu	1	C160			Concentration of grid #160 (Level N =8)
LGu	1	C161			Concentration of grid #161 (Level N =9)
LGu	1	C162			Concentration of grid #162 (Level N =9)
LGu	1	C163			Concentration of grid #163 (Level N =9)
.....					
.....					
.....					
LGu	1	C180			Concentration of grid #180 (Level N =9)
LGu	1	C181			Concentration of grid #181 (Level N =10)
LGu	1	C182			Concentration of grid #182 (Level N =10)
LGu	1	C183			Concentration of grid #183 (Level N =10)
.....					
.....					
.....					
LGu	1	C200			Concentration of grid #200 (Level N =10)
O		AC1	*yyy*		Ave. conc. at Level M = 1 (Defined in Rule sheet)
O		AC2	*yyy*		Ave. conc. at Level M = 2 (Defined in Rule sheet)
O		AC3	*yyy*		Ave. conc. at Level M = 3 (Defined in Rule sheet)
O		AC4	*yyy*		Ave. conc. at Level M = 4 (Defined in Rule sheet)
O		AC5	*yyy*		Ave. conc. at Level M = 5 (Defined in Rule sheet)
O		AC6	*yyy*		Ave. conc. at Level M = 6 (Defined in Rule sheet)
O		AC7	*yyy*		Ave. conc. at Level M = 7 (Defined in Rule sheet)
O		AC8	*yyy*		Ave. conc. at Level M = 8 (Defined in Rule sheet)
O		AC9	*yyy*		Ave. conc. at Level M = 9 (Defined in Rule sheet)
O		AC10	*yyy*		Ave. conc. at Level M = 10 (Defined in Rule sheet)
O		AC11	*yyy*		Ave. conc. at Level M = 11 (Defined in Rule sheet)
O		AC12	*yyy*		Ave. conc. at Level M = 12 (Defined in Rule sheet)
O		AC13	*yyy*		Ave. conc. at Level M = 13 (Defined in Rule sheet)
O		AC14	*yyy*		Ave. conc. at Level M = 14 (Defined in Rule sheet)
O		AC15	*yyy*		Ave. conc. at Level M = 15 (Defined in Rule sheet)
O		AC16	*yyy*		Ave. conc. at Level M = 16 (Defined in Rule sheet)
O		AC17	*yyy*		Ave. conc. at Level M = 17 (Defined in Rule sheet)
O		AC18	*yyy*		Ave. conc. at Level M = 18 (Defined in Rule sheet)
O		AC19	*yyy*		Ave. conc. at Level M = 19 (Defined in Rule sheet)

The Rule Worksheet
Nomenclature

1. "Rules" are the equations linking the variables declared in the Variable sheet. The description after the ";" mark is the comments to the rule, which does not affect model execution. In the model, the comment "POINT XX" means the algebraic equation at the grid XX (XX = 1 to 200).
2. "St" column declares the status of the rule. After execution, if the model does not converge to a solution, there will be "*" marks in the "St" column to notify the user. If converged solution are derived, the "*" mark will disappear.

St	Rule
*	C=1+2/p/dp*(6.32+2.01*exp(-0.1095*p*dp))
*	B=C/3/3.14159/u/10/(dp*0.0001)
*	T95=B*Dp/1000*3.14159/6*(dp*0.0001)^3
*	D=KB*B*(T+273)
*	Vt=T95*9.8
*	d=H/2
*	SIG=Vt*d/D
*	PE=2*d*V/D
*	X=2*L/d/PE
*	h=X/20
*	k=2/11
*	V1=1.5*(1-(9/11)^2)/h
*	V2=1.5*(1-(7/11)^2)/h
*	V3=1.5*(1-(5/11)^2)/h
*	V4=1.5*(1-(3/11)^2)/h
*	V5=1.5*(1-(1/11)^2)/h
*	S=2*SIG*SIND(ALPHA)/PE/h
*	S1=SIG*COSD(ALPHA)/k
*	P=4/h^2/PE^2
*	K=1/k^2
*	-(V1-S+P)*B1+(V1-S+S1+2*P+2*K)*C1-P*C2-K*C21=0
*	-(V1-S+P)*C1+(V1-S+S1+2*P+2*K)*C2-P*C3-K*C22=0
*	-(V1-S+P)*C2+(V1-S+S1+2*P+2*K)*C3-P*C4-K*C23=0
*	-(V1-S+P)*C3+(V1-S+S1+2*P+2*K)*C4-P*C5-K*C24=0
*	-(V1-S+P)*C4+(V1-S+S1+2*P+2*K)*C5-P*C6-K*C25=0
*	-(V1-S+P)*C5+(V1-S+S1+2*P+2*K)*C6-P*C7-K*C26=0
*	-(V1-S+P)*C6+(V1-S+S1+2*P+2*K)*C7-P*C8-K*C27=0
*	-(V1-S+P)*C7+(V1-S+S1+2*P+2*K)*C8-P*C9-K*C28=0
*	-(V1-S+P)*C8+(V1-S+S1+2*P+2*K)*C9-P*C10-K*C29=0
*	-(V1-S+P)*C9+(V1-S+S1+2*P+2*K)*C10-P*C11-K*C30=0
*	-(V1-S+P)*C10+(V1-S+S1+2*P+2*K)*C11-P*C12-K*C31=0
*	-(V1-S+P)*C11+(V1-S+S1+2*P+2*K)*C12-P*C13-K*C32=0
*	-(V1-S+P)*C12+(V1-S+S1+2*P+2*K)*C13-P*C14-K*C33=0
*	-(V1-S+P)*C13+(V1-S+S1+2*P+2*K)*C14-P*C15-K*C34=0
*	-(V1-S+P)*C14+(V1-S+S1+2*P+2*K)*C15-P*C16-K*C35=0
*	-(V1-S+P)*C15+(V1-S+S1+2*P+2*K)*C16-P*C17-K*C36=0
*	-(V1-S+P)*C16+(V1-S+S1+2*P+2*K)*C17-P*C18-K*C37=0
*	-(V1-S+P)*C17+(V1-S+S1+2*P+2*K)*C18-P*C19-K*C38=0
*	-(V1-S+P)*C18+(V1-S+S1+2*P+2*K)*C19-P*C20-K*C39=0
*	-(V1-S+P)*C19+(V1-S+S1+2*K+P)*C20-K*C40=0
*	-(S1+K)*C1-(V2-S+P)*B21+(V2-S+S1+2*P+2*K)*C21-P*C22-K*C41=0
*	-(S1+K)*C2-(V2-S+P)*C21+(V2-S+S1+2*P+2*K)*C22-P*C23-K*C42=0
*	-(S1+K)*C3-(V2-S+P)*C22+(V2-S+S1+2*P+2*K)*C23-P*C24-K*C43=0
*	-(S1+K)*C4-(V2-S+P)*C23+(V2-S+S1+2*P+2*K)*C24-P*C25-K*C44=0
*	-(S1+K)*C5-(V2-S+P)*C24+(V2-S+S1+2*P+2*K)*C25-P*C26-K*C45=0
*	-(S1+K)*C6-(V2-S+P)*C25+(V2-S+S1+2*P+2*K)*C26-P*C27-K*C46=0
*	-(S1+K)*C7-(V2-S+P)*C26+(V2-S+S1+2*P+2*K)*C27-P*C28-K*C47=0
*	-(S1+K)*C8-(V2-S+P)*C27+(V2-S+S1+2*P+2*K)*C28-P*C29-K*C48=0
*	-(S1+K)*C9-(V2-S+P)*C28+(V2-S+S1+2*P+2*K)*C29-P*C30-K*C49=0
*	-(S1+K)*C10-(V2-S+P)*C29+(V2-S+S1+2*P+2*K)*C30-P*C31-K*C50=0
*	-(S1+K)*C11-(V2-S+P)*C30+(V2-S+S1+2*P+2*K)*C31-P*C32-K*C51=0
*	-(S1+K)*C12-(V2-S+P)*C31+(V2-S+S1+2*P+2*K)*C32-P*C33-K*C52=0
*	-(S1+K)*C13-(V2-S+P)*C32+(V2-S+S1+2*P+2*K)*C33-P*C34-K*C53=0
*	-(S1+K)*C14-(V2-S+P)*C33+(V2-S+S1+2*P+2*K)*C34-P*C35-K*C54=0
*	-(S1+K)*C15-(V2-S+P)*C34+(V2-S+S1+2*P+2*K)*C35-P*C36-K*C55=0

St	Rule
*	-(S1+K)*C16-(V2-S+P)*C35+(V2-S+S1+2*P+2*K)*C36-P*C37-K*C56=0
*	-(S1+K)*C17-(V2-S+P)*C36+(V2-S+S1+2*P+2*K)*C37-P*C38-K*C57=0
*	-(S1+K)*C18-(V2-S+P)*C37+(V2-S+S1+2*P+2*K)*C38-P*C39-K*C58=0
*	-(S1+K)*C19-(V2-S+P)*C38+(V2-S+S1+2*P+2*K)*C39-P*C40-K*C59=0
*	-(S1+K)*C20-(V2-S+P)*C39+(V2-S+S1+2*K+P)*C40-K*C60=0
*	-(S1+K)*C21-(V3-S+P)*B41+(V3-S+S1+2*P+2*K)*C41-P*C42-K*C61=0
*	-(S1+K)*C22-(V3-S+P)*C41+(V3-S+S1+2*P+2*K)*C42-P*C43-K*C62=0
*	-(S1+K)*C23-(V3-S+P)*C42+(V3-S+S1+2*P+2*K)*C43-P*C44-K*C63=0
*	-(S1+K)*C24-(V3-S+P)*C43+(V3-S+S1+2*P+2*K)*C44-P*C45-K*C64=0
*	-(S1+K)*C25-(V3-S+P)*C44+(V3-S+S1+2*P+2*K)*C45-P*C46-K*C65=0
*	-(S1+K)*C26-(V3-S+P)*C45+(V3-S+S1+2*P+2*K)*C46-P*C47-K*C66=0
*	-(S1+K)*C27-(V3-S+P)*C46+(V3-S+S1+2*P+2*K)*C47-P*C48-K*C67=0
*	-(S1+K)*C28-(V3-S+P)*C47+(V3-S+S1+2*P+2*K)*C48-P*C49-K*C68=0
*	-(S1+K)*C29-(V3-S+P)*C48+(V3-S+S1+2*P+2*K)*C49-P*C50-K*C69=0
*	-(S1+K)*C30-(V3-S+P)*C49+(V3-S+S1+2*P+2*K)*C50-P*C51-K*C70=0
*	-(S1+K)*C31-(V3-S+P)*C50+(V3-S+S1+2*P+2*K)*C51-P*C52-K*C71=0
*	-(S1+K)*C32-(V3-S+P)*C51+(V3-S+S1+2*P+2*K)*C52-P*C53-K*C72=0
*	-(S1+K)*C33-(V3-S+P)*C52+(V3-S+S1+2*P+2*K)*C53-P*C54-K*C73=0
*	-(S1+K)*C34-(V3-S+P)*C53+(V3-S+S1+2*P+2*K)*C54-P*C55-K*C74=0
*	-(S1+K)*C35-(V3-S+P)*C54+(V3-S+S1+2*P+2*K)*C55-P*C56-K*C75=0
*	-(S1+K)*C36-(V3-S+P)*C55+(V3-S+S1+2*P+2*K)*C56-P*C57-K*C76=0
*	-(S1+K)*C37-(V3-S+P)*C56+(V3-S+S1+2*P+2*K)*C57-P*C58-K*C77=0
*	-(S1+K)*C38-(V3-S+P)*C57+(V3-S+S1+2*P+2*K)*C58-P*C59-K*C78=0
*	-(S1+K)*C39-(V3-S+P)*C58+(V3-S+S1+2*P+2*K)*C59-P*C60-K*C79=0
*	-(S1+K)*C40-(V3-S+P)*C59+(V3-S+S1+2*K+P)*C60-K*C80=0
*	-(S1+K)*C41-(V4-S+P)*B61+(V4-S+S1+2*P+2*K)*C61-P*C62-K*C81=0
*	-(S1+K)*C42-(V4-S+P)*C61+(V4-S+S1+2*P+2*K)*C62-P*C63-K*C82=0
*	-(S1+K)*C43-(V4-S+P)*C62+(V4-S+S1+2*P+2*K)*C63-P*C64-K*C83=0
*	-(S1+K)*C44-(V4-S+P)*C63+(V4-S+S1+2*P+2*K)*C64-P*C65-K*C84=0
*	-(S1+K)*C45-(V4-S+P)*C64+(V4-S+S1+2*P+2*K)*C65-P*C66-K*C85=0
*	-(S1+K)*C46-(V4-S+P)*C65+(V4-S+S1+2*P+2*K)*C66-P*C67-K*C86=0
*	-(S1+K)*C47-(V4-S+P)*C66+(V4-S+S1+2*P+2*K)*C67-P*C68-K*C87=0
*	-(S1+K)*C48-(V4-S+P)*C67+(V4-S+S1+2*P+2*K)*C68-P*C69-K*C88=0
*	-(S1+K)*C49-(V4-S+P)*C68+(V4-S+S1+2*P+2*K)*C69-P*C70-K*C89=0
*	-(S1+K)*C50-(V4-S+P)*C69+(V4-S+S1+2*P+2*K)*C70-P*C71-K*C90=0
*	-(S1+K)*C51-(V4-S+P)*C70+(V4-S+S1+2*P+2*K)*C71-P*C72-K*C91=0
*	-(S1+K)*C52-(V4-S+P)*C71+(V4-S+S1+2*P+2*K)*C72-P*C73-K*C92=0
*	-(S1+K)*C53-(V4-S+P)*C72+(V4-S+S1+2*P+2*K)*C73-P*C74-K*C93=0
*	-(S1+K)*C54-(V4-S+P)*C73+(V4-S+S1+2*P+2*K)*C74-P*C75-K*C94=0
*	-(S1+K)*C55-(V4-S+P)*C74+(V4-S+S1+2*P+2*K)*C75-P*C76-K*C95=0
*	-(S1+K)*C56-(V4-S+P)*C75+(V4-S+S1+2*P+2*K)*C76-P*C77-K*C96=0
*	-(S1+K)*C57-(V4-S+P)*C76+(V4-S+S1+2*P+2*K)*C77-P*C78-K*C97=0
*	-(S1+K)*C58-(V4-S+P)*C77+(V4-S+S1+2*P+2*K)*C78-P*C79-K*C98=0
*	-(S1+K)*C59-(V4-S+P)*C78+(V4-S+S1+2*P+2*K)*C79-P*C80-K*C99=0
*	-(S1+K)*C60-(V4-S+P)*C79+(V4-S+S1+2*K+P)*C80-K*C100=0
*	-(S1+K)*C61-(V5-S+P)*B81+(V5-S+S1+2*P+2*K)*C81-P*C82-K*C101=0
*	-(S1+K)*C62-(V5-S+P)*C81+(V5-S+S1+2*P+2*K)*C82-P*C83-K*C102=0
*	-(S1+K)*C63-(V5-S+P)*C82+(V5-S+S1+2*P+2*K)*C83-P*C84-K*C103=0
*	-(S1+K)*C64-(V5-S+P)*C83+(V5-S+S1+2*P+2*K)*C84-P*C85-K*C104=0
*	-(S1+K)*C65-(V5-S+P)*C84+(V5-S+S1+2*P+2*K)*C85-P*C86-K*C105=0
*	-(S1+K)*C66-(V5-S+P)*C85+(V5-S+S1+2*P+2*K)*C86-P*C87-K*C106=0
*	-(S1+K)*C67-(V5-S+P)*C86+(V5-S+S1+2*P+2*K)*C87-P*C88-K*C107=0
*	-(S1+K)*C68-(V5-S+P)*C87+(V5-S+S1+2*P+2*K)*C88-P*C89-K*C108=0
*	-(S1+K)*C69-(V5-S+P)*C88+(V5-S+S1+2*P+2*K)*C89-P*C90-K*C109=0
*	-(S1+K)*C70-(V5-S+P)*C89+(V5-S+S1+2*P+2*K)*C90-P*C91-K*C110=0

St	Rule
*	-(S1+K)*C71-(V5-S+P)*C90+(V5-S+S1+2*P+2*K)*C91-P*C92-K*C111=0
*	-(S1+K)*C72-(V5-S+P)*C91+(V5-S+S1+2*P+2*K)*C92-P*C93-K*C112=0
*	-(S1+K)*C73-(V5-S+P)*C92+(V5-S+S1+2*P+2*K)*C93-P*C94-K*C113=0
*	-(S1+K)*C74-(V5-S+P)*C93+(V5-S+S1+2*P+2*K)*C94-P*C95-K*C114=0
*	-(S1+K)*C75-(V5-S+P)*C94+(V5-S+S1+2*P+2*K)*C95-P*C96-K*C115=0
*	-(S1+K)*C76-(V5-S+P)*C95+(V5-S+S1+2*P+2*K)*C96-P*C97-K*C116=0
*	-(S1+K)*C77-(V5-S+P)*C96+(V5-S+S1+2*P+2*K)*C97-P*C98-K*C117=0
*	-(S1+K)*C78-(V5-S+P)*C97+(V5-S+S1+2*P+2*K)*C98-P*C99-K*C118=0
*	-(S1+K)*C79-(V5-S+P)*C98+(V5-S+S1+2*P+2*K)*C99-P*C100-K*C119=0
*	-(S1+K)*C80-(V5-S+P)*C99+(V5-S+S1+2*K+P)*C100-K*C120=0
*	-(S1+K)*C81-(V5-S+P)*B101+(V5-S+S1+2*P+2*K)*C101-P*C102-K*C121=0
*	-(S1+K)*C82-(V5-S+P)*C101+(V5-S+S1+2*P+2*K)*C102-P*C103-K*C122=0
*	-(S1+K)*C83-(V5-S+P)*C102+(V5-S+S1+2*P+2*K)*C103-P*C104-K*C123=0
*	-(S1+K)*C84-(V5-S+P)*C103+(V5-S+S1+2*P+2*K)*C104-P*C105-K*C124=0
*	-(S1+K)*C85-(V5-S+P)*C104+(V5-S+S1+2*P+2*K)*C105-P*C106-K*C125=0
*	-(S1+K)*C86-(V5-S+P)*C105+(V5-S+S1+2*P+2*K)*C106-P*C107-K*C126=0
*	-(S1+K)*C87-(V5-S+P)*C106+(V5-S+S1+2*P+2*K)*C107-P*C108-K*C127=0
*	-(S1+K)*C88-(V5-S+P)*C107+(V5-S+S1+2*P+2*K)*C108-P*C109-K*C128=0
*	-(S1+K)*C89-(V5-S+P)*C108+(V5-S+S1+2*P+2*K)*C109-P*C110-K*C129=0
*	-(S1+K)*C90-(V5-S+P)*C109+(V5-S+S1+2*P+2*K)*C110-P*C111-K*C130=0
*	-(S1+K)*C91-(V5-S+P)*C110+(V5-S+S1+2*P+2*K)*C111-P*C112-K*C131=0
*	-(S1+K)*C92-(V5-S+P)*C111+(V5-S+S1+2*P+2*K)*C112-P*C113-K*C132=0
*	-(S1+K)*C93-(V5-S+P)*C112+(V5-S+S1+2*P+2*K)*C113-P*C114-K*C133=0
*	-(S1+K)*C94-(V5-S+P)*C113+(V5-S+S1+2*P+2*K)*C114-P*C115-K*C134=0
*	-(S1+K)*C95-(V5-S+P)*C114+(V5-S+S1+2*P+2*K)*C115-P*C116-K*C135=0
*	-(S1+K)*C96-(V5-S+P)*C115+(V5-S+S1+2*P+2*K)*C116-P*C117-K*C136=0
*	-(S1+K)*C97-(V5-S+P)*C116+(V5-S+S1+2*P+2*K)*C117-P*C118-K*C137=0
*	-(S1+K)*C98-(V5-S+P)*C117+(V5-S+S1+2*P+2*K)*C118-P*C119-K*C138=0
*	-(S1+K)*C99-(V5-S+P)*C118+(V5-S+S1+2*P+2*K)*C119-P*C120-K*C139=0
*	-(S1+K)*C100-(V5-S+P)*C119+(V5-S+S1+2*K+P)*C120-K*C140=0
*	-(S1+K)*C101-(V4-S+P)*B121+(V4-S+S1+2*P+2*K)*C121-P*C122-K*C141=0
*	-(S1+K)*C102-(V4-S+P)*C121+(V4-S+S1+2*P+2*K)*C122-P*C123-K*C142=0
*	-(S1+K)*C103-(V4-S+P)*C122+(V4-S+S1+2*P+2*K)*C123-P*C124-K*C143=0
*	-(S1+K)*C104-(V4-S+P)*C123+(V4-S+S1+2*P+2*K)*C124-P*C125-K*C144=0
*	-(S1+K)*C105-(V4-S+P)*C124+(V4-S+S1+2*P+2*K)*C125-P*C126-K*C145=0
*	-(S1+K)*C106-(V4-S+P)*C125+(V4-S+S1+2*P+2*K)*C126-P*C127-K*C146=0
*	-(S1+K)*C107-(V4-S+P)*C126+(V4-S+S1+2*P+2*K)*C127-P*C128-K*C147=0
*	-(S1+K)*C108-(V4-S+P)*C127+(V4-S+S1+2*P+2*K)*C128-P*C129-K*C148=0
*	-(S1+K)*C109-(V4-S+P)*C128+(V4-S+S1+2*P+2*K)*C129-P*C130-K*C149=0
*	-(S1+K)*C110-(V4-S+P)*C129+(V4-S+S1+2*P+2*K)*C130-P*C131-K*C150=0
*	-(S1+K)*C111-(V4-S+P)*C130+(V4-S+S1+2*P+2*K)*C131-P*C132-K*C151=0
*	-(S1+K)*C112-(V4-S+P)*C131+(V4-S+S1+2*P+2*K)*C132-P*C133-K*C152=0
*	-(S1+K)*C113-(V4-S+P)*C132+(V4-S+S1+2*P+2*K)*C133-P*C134-K*C153=0
*	-(S1+K)*C114-(V4-S+P)*C133+(V4-S+S1+2*P+2*K)*C134-P*C135-K*C154=0
*	-(S1+K)*C115-(V4-S+P)*C134+(V4-S+S1+2*P+2*K)*C135-P*C136-K*C155=0
*	-(S1+K)*C116-(V4-S+P)*C135+(V4-S+S1+2*P+2*K)*C136-P*C137-K*C156=0
*	-(S1+K)*C117-(V4-S+P)*C136+(V4-S+S1+2*P+2*K)*C137-P*C138-K*C157=0
*	-(S1+K)*C118-(V4-S+P)*C137+(V4-S+S1+2*P+2*K)*C138-P*C139-K*C158=0
*	-(S1+K)*C119-(V4-S+P)*C138+(V4-S+S1+2*P+2*K)*C139-P*C140-K*C159=0
*	-(S1+K)*C120-(V4-S+P)*C139+(V4-S+S1+2*K+P)*C140-K*C160=0
*	-(S1+K)*C121-(V3-S+P)*B141+(V3-S+S1+2*P+2*K)*C141-P*C142-K*C161=0
*	-(S1+K)*C122-(V3-S+P)*C141+(V3-S+S1+2*P+2*K)*C142-P*C143-K*C162=0
*	-(S1+K)*C123-(V3-S+P)*C142+(V3-S+S1+2*P+2*K)*C143-P*C144-K*C163=0
*	-(S1+K)*C124-(V3-S+P)*C143+(V3-S+S1+2*P+2*K)*C144-P*C145-K*C164=0
*	-(S1+K)*C125-(V3-S+P)*C144+(V3-S+S1+2*P+2*K)*C145-P*C146-K*C165=0

St	Rule
*	-(S1+K)*C126-(V3-S+P)*C145+(V3-S+S1+2*P+2*K)*C146-P*C147-K*C166=0
*	-(S1+K)*C127-(V3-S+P)*C146+(V3-S+S1+2*P+2*K)*C147-P*C148-K*C167=0
*	-(S1+K)*C128-(V3-S+P)*C147+(V3-S+S1+2*P+2*K)*C148-P*C149-K*C168=0
*	-(S1+K)*C129-(V3-S+P)*C148+(V3-S+S1+2*P+2*K)*C149-P*C150-K*C169=0
*	-(S1+K)*C130-(V3-S+P)*C149+(V3-S+S1+2*P+2*K)*C150-P*C151-K*C170=0
*	-(S1+K)*C131-(V3-S+P)*C150+(V3-S+S1+2*P+2*K)*C151-P*C152-K*C171=0
*	-(S1+K)*C132-(V3-S+P)*C151+(V3-S+S1+2*P+2*K)*C152-P*C153-K*C172=0
*	-(S1+K)*C133-(V3-S+P)*C152+(V3-S+S1+2*P+2*K)*C153-P*C154-K*C173=0
*	-(S1+K)*C134-(V3-S+P)*C153+(V3-S+S1+2*P+2*K)*C154-P*C155-K*C174=0
*	-(S1+K)*C135-(V3-S+P)*C154+(V3-S+S1+2*P+2*K)*C155-P*C156-K*C175=0
*	-(S1+K)*C136-(V3-S+P)*C155+(V3-S+S1+2*P+2*K)*C156-P*C157-K*C176=0
*	-(S1+K)*C137-(V3-S+P)*C156+(V3-S+S1+2*P+2*K)*C157-P*C158-K*C177=0
*	-(S1+K)*C138-(V3-S+P)*C157+(V3-S+S1+2*P+2*K)*C158-P*C159-K*C178=0
*	-(S1+K)*C139-(V3-S+P)*C158+(V3-S+S1+2*P+2*K)*C159-P*C160-K*C179=0
*	-(S1+K)*C140-(V3-S+P)*C159+(V3-S+S1+2*K+P)*C160-K*C180=0
*	-(S1+K)*C141-(V2-S+P)*B161+(V2-S+S1+2*P+2*K)*C161-P*C162-K*C181=0
*	-(S1+K)*C142-(V2-S+P)*C161+(V2-S+S1+2*P+2*K)*C162-P*C163-K*C182=0
*	-(S1+K)*C143-(V2-S+P)*C162+(V2-S+S1+2*P+2*K)*C163-P*C164-K*C183=0
*	-(S1+K)*C144-(V2-S+P)*C163+(V2-S+S1+2*P+2*K)*C164-P*C165-K*C184=0
*	-(S1+K)*C145-(V2-S+P)*C164+(V2-S+S1+2*P+2*K)*C165-P*C166-K*C185=0
*	-(S1+K)*C146-(V2-S+P)*C165+(V2-S+S1+2*P+2*K)*C166-P*C167-K*C186=0
*	-(S1+K)*C147-(V2-S+P)*C166+(V2-S+S1+2*P+2*K)*C167-P*C168-K*C187=0
*	-(S1+K)*C148-(V2-S+P)*C167+(V2-S+S1+2*P+2*K)*C168-P*C169-K*C188=0
*	-(S1+K)*C149-(V2-S+P)*C168+(V2-S+S1+2*P+2*K)*C169-P*C170-K*C189=0
*	-(S1+K)*C150-(V2-S+P)*C169+(V2-S+S1+2*P+2*K)*C170-P*C171-K*C190=0
*	-(S1+K)*C151-(V2-S+P)*C170+(V2-S+S1+2*P+2*K)*C171-P*C172-K*C191=0
*	-(S1+K)*C152-(V2-S+P)*C171+(V2-S+S1+2*P+2*K)*C172-P*C173-K*C192=0
*	-(S1+K)*C153-(V2-S+P)*C172+(V2-S+S1+2*P+2*K)*C173-P*C174-K*C193=0
*	-(S1+K)*C154-(V2-S+P)*C173+(V2-S+S1+2*P+2*K)*C174-P*C175-K*C194=0
*	-(S1+K)*C155-(V2-S+P)*C174+(V2-S+S1+2*P+2*K)*C175-P*C176-K*C195=0
*	-(S1+K)*C156-(V2-S+P)*C175+(V2-S+S1+2*P+2*K)*C176-P*C177-K*C196=0
*	-(S1+K)*C157-(V2-S+P)*C176+(V2-S+S1+2*P+2*K)*C177-P*C178-K*C197=0
*	-(S1+K)*C158-(V2-S+P)*C177+(V2-S+S1+2*P+2*K)*C178-P*C179-K*C198=0
*	-(S1+K)*C159-(V2-S+P)*C178+(V2-S+S1+2*P+2*K)*C179-P*C180-K*C199=0
*	-(S1+K)*C160-(V2-S+P)*C179+(V2-S+S1+2*K+P)*C180-K*C200=0
*	-(V1-S+P)*B181+(V1-S+S1+2*P+2*K)*C181-P*C182+-(S1+K)*C161=0
*	-(V1-S+P)*C181+(V1-S+S1+2*P+2*K)*C182-P*C183+-(S1+K)*C162=0
*	-(V1-S+P)*C182+(V1-S+S1+2*P+2*K)*C183-P*C184+-(S1+K)*C163=0
*	-(V1-S+P)*C183+(V1-S+S1+2*P+2*K)*C184-P*C185+-(S1+K)*C164=0
*	-(V1-S+P)*C184+(V1-S+S1+2*P+2*K)*C185-P*C186+-(S1+K)*C165=0
*	-(V1-S+P)*C185+(V1-S+S1+2*P+2*K)*C186-P*C187+-(S1+K)*C166=0
*	-(V1-S+P)*C186+(V1-S+S1+2*P+2*K)*C187-P*C188+-(S1+K)*C167=0
*	-(V1-S+P)*C187+(V1-S+S1+2*P+2*K)*C188-P*C189+-(S1+K)*C168=0
*	-(V1-S+P)*C188+(V1-S+S1+2*P+2*K)*C189-P*C190+-(S1+K)*C169=0
*	-(V1-S+P)*C189+(V1-S+S1+2*P+2*K)*C190-P*C191+-(S1+K)*C170=0
*	-(V1-S+P)*C190+(V1-S+S1+2*P+2*K)*C191-P*C192+-(S1+K)*C171=0
*	-(V1-S+P)*C191+(V1-S+S1+2*P+2*K)*C192-P*C193+-(S1+K)*C172=0
*	-(V1-S+P)*C192+(V1-S+S1+2*P+2*K)*C193-P*C194+-(S1+K)*C173=0
*	-(V1-S+P)*C193+(V1-S+S1+2*P+2*K)*C194-P*C195+-(S1+K)*C174=0
*	-(V1-S+P)*C194+(V1-S+S1+2*P+2*K)*C195-P*C196+-(S1+K)*C175=0
*	-(V1-S+P)*C195+(V1-S+S1+2*P+2*K)*C196-P*C197+-(S1+K)*C176=0
*	-(V1-S+P)*C196+(V1-S+S1+2*P+2*K)*C197-P*C198+-(S1+K)*C177=0
*	-(V1-S+P)*C197+(V1-S+S1+2*P+2*K)*C198-P*C199+-(S1+K)*C178=0
*	-(V1-S+P)*C198+(V1-S+S1+2*P+2*K)*C199-P*C200+-(S1+K)*C179=0
*	-(V1-S+P)*C199+(V1-S+S1+2*K+P)*C200+-(S1+K)*C180=0

St	Rule
*	AC1=((C1+C181)*V1+(C21+C161)*V2+(C41+C141)*V3+(C61+C121)*V4+(C81+C101)*V5)/(V1+V2+V3+V4+V5)/2
*	AC2=((C2+C182)*V1+(C22+C162)*V2+(C42+C142)*V3+(C62+C122)*V4+(C82+C102)*V5)/(V1+V2+V3+V4+V5)/2
*	AC3=((C3+C183)*V1+(C23+C163)*V2+(C43+C143)*V3+(C63+C123)*V4+(C83+C103)*V5)/(V1+V2+V3+V4+V5)/2
*	AC4=((C4+C184)*V1+(C24+C164)*V2+(C44+C144)*V3+(C64+C124)*V4+(C84+C104)*V5)/(V1+V2+V3+V4+V5)/2
*	AC5=((C5+C185)*V1+(C25+C165)*V2+(C45+C145)*V3+(C65+C125)*V4+(C85+C105)*V5)/(V1+V2+V3+V4+V5)/2
*	AC6=((C6+C186)*V1+(C26+C166)*V2+(C46+C146)*V3+(C66+C126)*V4+(C86+C106)*V5)/(V1+V2+V3+V4+V5)/2
*	AC7=((C7+C187)*V1+(C27+C167)*V2+(C47+C147)*V3+(C67+C127)*V4+(C87+C107)*V5)/(V1+V2+V3+V4+V5)/2
*	AC8=((C8+C188)*V1+(C28+C168)*V2+(C48+C148)*V3+(C68+C128)*V4+(C88+C108)*V5)/(V1+V2+V3+V4+V5)/2
*	AC9=((C9+C189)*V1+(C29+C169)*V2+(C49+C149)*V3+(C69+C129)*V4+(C89+C109)*V5)/(V1+V2+V3+V4+V5)/2
*	AC10=((C10+C190)*V1+(C30+C170)*V2+(C50+C150)*V3+(C70+C130)*V4+(C90+C110)*V5)/(V1+V2+V3+V4+V5)/2
*	AC11=((C11+C191)*V1+(C31+C171)*V2+(C51+C151)*V3+(C71+C131)*V4+(C91+C111)*V5)/(V1+V2+V3+V4+V5)/2
*	AC12=((C12+C192)*V1+(C32+C172)*V2+(C52+C152)*V3+(C72+C132)*V4+(C92+C112)*V5)/(V1+V2+V3+V4+V5)/2
*	AC13=((C13+C193)*V1+(C33+C173)*V2+(C53+C153)*V3+(C73+C133)*V4+(C93+C113)*V5)/(V1+V2+V3+V4+V5)/2
*	AC14=((C14+C194)*V1+(C34+C174)*V2+(C54+C154)*V3+(C74+C134)*V4+(C94+C114)*V5)/(V1+V2+V3+V4+V5)/2
*	AC15=((C15+C195)*V1+(C35+C175)*V2+(C55+C155)*V3+(C75+C135)*V4+(C95+C115)*V5)/(V1+V2+V3+V4+V5)/2
*	AC16=((C16+C196)*V1+(C36+C176)*V2+(C56+C156)*V3+(C76+C136)*V4+(C96+C116)*V5)/(V1+V2+V3+V4+V5)/2
*	AC17=((C17+C197)*V1+(C37+C177)*V2+(C57+C157)*V3+(C77+C137)*V4+(C97+C117)*V5)/(V1+V2+V3+V4+V5)/2
*	AC18=((C18+C198)*V1+(C38+C178)*V2+(C58+C158)*V3+(C78+C138)*V4+(C98+C118)*V5)/(V1+V2+V3+V4+V5)/2
*	AC19=((C19+C199)*V1+(C39+C179)*V2+(C59+C159)*V3+(C79+C139)*V4+(C99+C119)*V5)/(V1+V2+V3+V4+V5)/2
*	AC20=((C20+C200)*V1+(C40+C180)*V2+(C60+C160)*V3+(C80+C140)*V4+(C100+C120)*V5)/(V1+V2+V3+V4+V5)/2
*	B20=C20
*	B40=C40
*	B60=C60
*	B80=C80
*	B100=C100
*	B120=C120
*	B140=C140
*	B160=C160
*	B180=C180
*	B200=C200

Appendix H Summary of Air Infiltration Data

Crack Type	Rectangular crack						Rectangular crack					
Crack Length	60 mm						60 mm					
Crack Height	0.508 mm						0.406 mm					
Crack Width	100 mm						100 mm					
Test Run	Test 1		Test 2		Test 3		Test 1		Test 2		Test 3	
Run No.	ΔP	Q	ΔP	Q	ΔP	Q	ΔP	Q	ΔP	Q	ΔP	Q
	(Pa)	(L/min)	(Pa)	(L/min)	(Pa)	(L/min)	(Pa)	(L/min)	(Pa)	(L/min)	(Pa)	(L/min)
1	0.0	0.02	0.0	0.03	-0.1	0.02	0.3	0.01	0.2	0.01	0.0	0.01
2	0.7	0.07	0.6	0.06	0.9	0.08	0.9	0.04	0.6	0.03	1.5	0.04
3	1.3	0.10	1.2	0.09	1.4	0.11	1.8	0.06	1.4	0.05	1.7	0.06
4	1.6	0.12	1.7	0.13	1.7	0.12	1.9	0.07	1.8	0.07	2.0	0.07
5	2.3	0.16	2.4	0.16	2.3	0.16	2.9	0.09	3.0	0.09	2.4	0.09
6	2.9	0.20	3.4	0.22	2.9	0.20	3.0	0.11	3.7	0.12	3.0	0.11
7	3.6	0.23	4.0	0.26	3.5	0.23	4.2	0.13	4.2	0.14	4.0	0.13
8	4.2	0.26	4.6	0.29	4.1	0.26	4.2	0.15	4.8	0.16	4.5	0.15
9	5.1	0.32	4.8	0.30	5.2	0.32	5.2	0.18	5.3	0.16	5.7	0.18
10	5.8	0.37	5.6	0.35	5.7	0.35	6.4	0.20	6.0	0.19	5.9	0.19
11	6.5	0.40	6.4	0.38	6.2	0.37	6.8	0.22	6.4	0.21	6.9	0.21
12	6.7	0.41	6.7	0.40	6.9	0.42	6.8	0.23	6.8	0.22	7.0	0.23
13	7.6	0.46	7.5	0.45	7.5	0.45	7.9	0.25	7.6	0.25	7.5	0.25
14	8.0	0.48	8.0	0.46	8.0	0.48	8.3	0.26	8.0	0.25	8.5	0.26
15	8.6	0.51	8.9	0.53	8.6	0.50	9.2	0.28	9.4	0.29	8.7	0.28
16	9.2	0.54	9.5	0.55	9.2	0.54	9.6	0.30	9.7	0.31	9.7	0.30
17	9.9	0.57	10.2	0.59	9.8	0.57	10.3	0.31	10.3	0.32	10.1	0.31
18	10.4	0.60	10.7	0.62	10.5	0.60	10.8	0.33	11.3	0.34	10.5	0.33
19	11.0	0.63	11.3	0.65	11.1	0.64	11.2	0.35	11.6	0.36	11.1	0.35
20	11.6	0.66	11.9	0.68	11.8	0.67	12.0	0.37	12.2	0.38	12.3	0.37
21	12.5	0.71	12.3	0.70	12.6	0.71	13.0	0.39	12.4	0.39	12.8	0.39
22	13.0	0.74	13.0	0.74	12.9	0.73	13.0	0.41	13.5	0.41	13.4	0.40
23	13.6	0.77	13.8	0.79	13.8	0.79	13.7	0.43	13.9	0.44	14.3	0.44
24	14.1	0.81	14.5	0.82	14.4	0.82	14.3	0.45	14.6	0.46	14.9	0.46
25	14.9	0.85	14.8	0.84	14.7	0.84	15.4	0.47	14.9	0.46	15.1	0.46

Crack Type	Rectangular crack						Rectangular crack					
Crack Length	60 mm						60 mm					
Crack Height	0.305 mm						0.203 mm					
Crack Width	100 mm						100 mm					
Test Run	Test 1		Test 2		Test 3		Test 1		Test 2		Test 3	
Run No.	ΔP	Q	ΔP	Q	ΔP	Q	ΔP	Q	ΔP	Q	ΔP	Q
	(Pa)	(L/min)	(Pa)	(L/min)	(Pa)	(L/min)	(Pa)	(L/min)	(Pa)	(L/min)	(Pa)	(L/min)
1	0.6	0.026	0.9	0.026	0.3	0.026	0.2	0.009	0.1	0.009	0.1	0.009
2	1.4	0.039	1.1	0.026	1.3	0.039	0.9	0.014	1.1	0.014	0.4	0.014
3	2.1	0.039	1.6	0.039	1.9	0.039	1.8	0.014	1.2	0.014	1.1	0.014
4	2.7	0.039	2.3	0.039	2.3	0.039	1.9	0.014	2.0	0.018	1.6	0.018
5	2.9	0.052	2.9	0.052	3.2	0.052	2.5	0.018	2.6	0.018	2.2	0.018
6	4.0	0.052	3.5	0.052	3.8	0.052	2.9	0.018	3.7	0.023	2.4	0.023
7	4.3	0.065	4.3	0.065	4.6	0.065	4.2	0.023	4.2	0.023	2.9	0.023
8	5.1	0.065	4.9	0.065	5.3	0.065	4.8	0.023	5.0	0.027	4.0	0.023
9	5.6	0.065	5.8	0.078	5.5	0.065	5.6	0.023	5.1	0.027	4.1	0.027
10	6.4	0.078	6.4	0.078	6.1	0.078	5.9	0.027	5.7	0.027	5.3	0.027
11	6.8	0.078	6.9	0.078	6.6	0.078	6.9	0.027	6.4	0.032	6.1	0.032
12	7.7	0.091	7.6	0.091	7.4	0.091	7.1	0.032	7.1	0.032	6.6	0.032
13	8.0	0.091	8.4	0.091	7.9	0.091	7.8	0.032	8.1	0.036	7.0	0.036
14	8.9	0.104	8.9	0.104	8.5	0.104	8.4	0.036	8.0	0.036	7.9	0.041
15	9.2	0.104	9.6	0.104	9.4	0.117	9.0	0.036	9.4	0.036	8.1	0.041
16	10.2	0.104	9.9	0.104	10.1	0.117	9.5	0.036	9.9	0.041	9.0	0.041
17	10.8	0.117	10.6	0.117	10.4	0.117	10.1	0.041	10.3	0.041	9.3	0.045
18	11.5	0.117	11.5	0.117	11.2	0.13	10.7	0.041	10.8	0.045	9.9	0.045
19	11.8	0.117	12.0	0.13	11.7	0.13	11.3	0.041	11.5	0.045	10.6	0.050
20	12.7	0.13	12.7	0.13	12.3	0.143	11.7	0.045	12.1	0.045	11.4	0.050
21	13.3	0.13	13.3	0.13	13.2	0.143	13.1	0.045	12.9	0.050	11.9	0.050
22	13.6	0.143	13.8	0.143	13.9	0.143	13.4	0.050	13.2	0.050	12.9	0.050
23	14.2	0.143	14.5	0.143	14.0	0.143	14.1	0.052	14.1	0.054	13.2	0.054
24	14.8	0.143	15.2	0.156	15.0	0.156	14.4	0.057	15.1	0.061		
25							15.1	0.060				

Crack Type	Rectangular crack						Rectangular crack					
Crack Length	30 mm						30 mm					
Crack Height	0.508 mm						0.406 mm					
Crack Width	100 mm						100 mm					
Test Run	Test 1		Test 2		Test 3		Test 1		Test 2		Test 3	
Run No.	ΔP	Q	ΔP	Q	ΔP	Q	ΔP	Q	ΔP	Q	ΔP	Q
	(Pa)	(L/min)	(Pa)	(L/min)	(Pa)	(L/min)	(Pa)	(L/min)	(Pa)	(L/min)	(Pa)	(L/min)
1	0.1	0.04	0.1	0.04	-0.1	0.03	0.6	0.02	0.6	0.02	-0.1	0.02
2	0.9	0.13	0.8	0.12	0.6	0.1	1.1	0.07	1.4	0.07	1.0	0.06
3	1.0	0.14	1.2	0.16	1.0	0.15	1.2	0.08	1.4	0.09	1.3	0.08
4	1.7	0.21	2.0	0.24	1.8	0.22	1.8	0.12	2.3	0.13	2.2	0.12
5	2.3	0.27	2.8	0.33	2.3	0.28	2.6	0.15	3.2	0.18	2.5	0.15
6	3.4	0.39	3.3	0.38	3.2	0.37	3.4	0.21	3.3	0.21	3.2	0.20
7	3.6	0.42	4.0	0.46	3.9	0.46	4.1	0.23	4.1	0.25	4.4	0.25
8	4.3	0.49	4.6	0.53	4.3	0.5	4.9	0.27	4.7	0.29	4.6	0.28
9	4.9	0.56	5.1	0.58	4.9	0.57	5.2	0.31	5.4	0.32	5.4	0.31
10	5.5	0.63	5.8	0.65	5.6	0.64	6.0	0.35	6.3	0.36	5.9	0.35
11	6.0	0.68	6.4	0.73	6.1	0.68	6.2	0.37	7.0	0.40	6.2	0.37
12	6.9	0.77	6.9	0.77	7.1	0.79	7.2	0.42	7.0	0.42	7.3	0.43
13	7.4	0.81	7.6	0.85	7.5	0.84	7.9	0.45	7.6	0.47	7.5	0.46
14	8.0	0.89	8.3	0.93	8.0	0.9	8.1	0.49	8.8	0.51	8.0	0.50
15	9.0	1.01	8.8	0.99	8.8	1	9.5	0.56	9.4	0.54	9.3	0.55
16	9.3	1.04	9.4	1.07	9.5	1.09	9.4	0.57	9.5	0.59	9.6	0.60
17	9.9	1.12	9.9	1.12	10.2	1.16	10.1	0.62	10.1	0.62	10.6	0.64
18	10.5	1.19	10.7	1.22	10.6	1.2	11.0	0.65	10.9	0.67	10.8	0.66
19	11.5	1.31	11.3	1.29	11.1	1.26	11.6	0.72	11.4	0.71	11.1	0.69
20	12.0	1.36	12.0	1.37	11.7	1.33	12.5	0.75	12.0	0.75	12.2	0.73
21	12.3	1.4	12.4	1.41	12.3	1.4	12.4	0.77	12.9	0.78	12.7	0.77
22	13.3	1.51	13.2	1.5	13.2	1.5	13.6	0.83	13.6	0.83	13.3	0.83
23	13.7	1.55	13.8	1.56	13.6	1.54	13.9	0.85	14.3	0.86		
24	14.2	1.6	14.3	1.61	14.3	1.62	14.5	0.88	14.8	0.89		
25	14.9	1.67	14.9	1.68	14.9	1.68	15.1	0.92	14.9	0.92		

Crack Type	Rectangular crack						Rectangular crack					
Crack Length	30 mm						30 mm					
Crack Height	0.305 mm						0.203 mm					
Crack Width	100 mm						100 mm					
Test Run	Test 1		Test 2		Test 3		Test 1		Test 2		Test 3	
Run No.	ΔP	Q	ΔP	Q	ΔP	Q	ΔP	Q	ΔP	Q	ΔP	Q
	(Pa)	(L/min)	(Pa)	(L/min)	(Pa)	(L/min)	(Pa)	(L/min)	(Pa)	(L/min)	(Pa)	(L/min)
1	0.3	0.036	0.0	0.024	0.2	0.024	0.7	0.012	0.3	0.012	0.4	0.012
2	0.5	0.036	0.5	0.036	0.6	0.036	1.0	0.012	1.2	0.018	1.2	0.018
3	1.2	0.048	1.3	0.048	1.3	0.048	1.7	0.018	2.0	0.024	1.9	0.024
4	1.8	0.06	1.9	0.06	2.2	0.072	2.6	0.024	2.7	0.024	2.6	0.024
5	2.5	0.084	2.7	0.084	2.6	0.084	3.3	0.029	3.3	0.029	3.3	0.029
6	3.4	0.096	3.3	0.096	3.1	0.084	3.9	0.029	3.9	0.035	3.6	0.035
7	3.5	0.096	3.9	0.108	3.7	0.108	4.4	0.035	4.3	0.035	4.3	0.035
8	4.4	0.12	4.3	0.12	4.4	0.12	5.0	0.041	4.9	0.041	5.2	0.041
9	4.9	0.132	4.9	0.132	5.2	0.132	5.6	0.041	5.8	0.047	5.8	0.047
10	5.7	0.144	5.7	0.144	5.7	0.144	6.3	0.047	6.3	0.047	6.3	0.053
11	6.1	0.156	6.2	0.156	6.1	0.156	6.9	0.053	6.8	0.053	7.0	0.053
12	7.1	0.168	6.7	0.168	7.0	0.168	7.4	0.053	7.3	0.059	7.5	0.059
13	7.5	0.18	7.7	0.192	7.5	0.18	7.9	0.059	8.0	0.059	8.2	0.065
14	8.1	0.192	8.2	0.192	8.0	0.192	8.5	0.065	8.5	0.065	8.9	0.065
15	8.8	0.204	8.7	0.204	8.5	0.204	9.4	0.071	9.6	0.071	9.2	0.071
16	9.2	0.216	9.5	0.228	9.1	0.216	9.9	0.071	10.0	0.076	9.8	0.076
17	9.8	0.228	10.0	0.24	10.1	0.24	10.4	0.076	10.5	0.076	10.6	0.076
18	10.3	0.24	10.6	0.252	10.7	0.252	10.9	0.076	11.3	0.082	11.0	0.082
19	11.0	0.252	11.3	0.264	11.1	0.252	12.1	0.082	11.7	0.088	11.9	0.088
20	11.6	0.264	11.6	0.264	11.8	0.276	12.4	0.088	12.6	0.088	12.5	0.088
21	12.3	0.276	12.4	0.288	12.2	0.276	13.0	0.094	12.8	0.094	13.0	0.094
22	12.8	0.288	13.0	0.3	12.8	0.288	13.7	0.094	13.8	0.100	13.6	0.100
23	13.5	0.312	13.6	0.312	13.6	0.3	14.4	0.100	14.1	0.103	14.3	0.100
24	14.1	0.324	14.5	0.324	14.3	0.324	14.8	0.100	15.0	0.106	15.2	0.106
25	14.8	0.336	15.3	0.336	15.0	0.336						

Crack Type	L-shaped crack						L-shaped crack					
Crack Length	60 mm						60 mm					
Crack Height	0.508 mm						0.406 mm					
Crack Width	100 mm						100 mm					
Test Run	Test 1		Test 2		Test 3		Test 1		Test 2		Test 3	
Run No.	ΔP (Pa)	Q (L/min)	ΔP (Pa)	Q (L/min)	ΔP (Pa)	Q (L/min)	ΔP (Pa)	Q (L/min)	ΔP (Pa)	Q (L/min)	ΔP (Pa)	Q (L/min)
1	0.0	0.03	0.6	0.04	0.5	0.02	0.0	-0.01	-0.2	0.00	-0.3	-0.01
2	1.1	0.07	1.0	0.06	1.1	0.08	0.4	0.01	0.2	0.02	1.1	0.04
3	1.8	0.10	1.6	0.10	1.7	0.12	1.6	0.03	0.8	0.04	1.3	0.05
4	1.9	0.13	1.9	0.13	1.8	0.14	1.8	0.05	1.4	0.06	1.9	0.05
5	2.8	0.18	2.4	0.19	2.7	0.18	2.6	0.08	2.6	0.08	2.0	0.08
6	3.2	0.22	3.7	0.23	3.4	0.21	2.6	0.10	3.1	0.10	2.6	0.10
7	3.7	0.24	4.6	0.27	3.6	0.23	4.0	0.10	4.2	0.11	3.7	0.11
8	4.2	0.29	5.0	0.31	4.4	0.27	3.6	0.12	4.2	0.14	4.2	0.14
9	5.2	0.33	5.2	0.30	5.3	0.33	4.9	0.17	5.0	0.14	5.3	0.16
10	5.9	0.37	6.0	0.35	6.2	0.35	6.3	0.20	5.5	0.16	5.6	0.19
11	6.8	0.42	6.8	0.40	6.6	0.38	6.7	0.20	6.0	0.20	6.3	0.18
12	7.0	0.43	7.2	0.41	7.4	0.43	6.5	0.21	6.4	0.20	6.7	0.21
13	8.1	0.49	7.8	0.47	7.9	0.46	7.8	0.23	7.1	0.23	7.3	0.23
14	8.4	0.48	8.5	0.48	8.4	0.48	7.7	0.24	7.8	0.25	8.1	0.25
15	8.8	0.52	9.1	0.53	8.8	0.52	9.0	0.27	9.1	0.27	8.4	0.25
16	9.4	0.56	9.9	0.56	9.6	0.54	9.3	0.29	9.3	0.30	9.4	0.28
17	10.1	0.59	10.3	0.60	9.9	0.59	10.0	0.31	10.1	0.32	9.9	0.30
18	10.5	0.61	11.2	0.64	11.0	0.63	10.2	0.32	10.8	0.34	10.1	0.32
19	11.6	0.64	11.6	0.65	11.6	0.67	11.1	0.34	11.2	0.33	10.6	0.33
20	12.1	0.68	12.2	0.71	12.2	0.68	11.8	0.34	11.6	0.37	11.7	0.35
21	12.6	0.71	12.5	0.72	13.0	0.73	12.5	0.37	12.4	0.37	12.4	0.36
22	13.5	0.76	13.5	0.75	13.2	0.74	12.8	0.41	13.1	0.39	13.0	0.39
23	13.9	0.78	14.2	0.81	14.2	0.80	13.2	0.40	13.7	0.42	13.8	0.43
24	14.6	0.81	15.0	0.84	14.4	0.83	14.0	0.43	14.0	0.44	14.5	0.45
25	15.3	0.87	15.4	0.85	15.2	0.86	14.9	0.45	14.5	0.45	14.9	0.46

Crack Type	L-shaped crack						L-shaped crack					
Crack Length	60 mm						60 mm					
Crack Height	0.305 mm						0.203 mm					
Crack Width	100 mm						100 mm					
Test Run	Test 1		Test 2		Test 3		Test 1		Test 2		Test 3	
Run No.	ΔP	Q	ΔP	Q	ΔP	Q	ΔP	Q	ΔP	Q	ΔP	Q
	(Pa)	(L/min)	(Pa)	(L/min)	(Pa)	(L/min)	(Pa)	(L/min)	(Pa)	(L/min)	(Pa)	(L/min)
1	0.3	0.001	0.4	0.004	0.0	0.001	0.3	0.003	0.1	0.000	0.7	0.007
2	1.2	0.011	0.9	0.004	1.1	0.003	1.5	0.011	1.7	0.010	0.9	0.009
3	2.0	0.014	1.3	0.009	1.3	0.004	2.3	0.005	1.7	0.008	1.7	0.004
4	2.2	0.017	1.8	0.013	2.1	0.011	2.5	0.007	2.3	0.010	1.9	0.011
5	2.9	0.024	2.3	0.025	2.8	0.014	2.9	0.010	2.8	0.012	2.7	0.010
6	3.5	0.044	3.2	0.035	3.6	0.025	3.0	0.010	4.1	0.020	3.0	0.020
7	4.2	0.040	4.3	0.042	4.5	0.033	4.2	0.021	4.5	0.022	3.5	0.022
8	4.9	0.053	4.5	0.048	4.7	0.038	5.3	0.021	5.1	0.018	4.2	0.021
9	5.0	0.061	5.4	0.060	5.2	0.048	6.2	0.015	5.4	0.027	4.2	0.022
10	6.0	0.074	6.1	0.065	5.6	0.053	6.1	0.020	6.2	0.025	5.8	0.022
11	6.5	0.073	6.6	0.075	6.0	0.059	7.2	0.019	6.7	0.023	6.5	0.031
12	7.6	0.088	7.1	0.079	7.1	0.069	7.3	0.025	7.5	0.031	6.9	0.030
13	7.5	0.092	7.9	0.089	7.8	0.078	8.1	0.022	8.5	0.034	7.4	0.034
14	8.7	0.101	8.6	0.099	8.4	0.085	8.7	0.029	8.5	0.028	8.0	0.036
15	9.1	0.112	9.6	0.108	9.2	0.100	9.2	0.029	9.5	0.031	8.5	0.035
16	10.0	0.118	9.5	0.110	9.5	0.105	9.8	0.031	10.3	0.033	9.6	0.039
17	10.2	0.130	10.5	0.122	10.4	0.116	10.5	0.032	10.6	0.032	9.7	0.044
18	11.3	0.137	11.3	0.129	10.7	0.128	11.0	0.038	11.1	0.042	10.2	0.036
19	11.2	0.155	11.8	0.139	11.2	0.135	11.7	0.034	11.7	0.036	10.8	0.044
20	12.1	0.162	12.3	0.154	12.1	0.137	11.7	0.036	12.5	0.045	11.8	0.048
21	12.8	0.164	12.8	0.163	13.2	0.147	13.6	0.044	13.1	0.043	12.4	0.043
22	13.4	0.172	13.5	0.163	13.8	0.155	13.8	0.047	13.8	0.047	13.5	0.049
23	14.2	0.183	14.2	0.177	13.9	0.165	14.3	0.047	14.4	0.046	13.4	0.052
24	14.5	0.184	14.9	0.181	14.6	0.172	14.6	0.054	15.3	0.058		
25							15.5	0.054				

Appendix I Summary of Aerosol Generator Data

Aerosol Material Atomizer Flow Rate Cond. Chimney	22°C DEHS 1.90 sLpm 29 mm																			
Test Number	Test 1					Test 2					Test 3					Test 4				
Run Number Channel Midpoint	Run 1 Conc.	Run 2 Conc.	Run 3 Conc.	Run 4 Conc.	Run 5 Conc.	Run 1 Conc.	Run 2 Conc.	Run 3 Conc.	Run 4 Conc.	Run 5 Conc.	Run 1 Conc.	Run 2 Conc.	Run 3 Conc.	Run 4 Conc.	Run 5 Conc.	Run 1 Conc.	Run 2 Conc.	Run 3 Conc.	Run 4 Conc.	Run 5 Conc.
<0.523	277588.0	278725.0	281190.0	288825.0	289170.0	311217.0	315052.0	311720.0	324708.0	313974.0	215304.0	215450.0	208981.0	238747.0	263382.0	262699.0	257704.0	260340.0	259065.0	263267.0
0.542	46313.7	46185.8	46120.2	48156.9	45576.0	47501.1	47388.6	47393.1	48336.2	46815.8	44178.5	44096.8	43101.3	46105.5	47411.7	46543.5	46599.9	46211.4	46300.8	46804.8
0.583	50117.8	49607.0	49441.1	48545.6	47351.7	49577.9	49224.8	49742.8	47385.9	48700.4	52821.0	51910.7	51506.9	53017.9	52650.4	51779.3	51988.1	52042.7	51974.6	51856.7
0.626	47738.6	48943.1	48687.1	45364.6	43841.3	45801.3	45045.0	45918.3	42198.4	44248.5	59857.5	59913.8	58137.9	58114.9	52888.9	51193.4	52032.5	52901.2	52243.1	51547.7
0.673	39363.4	38576.2	38607.7	38832.3	38032.1	38714.2	38454.2	38303.2	32255.4	34808.7	54759.4	54172.3	54947.8	50866.6	47454.3	46363.9	46445.1	47361.4	46633.5	46335.1
0.723	29887.3	27997.8	27718.8	29966.6	24506.2	25706.5	24292.0	25108.0	21390.2	23606.0	47340.9	46730.1	48152.9	42079.9	37702.0	36245.4	36539.0	37714.3	37086.8	35428.4
0.777	17045.7	16301.1	16331.7	14865.4	13873.8	14836.9	13589.1	14291.1	11982.4	13076.4	34251.8	33794.3	36300.0	29887.3	24669.8	22383.2	23893.3	25025.5	24205.9	22678.8
0.835	8295.1	7925.5	8051.5	7115.6	6802.9	7231.1	6356.6	6787.0	5319.2	6128.3	20981.9	20450.9	21755.8	16814.3	13630.9	11986.6	12937.5	13877.8	13159.5	12155.2
0.898	3783.8	3561.8	3682.9	3214.7	2920.4	3282.2	2918.9	3040.7	2457.6	2858.8	11394.4	11282.5	12082.3	8641.9	6717.2	5791.7	6322.1	6786.1	6456.3	5840.2
0.965	1647.3	1539.6	1590.3	1389.9	1400.7	1729.2	1757.1	1606.2	1757.1	1725.6	6376.2	6384.8	6770.7	3941.0	2964.6	2473.8	2727.9	2999.6	2804.3	2908.0
1.037	1108.4	1209.0	1123.8	1577.7	1440.3	1564.0	1720.5	1726.8	1916.1	1777.5	2469.0	2455.8	2673.6	1767.8	1408.8	1184.7	1246.2	1373.4	1285.8	1188.9
1.114	2024.1	2231.4	2000.7	2318.4	2739.8	1476.3	1479.3	1671.3	1419.0	1531.2	1127.4	1111.2	1223.7	997.5	970.2	896.7	734.4	789.8	808.5	823.8
1.197	2744.4	2899.7	2920.1	2690.7	3053.3	1200.3	1133.7	1287.6	1013.4	1158.3	704.7	701.7	731.7	975.3	1357.5	1574.7	1214.1	1118.4	1185.3	1361.5
1.286	2368.7	2324.4	2447.7	2131.2	2223.0	903.8	802.2	921.9	883.4	833.1	957.0	1008.2	865.5	1494.1	1657.5	1805.1	1627.3	1668.9	1740.6	1770.8
1.382	1672.8	1693.2	1851.8	1510.8	1608.3	624.9	580.5	645.3	451.8	531.0	1378.2	1502.4	1539.0	1725.0	1618.8	1577.4	1713.6	1812.0	1691.7	1823.0
1.488	1256.1	1208.4	1363.8	1085.7	1142.1	432.3	337.2	407.4	239.7	348.0	1365.3	1570.2	1694.7	1483.7	1342.5	1218.3	1385.1	1536.9	1322.7	1312.8
1.596	787.5	671.4	758.7	580.5	644.8	258.0	170.4	184.5	127.2	168.8	1150.2	1370.7	1512.0	1204.2	981.0	894.4	1014.3	1152.0	983.6	995.7
1.715	218.4	174.3	208.1	153.3	143.1	98.4	80.7	85.8	73.5	80.7	674.1	779.4	920.1	680.3	496.5	390.1	503.1	559.5	512.4	480.6
1.843	90.0	78.5	78.0	75.0	67.8	74.1	72.0	68.1	71.4	68.4	463.8	496.2	643.5	423.3	213.9	188.1	218.0	273.0	256.2	212.7
1.981	66.7	63.9	74.4	57.9	66.6	74.7	61.8	65.1	62.4	72.0	186.6	231.9	316.2	166.0	98.1	81.6	94.8	95.4	104.1	90.9
2.129	60.0	52.8	66.0	56.4	63.3	66.3	65.1	61.5	66.0	61.8	89.7	99.9	100.2	73.5	74.4	80.3	85.7	82.1	80.4	71.4
2.288	54.0	48.9	57.9	53.1	52.5	59.4	56.8	57.5	53.6	56.2	71.4	64.5	71.7	62.7	63.9	60.0	64.8	63.9	64.5	59.4
2.458	45.3	47.4	51.0	48.3	57.9	60.4	66.3	61.8	54.6	54.6	60.0	63.0	53.4	54.9	56.7	51.0	54.6	54.6	53.4	50.7
2.642	41.4	44.1	42.0	41.1	44.4	43.8	46.9	43.8	46.3	52.2	53.7	47.1	52.8	50.4	47.1	50.1	44.7	42.3	44.1	46.5
2.839	39.3	44.1	39.8	44.7	43.8	46.2	46.2	42.9	45.3	43.8	51.0	44.7	47.7	39.3	50.1	51.9	51.6	39.6	43.5	38.7
3.051	43.8	39.0	38.6	45.0	40.2	45.9	47.7	46.2	47.1	40.2	44.4	42.9	43.2	39.6	49.5	44.1	45.0	44.4	49.5	47.7
3.278	44.1	38.7	33.9	39.3	38.7	39.9	45.6	39.6	43.5	44.7	41.1	46.5	45.9	47.4	45.9	48.9	46.2	46.9	47.1	46.2
3.523	38.7	39.0	39.3	40.2	36.4	39.6	37.2	42.0	41.1	39.0	43.5	37.8	45.6	33.6	41.1	40.5	43.8	39.9	43.2	40.5
3.786	35.7	33.3	43.8	34.8	37.5	44.4	39.4	36.6	43.8	36.1	34.8	35.7	32.4	36.6	41.7	36.3	43.3	40.5	36.9	40.8
4.066	29.8	29.1	33.9	33.6	32.4	31.5	36.6	33.0	33.9	30.9	28.5	35.1	36.1	34.5	33.0	34.2	36.0	36.3	30.6	36.6
4.371	29.4	30.6	23.4	25.5	29.4	34.5	28.2	33.6	30.3	33.3	31.2	31.8	29.4	37.8	29.1	32.7	35.7	30.0	31.5	33.3
4.698	27.0	29.7	23.1	24.9	28.1	29.4	24.6	28.8	32.7	29.7	29.8	31.2	28.5	30.3	26.4	30.0	28.5	27.6	28.2	23.7
5.046	23.1	23.1	19.8	25.2	21.8	22.8	25.2	21.9	23.7	24.9	24.3	19.2	25.8	24.6	20.4	26.1	18.5	25.2	29.7	24.9
5.425	21.8	21.0	18.9	19.5	20.1	25.5	23.7	18.9	21.3	19.8	25.8	24.9	21.0	27.3	25.2	21.8	23.4	29.1	21.0	23.1
5.829	23.1	16.3	18.6	18.3	20.4	18.0	21.9	17.7	18.6	21.3	18.6	20.4	20.4	22.8	23.7	22.8	20.7	17.1	20.7	23.4
6.264	15.9	19.8	18.6	19.8	19.5	16.9	22.5	17.1	23.1	17.1	17.7	23.7	24.0	25.2	20.7	17.4	19.2	17.1	21.3	17.1
6.732	18.6	17.4	15.6	17.4	16.2	16.8	20.4	19.5	16.5	18.9	15.0	18.9	18.9	20.4	18.6	18.3	19.8	17.4	22.2	19.2
7.234	18.6	15.0	19.2	16.2	18.3	18.6	18.3	18.5	15.9	13.8	15.0	21.3	17.4	15.9	20.4	18.6	16.2	19.8	15.9	13.8
7.774	13.2	17.1	18.5	14.4	15.6	18.0	12.3	16.8	18.3	12.9	12.6	17.1	20.4	19.8	16.8	14.1	15.6	15.3	18.3	14.7
8.364	15.3	14.1	19.8	13.5	15.9	11.4	10.8	13.8	15.6	14.4	17.4	17.1	13.5	13.5	15.6	14.4	12.3	15.9	12.0	12.9
8.977	14.7	9.0	9.9	11.1	12.9	10.8	13.8	11.1	12.3	10.8	12.6	13.2	11.4	11.1	8.7	10.8	12.0	8.4	15.6	12.0
9.647	9.0	7.8	9.3	15.0	8.4	9.9	11.1	10.5	12.0	7.8	9.3	11.1	12.3	8.3	11.1	11.1	9.0	11.1	9.9	8.7
10.370	8.7	12.0	9.6	8.9	8.9	10.2	7.8	9.4	7.2	8.1	12.3	8.6	7.2	11.1	8.7	7.5	8.6	9.0	8.7	9.0
11.140	7.2	8.3	11.4	8.3	9.9	7.8	7.8	8.6	7.5	7.2	10.2	7.2	8.1	9.0	8.7	8.6	8.4	9.0	8.6	8.6
11.970	8.0	8.9	8.9	10.2	8.7	8.1	7.2	7.8	7.2	8.1	8.0	8.7	8.9	8.9	8.0	4.8	8.3	7.5	8.9	9.4
12.860	8.9	7.5	8.6	8.3	7.2	7.2	8.4	8.1	8.0	8.3	8.0	8.3	8.1	8.7	8.3	8.4	2.7	8.3	7.2	9.4
13.820	8.9	8.7	8.7	8.6	7.2	4.5	4.8	7.2	8.4	8.9	8.1	8.7	8.6	4.5	4.8	3.6	8.4	4.8	4.5	8.7
14.880	8.1	8.4	3.9	8.4	2.7	8.0	8.4	8.1	3.9	8.7	4.2	2.4	3.9	4.2	3.0	4.8	4.5	3.0	4.2	4.5
15.960	3.0	4.2	8.0	4.5	8.4	8.0	3.9	3.6	8.1	8.0	4.5	3.3	4.8	2.7	8.0	3.0	3.0	4.2	3.9	2.4
17.150	4.8	4.8	4.8	4.5	4.2	8.1	4.5	3.0	4.2	8.7	4.8	8.7	2.7	3.3	8.9	4.2	3.6	3.0	2.1	4.8
18.430	2.7	3.6	4.5	8.3	4.5	8.0	8.7	3.9	8.1	4.5	4.8	4.5	3.6	2.1	4.5	3.6	1.8	3.9	3.3	3.3
19.810	3.0	2.1	1.8	3.9	4.2	2.1	3.9	3.6	3.0	4.8	2.7	2.4	3.3	4.8	4.2	4.8	2.1	3.6	2.1	3.6

Aerosol Material	22°C DEHS																			
Atomizer Flow Rate	2.28 sLpm																			
Cond. Chimney	20 mm																			
Test Number	Test 1					Test 2					Test 3					Test 4				
Run Number	Run 1	Run 2	Run 3	Run 4	Run 5	Run 1	Run 2	Run 3	Run 4	Run 5	Run 1	Run 2	Run 3	Run 4	Run 5	Run 1	Run 2	Run 3	Run 4	Run 5
Channel Midpoint	Conc.	Conc.	Conc.	Conc.	Conc.	Conc.	Conc.	Conc.	Conc.	Conc.	Conc.	Conc.	Conc.	Conc.	Conc.	Conc.	Conc.	Conc.	Conc.	Conc.
<0.523	66981.2	71389.2	81943.4	81373.4	86529.7	103392.0	107943.0	97778.1	102440.0	104389.0	51189.8	66059.9	76907.7	87768.8	95818.1	84443.0	90832.1	95828.2	89838.9	87160.0
0.542	17647.4	18980.5	21198.5	20782.3	21870.8	24579.7	25138.8	23081.8	24278.1	24597.1	14082.2	18138.1	20739.8	23298.7	25077.1	20744.8	21051.2	22558.3	21108.5	20413.7
0.583	23272.9	24981.7	27382.9	26800.8	28065.3	30899.4	31132.8	28814.3	30324.3	30339.1	18880.4	24544.0	27584.8	31220.7	33301.4	25940.8	25821.1	28085.4	26097.4	25219.0
0.626	28702.8	31091.4	33504.5	32470.8	34087.4	36027.8	36172.4	33236.9	35039.3	35311.7	24126.7	30987.0	34927.1	39079.3	41253.7	30158.4	29007.3	32361.1	29863.5	28990.2
0.673	33119.6	35699.9	38293.6	36484.7	38391.1	38880.4	38662.0	35839.3	37543.9	37982.8	28803.3	36848.3	40932.4	45373.8	47526.2	32036.4	30471.8	34013.3	31566.1	30832.7
0.723	35624.0	38298.4	40298.8	37803.7	39612.7	38360.5	37897.8	35108.8	36857.5	37101.8	32084.0	40307.8	43982.0	48597.8	50343.8	31011.6	29414.4	32780.5	30312.0	29863.2
0.777	33470.3	35721.2	38571.1	34284.5	35785.0	32587.4	31549.2	29782.4	31449.0	31527.3	30972.0	38272.3	41316.1	44965.2	48018.8	26012.2	24459.7	27910.4	25482.7	25150.3
0.836	27104.5	28700.7	28849.8	26581.3	27943.2	24017.5	23012.2	22097.1	23108.5	23195.2	28048.2	31218.8	33040.7	36549.3	35746.1	18909.8	17875.9	19871.6	18307.4	18368.2
0.896	20261.3	21292.7	20835.1	19048.7	19946.1	16214.7	15395.7	15035.7	15818.9	15987.8	20369.3	23471.8	24303.7	25588.9	25627.1	12839.9	11893.3	13113.6	12205.6	12370.9
0.960	12874.5	13548.2	12960.3	11836.9	12002.2	9327.4	8878.2	8820.7	9035.5	9022.9	13482.0	15018.8	15296.4	15863.9	15466.0	7360.4	6873.5	7481.8	7001.6	7313.9
1.037	7820.5	8174.2	7995.3	6982.5	7088.5	5174.6	4948.9	4999.1	5078.3	5117.6	8489.1	9102.7	9103.0	9093.2	8863.0	4114.7	3888.7	4132.4	3967.8	4148.8
1.114	4217.3	4295.4	3982.1	3688.2	3957.9	2582.4	2413.8	2483.3	2511.0	2538.6	4804.3	4781.0	4874.5	4867.8	4469.3	2189.8	1985.3	2106.7	2085.6	2170.5
1.197	2320.2	2318.7	2084.1	1896.0	1912.5	1412.4	1324.5	1371.9	1371.0	1416.6	2682.2	2609.7	2639.2	2412.9	2319.9	1225.5	1165.3	1227.9	1209.6	1240.5
1.286	1269.4	1252.5	1128.6	1085.9	1061.1	843.6	788.9	814.8	837.3	808.4	1477.5	1366.0	1291.2	1236.9	1234.5	816.9	766.5	821.4	810.6	831.9
1.382	815.4	773.7	736.3	704.7	718.1	610.8	630.3	629.1	627.6	629.4	887.1	844.8	820.5	729.9	749.4	687.0	658.9	686.2	686.3	680.7
1.496	670.8	639.3	651.9	605.1	629.4	612.9	648.0	616.8	606.3	644.4	666.6	670.8	626.1	615.3	655.2	679.2	685.8	697.2	680.3	699.8
1.596	647.4	640.2	652.5	706.5	682.4	660.5	669.4	764.1	801.0	929.4	917.1	981.8	838.5	1061.8	1276.5	972.6	960.1	1239.6	1071.3	816.3
1.715	822.8	987.9	1308.4	1546.0	1661.8	2090.1	3218.0	1994.7	2767.7	2770.4	706.0	1214.1	1754.4	2013.3	1903.8	2669.5	2537.7	3471.5	2935.1	2077.2
1.843	2716.8	3259.4	4264.1	3982.9	4444.7	6484.4	7421.0	5669.7	6521.3	6478.3	2112.6	3096.8	2600.3	3259.4	2736.1	6143.0	6633.5	6833.0	6362.9	6060.2
1.991	7241.8	7451.9	7383.1	6044.0	7978.5	9435.7	9678.7	10899.8	9686.8	9780.8	5124.2	6021.5	4868.2	4463.3	3423.2	10471.0	12097.0	10181.2	10911.7	11984.4
2.129	9844.8	8824.0	7745.3	9032.8	7982.4	7298.0	8984.4	9112.8	7987.2	7299.2	8403.7	7109.9	5432.8	3943.4	3496.4	12182.4	12474.4	10001.5	11243.8	12327.4
2.296	8194.9	6789.4	5484.2	6039.5	4825.8	3004.1	2335.8	3623.1	3179.3	2745.0	10473.4	9831.2	9102.0	2783.3	2618.7	5983.3	6375.8	4400.0	5871.5	5444.0
2.456	2834.9	2250.0	1491.7	1623.8	1087.2	466.8	318.8	822.0	460.9	386.9	5289.4	2279.8	2278.2	1143.9	1196.8	985.2	858.2	884.5	1075.8	706.8
2.642	288.9	286.3	183.0	192.0	163.2	114.9	106.3	129.7	108.0	103.5	571.5	263.7	397.8	236.8	251.7	129.6	126.3	117.9	148.5	121.8
2.839	78.9	74.7	66.1	67.2	62.1	58.4	52.8	48.8	65.5	64.3	96.7	81.0	78.0	64.8	69.8	45.9	51.0	44.1	51.6	52.8
3.061	47.4	48.0	42.6	46.3	42.6	39.0	36.3	33.9	41.1	39.7	49.2	50.4	47.7	48.3	48.0	40.2	38.0	36.4	33.9	39.0
3.270	40.2	39.1	40.8	38.4	39.4	34.2	36.6	32.7	36.0	32.7	39.6	36.0	36.6	44.7	44.7	23.4	27.3	30.6	28.5	27.9
3.523	27.3	30.9	32.1	30.0	35.1	29.1	32.4	31.5	36.4	32.1	28.5	37.8	30.0	37.5	36.0	32.1	26.4	24.6	33.9	28.2
3.796	27.9	27.3	34.5	29.4	33.0	30.3	27.0	27.6	32.7	21.8	28.5	28.5	32.4	31.5	36.3	25.8	28.2	26.4	27.0	25.5
4.088	21.0	30.3	26.1	22.8	22.5	23.4	26.1	24.3	25.8	24.3	24.6	26.1	24.3	36.4	29.7	23.7	27.6	24.0	21.9	20.7
4.371	23.4	29.5	25.5	27.3	21.6	18.6	25.8	20.4	19.8	25.5	24.9	20.7	24.9	24.0	31.2	19.8	22.8	19.5	21.3	17.7
4.699	20.1	20.1	22.8	17.7	20.4	21.6	22.8	18.6	19.5	19.8	19.8	19.8	22.8	24.3	21.6	20.7	18.5	17.4	16.8	19.8
5.048	20.4	16.2	24.8	19.8	18.3	14.4	21.6	16.2	17.4	14.4	18.3	21.6	19.8	20.4	22.5	15.0	17.7	20.7	16.2	14.1
5.425	16.2	13.5	18.6	16.2	19.8	16.8	16.3	17.7	11.4	15.0	14.4	13.2	16.2	18.9	21.6	10.8	10.5	15.3	14.7	11.1
5.829	9.6	14.7	14.4	19.2	18.6	17.7	14.4	15.3	16.2	13.8	11.4	15.6	16.2	18.6	18.9	14.1	13.2	12.9	9.6	14.7
6.264	13.2	16.5	13.5	12.6	12.6	16.8	15.0	12.3	10.5	9.9	13.5	12.9	10.8	14.1	18.6	11.1	12.9	12.6	10.5	12.0
6.732	15.0	9.3	12.9	16.2	14.7	14.4	11.1	12.3	12.3	15.0	11.4	11.4	16.8	15.0	18.3	12.0	11.7	11.1	10.2	8.7
7.234	10.8	13.5	16.5	12.6	10.5	15.3	12.0	12.9	16.2	14.7	10.2	15.0	12.9	13.8	13.8	13.2	12.6	12.9	9.3	9.3
7.774	13.2	14.4	16.5	12.6	9.6	13.5	13.2	14.4	11.1	15.3	12.3	12.9	10.8	14.1	15.3	10.5	10.2	12.0	7.5	8.1
8.354	11.4	10.5	12.3	10.2	8.7	11.7	10.9	11.7	9.9	12.3	12.6	10.2	11.4	12.6	15.0	7.5	9.6	8.7	9.9	7.2
8.977	11.1	9.3	12.9	11.4	13.5	11.4	12.3	11.1	11.4	10.8	12.9	10.8	11.7	10.5	12.0	7.8	8.4	8.1	9.9	9.6
9.647	8.4	8.4	8.7	8.4	9.0	10.5	8.7	10.5	7.8	9.6	8.9	14.4	9.6	8.7	11.4	3.6	8.1	7.8	6.0	9.3
10.370	10.8	6.9	9.6	9.0	6.9	11.7	8.7	9.6	11.4	7.2	8.4	7.8	7.2	7.5	8.1	8.1	11.4	7.5	7.8	8.1
11.140	9.9	9.4	7.5	7.8	8.1	7.5	8.4	4.8	11.1	6.3	8.1	7.8	6.9	7.2	9.9	6.0	8.7	8.1	6.3	7.2
11.970	7.5	8.6	6.3	8.7	7.2	9.0	4.2	7.2	8.7	8.1	8.4	7.5	6.0	7.8	8.6	7.8	5.4	5.4	5.7	4.5
12.860	6.6	6.9	7.5	4.8	6.0	6.0	6.0	6.3	5.7	3.9	6.0	7.5	6.0	4.5	7.2	4.5	5.4	6.3	3.3	5.4
13.820	4.8	6.9	3.0	4.2	5.1	5.4	5.1	4.8	4.8	6.6	4.5	3.0	6.9	4.8	6.6	4.8	4.2	6.0	3.8	6.3
14.960	3.6	7.5	4.8	3.9	7.8	4.2	5.1	3.6	5.7	3.9	4.8	6.0	6.0	3.3	4.2	6.9	3.3	4.8	5.7	5.1
16.960	2.7	3.6	3.6	3.9	3.9	4.8	3.0	4.5	3.0	3.6	4.5	3.6	5.1	5.1	2.7	3.9	6.6	5.7	6.3	1.8
17.180	3.0	4.5	2.4	4.2	3.9	3.3	3.6	3.6	4.2	3.6	4.8	4.5	3.0	4.2	2.7	3.0	1.8	4.5	2.4	4.2
18.430	4.2	3.3	3.6	3.3	5.7	3.6	3.9	3.6	3.6	3.0	2.7	1.8	3.9	4.2	3.0	3.3	3.3	2.4	2.1	3.6
19.810	4.8	2.4	4.2	2.7	1.8	2.1	3.0	1.8	2.4	2.7	1.8	2.4	7.8	2.7	2.4	1.2	4.5	2.7	2.1	1.8

Aerosol Material	22°C DEHS																			
Atomizer Flow Rate	2.89 aLpm																			
Cond. Chimney	29 mm																			
Test Number	Test 1					Test 2					Test 3					Test 4				
Run Number	Run 1	Run 2	Run 3	Run 4	Run 5	Run 1	Run 2	Run 3	Run 4	Run 5	Run 1	Run 2	Run 3	Run 4	Run 5	Run 1	Run 2	Run 3	Run 4	Run 5
Channel Midpoint	Conc.	Conc.	Conc.	Conc.	Conc.	Conc.	Conc.	Conc.	Conc.	Conc.	Conc.	Conc.	Conc.	Conc.	Conc.	Conc.	Conc.	Conc.	Conc.	Conc.
<0.523	595.5	636.9	605.7	600.3	605.1	423.0	472.2	523.5	589.5	592.2	1389.6	617.4	614.7	587.7	585.3	508.1	504.9	496.0	480.6	504.3
0.542	21.6	20.4	19.8	21.3	24.3	10.8	12.6	19.5	20.1	15.0	216.6	30.9	35.4	26.4	24.9	13.8	9.9	15.9	15.9	15.9
0.583	27.6	25.5	28.2	32.7	32.4	15.6	19.5	25.2	21.0	24.6	261.3	39.3	43.8	32.4	33.0	18.0	17.4	18.9	20.7	18.0
0.626	41.4	36.9	34.8	43.8	36.6	25.2	25.5	30.0	30.6	30.3	291.9	50.4	51.6	41.1	46.2	27.0	25.5	28.2	28.2	28.2
0.673	53.1	55.5	54.9	58.5	53.1	33.3	32.1	36.1	44.4	46.5	302.4	63.9	71.4	57.6	60.1	32.4	32.1	36.6	33.6	43.2
0.723	78.9	74.4	76.8	70.5	70.5	40.2	42.6	58.4	67.5	64.2	282.0	78.9	82.8	64.2	68.1	39.6	48.0	57.0	45.9	51.3
0.777	86.7	94.2	93.9	108.0	92.7	48.0	62.1	80.3	86.1	88.1	275.4	96.3	92.7	87.0	79.5	64.5	57.3	55.5	62.7	73.8
0.835	120.0	118.5	123.3	132.3	120.6	66.0	70.5	86.1	103.5	90.9	215.7	120.6	117.0	107.7	108.3	77.1	74.1	82.8	81.3	90.6
0.898	157.8	151.8	159.3	168.6	155.4	84.6	95.4	102.0	133.8	123.9	196.9	137.1	132.3	138.0	129.6	97.5	107.1	101.4	105.9	105.3
0.965	200.4	194.1	198.0	192.0	198.0	89.1	113.1	132.6	173.1	161.7	203.1	176.4	179.7	169.8	148.5	143.7	120.6	129.9	124.8	120.3
1.037	233.1	244.2	258.0	266.1	246.9	122.4	144.3	186.0	242.1	205.5	218.1	210.6	210.9	211.8	202.5	207.9	195.4	154.5	177.3	176.1
1.114	287.4	288.3	303.9	334.2	316.2	150.3	169.8	227.7	268.8	256.5	261.0	265.8	254.7	261.6	255.3	262.2	214.2	196.2	186.9	206.7
1.197	404.1	411.9	419.7	440.4	447.9	177.0	216.9	287.4	393.6	356.2	339.3	342.3	319.5	326.4	328.8	290.1	256.8	258.9	243.9	278.1
1.286	558.3	536.4	548.1	612.3	567.1	249.3	287.7	370.5	547.2	452.7	447.9	445.8	464.7	448.2	426.0	330.9	314.7	325.2	309.6	324.9
1.382	823.5	809.4	859.8	911.1	866.4	345.3	411.9	545.4	788.0	700.5	626.4	646.5	680.7	670.8	640.8	462.6	428.4	445.8	467.4	510.3
1.486	1416.0	1368.0	1471.2	1599.6	1439.1	519.6	647.7	897.0	1306.5	1119.0	1051.2	1063.2	1080.5	1057.2	1043.4	717.0	671.4	734.7	748.5	829.2
1.599	2986.4	2890.4	3226.5	3427.1	3192.2	896.4	1188.9	1639.8	2690.1	2364.0	2031.3	2085.0	2072.4	2025.3	1991.7	1237.2	1247.4	1283.4	1329.0	1470.3
1.715	23475.1	18638.8	28528.2	31779.9	24270.1	1298.1	1849.2	3773.0	27859.8	14164.8	3972.8	4150.4	4398.2	4228.4	4061.0	1796.1	1896.8	1945.2	2077.2	2426.1
1.843	135358.0	128352.0	142288.0	146354.0	138822.0	5634.8	20020.1	56299.3	135786.0	106308.0	45891.3	54373.6	57091.9	54130.9	51679.7	11869.6	15057.9	16728.3	20025.5	29210.7
1.981	89131.8	78685.7	87790.2	93095.3	85530.1	59136.6	113615.0	134730.0	71278.5	101824.0	137059.0	135423.0	136466.0	137291.0	140823.0	101831.0	110470.0	115857.0	125120.0	127948.0
2.129	3981.8	4348.4	3257.3	3000.8	3322.4	109206.0	63456.2	22265.6	3855.2	6167.6	28281.8	24895.6	22297.1	23161.6	22253.6	82875.4	72093.4	64859.0	54365.3	46861.8
2.288	1156.2	1227.0	1095.9	1102.5	1149.9	18973.5	4145.8	1944.3	1200.6	1324.8	2414.1	2098.2	1992.6	2046.9	2027.7	4889.9	4999.5	3800.8	3435.5	3139.7
2.458	477.6	515.1	456.9	420.6	470.4	1774.5	1103.1	648.4	531.8	618.9	866.7	906.0	839.4	864.6	882.6	1266.9	1183.2	1148.4	1044.3	1063.8
2.642	136.5	161.1	137.1	141.0	145.5	777.9	444.0	262.6	157.5	189.9	308.7	268.8	275.1	267.3	272.4	560.4	507.3	462.9	424.2	386.7
2.839	64.8	60.0	63.0	63.9	65.7	180.0	117.3	81.0	57.0	64.8	83.7	82.5	91.5	81.0	79.2	127.2	119.1	113.4	96.3	112.8
3.051	46.6	44.7	45.0	45.9	39.6	68.1	51.9	45.6	41.4	44.7	43.8	52.2	53.4	48.9	36.4	44.1	64.5	54.6	52.8	53.4
3.278	46.5	50.7	37.8	45.0	45.3	47.4	43.5	45.6	44.1	44.1	43.2	40.8	42.6	45.6	43.2	44.1	50.1	44.7	44.4	46.5
3.523	41.1	44.4	38.4	38.7	37.2	40.2	33.3	42.6	44.4	43.8	43.8	41.7	36.0	45.6	38.4	46.8	39.9	41.1	39.3	39.6
3.786	33.3	27.0	33.0	27.3	34.5	37.5	37.8	31.8	33.6	36.0	34.2	36.9	38.4	33.9	33.6	35.7	40.8	37.8	40.2	36.3
4.068	21.8	22.7	16.4	23.0	18.5	27.0	31.2	22.1	24.5	19.7	23.8	22.4	26.7	30.0	25.2	30.0	32.4	26.7	27.9	30.0
4.371	11.6	12.9	18.1	15.3	13.5	21.1	19.0	18.8	15.9	13.5	16.2	17.1	15.9	17.4	15.9	22.3	23.6	14.7	19.0	20.5
4.698	10.8	9.9	11.4	11.4	10.2	14.2	9.3	10.8	10.5	13.0	11.8	8.0	9.6	12.1	13.0	9.9	9.6	9.9	9.0	12.4
5.048	3.2	8.8	9.2	8.2	9.2	7.9	8.8	8.5	8.8	8.5	6.9	6.4	9.5	8.2	6.6	6.3	6.3	6.6	7.9	8.2
5.429	8.4	10.0	8.4	8.1	8.4	5.5	8.7	10.6	6.8	7.4	6.1	9.4	10.3	9.0	3.9	6.6	6.1	7.4	6.1	5.8
5.829	6.7	7.7	6.0	8.0	6.7	6.7	6.7	6.7	8.0	7.3	5.3	8.0	5.7	6.7	5.3	9.0	5.0	7.0	6.0	4.7
6.264	2.1	7.2	5.5	6.2	5.5	4.5	4.8	4.1	6.2	7.2	5.9	7.9	5.2	8.3	6.6	5.5	6.9	6.2	4.8	4.1
6.732	3.6	3.9	6.7	4.9	6.4	3.5	6.4	6.1	6.7	4.9	4.9	4.6	3.9	4.9	9.2	5.6	4.2	7.1	2.8	8.1
7.234	3.7	4.4	6.6	5.1	4.0	4.4	4.4	6.6	5.5	7.7	6.6	4.6	4.4	5.5	6.2	3.7	4.6	4.4	4.6	5.9
7.774	4.2	9.9	4.9	4.2	6.6	6.5	5.7	9.5	4.2	3.6	4.9	8.7	6.5	9.1	3.4	6.1	6.5	4.6	4.2	3.8
8.354	4.7	4.7	4.3	4.3	4.7	5.1	6.3	6.7	3.6	4.7	6.7	5.1	6.3	7.5	3.6	6.3	5.1	7.5	5.1	5.1
8.977	4.9	4.1	2.9	2.9	7.0	3.7	4.5	6.6	6.6	2.9	5.6	6.6	4.1	6.6	3.7	3.3	2.9	4.5	4.1	4.9
9.647	5.6	2.1	1.3	4.7	4.3	4.3	4.3	5.1	3.4	6.4	5.1	4.3	5.6	2.6	3.0	3.9	5.6	5.6	3.4	6.0
10.370	4.9	1.8	1.8	3.6	1.6	6.3	3.1	4.5	5.6	5.4	4.0	4.0	6.1	3.1	3.1	6.3	2.7	5.4	4.0	2.2
11.140	4.6	1.9	3.6	3.6	3.6	1.4	6.7	4.6	3.6	2.9	5.2	3.6	5.2	4.6	5.2	1.4	4.3	4.6	3.6	2.9
11.970	3.0	1.0	4.5	3.5	1.5	2.5	3.5	3.0	5.0	5.0	3.0	3.0	5.5	3.0	5.0	6.5	5.0	4.0	6.0	6.5
12.860	4.3	6.4	2.1	3.7	3.7	3.7	3.7	3.2	1.1	6.4	5.4	4.3	3.2	2.1	3.7	2.1	5.4	3.7	4.3	4.3
13.820	2.3	4.5	3.4	1.7	4.0	4.0	4.5	2.6	2.3	5.7	4.0	2.3	2.3	4.0	2.3	6.2	2.3	5.1	4.0	4.0
14.880	1.2	4.6	1.6	3.0	1.2	2.4	3.6	7.2	3.6	3.0	2.4	4.2	3.0	4.2	3.0	5.4	1.2	3.6	2.4	3.0
15.980	0.0	1.9	4.5	3.6	2.6	5.3	5.1	5.1	1.3	2.6	5.7	1.9	4.5	3.2	3.2	2.6	4.5	6.3	6.4	3.2
17.150	2.6	1.4	0.7	2.6	2.6	5.6	3.5	2.6	4.2	4.2	2.6	7.0	3.5	0.0	2.6	2.6	2.1	4.2	4.2	3.5
18.430	3.0	3.7	3.7	1.5	5.2	4.5	4.5	4.5	3.0	3.7	3.7	3.7	0.7	2.2	3.7	5.2	3.0	5.2	0.7	6.0
19.810	5.7	4.9	4.1	2.4	0.8	2.4	0.8	3.2	3.2	3.2	1.6	4.1	0.0	4.9	4.1	4.1	0.8	3.2	7.3	5.7

Aerosol Material Atomizer Flow Rate Cond. Chimney	22°C DEHS 3.73 sLpm 25 mm																			
Test Number	Test 1					Test 2					Test 3					Test 4				
Run Number	Run 1	Run 2	Run 3	Run 4	Run 5	Run 1	Run 2	Run 3	Run 4	Run 5	Run 1	Run 2	Run 3	Run 4	Run 5	Run 1	Run 2	Run 3	Run 4	Run 5
Channel Midpoint	Conc.	Conc.	Conc.	Conc.	Conc.	Conc.	Conc.	Conc.	Conc.	Conc.	Conc.	Conc.	Conc.	Conc.	Conc.	Conc.	Conc.	Conc.	Conc.	Conc.
<0.523	27103.3	25629.8	25802.2	25549.6	25826.2	13115.1	20854.9	27330.7	32271.3	35115.5	37291.1	39012.4	39184.2	39200.8	38687.9	41532.4	41662.0	39913.9	40201.3	39939.7
0.542	110.7	102.3	98.7	102.0	102.6	82.4	86.4	122.1	137.1	144.3	174.6	183.9	181.8	176.7	172.6	241.2	241.8	227.1	225.3	210.9
0.583	136.3	134.1	134.7	132.0	140.4	84.3	121.5	153.3	177.6	196.8	225.6	237.6	261.0	250.2	235.8	330.9	320.1	286.5	298.2	284.7
0.626	196.2	196.8	188.4	185.4	177.3	123.3	163.8	208.8	253.8	273.9	304.5	336.3	343.8	335.4	337.5	446.2	447.3	392.4	395.2	383.4
0.673	286.2	254.1	261.0	258.9	245.1	180.0	232.2	296.7	354.0	382.8	452.1	478.2	492.0	487.5	482.4	636.0	610.8	567.3	569.1	568.9
0.723	406.2	393.6	375.3	378.9	360.1	248.1	327.0	420.0	510.0	560.2	663.6	696.0	716.1	699.3	705.9	919.5	884.1	858.6	858.3	813.9
0.777	590.7	580.2	537.6	571.5	567.6	356.2	513.0	617.7	797.4	848.7	1020.0	1070.1	1042.5	1037.4	1056.3	1370.4	1371.9	1247.1	1342.8	1235.4
0.835	937.2	850.2	811.5	883.8	843.3	533.7	716.7	945.3	1161.0	1298.1	1502.1	1590.6	1600.2	1607.7	1605.3	2139.9	2046.6	1954.2	1997.7	1929.0
0.898	1461.0	1327.8	1209.6	1292.1	1285.2	830.7	1109.7	1468.5	1823.7	2090.1	2322.0	2454.9	2487.3	2507.7	2493.6	3307.4	3271.4	3057.8	3223.7	2998.7
0.965	2215.2	1983.3	1903.5	1986.2	1966.2	1228.5	1713.0	2238.9	2782.7	3117.8	3658.1	3850.7	3933.8	3860.0	3843.6	5308.7	5229.8	4820.3	5091.2	4768.1
1.037	3491.3	3316.7	3081.2	3146.0	3089.9	1907.7	2711.4	3587.6	4503.5	5050.4	5915.6	6152.9	6370.7	6295.4	6229.4	8895.8	8710.9	8136.4	8327.8	7875.4
1.114	5437.1	5088.5	4731.2	4885.7	4775.6	2915.9	4215.2	5598.5	6906.2	8016.1	9467.5	10010.5	10096.9	10278.4	10039.9	15074.4	14752.2	13421.7	13998.6	12921.8
1.197	9429.4	8745.7	8091.1	8428.9	8298.4	4736.3	7139.3	9589.9	12387.4	14469.6	17843.6	19047.8	19582.1	19627.4	19011.8	33232.1	32173.8	28244.4	30112.2	29953.6
1.286	17144.7	15568.5	14446.8	14944.8	14965.9	7845.4	12650.1	17997.2	25627.9	31704.9	42217.9	45721.2	47905.7	48145.7	46910.4	82360.1	79911.8	70682.2	75167.4	69979.1
1.382	31150.5	45291.9	39131.8	42853.2	41665.8	17085.0	33735.5	56503.4	83539.0	99512.2	119536.0	122950.0	126564.0	126184.0	124288.0	132647.0	132273.0	132611.0	134804.0	132449.0
1.486	142850.0	136092.0	128107.0	132041.0	128914.0	61503.6	115608.0	150205.0	158529.0	152362.0	136518.0	130480.0	128963.0	128543.0	128914.0	81184.1	84559.9	97232.6	90678.5	101270.0
1.598	141308.0	154156.0	163112.0	156941.0	157045.0	196453.0	175254.0	133484.0	93408.2	74557.8	54125.2	48743.6	46029.0	46871.9	48419.3	25003.3	28151.4	31243.2	28049.4	33284.3
1.715	33849.7	37372.1	43911.6	40290.1	43249.8	99341.2	55708.5	31811.1	20988.8	17092.8	13373.4	12706.8	12461.8	12609.6	12770.7	9122.5	9348.7	10096.9	9573.1	10507.6
1.843	11936.2	12701.7	13787.1	13201.8	13757.1	24118.9	14657.4	11084.7	9016.6	8132.2	7181.3	7208.6	6898.4	7001.9	7049.0	6319.2	6404.7	6824.7	6485.7	6006.9
1.981	6237.2	6650.0	7064.6	6836.9	7027.7	6963.8	6909.3	5833.3	4823.2	4036.4	3801.8	3428.6	3373.4	3328.7	3467.6	2739.3	2789.0	2899.4	2812.7	3071.9
2.129	2460.3	2646.9	2801.0	2789.5	2874.2	3974.3	2721.0	2154.3	1827.8	1734.6	1605.3	1627.2	1610.7	1627.2	1663.2	1489.2	1551.9	1496.4	1475.1	1572.9
2.288	1075.2	1097.4	1200.0	1148.4	1173.3	1428.6	1101.6	954.9	841.2	840.0	828.8	875.7	864.0	870.0	858.9	896.4	891.3	854.1	840.6	879.9
2.458	548.1	556.2	601.2	581.7	594.3	651.3	517.5	449.1	443.1	481.8	485.4	491.7	511.2	513.0	492.3	582.9	566.5	533.1	552.3	563.4
2.642	312.3	309.3	336.1	324.9	328.5	336.9	280.5	253.5	287.1	297.6	323.7	318.9	332.1	352.5	346.2	408.6	394.5	401.1	388.8	376.5
2.839	175.8	168.0	191.7	179.1	183.9	172.5	170.7	171.3	198.9	200.4	219.9	267.1	236.1	237.0	252.6	332.7	309.6	293.1	310.2	295.2
3.051	137.4	120.3	115.2	127.2	132.9	102.6	114.3	123.9	140.4	184.8	182.1	208.1	193.2	209.4	207.3	298.8	274.8	245.4	280.4	247.2
3.278	99.0	91.8	93.6	88.5	100.8	77.4	80.4	95.7	117.6	135.0	164.1	176.1	178.5	180.3	158.1	247.2	244.8	205.5	238.5	213.3
3.523	66.3	63.3	61.5	64.2	69.0	48.8	60.9	78.3	95.1	101.7	106.2	134.7	133.5	138.9	150.0	192.6	203.7	174.6	177.6	165.9
3.786	49.5	49.5	48.3	43.2	58.7	34.5	36.3	51.6	60.3	78.3	100.2	99.9	106.5	105.6	102.9	167.4	154.8	138.6	144.6	131.4
4.068	33.6	31.2	34.5	29.1	30.3	20.0	27.3	41.8	44.5	53.9	62.4	65.5	68.7	77.6	69.1	104.2	111.2	98.8	100.0	78.5
4.371	29.4	29.4	20.2	20.8	20.8	18.4	20.8	25.1	32.1	39.2	44.4	45.0	47.8	48.1	48.7	69.8	75.0	60.5	63.1	62.8
4.699	25.4	25.7	22.6	20.7	20.7	13.3	17.6	20.7	27.2	30.3	40.2	40.5	37.7	41.8	34.6	57.2	48.9	50.4	43.9	43.9
5.048	23.7	16.7	21.8	20.8	18.6	11.7	18.9	23.1	26.2	30.3	29.4	33.2	33.2	35.7	27.8	48.9	46.4	41.4	42.9	41.1
5.425	21.0	16.8	16.5	17.7	17.7	9.4	17.1	19.7	21.3	25.5	33.9	34.2	30.3	28.4	31.0	42.6	44.5	38.4	39.4	34.2
5.829	16.7	14.3	14.3	17.0	18.7	9.7	16.3	16.7	18.3	30.3	29.0	29.3	30.0	28.0	31.3	46.3	36.3	44.0	38.7	39.7
6.264	17.2	17.2	19.3	12.4	22.4	11.0	12.1	19.7	23.1	22.4	30.7	31.0	28.3	30.0	23.8	43.4	50.7	37.2	45.5	33.8
6.732	15.5	15.9	22.2	16.9	18.0	10.9	14.5	19.1	24.4	23.6	32.8	32.1	39.9	31.4	32.8	45.2	50.1	43.4	44.1	40.9
7.234	19.4	16.5	16.5	20.1	20.9	9.9	14.6	16.8	23.0	27.1	32.6	42.1	41.0	31.8	36.2	60.0	59.8	42.8	46.8	40.2
7.774	19.7	16.3	15.9	18.2	15.8	9.9	17.5	20.9	28.1	33.4	35.7	39.1	38.0	37.2	32.3	62.3	50.9	51.3	46.3	48.6
8.354	20.5	15.0	13.8	17.4	20.1	12.8	18.2	20.9	19.3	30.0	37.5	32.0	38.7	33.9	41.4	46.2	44.2	44.8	53.3	41.8
8.977	23.8	20.5	20.5	21.8	16.8	9.5	15.6	18.9	24.7	22.2	31.2	27.5	24.7	34.5	28.7	32.5	38.2	33.3	38.6	34.5
9.647	18.9	18.4	21.9	16.3	20.1	11.1	12.4	13.3	18.4	21.0	20.1	24.4	24.4	21.4	26.1	24.0	23.6	29.6	28.7	27.4
10.370	10.7	18.4	17.9	16.8	19.3	9.0	13.0	18.4	17.9	17.5	17.0	17.0	17.0	18.4	13.9	11.2	14.8	13.0	14.8	18.4
11.140	18.2	12.4	8.1	11.4	12.4	7.1	11.0	12.9	10.0	9.5	8.1	12.4	10.5	12.9	16.7	16.7	18.6	16.2	14.8	14.3
11.970	16.0	12.0	7.5	14.0	14.0	8.0	5.0	11.5	12.5	16.0	14.5	18.5	10.0	14.5	12.5	16.0	17.5	16.5	14.0	13.0
12.860	14.5	11.8	16.6	12.3	8.0	11.2	11.8	11.2	13.4	11.8	7.5	12.9	9.1	10.2	9.1	10.2	10.2	11.2	9.6	12.9
13.820	12.5	12.5	7.4	13.6	10.8	6.8	15.3	10.8	9.1	6.7	8.5	6.2	8.5	11.3	10.8	13.0	10.8	13.0	6.2	13.0
14.880	13.2	8.4	12.6	11.4	15.6	6.0	8.4	9.0	10.8	9.0	9.0	8.4	6.0	10.8	8.4	12.6	8.4	12.6	12.6	10.2
15.990	10.9	12.1	12.1	12.8	9.6	9.6	12.8	9.6	5.7	9.6	6.4	7.7	10.2	5.1	9.6	13.4	12.8	9.6	10.2	7.7
17.180	12.6	13.3	16.7	14.0	12.6	10.5	15.3	12.6	11.9	11.9	13.3	7.7	4.9	7.0	8.4	9.6	10.5	7.0	9.1	8.4
18.430	12.7	13.5	13.5	12.7	6.7	9.0	11.2	12.0	9.7	6.7	6.7	7.5	6.7	5.2	11.2	12.7	9.0	5.2	7.5	13.5
19.810	8.1	13.8	17.0	17.8	12.2	7.3	12.2	13.0	9.7	11.4	8.9	5.7	6.5	10.5	7.3	9.7	11.4	12.2	9.7	8.9

Aerosol Material	22°C DEHS																			
Atomizer Flow Rate	4.42 sLpm																			
Cond. Chimney	25 mm																			
Test Number	Test 1					Test 2					Test 3					Test 4				
Run Number	Run 1	Run 2	Run 3	Run 4	Run 5	Run 1	Run 2	Run 3	Run 4	Run 5	Run 1	Run 2	Run 3	Run 4	Run 5	Run 1	Run 2	Run 3	Run 4	Run 5
Channel Midpoint	Conc.	Conc.	Conc.	Conc.	Conc.	Conc.	Conc.	Conc.	Conc.	Conc.	Conc.	Conc.	Conc.	Conc.	Conc.	Conc.	Conc.	Conc.	Conc.	Conc.
<0.523	130011.0	131445.0	126507.0	132087.0	129238.0	127802.0	131898.0	148027.0	170587.0	188418.0	182520.0	186858.0	178379.0	185219.0	180385.0	193431.0	200037.0	203535.0	204834.0	207421.0
0.542	875.1	926.4	871.8	922.8	891.6	863.4	933.9	1131.0	1440.6	1659.9	1399.5	1313.4	1196.4	1046.7	1026.3	1311.9	1402.8	1452.9	1517.1	1537.5
0.563	1159.5	1184.4	1158.9	1243.5	1171.8	1185.9	1241.7	1494.3	1922.1	2179.8	1769.1	1733.4	1582.8	1391.7	1342.8	1723.5	1890.0	1920.3	1996.8	2059.2
0.626	1613.4	1647.3	1579.8	1693.5	1568.5	1577.4	1713.9	2014.2	2649.8	2918.6	2458.5	2348.3	2124.3	1912.2	1778.7	2295.9	2590.5	2649.9	2753.0	2819.0
0.676	2241.8	2303.7	2217.0	2409.6	2310.9	2296.2	2441.7	2858.0	3702.5	4238.0	3427.7	3283.3	3037.1	2607.0	2511.3	3236.3	3562.7	3623.0	3746.9	3893.0
0.723	3273.2	3357.5	3255.2	3542.1	3395.9	3402.2	3567.8	4208.6	5360.4	6075.5	4906.4	4748.9	4398.5	3825.8	3668.2	4697.7	5080.7	5176.4	5307.5	5497.4
0.777	5097.8	5284.9	5117.9	5601.5	5363.3	5296.1	5691.5	6616.4	8297.2	9215.8	7254.8	7052.3	6514.4	5619.3	5514.8	6763.1	7526.9	7722.8	7861.6	8151.1
0.835	8366.2	8782.3	8401.3	9139.0	8696.2	8799.4	9235.3	10791.4	13292.1	14602.8	11333.5	11034.7	10187.8	9028.0	8733.7	10470.1	11602.0	11739.7	12047.5	12465.4
0.896	14368.2	14980.7	14278.1	15711.3	14922.8	15074.1	16045.2	18784.4	23090.8	25885.3	19527.3	19145.7	18018.8	15158.1	14484.0	16956.1	18722.8	18929.4	19379.3	19908.2
0.966	24987.3	27763.5	27021.4	29556.8	27842.2	27948.0	30122.7	36140.0	45630.9	48746.0	32334.6	31952.4	29348.1	26967.1	25309.3	28708.4	32229.3	32548.4	33458.3	34329.8
1.037	57323.8	59830.2	58435.8	64084.9	59854.2	60549.3	64838.6	73182.0	78266.8	78191.9	58853.1	59140.5	55855.0	51226.7	49614.5	52903.0	58373.7	58296.8	59757.8	59893.1
1.114	94555.4	95602.1	95925.5	98089.2	95925.5	96222.8	96584.8	87399.5	65509.1	54111.4	70748.8	73091.4	77680.7	80656.5	81843.2	73858.4	69448.0	67012.4	64961.9	62971.1
1.197	74948.3	71202.1	75345.6	65722.4	72227.8	71481.4	64170.2	46344.3	29733.3	24392.2	41207.5	43571.1	51814.7	64426.1	68056.2	47793.2	38269.0	36872.3	34985.9	33355.1
1.286	26704.0	24407.2	26210.5	22190.0	24684.4	23655.4	21500.3	17271.9	13982.1	12983.4	18148.7	18514.4	20469.8	24639.7	26360.8	19742.0	17169.8	17211.6	17045.1	16494.3
1.382	11262.7	10918.8	11041.9	10395.7	10957.8	10561.6	10249.3	9561.4	8926.0	8995.9	11206.3	11299.0	11590.6	12268.9	12529.8	11839.8	11025.4	11331.1	10910.8	10885.9
1.486	7253.6	7196.0	7142.9	6992.6	7103.9	6936.2	6606.9	6792.8	6851.9	7085.8	8479.9	8319.1	8402.2	8558.8	8587.9	8868.4	8456.2	8550.1	8491.9	8459.8
1.596	5427.2	5297.9	5251.7	5277.8	5341.1	5161.7	5148.8	5260.4	5408.5	5641.1	6715.4	6548.3	6693.8	6834.1	6858.0	6989.9	6773.9	6827.6	6814.7	6790.7
1.715	4249.1	4208.6	4087.9	4064.0	4159.4	4038.2	4064.6	4228.7	4401.8	4483.3	5303.0	5271.8	5374.1	5185.1	5231.6	5555.3	5458.7	5502.5	5461.4	5424.5
1.843	3371.0	3256.4	3195.5	3277.1	3271.1	3227.0	3229.4	3365.3	3439.7	3564.2	4287.8	4197.2	4263.9	4182.2	4157.6	4414.4	4268.0	4298.3	4326.8	4253.9
1.981	2647.0	2549.4	2491.8	2480.4	2510.4	2457.6	2526.3	2589.6	2719.5	2806.7	3298.1	3260.7	3260.3	3156.2	3173.0	3370.7	3402.8	3404.9	3353.3	3340.4
2.129	1981.2	1958.7	1869.0	1975.8	1945.8	1904.1	1904.4	2073.3	2202.3	2275.2	2600.1	2606.7	2570.1	2485.4	2475.0	2703.0	2682.0	2709.6	2653.5	2671.8
2.286	1588.2	1560.0	1547.1	1536.0	1566.2	1557.9	1562.7	1699.2	1824.8	1904.4	2121.0	2113.8	2108.7	2002.2	1956.3	2196.3	2184.2	2294.4	2190.0	2178.9
2.468	1333.2	1329.4	1299.0	1299.4	1299.0	1299.2	1297.8	1470.9	1560.6	1676.1	1783.8	1825.8	1771.2	1681.5	1677.0	1862.7	1866.3	1883.4	1881.9	1890.9
2.642	1167.3	1224.0	1156.5	1170.3	1154.4	1135.5	1201.5	1307.4	1456.2	1508.3	1633.2	1604.4	1584.3	1476.3	1482.9	1655.4	1669.2	1686.0	1684.5	1686.3
2.839	1131.9	1118.0	1094.1	1113.0	1079.7	1125.0	1131.6	1223.7	1351.5	1442.7	1513.8	1508.4	1464.0	1368.1	1346.4	1554.9	1510.2	1569.3	1561.2	1575.3
3.051	1046.1	1032.6	1036.0	1034.4	1037.4	1038.3	1060.0	1101.6	1268.7	1285.7	1374.3	1325.7	1344.0	1287.6	1320.6	1416.6	1382.4	1404.6	1413.0	1439.7
3.278	916.3	932.1	889.5	915.9	862.6	891.6	907.8	1009.8	1046.7	1001.7	1143.0	1132.5	1125.9	1089.0	1089.9	1179.9	1148.4	1190.4	1165.8	1184.0
3.523	671.1	715.5	694.8	696.7	687.0	693.0	699.1	766.0	687.9	693.8	820.2	820.2	859.8	811.8	821.4	877.2	838.7	848.3	847.2	826.5
3.786	446.1	423.0	412.2	419.4	436.8	407.1	415.5	437.4	432.0	422.1	514.5	500.5	537.0	509.1	540.9	556.8	531.6	548.4	531.6	552.3
4.086	270.0	256.7	253.3	261.2	254.5	261.6	260.6	267.0	307.0	319.1	371.2	345.4	341.5	349.4	334.5	380.0	367.0	382.1	371.2	380.0
4.371	208.1	207.5	200.2	202.6	200.8	193.5	212.4	236.4	263.6	288.4	320.5	289.9	293.9	262.8	246.4	304.6	312.5	307.0	307.0	327.9
4.698	178.6	183.1	180.9	180.9	186.8	188.7	191.7	201.6	233.5	263.5	273.7	244.3	256.7	221.4	223.3	278.3	268.9	257.9	263.2	267.5
5.048	187.9	188.7	183.2	175.9	184.8	171.8	183.5	193.3	234.6	230.8	232.1	241.8	218.8	201.8	214.1	231.2	242.5	256.6	245.7	252.3
5.425	198.1	181.9	162.9	181.8	178.4	171.3	153.9	184.2	213.2	233.2	220.3	221.0	208.5	194.5	188.1	231.9	227.1	224.5	228.1	244.8
5.839	156.7	171.3	176.0	165.0	182.7	187.7	158.7	188.0	190.0	207.3	201.7	218.0	210.0	188.0	188.7	207.7	215.3	194.3	197.0	219.0
6.284	161.0	196.8	166.2	166.2	149.0	154.5	159.7	188.3	186.2	181.7	191.0	197.8	180.7	167.6	168.8	196.2	184.5	182.1	186.9	182.8
6.732	155.6	151.1	164.6	156.3	199.2	146.1	164.1	146.5	152.5	183.8	171.9	188.5	169.1	158.1	162.4	186.1	160.2	158.1	158.5	182.1
7.234	142.3	121.1	118.0	141.2	121.8	130.6	132.8	137.6	115.2	115.6	131.0	142.3	140.9	143.0	148.2	124.4	139.8	133.9	136.8	129.5
7.774	95.7	81.3	87.3	101.0	84.9	100.6	102.9	93.4	86.2	86.8	80.1	98.4	96.8	104.8	104.8	98.7	94.6	87.7	82.4	89.2
8.354	64.3	66.3	66.3	63.2	63.2	66.4	57.2	57.2	54.5	55.3	62.4	68.3	50.1	63.9	67.9	60.0	71.4	70.7	60.8	63.9
8.977	40.7	39.3	41.9	31.2	34.5	44.8	41.1	37.8	39.3	46.0	46.8	49.7	44.4	37.4	41.8	43.6	48.5	47.3	37.8	44.0
9.647	32.8	22.3	26.8	26.3	26.1	23.6	30.4	45.9	32.6	41.6	37.7	33.9	32.6	32.1	32.6	39.4	38.6	37.3	41.1	35.1
10.370	27.8	29.9	32.2	23.3	32.7	33.1	34.5	33.1	44.3	36.3	39.0	42.1	35.8	36.7	33.6	39.4	38.7	40.7	39.4	51.0
11.140	29.5	35.2	37.1	36.7	28.1	31.9	31.9	46.2	46.7	48.1	54.8	40.0	40.0	38.1	35.7	46.2	48.7	44.8	44.8	54.3
11.970	31.0	33.0	42.5	35.5	31.0	37.0	43.0	42.5	40.0	56.0	52.5	51.5	46.0	46.5	45.0	49.0	54.5	52.5	49.5	51.5
12.860	39.1	38.6	37.5	45.5	33.2	27.9	38.0	38.9	52.0	54.1	56.4	48.7	46.0	52.5	35.9	53.6	56.2	54.6	56.8	53.6
13.820	43.6	29.4	42.5	46.3	39.2	31.1	36.8	39.1	56.0	57.7	54.3	47.5	53.8	49.2	59.4	54.3	61.7	47.0	53.2	54.3
14.860	34.8	33.8	42.0	39.8	36.6	37.8	39.8	43.8	46.2	57.0	52.2	48.0	51.8	48.8	48.0	52.8	60.0	58.8	69.0	52.8
15.960	38.7	43.4	37.7	36.4	41.5	29.4	37.7	46.3	42.1	57.4	67.0	51.1	40.9	42.1	38.3	48.5	51.1	53.0	49.8	52.3
17.150	37.7	33.5	28.8	34.2	37.0	41.9	26.5	36.3	50.9	42.8	53.7	58.8	55.1	46.7	44.0	41.9	53.0	53.7	55.1	46.0
18.430	33.7	36.0	37.7	41.2	38.2	29.2	38.2	38.2	42.7	39.0	50.2	47.2	48.5	48.7	51.0	47.2	43.8	48.0	54.7	69.7
19.810	38.9	36.5	34.9	34.9	38.9	32.4	42.2	35.7	50.3	39.7	48.6	39.7	34.1	43.0	39.7	48.6	54.3	34.9	35.7	48.6

Aerosol Material	120°C DEHS																			
Atomizer Flow Rate	1.9 sLpm					2.29 sLpm					2.45 sLpm					2.69 sLpm				
Run Number	Run 1	Run 2	Run 3	Run 4	Run 5	Run 1	Run 2	Run 3	Run 4	Run 5	Run 1	Run 2	Run 3	Run 4	Run 5	Run 1	Run 2	Run 3	Run 4	Run 5
Channel Midpoint	Conc.	Conc.	Conc.	Conc.	Conc.	Conc.	Conc.	Conc.	Conc.	Conc.	Conc.	Conc.	Conc.	Conc.	Conc.	Conc.	Conc.	Conc.	Conc.	Conc.
<0.523	210.5	221.0	240.8	224.0	213.8	1994.0	1859.8	1908.1	1990.8	1920.5	4431.8	3941.2	4119.5	4150.1	4347.3	10550.5	10124.8	9831.7	9808.4	9634.2
0.542	47.6	53.9	49.4	48.2	44.3	427.1	434.3	434.0	414.8	431.6	970.1	884.9	911.3	920.8	913.18	2250.5	2157.8	2111.6	2030.6	2062.8
0.583	90.6	81.7	86.0	88.7	83.9	827.6	806.0	820.1	820.1	821.6	1154.6	1103.3	1110.8	1089.8	1091.0	2673.5	2562.3	2519.6	2483.2	2443.4
0.626	62.0	66.8	68.9	74.0	70.4	614.9	608.3	607.7	587.6	596.3	1330.1	1267.4	1262.9	1299.5	1292.6	3156.5	3034.6	2978.6	2950.5	2839.8
0.673	66.5	76.7	69.1	80.6	83.3	667.1	686.0	663.8	656.7	669.6	1483.4	1422.8	1419.8	1477.1	1466.3	3632.6	3420.5	3399.5	3305.9	3219.2
0.723	77.0	89.4	93.2	86.9	82.7	731.9	730.4	722.0	739.4	726.2	1594.7	1575.6	1552.4	1564.4	1538.3	3951.2	3780.4	3719.9	3658.4	3475.1
0.777	83.0	85.7	95.6	82.4	99.2	747.2	740.3	730.4	731.6	755.3	1662.5	1583.5	1566.0	1581.8	1608.2	4134.8	3914.3	3807.8	3752.6	3596.9
0.836	75.5	90.5	83.3	80.0	84.8	736.1	784.4	756.8	748.4	738.8	1658.9	1670.7	1620.2	1611.2	1592.0	4043.9	3836.4	3788.8	3752.3	3640.4
0.899	82.4	75.2	80.0	83.0	89.3	751.7	729.8	731.3	715.7	726.2	1578.8	1590.2	1607.1	1563.5	1582.1	3991.2	3800.6	3816.8	3629.6	3551.6
0.965	83.8	78.8	78.1	89.8	79.4	674.9	667.4	668.0	677.8	675.2	1508.3	1466.0	1438.4	1456.1	1435.7	3865.6	3629.7	3441.5	3370.7	3323.9
1.037	72.8	78.7	79.4	67.4	71.6	658.4	663.3	669.9	635.9	669.8	1416.8	1393.1	1429.8	1429.5	1411.4	3592.7	3468.5	3407.3	3340.7	3279.2
1.114	64.1	66.8	74.0	65.0	67.1	663.9	675.3	665.7	663.0	670.5	1253.6	1193.0	1253.9	1236.2	1180.4	3120.5	3037.7	2982.8	2985.8	2831.9
1.197	66.3	68.0	60.8	68.0	62.0	672.6	687.9	699.7	612.8	670.5	1274.0	1220.9	1268.4	1267.5	1280.0	3178.7	3067.2	3096.2	2954.3	2873.9
1.286	58.7	70.7	64.1	60.8	61.7	643.5	660.0	634.2	633.3	650.7	1166.6	1139.9	1137.2	1150.7	1115.6	2998.0	2734.4	2656.8	2757.8	2618.9
1.382	61.4	67.4	67.7	68.6	72.2	689.1	688.4	663.8	674.4	675.6	1238.9	1238.3	1189.7	1241.6	1232.6	3159.8	2987.0	2943.5	2948.3	2837.6
1.486	63.2	64.4	72.5	68.0	70.7	621.8	619.1	614.6	610.4	604.4	1342.4	1272.8	1298.6	1312.4	1307.0	3367.4	3185.9	3120.2	3091.4	3014.6
1.599	56.9	69.6	76.7	61.2	66.6	637.1	616.2	621.2	631.1	613.7	1326.2	1336.2	1336.1	1346.7	1327.7	3356.9	3220.7	3153.8	3119.0	3039.2
1.719	53.3	48.8	57.2	61.1	60.8	631.8	497.3	619.2	611.1	606.0	1105.1	1034.9	1065.9	1066.8	1100.0	2850.2	2683.4	2669.9	2603.9	2568.3
1.843	51.2	52.1	53.9	55.1	55.7	489.2	504.5	483.8	471.5	488.3	1098.5	1098.8	1078.9	1083.7	1053.5	2787.5	2696.7	2521.7	2513.0	2435.0
1.991	54.8	59.9	59.3	58.4	61.4	518.6	531.5	534.2	518.9	541.4	1113.2	1078.7	1143.2	1096.5	1115.0	2849.8	2712.8	2633.6	2542.9	2518.1
2.129	51.5	53.0	52.7	58.3	56.8	517.1	499.1	483.5	496.1	498.8	1091.0	1014.8	1078.9	1052.9	1073.8	2714.0	2621.3	2569.4	2504.6	2482.7
2.286	46.7	51.5	56.0	54.5	49.1	481.1	466.6	467.0	484.6	463.1	1003.4	987.2	988.7	1002.5	1005.2	2551.7	2488.0	2405.6	2384.3	2327.9
2.468	39.5	47.9	56.3	48.8	51.2	480.5	457.7	492.2	480.7	485.6	1013.3	1014.2	1027.1	1020.5	1018.7	2531.3	2441.0	2351.9	2339.3	2354.3
2.642	50.6	56.1	59.9	52.4	55.1	565.4	555.5	545.6	564.5	536.7	1181.9	1136.4	1137.8	1166.7	1157.6	2834.9	2748.8	2699.7	2627.9	2561.0
2.839	44.9	44.6	46.1	47.3	47.3	472.7	451.4	436.1	429.2	468.5	887.6	920.3	912.2	961.8	914.3	2181.2	2116.4	2022.2	1992.8	2043.5
3.061	34.7	37.7	45.8	47.3	43.7	399.5	370.1	389.9	381.8	381.5	795.8	768.2	796.5	838.7	800.0	1888.7	1804.7	1820.9	1784.2	1693.1
3.278	43.4	48.8	44.8	43.7	49.7	440.0	451.7	439.1	431.3	428.8	878.3	879.5	880.8	883.1	908.8	2000.9	1969.1	1923.8	1883.0	1844.3
3.523	36.2	45.2	37.1	47.8	38.6	385.9	368.8	367.4	356.9	385.0	713.0	719.8	687.2	741.8	701.9	1579.4	1508.0	1519.7	1487.0	1481.0
3.790	31.4	32.9	36.9	37.1	41.9	289.7	303.5	308.0	312.5	308.3	898.6	808.5	894.2	815.5	817.3	1312.4	1256.0	1232.0	1215.5	1198.4
4.098	33.0	34.2	40.3	29.9	36.0	303.6	288.7	296.1	309.0	305.7	598.3	545.1	570.8	573.0	563.0	1261.7	1208.9	1159.3	1169.0	1129.0
4.371	29.0	40.4	43.1	30.9	36.1	282.2	279.7	293.8	289.5	296.5	647.9	636.0	669.8	594.8	532.9	1143.0	1131.1	1040.4	1078.6	1085.4
4.666	25.9	28.4	24.1	27.8	27.1	240.6	241.2	232.5	214.3	233.8	432.6	404.5	419.9	424.0	396.7	857.8	775.8	773.7	808.6	777.5
5.048	22.4	23.3	27.7	31.2	27.7	213.1	200.5	217.2	207.4	212.8	382.2	367.4	373.5	379.2	367.5	714.3	672.6	634.4	663.7	651.1
5.425	18.3	25.4	24.8	29.6	21.6	173.2	183.2	184.8	172.9	182.9	302.6	289.3	308.3	317.7	292.5	562.5	522.2	527.0	506.7	529.3
5.829	14.9	20.9	16.6	22.6	23.3	126.9	139.6	136.3	134.9	129.9	230.6	207.6	232.6	231.8	226.3	403.3	383.6	389.6	361.6	363.6
6.264	16.8	16.2	22.7	18.9	23.7	142.0	134.4	153.4	147.9	142.7	225.8	220.6	208.9	239.3	216.2	394.1	387.9	373.4	384.4	347.5
6.732	18.5	18.7	18.3	20.1	12.7	107.9	111.1	91.7	113.6	103.0	187.0	189.5	163.4	171.8	169.0	238.9	260.5	239.6	245.9	242.4
7.234	9.1	12.0	17.9	11.7	13.1	88.1	88.9	84.8	87.8	92.1	139.0	139.7	137.5	136.0	143.0	214.0	199.7	199.7	203.7	203.7
7.774	8.8	15.9	13.2	12.1	12.9	67.5	66.8	69.1	63.0	72.5	102.5	96.8	110.1	107.8	92.6	150.7	149.6	145.8	146.8	154.1
8.364	8.2	12.8	6.7	7.8	11.8	43.8	47.3	46.5	44.9	50.1	69.8	68.6	69.9	62.3	50.5	95.1	88.4	81.3	94.3	75.3
8.977	4.9	6.1	6.3	6.7	10.6	23.4	26.0	16.0	24.2	21.3	30.4	30.8	32.0	36.3	23.8	37.8	41.0	37.3	30.8	29.9
9.647	0.8	0.4	1.2	0.8	0	9.8	6.8	8.1	8.9	8.0	9.0	8.0	8.1	7.7	9.8	8.9	10.2	8.1	10.7	8.5
10.37	0.4	2.8	0.8	0.8	0.4	3.1	4.0	3.1	4.9	4.4	6.2	7.1	7.1	4.4	6.2	9.4	11.8	7.8	9.8	8.0
11.14	0.9	0	1.4	0.4	0.4	3.3	2.3	2.3	5.2	1.9	2.3	7.1	7.8	2.8	2.8	7.8	7.1	4.7	8.0	8.0
11.97	0	0	0	0	0	0.9	2.4	0.4	1.0	0	3.0	2.5	2.9	2.9	1.4	6.9	5.4	3.9	8.4	5.9
12.86	0	0	0	0.8	0	0.5	1.6	1.6	0	1.0	1.6	2.1	1.6	2.1	1.6	2.1	4.2	2.6	2.6	5.6
13.82	0	0	0	0.5	0	1.6	1.6	1.1	1.6	1.1	4.5	1.1	1.1	1.6	1.1	3.3	2.6	6.6	4.5	2.2
14.86	0.6	0	0	0	0	0	1.7	2.3	1.2	0.6	2.4	0.6	1.7	1.1	2.9	4.7	5.9	4.1	7.7	2.3
15.96	0	0	0	0	0	0	1.2	0.6	0.6	0	2.5	3.2	1.2	1.2	0.6	6.1	5.7	3.8	3.8	2.5
17.15	0	0	0	0	0	1.3	0	1.3	0.7	0	0.7	1.4	0	2.0	1.3	4.8	3.4	2.0	3.4	4.1
18.43	0	0	0	0	0	0.7	0.7	0.7	0.7	0.7	1.5	2.2	2.9	0.7	0.7	3.7	2.9	2.2	2.2	0.7
19.81	0	0	0	0	0	0.8	0.8	0.8	1.6	0	3.2	0.8	2.4	0.8	0.8	4.0	1.6	1.6	1.6	3.2

Aerosol Material	120°C DEHS														
Atomizer Flow Rate	3.17 sLpm					3.73 sLpm					4.42 sLpm				
Run Number	Run 1	Run 2	Run 3	Run 4	Run 5	Run 1	Run 2	Run 3	Run 4	Run 5	Run 1	Run 2	Run 3	Run 4	Run 5
Channel Midpoint	Conc.	Conc.	Conc.	Conc.	Conc.	Conc.	Conc.	Conc.	Conc.	Conc.	Conc.	Conc.	Conc.	Conc.	Conc.
<0.523	28547.1	29090.7	28128.8	27673.5	27645.8	44578.8	43624.5	42327.1	42602.7	43104.9	48069.8	48218.0	48289.4	48723.8	48450.8
0.542	6024.4	6006.7	5886.1	5731.9	5726.2	9472.3	9236.5	9103.3	8933.2	8927.5	11391.1	11404.0	11368.3	11498.2	11503.3
0.583	7261.0	7170.7	7186.6	6972.1	6905.8	11554.0	11217.1	11184.9	10980.7	10912.9	14399.7	14559.9	14632.9	14824.4	14549.7
0.626	8600.5	8491.9	8318.2	8171.8	8172.1	13583.7	13433.1	13271.1	13014.9	12844.8	17505.0	17589.2	17661.3	17495.4	17537.0
0.673	9705.1	9721.3	9633.1	9467.5	9432.1	15783.0	15532.2	15333.9	15054.0	14973.9	20656.4	20721.2	20559.8	20693.0	20690.9
0.723	10841.2	10759.0	10654.8	10456.9	10401.4	17903.3	17498.4	17288.7	16913.7	16854.9	23647.1	23889.1	23817.4	23558.2	23661.7
0.777	11179.0	11121.4	10989.1	10882.3	10741.3	18450.2	17980.7	18041.0	17560.7	17425.8	25277.2	25161.7	25211.5	25065.7	25159.9
0.835	11041.6	11011.6	10909.0	10698.4	10678.0	18390.8	18014.9	17862.2	17440.8	17459.7	25333.0	25252.0	25201.9	25265.8	25331.2
0.898	10956.1	10774.9	10685.8	10567.6	10489.0	17824.4	17596.7	17590.7	17105.4	17068.2	24998.5	24880.2	24671.8	24664.6	24694.6
0.965	10301.8	10181.2	9910.9	9820.3	9825.7	16756.5	16470.6	16373.1	15911.1	15805.5	23183.8	23267.5	23222.5	23261.8	23235.1
1.037	9682.7	9846.1	9825.4	9597.1	9590.2	16215.3	15861.3	15833.7	15397.2	15409.2	22077.8	22221.5	22015.7	22006.8	22041.8
1.114	8698.9	8672.8	8417.2	8318.2	8264.8	14145.6	13887.6	13770.9	13518.9	13370.1	19183.4	19116.5	19211.6	19012.1	19059.6
1.197	8761.0	8865.4	8619.7	8528.2	8476.0	14190.3	13992.0	14041.5	13656.0	13589.7	18646.7	18735.5	18782.3	18689.3	18822.8
1.286	7920.4	7897.9	7721.2	7689.4	7718.5	12825.9	12613.8	12554.4	12251.2	12169.6	16816.1	16703.4	16700.4	16622.7	16693.5
1.382	8421.1	8556.1	8417.5	8262.1	8257.3	13646.7	13483.5	13326.3	12946.2	13020.3	16686.4	16815.0	16619.5	16763.7	16774.2
1.486	8948.2	9030.1	8868.4	8631.7	8688.9	14397.6	14085.6	13945.5	13629.3	13693.6	16647.6	16686.9	16529.1	16675.2	16623.9
1.596	9082.6	8940.7	8897.8	8777.2	8680.0	14149.5	14133.6	14179.5	13840.2	13721.1	16057.2	16204.5	16285.6	16010.4	16140.0
1.715	7869.1	7567.0	7480.0	7363.9	7206.7	12184.3	11968.6	11723.5	11529.1	11614.3	14203.2	14262.0	14154.3	14204.1	14136.6
1.843	7356.7	7184.5	7065.1	6988.0	6983.1	11325.1	11196.7	11115.1	10882.3	10820.1	13105.5	13080.2	12951.8	13093.5	13050.3
1.981	7471.0	7465.8	7301.2	7192.3	7225.0	11344.9	11281.8	11226.7	11002.0	11047.3	12699.9	12578.7	12823.1	12580.5	12599.4
2.129	7109.8	7147.6	7078.8	6995.5	6916.8	10735.9	10531.3	10472.5	10384.0	10391.8	11741.2	11617.0	11680.0	11642.2	11638.6
2.288	6544.0	6467.5	6369.1	6400.9	6359.2	9636.2	9507.7	9507.4	9171.1	9235.3	10343.2	10341.1	10216.6	10156.9	10282.3
2.458	6468.7	6437.6	6359.5	6308.1	6248.5	9344.5	9265.8	9116.2	9044.8	8920.6	9843.7	9923.5	9845.8	9818.4	9844.6
2.642	6919.3	6955.3	6916.6	6762.4	6845.2	9523.6	9400.6	9436.9	9274.0	9154.9	9919.9	9991.3	9946.4	9918.9	9779.5
2.839	5274.1	5144.9	5216.6	4994.3	5059.4	6982.0	6907.3	6972.1	6846.1	6679.3	7233.1	7216.3	7179.4	7135.3	7102.0
3.051	4311.2	4291.1	4205.9	4161.8	4126.1	5450.5	5455.6	5425.6	5269.3	5301.4	5661.8	5568.1	5658.2	5524.3	5542.3
3.278	4350.5	4268.9	4307.6	4232.0	4219.1	5180.8	5169.2	5127.8	4997.0	5027.9	5189.5	4967.0	5042.6	5011.1	5062.4
3.523	3308.3	3347.3	3364.1	3207.5	3222.8	4000.1	4026.5	3920.0	3869.3	3863.0	4103.9	4159.1	4108.4	4079.6	4074.5
3.786	2851.4	2862.6	2862.5	2787.8	2775.5	3789.2	3633.5	3615.5	3512.0	3484.4	4313.3	4289.3	4211.6	4282.1	4255.7
4.068	2642.3	2580.5	2571.7	2509.9	2556.9	3411.4	3358.7	3227.5	3096.3	3182.3	4105.3	4064.4	4060.2	4019.3	4040.5
4.371	2355.2	2258.8	2267.1	2200.0	2233.1	2856.0	2810.1	2803.4	2663.8	2812.7	3477.4	3372.4	3449.0	3357.4	3379.2
4.698	1844.4	1805.1	1782.8	1817.9	1760.9	1960.1	1995.1	1870.7	1844.5	1882.2	2438.9	2401.1	2433.0	2399.9	2349.2
5.048	1275.7	1237.5	1264.0	1229.0	1237.5	1497.1	1474.0	1454.5	1394.5	1367.3	1833.4	1824.2	1796.4	1800.2	1790.4
5.425	946.1	959.0	934.1	923.8	885.4	1144.8	1111.2	1082.8	1037.4	1022.2	1389.0	1375.1	1371.5	1381.2	1319.0
5.829	683.9	648.6	669.6	671.6	631.9	775.6	745.6	760.6	680.3	720.9	968.9	988.3	955.6	960.9	958.6
6.264	597.2	576.9	571.7	548.9	562.4	663.0	666.5	637.5	586.5	595.1	831.3	856.8	828.5	823.0	801.0
6.732	386.1	383.8	385.2	370.9	353.2	438.6	416.8	415.7	378.3	385.0	583.7	561.8	552.3	552.3	540.3
7.234	295.9	292.6	275.8	282.7	267.0	319.7	308.0	314.2	281.7	282.0	407.5	413.4	396.9	396.0	389.6
7.774	185.6	191.7	188.7	188.3	173.1	202.7	217.5	204.6	184.1	195.5	297.7	315.5	297.3	272.2	266.5
8.354	114.0	115.2	90.3	100.6	101.8	138.5	127.8	123.1	117.2	99.0	178.4	175.6	172.8	166.1	166.1
8.977	49.3	39.8	47.2	45.6	44.3	55.0	54.2	66.1	48.4	47.6	85.0	89.5	71.5	69.8	83.8
9.647	16.7	17.9	13.2	14.5	16.2	24.8	20.5	24.4	19.2	24.8	38.9	25.7	31.2	29.5	32.1
10.37	14.3	14.7	16.5	12.0	14.3	18.3	20.1	18.3	14.3	17.0	29.1	26.8	33.1	27.3	29.5
11.14	15.7	9.5	11.9	11.4	12.8	14.7	15.7	18.5	12.3	16.1	19.0	24.2	20.4	19.9	17.6
11.97	7.4	10.4	7.9	8.9	8.9	16.4	15.9	12.4	14.4	10.9	15.4	16.4	16.9	19.9	14.4
12.86	8.9	5.3	10.7	10.1	10.1	12.8	12.3	9.1	10.7	9.1	16.6	18.7	12.8	18.2	16.0
13.82	6.2	10.1	6.7	9.0	6.2	11.8	9.6	10.7	10.7	13.5	20.9	12.4	15.8	14.1	14.7
14.86	10.7	5.3	7.7	4.7	7.1	5.9	8.3	5.3	7.1	11.3	9.5	12.5	13.1	11.3	13.7
15.96	7.6	7.6	7.6	5.7	8.9	8.2	8.2	12.1	7.0	9.5	20.4	12.1	12.7	18.5	18.1
17.15	8.3	8.3	5.5	6.2	6.2	9.0	8.3	9.7	2.7	11.1	20.2	15.3	14.6	13.9	16.7
18.43	11.9	3.7	4.4	7.4	2.9	14.9	7.4	11.2	5.9	8.2	14.9	14.2	13.4	14.9	21.7
19.81	8.1	12.9	7.2	8.4	4.8	12.9	15.4	11.3	13.7	8.1	17.0	14.5	19.4	12.1	12.9

Appendix J Summary of APS & PDA Validation Data

Table J-1 Particle Size Distributions for the Aerodynamic Particle Sizer Validation Tests Using 1.020 μm PSL Microspheres (Particle Counts)

Run Number	1	2	3	4	5	6	7	8	9	10	11	12	13	14	15	16	17	18	19	20	21
Channel Midpoint	Count	Count	Count	Count	Count	Count	Count	Count	Count	Count	Count	Count	Count	Count	Count	Count	Count	Count	Count	Count	Count
<0.523	541	431	309	219	285	234	211	172	134	263	220	151	154	168	3839	4110	3831	1028	1096	1045	897
0.542	65	40	35	21	33	23	25	17	13	33	27	15	10	20	301	327	297	106	103	108	80
0.583	59	49	42	33	27	28	29	19	14	27	35	20	17	20	296	302	285	105	98	95	72
0.626	70	47	44	33	29	30	24	17	27	18	24	21	10	21	233	269	245	83	89	102	65
0.673	58	51	40	33	30	14	32	16	16	24	20	14	17	21	177	226	196	71	81	80	54
0.723	31	31	29	27	22	21	24	21	15	19	14	12	15	19	105	139	146	47	68	72	45
0.777	26	26	23	19	17	13	25	19	11	15	9	17	13	11	89	86	85	37	31	44	36
0.835	26	25	18	26	14	11	12	8	8	11	8	9	3	11	65	73	73	24	23	29	16
0.898	78	71	62	63	67	77	79	63	78	142	95	90	95	68	1017	994	918	161	196	93	162
0.965	1454	1211	724	745	871	1003	952	792	833	1875	1554	1192	1030	1098	18781	19976	20304	3605	3871	2471	3161
1.037	4074	3214	1856	1683	2142	2328	2212	1746	1617	4194	3946	2648	2407	2477	47081	52828	56345	8960	9763	7832	8249
1.114	1435	1152	612	486	667	686	644	500	448	1308	1288	694	546	712	14094	17334	19688	2826	3139	3082	2780
1.197	331	267	143	136	181	157	154	110	115	391	350	190	149	183	4799	5702	6012	881	1042	757	892
1.286	262	186	164	114	124	134	110	99	92	201	215	128	82	124	2181	2714	2886	485	575	494	473
1.382	144	123	84	73	83	83	72	63	68	106	89	54	61	71	983	1169	1242	255	278	236	216
1.486	123	119	76	65	74	80	79	63	59	78	61	55	48	64	444	567	619	144	186	197	165
1.596	63	76	60	55	52	39	43	46	33	51	32	27	34	35	351	424	422	86	112	74	82
1.715	90	98	83	78	66	64	72	54	45	70	63	48	55	46	339	386	407	120	126	146	122
1.843	67	52	46	43	38	46	37	36	38	37	47	30	21	29	197	206	245	71	83	95	57
1.981	35	55	34	35	37	39	25	29	20	26	21	21	15	24	180	244	234	49	47	87	67
2.129	29	30	25	21	16	19	26	18	16	20	19	14	16	22	142	184	182	32	51	48	39
2.288	17	29	13	10	21	24	16	24	12	18	14	11	12	8	121	140	166	25	28	39	20
2.458	14	15	8	5	7	8	4	12	6	10	4	5	3	5	91	103	107	12	24	24	17
2.642	7	9	4	3	5	2	3	4	4	9	8	4	0	2	57	59	84	9	10	21	9
2.839	10	13	0	1	1	5	5	2	4	3	2	5	1	0	29	39	54	6	7	13	3
3.051	3	5	2	4	2	2	3	5	0	0	3	2	3	0	15	32	36	4	2	5	3
3.278	12	3	0	0	2	0	2	3	0	1	1	2	0	6	16	27	27	4	7	9	4
3.523	2	0	1	0	0	1	0	0	0	1	0	0	0	2	9	19	22	3	1	4	2
3.786	8	0	1	0	0	1	0	1	0	0	2	1	1	1	17	23	17	1	3	3	3
4.068	0	2	2	0	2	0	0	0	1	0	0	1	0	0	11	20	11	1	3	4	2
4.371	4	1	1	1	1	1	1	0	0	0	1	0	0	0	4	9	13	2	1	3	1
4.696	4	1	1	1	0	0	0	2	0	0	1	0	1	1	7	3	12	2	4	3	1
5.048	3	2	0	0	0	1	0	0	1	1	0	0	0	1	4	6	8	0	0	2	2

Table J-2 Particle Size Distributions for the Particle Dynamic Analyzer Tests Using 1.020 μm PSL Microspheres (Particle Counts)

Run Number	1	2	3	4	5	6	7	8	9	10	11	12	13	14	15	16	17	18
Channel Midpoint	Count	Count	Count	Count	Count	Count	Count	Count	Count	Count	Count	Count	Count	Count	Count	Count	Count	Count
<0.523	10	7	6	6	11	7	9	10	5	5	2	4	2	2	7	0	2	2
0.542	0	0	0	0	0	0	0	0	0	0	0	0	0	0	0	0	0	0
0.583	8	2	4	6	4	5	3	3	1	2	2	1	4	3	4	2	2	1
0.626	0	0	0	0	0	0	0	0	0	0	0	0	0	0	0	0	0	0
0.673	10	4	6	7	14	8	11	11	4	5	2	3	6	3	4	1	4	4
0.723	0	0	0	0	0	0	0	0	0	0	0	0	0	0	0	0	0	0
0.777	18	13	14	16	18	12	24	22	11	15	6	19	30	15	36	23	31	17
0.835	0	0	0	0	0	0	0	0	0	0	0	0	0	0	0	0	0	0
0.898	65	59	52	76	86	50	112	80	99	97	120	234	242	117	164	119	147	147
0.965	0	0	0	0	0	0	0	0	0	0	0	0	0	0	0	0	0	0
1.037	363	327	287	350	389	204	319	223	167	191	96	256	320	144	179	91	126	170
1.114	418	408	374	459	434	367	296	301	88	136	11	32	64	68	35	25	24	29
1.197	0	0	0	0	0	0	0	0	0	0	0	0	0	0	0	0	0	0
1.286	59	42	37	117	142	66	71	60	17	16	4	11	14	24	15	17	9	7
1.382	11	5	8	10	30	12	13	16	4	4	1	6	6	7	6	10	6	4
1.486	11	6	5	16	3	8	12	10	1	1	2	4	7	1	3	2	2	3
1.596	7	5	3	3	1	8	7	7	4	4	2	4	6	1	6	4	4	4
1.715	7	3	2	6	5	10	13	8	2	6	2	4	4	3	2	3	3	4
1.843	5	3	4	5	4	8	7	10	2	2	0	1	2	2	4	3	1	1
1.981	9	5	3	1	6	1	5	8	0	0	3	1	2	0	0	1	1	0
2.129	5	4	3	5	6	13	6	6	0	2	0	2	2	2	3	0	2	1
2.288	4	0	1	2	4	0	1	1	1	0	0	0	0	0	0	0	0	0
2.458	1	1	0	1	3	5	2	6	2	1	0	1	1	0	0	0	0	1
2.642	0	0	0	0	2	1	4	0	0	0	0	0	0	0	0	0	0	0
2.839	1	0	2	2	1	3	2	2	1	1	0	0	2	0	1	0	1	0
3.051	2	0	0	1	4	3	1	0	0	0	0	0	1	0	0	1	0	0
3.278	1	0	0	3	3	1	1	1	0	0	0	0	0	0	1	0	0	0
3.523	4	1	1	0	2	0	1	1	1	0	0	0	0	0	0	0	0	0
3.786	1	1	1	1	1	0	0	0	1	0	0	0	0	0	0	0	0	0
4.068	0	0	0	0	0	1	0	1	0	0	0	1	1	0	0	0	0	0
4.371	1	0	0	1	1	0	0	0	0	1	0	0	0	0	0	0	0	0
4.696	0	0	1	2	1	1	0	0	0	0	0	0	0	0	0	0	0	0
5.048	1	0	0	0	1	0	0	0	0	0	0	0	0	0	0	0	0	0

Table J-3 Particle Size Distributions for the Particle Dynamic Analyzer and Particle Dynamic Analyzer Tests Using 2.504 μm PSL Microspheres (Particle Counts)

	Aerodynamic Particle Sizer									Particle Dynamic Analyzer						
Run Number	1	2	3	4	5	6	7	8	9	1	2	3	4	5	6	7
Channel Midpoint	Count	Count	Count	Count	Count	Count	Count	Count	Count	Count	Count	Count	Count	Count	Count	Count
<0.523	31367	33662	49876	22781	21723	18969	179299	185260	183854	0	0	1	1	1	1	0
0.542	3849	4146	6359	2589	2411	2139	21488	22726	22348	0	0	0	0	0	0	0
0.583	4331	4677	7386	3003	2787	2438	24676	25958	26143	0	1	0	0	0	0	0
0.626	4576	4913	7738	2947	2909	2433	26562	28419	28401	0	0	0	0	0	0	0
0.673	4190	4542	7263	2686	2578	2168	25111	27844	27557	0	0	0	0	0	0	0
0.723	3400	3621	5880	1978	2104	1635	20822	23255	23127	0	0	0	0	0	0	0
0.777	2185	2449	3907	1323	1405	1095	13803	15784	15683	0	0	0	1	0	0	0
0.835	1332	1500	2281	752	763	699	8145	9428	8994	0	0	0	0	0	0	0
0.898	858	974	1373	447	484	414	4535	5211	4913	0	0	1	0	1	0	0
0.965	630	673	827	254	339	294	2644	2879	2682	0	0	0	0	0	0	0
1.037	370	459	554	237	227	214	1489	1631	1507	1	0	0	0	0	0	0
1.114	288	319	369	192	195	178	952	1035	950	0	0	0	0	1	0	0
1.197	188	231	298	142	141	114	663	698	668	0	0	0	0	0	0	0
1.286	147	152	224	103	132	111	460	446	436	0	0	0	0	0	0	0
1.382	112	98	158	91	93	96	327	310	337	0	0	0	0	0	0	0
1.486	77	79	108	82	76	76	239	244	253	0	0	0	0	0	0	0
1.596	53	63	95	62	61	76	192	201	195	0	0	0	0	0	0	0
1.715	63	43	60	61	56	50	155	150	159	0	0	0	1	2	0	1
1.843	35	43	66	45	40	45	120	138	126	1	0	0	1	3	0	1
1.981	32	45	48	34	28	34	125	132	124	1	0	0	1	2	1	1
2.129	30	31	47	28	28	42	110	128	119	5	5	10	8	10	6	14
2.288	21	26	44	22	21	39	184	174	163	8	9	18	13	22	17	18
2.458	9777	10296	12575	2898	2995	3551	45382	39048	40687	40	48	30	91	108	91	110
2.642	16022	17521	24754	10923	10971	9839	43960	54045	53989	6	9	4	9	19	26	26
2.839	255	267	461	58	68	65	906	984	936	0	1	0	2	3	1	5
3.051	48	38	89	27	22	25	119	124	137	0	0	0	0	0	1	0
3.278	18	11	23	19	9	10	39	59	39	0	0	0	0	0	0	0
3.523	7	8	16	10	4	11	20	31	24	0	0	0	0	0	0	0
3.786	8	6	15	2	7	8	24	23	24	0	0	0	0	0	0	0
4.068	12	9	14	10	8	5	21	32	35	0	0	0	0	0	0	0
4.371	6	10	14	9	7	9	42	37	41	0	0	0	0	0	0	0
4.698	8	14	20	4	6	9	41	33	41	0	0	0	0	0	0	0
5.048	10	11	23	4	7	6	33	55	45	0	0	0	0	0	0	0

Appendix K Summary of Particle Penetration Data For Rectangular Cracks

Table K-1 Summary of Particle Penetration Coefficients (P) for Rectangular Crack Experiments

Crack Length, L	30 mm												30 mm		
Crack Height, H	0.203 mm												0.305 mm		
Particle Diameter	1.0 μm			1.2 μm			1.4 μm			1.6 μm			1.0 μm		
ΔP	Entrance	Exit	P	Entrance	Exit	P	Entrance	Exit	P	Entrance	Exit	P	Entrance	Exit	P
2 Pa	494	346	0.700	727	366	0.503	731	142	0.194	731	142	0.194	1072	949	0.885
	850	565	0.665	753	313	0.416	657	119	0.181	657	119	0.181	1106	996	0.901
	674	438	0.650	655	285	0.435	630	126	0.200	630	126	0.200	1143	1010	0.884
	637	413	0.648	714	316	0.443	553	92	0.166	553	92	0.166	920	782	0.850
	725	464	0.640	666	362	0.544	615	152	0.247	615	152	0.247	782	708	0.905
4 Pa	779	614	0.788	644	465	0.722	502	269	0.536	502	269	0.536	1085	961	0.886
	751	588	0.783	711	510	0.717	571	269	0.471	571	269	0.471	961	904	0.941
	742	608	0.819	840	663	0.777	542	279	0.515	542	279	0.515	946	811	0.857
	590	433	0.734	820	581	0.709	442	238	0.538	442	238	0.538	1247	1231	0.987
	822	645	0.785	828	544	0.657	620	330	0.532	620	330	0.532	1393	1342	0.963
6 Pa	935	759	0.812	875	686	0.784	504	313	0.621	504	313	0.621	1414	1284	0.908
	900	761	0.846	786	687	0.874	422	291	0.690	422	291	0.690	1484	1366	0.920
	769	652	0.848	909	769	0.846	519	337	0.649	519	337	0.649	1404	1385	0.986
	744	616	0.828	872	714	0.819	517	381	0.737	517	381	0.737	1368	1422	1.039
	1041	889	0.854	939	755	0.804	475	330	0.695	475	330	0.695	1212	1092	0.901
8 Pa	1104	955	0.865	736	636	0.864	491	382	0.778	491	382	0.778	1601	1588	0.992
	1077	948	0.880	813	695	0.855	497	389	0.783	497	389	0.783	1044	1011	0.968
	763	727	0.953	748	656	0.877	420	325	0.774	420	325	0.774	1011	1045	1.034
	813	722	0.888	610	496	0.813	425	309	0.727	425	309	0.727	1319	1210	0.917
	1087	967	0.890	628	507	0.807	503	397	0.789	503	397	0.789	1317	1143	0.868
10 Pa	707	606	0.857	833	789	0.947	422	373	0.884	422	373	0.884	1296	1235	0.953
	879	786	0.894	1002	913	0.911	426	368	0.864	426	368	0.864	1244	1226	0.986
	917	855	0.932	927	799	0.862	432	345	0.799	432	345	0.799	1413	1386	0.981
	633	584	0.923	852	754	0.885	479	408	0.852	479	408	0.852	1310	1172	0.895
	666	655	0.955	980	893	0.911	504	379	0.752	504	379	0.752	1276	1249	0.979
12 Pa	713	696	0.976	998	896	0.907	532	458	0.861	532	458	0.861	1275	1275	1.000
	1016	926	0.911	1066	962	0.902	447	369	0.826	447	369	0.826	1265	1301	1.028
	813	728	0.895	865	791	0.914	572	505	0.883	572	505	0.883	1257	1211	0.963
	748	696	0.930	850	735	0.865	516	392	0.760	516	392	0.760	1442	1356	0.940
	1116	1032	0.925	994	818	0.823	520	449	0.863	520	449	0.863	1334	1299	0.974

Table K-2 Summary of Particle Penetration Experiments for Rectangular Cracks

Crack Length, L	30 mm						30 mm								
Crack Height, H	0.305 mm						0.406 mm								
Particle Diameter	1.4 μm			1.8 μm			1.0 μm			1.4 μm			1.8 μm		
ΔP	Entrance	Exit	P	Entrance	Exit	P	Entrance	Exit	P	Entrance	Exit	P	Entrance	Exit	P
2 Pa	932	697	0.748	1198	845	0.705	916	900	0.983	916	780	0.852	1077	931	0.864
	1046	808	0.772	996	626	0.629	1339	1240	0.926	950	882	0.928	903	810	0.897
	957	784	0.819	1474	1082	0.734	1423	1354	0.952	842	736	0.874	1213	945	0.779
	686	523	0.762	1660	982	0.581	1276	1256	0.984	746	690	0.925	1111	903	0.813
	697	516	0.740	1204	788	0.654	1366	1285	0.941	775	709	0.915	1112	1024	0.921
4 Pa	989	891	0.901	747	603	0.807	958	984	1.027	857	825	0.963	1092	997	0.913
	605	517	0.855	815	708	0.869	1099	972	0.884	906	846	0.934	1171	1127	0.962
	991	860	0.868	743	564	0.759	1390	1383	0.995	862	831	0.964	1348	1129	0.839
	724	633	0.874	714	580	0.812	1544	1474	0.955	914	857	0.938	1137	990	0.871
	926	806	0.870	656	597	0.910	1078	1029	0.955	595	548	0.921	1231	1160	0.959
6 Pa	948	892	0.941	662	617	0.932	1247	1210	0.970	867	831	0.958	1155	977	0.846
	1009	887	0.879	862	823	0.955	797	781	0.980	1030	1023	0.993	941	938	0.997
	1058	1045	0.988	630	568	0.902	734	763	1.040	1219	1149	0.943	927	1000	1.079
	694	628	0.905	946	800	0.846	843	841	0.998	1125	1020	0.907	1139	987	0.867
	722	670	0.928	886	773	0.872	1077	999	0.928	1271	1284	1.010	1290	1275	0.988
8 Pa	900	847	0.941	963	793	0.823	962	912	0.948	1215	1110	0.914	1289	1366	1.060
	1123	960	0.855	950	886	0.933	979	911	0.931	927	941	1.015	1382	1328	0.961
	955	978	1.024	764	670	0.877	781	822	1.052	1012	1030	1.018	1485	1587	1.069
	973	903	0.928	964	913	0.947	1000	1003	1.003	811	768	0.947	1368	1233	0.901
	902	812	0.900	1053	958	0.910	694	671	0.967	844	783	0.928	1313	1335	1.017
10 Pa	1021	896	0.878	909	788	0.867	1019	1000	0.981	532	552	1.038	1596	1476	0.925
	1037	1059	1.021	948	953	1.005	1052	1043	0.991	322	293	0.910	1621	1583	0.977
	951	883	0.928	1087	1010	0.929	941	931	0.989	413	392	0.949	1614	1474	0.913
	908	900	0.991	1019	967	0.949	976	956	0.980	435	423	0.972	1394	1348	0.967
	1090	955	0.876	1078	942	0.874	1049	1069	1.019	413	371	0.898	1413	1488	1.053
12 Pa	1105	1096	0.992	980	1006	1.027	784	803	1.024	499	529	1.060	1643	1520	0.925
	1150	1028	0.894	995	879	0.883	868	838	0.965	1126	1083	0.962	1310	1361	1.039
	1059	1185	1.119	1215	1078	0.887	724	723	0.999	850	778	0.913	1255	1222	0.974
	1234	1112	0.901	1332	1174	0.881	893	852	0.954	772	768	0.995	1197	1264	1.056
	1115	1127	1.011	1222	1203	0.984	672	716	1.065	579	570	0.984	1357	1467	1.081

Table K-3 Summary of Particle Penetration Experiments for Rectangular Cracks

Crack Length, L	30 mm									60 mm					
Crack Height, H	0.508 mm									0.203 mm					
Particle Diameter	1.0 μm			1.4 μm			1.8 μm			1.0 μm			1.2 μm		
ΔP	Entrance	Exit	P	Entrance	Exit	P	Entrance	Exit	P	Entrance	Exit	P	Entrance	Exit	P
2 Pa	910	836	0.919	362	366	1.011	198	187	0.944	*	*	*	*	*	*
	1143	1087	0.951	641	560	0.874	492	437	0.888	*	*	*	*	*	*
	1136	1102	0.970	482	476	0.988	396	367	0.927	*	*	*	*	*	*
	922	907	0.984	373	360	0.965	373	359	0.962	*	*	*	*	*	*
	1069	1014	0.949	761	770	1.012	248	235	0.948	*	*	*	*	*	*
4 Pa	931	921	0.989	1239	1089	0.879	596	549	0.921	1608	362	0.225	1161	128	0.110
	823	824	1.001	1031	1024	0.993	375	381	1.016	1720	416	0.242	1017	189	0.186
	856	885	1.034	921	909	0.987	426	422	0.991	1448	385	0.266	1381	200	0.145
	973	925	0.951	916	900	0.983	533	481	0.902	1328	390	0.294	1097	176	0.160
	866	856	0.988	606	562	0.927	593	580	0.978	1425	461	0.324	1535	188	0.122
6 Pa	937	956	1.020	476	455	0.956	885	805	0.910	917	490	0.534	1439	435	0.302
	986	968	0.982	490	465	0.949	952	993	1.043	1144	565	0.494	1438	521	0.362
	808	771	0.954	497	491	0.988	1088	1177	1.082	1063	515	0.484	1429	494	0.346
	1008	1031	1.023	681	647	0.950	747	762	1.020	983	508	0.517	1150	386	0.336
	918	907	0.988	695	680	0.978	918	900	0.980	1180	580	0.492	1451	442	0.305
8 Pa	841	883	1.050	451	464	1.029	301	296	0.983	991	664	0.670	1454	694	0.477
	868	820	0.945	594	615	1.035	412	444	1.078	1314	779	0.593	1456	646	0.444
	942	921	0.978	678	663	0.978	650	595	0.915	1202	739	0.615	1214	564	0.465
	970	956	0.986	494	509	1.030	496	473	0.954	841	540	0.642	1470	650	0.442
	929	929	1.000	571	612	1.072	476	473	0.994	1392	831	0.597	1509	716	0.474
10 Pa	801	789	0.985	509	496	0.978	609	572	0.939	899	634	0.705	1114	684	0.614
	768	767	0.999	456	498	1.092	323	346	1.071	1236	896	0.725	1200	687	0.573
	590	587	0.995	647	642	0.992	397	409	1.030	1066	782	0.734	1218	691	0.567
	725	748	1.032	454	457	1.007	459	451	0.983	825	565	0.685	1207	704	0.583
	733	726	0.990	394	372	0.944	419	441	1.053	1396	950	0.681	1420	881	0.620
12 Pa	1030	996	0.967	833	826	0.992	556	610	1.097	861	645	0.749	1153	714	0.619
	1165	1149	0.986	650	689	1.060	666	627	0.941	1183	938	0.793	1286	878	0.683
	1031	1003	0.973	723	693	0.959	633	569	0.899	1402	997	0.711	988	607	0.614
	981	967	0.986	720	745	1.035	476	453	0.952	1104	808	0.732	1262	741	0.587
	1080	1066	0.987	711	723	1.017	496	489	0.986	1492	1079	0.723	1396	919	0.658

Table K-4 Summary of Particle Penetration Experiments for Rectangular Cracks

Crack Length, L	60 mm						60 mm								
Crack Height, H	0.203 mm						0.305 mm								
Particle Diameter	1.4 μm			1.6 μm			1.0 μm			1.2 μm			1.6 μm		
ΔP	Entrance	Exit	P	Entrance	Exit	P	Entrance	Exit	P	Entrance	Exit	P	Entrance	Exit	P
2 Pa	•	•	•	•	•	•	1362	829	0.609	1009	374	0.371	724	94	0.130
	•	•	•	•	•	•	1208	655	0.542	1026	388	0.378	643	62	0.096
	•	•	•	•	•	•	1284	720	0.570	1023	362	0.354	688	76	0.110
	•	•	•	•	•	•	1117	626	0.562	1029	368	0.358	733	109	0.149
	•	•	•	•	•	•	•	•	•	981	374	0.389	700	114	0.163
4 Pa	•	•	•	•	•	•	738	559	0.757	714	500	0.700	701	303	0.432
	•	•	•	•	•	•	716	546	0.761	673	479	0.712	817	380	0.465
	•	•	•	•	•	•	757	569	0.752	783	500	0.664	726	332	0.457
	•	•	•	•	•	•	848	629	0.742	688	484	0.874	713	347	0.487
	•	•	•	•	•	•	837	639	0.763	712	507	0.712	760	377	0.496
6 Pa	1780	317	0.178	673	8	0.012	1165	1052	0.903	728	603	0.828	655	421	0.643
	1682	308	0.183	701	102	0.146	1214	1077	0.887	856	697	0.814	710	466	0.656
	1425	234	0.164	477	34	0.071	1031	860	0.834	768	591	0.770	699	451	0.645
	1617	332	0.205	617	22	0.043	1214	854	0.703	806	642	0.796	622	404	0.650
	1265	194	0.153	548	13	0.024	1031	952	0.923	858	650	0.758	651	412	0.633
8 Pa	1466	531	0.362	666	110	0.165	1305	1057	0.810	889	717	0.807	877	611	0.697
	1438	452	0.314	581	111	0.191	1077	893	0.829	841	731	0.869	858	598	0.697
	1375	495	0.360	586	117	0.207	1140	1015	0.890	835	702	0.841	818	559	0.683
	1590	485	0.307	626	120	0.192	1017	917	0.902	889	762	0.857	821	637	0.776
	1228	399	0.325	760	107	0.141	1017	924	0.909	796	659	0.828	819	586	0.716
10 Pa	1521	682	0.448	687	222	0.323	1016	995	0.980	1035	901	0.871	731	558	0.763
	1341	576	0.430	620	172	0.277	1036	1069	1.022	1091	954	0.874	732	594	0.811
	1358	534	0.393	663	189	0.285	1052	868	0.825	957	864	0.903	641	511	0.797
	1375	586	0.426	725	207	0.286	974	899	0.923	1020	848	0.831	706	570	0.807
	1393	601	0.431	791	203	0.260	1021	964	0.944	1039	897	0.863	711	546	0.768
12 Pa	1570	849	0.541	648	265	0.411	1242	1081	0.870	1054	919	0.872	989	849	0.858
	1548	807	0.521	686	276	0.403	1359	1179	0.868	1071	947	0.884	842	683	0.811
	1475	741	0.502	622	247	0.397	1285	1303	1.014	1157	1025	0.886	847	689	0.813
	1656	893	0.540	676	309	0.457	1228	1181	0.962	1098	1004	0.916	829	664	0.801
	1767	827	0.468	769	344	0.447	1348	1376	1.021	1090	956	0.877	843	707	0.839

Table K-5 Summary of Particle Penetration Experiments for Rectangular Cracks

Crack Length, L	60 mm			60 mm								
Crack Height, H	0.305 mm			0.508 mm								
Particle Diameter	1.8 μm			1.0 μm			1.4 μm			1.8 μm		
ΔP	Entrance	Exit	P	Entrance	Exit	P	Entrance	Exit	P	Entrance	Exit	P
2 Pa	•	•	•	945	892	0.944	877	647	0.738	125	94	0.752
	•	•	•	810	732	0.904	703	546	0.777	236	153	0.651
	•	•	•	783	705	0.924	580	495	0.853	504	350	0.694
	•	•	•	804	701	0.872	386	308	0.798	256	205	0.801
	•	•	•	813	720	0.886	489	368	0.753	147	114	0.776
4 Pa	775	277	0.357	831	802	0.965	531	444	0.836	351	340	0.942
	858	210	0.245	740	702	0.949	686	610	0.889	399	328	0.822
	1142	305	0.267	920	935	1.016	919	913	0.993	306	255	0.833
	906	315	0.348	825	766	0.928	389	368	0.946	420	326	0.776
	•	•	•	749	715	0.955	824	764	0.927	512	435	0.850
6 Pa	1001	614	0.613	889	862	0.970	952	896	0.943	508	433	0.852
	1008	544	0.540	967	948	0.980	804	705	0.877	684	605	0.885
	947	522	0.551	1044	987	0.945	779	772	0.991	643	626	0.974
	1055	556	0.526	856	872	1.019	698	629	0.901	485	461	0.951
	•	•	•	972	923	0.950	889	874	0.983	640	633	0.989
8 Pa	634	454	0.716	896	853	0.985	559	551	0.986	499	468	0.938
	671	415	0.618	863	819	0.960	780	735	0.942	572	560	0.979
	592	417	0.704	882	796	0.902	655	658	1.005	937	876	0.935
	587	383	0.618	594	628	1.057	452	430	0.951	616	559	0.907
	510	337	0.661	699	664	0.950	377	328	0.870	504	476	0.944
10 Pa	956	669	0.700	788	792	1.005	1333	1272	0.954	882	825	0.935
	975	709	0.727	880	824	0.936	1179	1162	0.986	1820	1834	1.009
	1037	785	0.757	1078	1004	0.931	939	880	0.937	934	896	0.959
	973	771	0.792	771	784	1.017	656	666	1.015	929	875	0.942
	639	532	0.833	684	712	1.041	661	586	0.887	1395	1271	0.911
12 Pa	993	740	0.745	1267	1209	0.954	806	787	0.976	1198	1135	0.947
	983	788	0.802	1654	1703	1.030	770	687	0.892	964	892	0.925
	1383	1025	0.741	1954	1891	0.968	894	873	0.977	701	636	0.907
	1287	965	0.750	1228	1156	0.943	1326	1297	0.978	797	818	1.026
	1281	1001	0.794	1234	1201	0.973	1308	1239	0.947	1113	1092	0.981

Appendix L Summary of Particle Penetration Data For L-shaped Cracks

Table L-1 Summary of Particle Penetration Experiments for L-Shaped Cracks

Crack Length, L	30 mm												30 mm		
Crack Height, H	0.203 mm												0.305 mm		
Particle Diameter	1.0 μm			1.3 μm			1.4 μm			1.6 μm			1.0 μm		
ΔP	Entrance	Exit	P	Entrance	Exit	P	Entrance	Exit	P	Entrance	Exit	P	Entrance	Exit	P
2 Pa	1154	273	0.237	1089	168	0.154	•	•	•	•	•	•	570	434	0.763
	1258	299	0.238	947	114	0.120	•	•	•	•	•	•	784	502	0.640
	1405	382	0.272	1101	93	0.084	•	•	•	•	•	•	957	663	0.693
	1350	364	0.270	1042	91	0.087	•	•	•	•	•	•	772	572	0.741
	1164	294	0.253	944	146	0.155	•	•	•	•	•	•	871	671	0.770
4 Pa	1341	802	0.598	878	434	0.494	750	230	0.307	666	117	0.176	927	794	0.857
	1303	753	0.578	781	327	0.419	820	235	0.287	614	106	0.173	921	811	0.881
	1277	736	0.576	796	364	0.457	795	218	0.274	637	107	0.168	798	598	0.751
	1332	786	0.590	679	338	0.498	703	208	0.296	728	118	0.162	902	800	0.887
	1017	591	0.581	875	361	0.413	837	262	0.313	709	141	0.199	1026	918	0.893
6 Pa	1053	751	0.713	876	534	0.610	864	435	0.503	653	251	0.384	989	903	0.913
	1050	766	0.730	687	443	0.645	836	453	0.542	709	310	0.437	1208	1158	0.959
	958	714	0.745	730	428	0.586	798	444	0.556	690	295	0.428	977	923	0.945
	954	705	0.739	768	488	0.635	739	376	0.509	715	299	0.418	1039	933	0.898
	1019	717	0.704	795	459	0.577	775	386	0.498	800	299	0.374	906	871	0.874
8 Pa	1071	821	0.767	579	424	0.732	607	402	0.603	525	277	0.528	911	807	0.886
	1104	828	0.750	552	390	0.707	693	474	0.682	544	310	0.570	971	836	0.860
	1028	819	0.797	702	492	0.701	650	404	0.622	515	288	0.559	1080	900	0.934
	1041	798	0.767	633	497	0.785	628	385	0.613	652	359	0.551	1073	996	0.928
	1084	857	0.791	642	495	0.771	684	429	0.627	689	342	0.496	1280	1226	0.973
10 Pa	1301	1073	0.825	723	524	0.725	946	659	0.697	522	344	0.659	1073	993	0.925
	1196	1043	0.872	560	430	0.768	801	536	0.669	558	349	0.625	1085	1013	0.960
	1138	921	0.809	754	558	0.740	838	621	0.741	560	344	0.614	983	1018	1.057
	1207	1002	0.830	699	486	0.737	750	527	0.703	642	352	0.548	936	872	0.932
	1271	1061	0.835	646	517	0.800	827	602	0.728	668	397	0.594	973	861	0.885
12 Pa	1426	1183	0.830	729	606	0.831	963	726	0.754	618	441	0.714	998	948	0.950
	1331	1146	0.861	723	601	0.831	836	653	0.781	692	447	0.646	1086	1105	1.017
	1199	995	0.830	849	680	0.801	813	646	0.795	702	493	0.702	1047	1003	0.958
	1293	1094	0.846	720	607	0.843	839	613	0.731	721	485	0.673	1010	981	0.971
	1439	1264	0.878	891	714	0.801	883	677	0.767	762	515	0.676	1188	1108	0.932

Table L-2 Summary of Particle Penetration Experiments for L-Shaped Cracks

Crack Length, L	30 mm			30 mm						30 mm					
Crack Height, H	0.305 mm			0.406 mm						0.508 mm					
Particle Diameter	1.4 μm			1.0 μm			1.4 μm			1.0 μm			1.4 μm		
ΔP	Entrance	Exit	P	Entrance	Exit	P	Entrance	Exit	P	Entrance	Exit	P	Entrance	Exit	P
2 Pa	911	570	0.626	820	767	0.935	1438	1064	0.740	1205	1187	0.985	984	898	0.913
	1331	651	0.489	999	878	0.879	1015	798	0.786	972	853	0.878	955	916	0.959
	980	513	0.540	770	745	0.968	1017	797	0.784	940	879	0.935	931	805	0.865
	1501	696	0.465	785	681	0.868	895	710	0.793	886	844	0.950	1093	1022	0.935
	1215	668	0.550	866	838	0.968	937	766	0.818	923	842	0.912	986	809	0.820
4 Pa	676	590	0.873	969	959	0.990	832	738	0.887	950	880	0.926	665	633	0.952
	821	713	0.868	1094	980	0.896	773	724	0.937	919	951	1.035	595	473	0.795
	822	649	0.790	747	692	0.926	643	529	0.823	979	850	0.868	649	644	0.992
	743	510	0.686	928	822	0.886	823	715	0.869	1106	1070	0.968	611	521	0.853
	831	688	0.828	1001	958	0.957	866	666	0.766	829	797	0.961	564	543	0.963
6 Pa	805	716	0.889	1244	1222	0.982	1029	1024	0.995	969	1083	1.118	907	851	0.938
	1017	939	0.923	1210	1152	0.952	788	744	0.944	918	810	0.882	1006	1038	1.033
	932	833	0.894	1179	1154	0.979	866	799	0.923	1221	1245	1.020	1014	986	0.972
	1100	924	0.840	1321	1235	0.935	1147	1092	0.952	1202	1145	0.953	908	868	0.956
	894	654	0.732	1092	1135	1.039	927	922	0.995	1087	1130	1.040	796	767	0.965
8 Pa	735	661	0.899	835	838	1.004	718	713	0.993	845	859	1.017	979	920	0.940
	819	694	0.847	810	788	0.973	839	782	0.932	1326	1366	1.030	994	869	0.874
	843	762	0.904	810	796	0.983	666	613	0.918	1061	1032	0.955	886	841	0.949
	785	727	0.926	741	706	0.953	673	967	1.108	1030	1009	0.980	909	872	0.959
	614	529	0.862	918	827	0.901	681	626	0.919	936	877	0.937	881	928	1.053
10 Pa	831	742	0.893	816	841	1.031	961	876	0.912	1122	1166	1.039	1096	1110	1.013
	869	843	0.948	842	833	0.989	901	899	0.998	959	1000	1.043	996	1030	1.034
	907	786	0.867	955	909	0.952	863	751	0.870	770	672	0.873	1041	1015	0.975
	872	790	0.906	816	776	0.951	950	916	0.964	1045	1091	1.044	1097	1035	0.943
	779	633	0.813	903	924	1.023	865	799	0.924	818	813	0.994	1003	959	0.956
12 Pa	816	797	0.977	1075	1022	0.951	1006	980	0.974	1333	1220	0.915	1095	1116	1.019
	749	739	0.987	1101	1145	1.040	1016	946	0.931	1178	1203	1.021	1157	1077	0.931
	867	793	0.915	1283	1299	1.012	966	1055	1.066	802	769	0.959	1181	1163	0.985
	880	797	0.906	1015	993	0.978	1110	1076	0.969	844	802	0.950	1309	1247	0.953
	785	796	1.017	1130	1013	0.896	1018	1044	1.026	858	831	0.969	1371	1303	0.950

Table L-3 Summary of Particle Penetration Experiments for L-Shaped Cracks

Crack Length, L	60 mm						60 mm								
Crack Height, H	0.305 mm						0.406 mm								
Particle Diameter	1.0 μm			1.8 μm			1.0 μm			1.4 μm			1.8 μm		
ΔP	Entrance	Exit	P	Entrance	Exit	P	Entrance	Exit	P	Entrance	Exit	P	Entrance	Exit	P
2 Pa	1362	829	0.609	*	*	*	1005	786	0.782	241	146	0.606	1291	604	0.468
	1206	655	0.542	*	*	*	1009	881	0.873	380	269	0.708	1146	591	0.516
	1264	720	0.570	*	*	*	974	815	0.837	1007	656	0.651	708	292	0.412
	1117	628	0.562	*	*	*	746	659	0.883	581	344	0.592	1100	413	0.375
	*	*	*	*	*	*	746	581	0.779	633	385	0.608	1189	433	0.364
4 Pa	738	559	0.757	775	277	0.357	976	890	0.912	547	431	0.788	1344	918	0.683
	718	545	0.761	858	210	0.245	570	551	0.967	893	776	0.869	1211	956	0.789
	757	569	0.752	1142	305	0.267	531	509	0.959	422	358	0.848	822	446	0.717
	848	629	0.742	906	315	0.348	626	559	0.893	475	388	0.817	1788	1256	0.702
	837	639	0.763				771	710	0.921	471	378	0.803	1320	849	0.643
6 Pa	1165	1052	0.903	1001	614	0.613	804	740	0.920	510	476	0.933	1054	885	0.840
	1214	1077	0.887	1008	544	0.540	766	716	0.935	520	478	0.919	700	620	0.886
	1031	860	0.834	947	822	0.551	674	787	0.900	606	519	0.856	489	406	0.830
	1214	854	0.703	1066	565	0.526	796	743	0.933	484	412	0.851	1413	1150	0.814
	1031	952	0.923	927			604	566	0.937	927	847	0.914	693	627	0.905
8 Pa	1306	1057	0.810	634	454	0.716	844	796	0.943	476	441	0.926	566	492	0.869
	1077	893	0.829	671	415	0.618	640	603	0.942	609	550	0.903	942	882	0.936
	1140	1015	0.890	582	417	0.704	761	674	0.886	524	475	0.906	868	725	0.835
	1017	917	0.902	587	363	0.618	515	515	1.000	483	430	0.890	1275	1010	0.792
	1017	924	0.909	510	337	0.661	693	645	0.931	501	470	0.938	1332	1064	0.799
10 Pa	1015	995	0.980	956	669	0.700	784	691	0.904	539	517	0.959	1337	1276	0.954
	1038	1059	1.022	978	709	0.727	705	680	0.936	574	552	0.962	1693	1365	0.806
	1052	868	0.825	1037	785	0.757	913	907	0.993	600	513	0.856	987	789	0.799
	974	899	0.923	973	771	0.792	767	758	0.988	464	392	0.845	1319	1186	0.899
	1021	964	0.944	639	532	0.833	713	670	0.940	680	651	0.957	1863	1826	0.980
12 Pa	1242	1081	0.870	993	740	0.745	823	810	0.984	883	773	0.875	1475	1419	0.962
	1359	1179	0.868	983	788	0.802	819	810	0.989	1261	1196	0.950	2206	1923	0.872
	1285	1303	1.014	1383	1025	0.741	946	885	0.937	942	838	0.890	1864	1636	0.877
	1228	1181	0.962	1287	965	0.750	760	727	0.957	668	632	0.946	2580	2400	0.930
	1348	1378	1.021	1261	1001	0.794	954	952	0.998	870	866	0.995	1429	1471	1.029

Table L-4 Summary of Particle Penetration Experiments for L-Shaped Cracks

Crack Length, L	60 mm								
Crack Height, H	0.505 mm								
Particle Diameter	1.0 μm			1.4 μm			1.8 μm		
ΔP	Entrance	Exit	P	Entrance	Exit	P	Entrance	Exit	P
2 Pa	945	892	0.944	877	647	0.738	125	94	0.752
	810	732	0.904	703	546	0.777	235	153	0.651
	763	705	0.924	580	495	0.853	504	350	0.694
	804	701	0.872	386	308	0.798	256	205	0.801
	813	720	0.886	489	368	0.753	147	114	0.776
4 Pa	831	802	0.965	531	444	0.836	361	340	0.942
	740	702	0.949	686	610	0.889	399	328	0.822
	920	935	1.016	919	913	0.993	306	255	0.833
	825	766	0.928	369	368	0.946	420	326	0.776
	749	715	0.955	824	764	0.927	512	435	0.850
6 Pa	889	862	0.970	952	898	0.943	508	433	0.852
	967	948	0.980	804	705	0.877	684	605	0.885
	1044	987	0.945	779	772	0.991	643	626	0.974
	856	872	1.019	698	629	0.901	485	461	0.951
	972	923	0.950	889	874	0.983	640	633	0.989
8 Pa	866	853	0.985	569	551	0.986	499	468	0.938
	853	819	0.960	760	735	0.942	572	560	0.979
	882	796	0.902	655	658	1.005	937	876	0.935
	594	628	1.057	452	430	0.951	616	559	0.907
	699	664	0.950	377	328	0.870	504	476	0.944
10 Pa	788	792	1.005	1333	1272	0.954	882	825	0.935
	880	824	0.936	1179	1162	0.986	1520	1534	1.009
	1078	1004	0.931	939	880	0.937	934	896	0.959
	771	784	1.017	656	666	1.015	929	875	0.942
	684	712	1.041	661	586	0.887	1395	1271	0.911
12 Pa	1267	1209	0.954	806	787	0.976	1198	1135	0.947
	1654	1703	1.030	770	687	0.892	964	892	0.925
	1954	1891	0.968	894	873	0.977	701	636	0.907
	1226	1156	0.943	1326	1297	0.978	797	818	1.026
	1234	1201	0.973	1308	1239	0.947	1113	1092	0.981